# Modelling and Compliance Control of a Linkage Chewing Robot and Its Application in Food Evaluation

A thesis presented in partial fulfilment of the requirements for the degree of

**Doctor of Philosophy**
**in**
**Engineering**

at Massey University, Albany

New Zealand

**Cheng Sun**

2012

# ABSTRACT

Many instrumental techniques have been developed to provide quantitative data on food texture as an alternative to sensory methods for food texture characterisation. However, most instrumental measurements are not able to simulate whole chewing sequences, the jaw movements and the influence of teeth geometry involved in mastication. Several devices have been proposed to simulate human mastication but they either cannot simulate human chewing trajectory or are difficult to be controlled. A novel simple linkage chewing robot was previously developed to reproduce human chewing trajectory. The aim of this thesis is to simulate human chewing behaviour by applying compliant chewing forces and velocity on the food during mastication.

In order to allow the entire mastication process to be continuously reproduced, the chewing robot was upgraded with a 3D force sensor, an automatic food manipulation system with 3D carved teeth and a spring mass system to apply passive force control. Aiming at the compliant chewing, the dynamic model of the chewing robotic system was developed, including the linkage mechanism, gear transmission, DC motor and food models. The simulation model of the chewing robot was validated by comparing the simulated torques and the experimental torques of the crank required to drive the robot. A control algorithm to achieve the compliant chewing for the robot is formulated in terms of adaptive fuzzy logic control, and is able to achieve fast coordination of chewing velocity and forces required for different type of foods, and validated in simulations in terms of chewing velocity and forces. The chewing experiments with the robot chewing on real foods were carried out and analyzed in terms of the adaptation of chewing velocity and force to the food texture changes during chewing process. Both simulation and experimental results show that the proposed algorithm is adaptive and able to simulate human chewing behaviour on foods with different texture, which indicates the usefulness of the developed robot in food texture evaluation.

The chewing robot developed has been used routinely in our laboratory and exhibited a great potential as a tool for the evaluation of food properties and bolus preparation.

# ACKNOWLEDGEMENT

Pursuing a Ph.D. project is a very unique experience, combined with excitement, hardships, frustration, encouragement and many people’s help. Although it‘s not enough to express my gratitude in words to all those people who helped me, I would still like to gratefully thank all these people.

First I would like to sincerely thank my three supervisors. To my supervisor Professor Peter Xu, I really appreciated that he gave me the opportunity to be his Ph.D. student in the fourth year of my Bachelor degree. This really encouraged me a lot and gave me big confidence. His guidance and support through the whole PhD program made me feel confident to overcome any difficulty. At the last stage of my thesis, he helped me review the thesis and gave me advices on possible improvements. I would like to thank my supervisor Professor John Bronlund for his knowledge in food background, his advice and great ideas. I would like to give special thanks to Professor Loulin Huang for his expertise in control system.

I would like to thank Riddet Centre of Food Research and the New Zealand Foundation for Research for funding this research. I would like to thank Marco Morgenstern from Plant and Food Research Ltd who has helped me a lot on the experiments. I would like to thank Dr Kylie Forster and Christine Flynn of Institute of Food, Nutrition and Human Health, Massey University, who provided the human chewing experiment results. I would like to thank Dr Scott who worked together with me in the beginning of the project and helped me collected necessary data for my case study. I would like to thank the workshop staff from both Palmerston North campus and Albany campus for their excellent work in building the mechanical parts.

I would like to express my appreciation to my parents, my wife’s parents and my brother in law. Their supports and understandings enable me to concentrate on my research, especially after I worked full time and studied my Ph.D. in part time. I would like to specially thank my father who patiently mentored me on my research.

Last but not least, I am terribly grateful to my wife Yin who has supported, encouraged, motivated, strengthened and most importantly loved me through my long journey of pursuing the Ph.D. project. I really appreciate her for her patience, understanding and great effort, especially during her pregnancy. I owe her big time. Now I’m free to accompany her in the weekends.

# *RELATED PUBLICATIONS*

Sun, C., Bronlund, J., Xu, W., & Huang, L. A linkage chewing machine for food texture analysis. *International Journal of Intelligent Systems Technologies and Applications*, 8(1), 303-318.

Sun, C., Bronlund, J., Huang, L., & Xu, W. Adaptive fuzzy control on a chewing machine, accepted by *The 5th IEEE International Conference on Cybernetics and Intelligent Systems*, pp. 202 – 207, Qingdao, China, September 2011.

Sun, C., Bronlund, J., Huang, L., Morgenstern, M. P., Xu, W., & Hutchings, S. C. Potential use of a novel simple chewing robot for food evaluation. *International Journal of Food Engineering.* Submitted in 2011

Sun, C., Xu, W., Bronlund, J., & Morgenstern, M. P. Dynamics and Compliance Control of a Linkage Robot for Foods Chewing. *Transactions on Industrial Electronics.* Manuscript submitted in 2012

## *TABLE OF CONTENTS*

## *LIST OF FIGURES*

# *LIST OF TABLES*

# 1. INTRODUCTION

## 1.1. Background

Mastication is a complex process that occurs as the food is crushed and ground by teeth and brought into a condition which is safe to be swallowed. During the chewing process, food particles are positioned on the surface of teeth by the cheek and tongue. As mastication continues, food is ground into fine particles, mixed with saliva, and formed into a bolus. During this process, the structure and properties of the food change dynamically. The term “texture” is used to describe these how a food properties respond during the mastication process with respect to all mechanical and tactile (and where appropriate visual and aural) properties of the food (Torrance et al., 2006). The extent to which the food is deformed, the forces and the direction of these forces that the food imparts in resisting this deformation and the rate the food is broken down during mastication are all important aspects of food texture.

Food texture can be measured by either sensory methods or instrumental methods. The consumer of a food is the ultimate judge of a foods texture and this assessment will utilise all the five senses. As such one of the key tools in evaluating food texture is through trained or untrained human sensory panels. Carefully defined textural attributes of foods can be assessed using these panels to identify changes or differences in food texture between samples. Because of inherent variability in human subjects, responses will vary from subject to subject, over the course of a day, or due to preference of the subject. As a result multiple subjects with appropriate repetition are required in sensory evaluation. Despite this, the science has developed to a point where reproducible and reliable testing can be performed (Bourne, 2002). Although sensory methods enable direct measurement of perception, there are many disadvantages, such as variability from person to person and variability from time to time, generally time consuming, expensive and not subject to absolute standards, only a limited daily sample throughput and the food sample must be acceptable to panel members, etc.

A number of instrumental testing techniques have been developed to overcome these difficulties. These include empirical tests where a mechanical property is measured in well defined conditions; imitative tests, which simulate aspects of oral processing; and fundamental tests, which measure engineering properties such as Youngs modulus (Torrance et al., 2006). For example, General Foods Texturometer analyzes food texture by compressing a bite-size piece of food two times in a motion that simulates jaw movement, and extracts the textural parameters from the resulting force-time curve (Bourne, 2002). Other universal testing machines, such as Instron and TA.XT2 Texture Analyzer, also have the same principle for texture evaluation but with a modified analysis such as the commonly used food science tool, texture profile analysis, TPA (Bourne, 2002). However, most instrumental measurements of food texture focus on initial food properties and rely on simple one dimensional crushing. They are not able to simulate complete complex functions and movements involved during mastication.

## *1.2. The Linkage Chewing Machine*

A linkage chewing machine was required for in-vitro digestion assays for glycaemic load as part of the Lifestyle Foods programme by Crop & Food Research Ltd. The chewing machine was then developed to simulate human chewing behaviour in terms of kinematics requirements and forces.

### 1.2.1. *The Design Specifications of The Chewing Machine*

First of all, the chewing machine was specified to reproduce the chewing trajectory of the first molar in 2D space, since the chewing is mostly performed on the molar teeth. A typical trajectory can be defined by vertical and lateral displacements and opening (exit) and closing (entry) angles (Figure 1.1). The chewing machine was specified by the parameters of a frontal chewing trajectory in Table 1-1. In the sagittal plane, the human chewing trajectory was approximated as a straight line. Therefore, the sagittal trajectory in chewing machine was required to have an angular adjustment up to 30 degree from vertical chewing to match that in human. Secondly, the chewing machine should be able to produce any trajectory between lateral and vertical trajectories to evaluate different foods. Furthermore, the machine was required to apply up to a maximum force of 150N on food sample during chewing (D. J. Anderson, 1956).

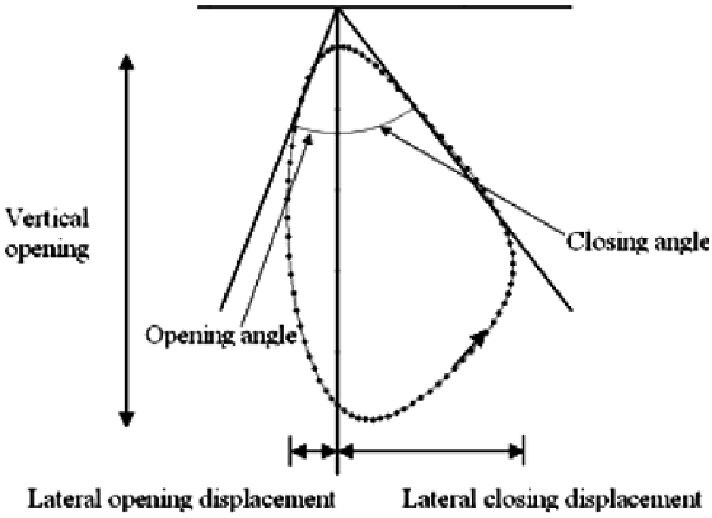

Figure 1.1 A tooth trajectory and its defining parameters (Xu et al., 2008)

Table 1-1 Values of the trajectory parameters for lateral and vertical chewing in frontal plane (Xu et al., 2008)

| | Lateral chewing | Vertical chewing |
|---|---|---|
| Closing angle (°) | 46.6 | 72.5 |
| Opening angle (°) | 113.1 | 78 |
| Total angle (°) | 66.5 | 5.5 |
| Vertical opening (mm) | 14.6 | 15.1 |
| Lateral displacement in opening (mm) | 1.1 | 0.4 |
| Lateral displacement in closing (mm) | 4.0 | 3.1 |
| Cycle time (s) | 0.77 | 0.7 |
| Occlusal time (s) | 0.12 | 0.16 |
| Opening/closing time (s) | 0.65 | 0.54 |

### 1.2.2. ***The Linkage Mechanism Design***

A four-bar linkage (Figure 1.2) consists of crank link ‘a’, coupler link ‘b’, follower link ‘c’ and ground link ‘d’. The point ‘P’ on the coupler is used to trace 2D trajectory. In order to achieve different trajectories, the ground link which drives the coupler with the point ‘P’ can be made adjustable manually.

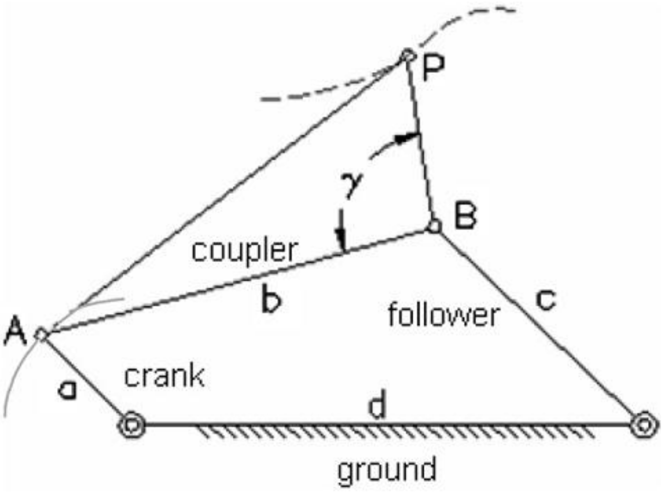

Figure 1.2 Kinematics parameters for a four-bar linkage (Thompson, 1999)

The Cedarville engineering atlas (Thompson, 1999) was used to find suitable trajectories that have entry and exit angles that closely match a lateral chewing cycle as specified in the above section. The possible trajectory was marked down when it matches the desired occlusal angles of a lateral chewing trajectory. Vertical chewing trajectories are required by further varying the ground link length. The final solution of the lateral chewing trajectory is shown in Figure 1.3, where the link parameters are shown on top with varying ‘BP’ length. The ratios of the link lengths in the final design was Crank link ‘a’ = 1, Follower link ‘c’ = 3, Ground link ‘d’ = 3.8-5 to perform vertical and lateral chewing, Coupler link ‘b’ = 3.5, Coupler distance ‘BP’ = 3, Coupler angle ‘$\gamma$’ $=60^\circ$. In order to build the linkage mechanism as compact as possible, 10mm was chosen as the smallest physical crank link length. And then the chewing trajectories produced by the linkages were compared with human chewing trajectories in Table 1-2. From this table, the trajectory produced by linkage closely matches with that by human while still having reasonable trajectories for the vertical chewing.

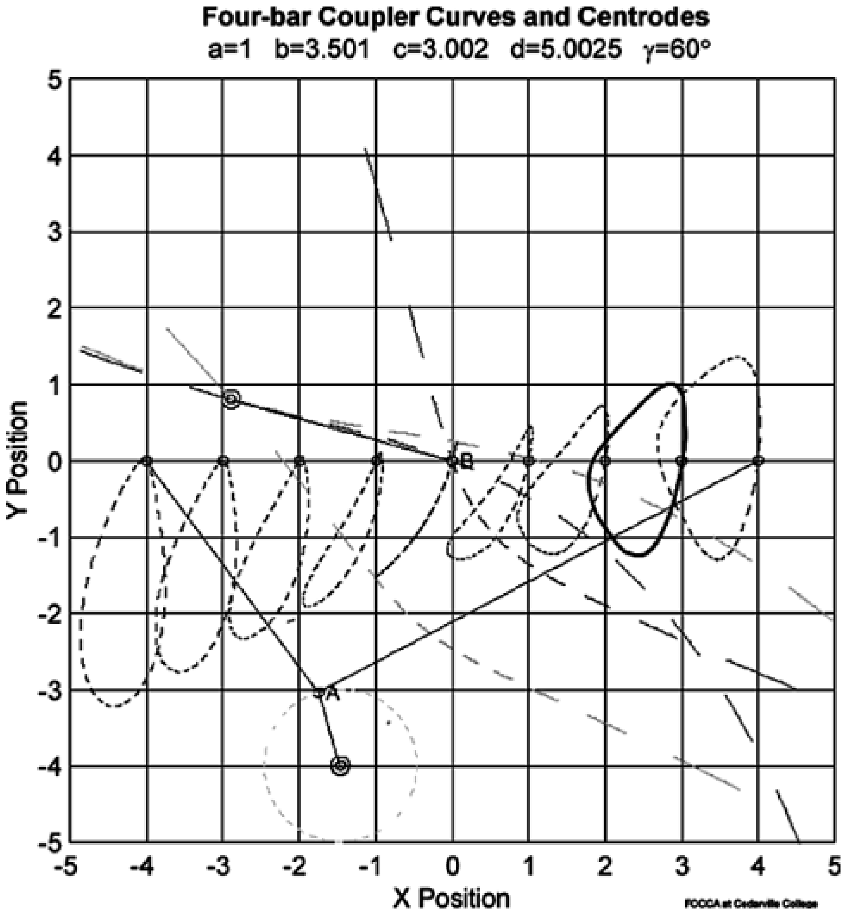

Figure 1.3 Produced trajectories by the four-bar linkage (Xu et al., 2008)

Table 1-2 Comparison between the trajectories by human and linkages (Xu et al., 2008)

| | Lateral chewing | | Vertical chewing | |
|---|---|---|---|---|
| | Human | Linkage | Human | Linkage |
| Closing angle (°) | 46.6 | 45 | 72.5 | 99 |
| Opening angle (°) | 113.1 | 112 | 78 | 105 |
| Total angle (°) | 66.5 | 67 | 5.5 | 6 |
| Vertical opening (mm) | 14.6 | 23 | 15.1 | 34 |
| Lateral displacement in opening (mm) | 1.1 | 3 | 0.4 | 3 |
| Lateral displacement in closing (mm) | 4.0 | 9 | 3.1 | 0 |

Three trajectories produced by the linkage with the ground link length of 38mm, 44mm and 50mm are shown in Figure 1.4. It can be seen that as the length of the ground link increases, the occlusal position shifts, the vertical opening displacement decreases and the lateral displacement increases. This proves that the linkage is able to reproduce different chewing trajectories. Figure 1.5 shows the final four-bar linkage 3D model where the adjustable ground link was achieved by rotating a threaded rod.

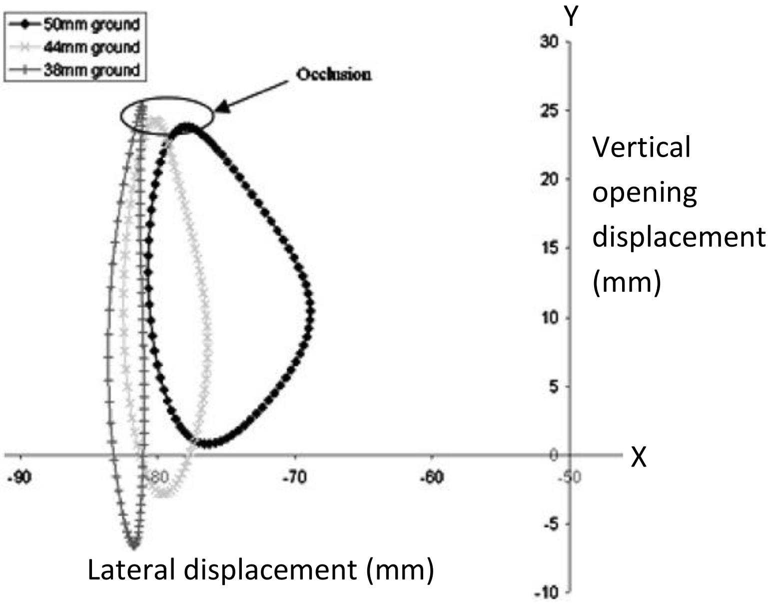

Figure 1.4 Three chewing trajectories produced by the four-bar linkage (Xu et al., 2008)

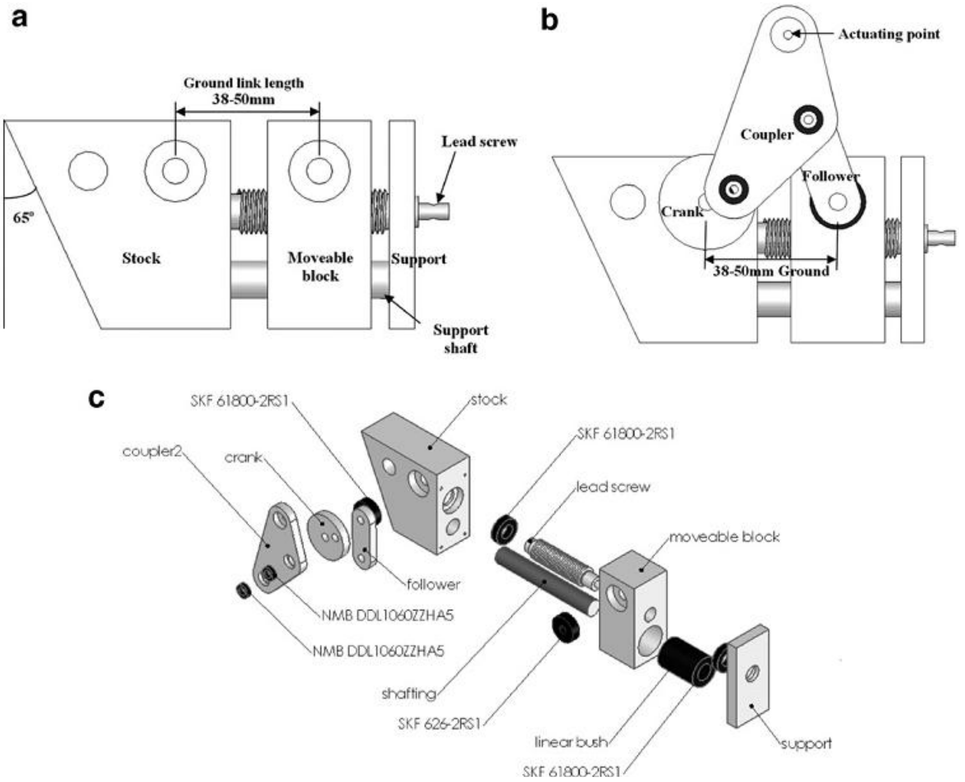

Figure 1.5 Construction of the adjustable four-bar linkage: a) adjustable ground link; b) adjustable four-bar linkage; c) major parts chosen. (Xu et al., 2008)

In order to keep the mandible or teeth in same proper orientation, another two links (links 5 and 6 in Figure 1.6) were added to the four-bar linkage, thus making it a six-bar linkage. The two links are connected by a sliding joint, and link 5 is attached onto the coupler by a revolute joint and link 6 is attached onto the ground by another sliding joint. The mandible teeth are mounted to link 5 and forced to move in a plane constrained by the two sliding joints. Therefore, by tilting the base of the six-bar linkage, the chewing trajectories in the sagittal plane of an angle ranging between $0^\circ$ and $30^\circ$ to the horizontal plane can be produced. The chewing device was constructed symmetrically with two identical four-bar linkages on each side for dynamics balance. The cranks of the two four-bar linkages were mounted on a shaft driven by a motor via a spur-gear train.

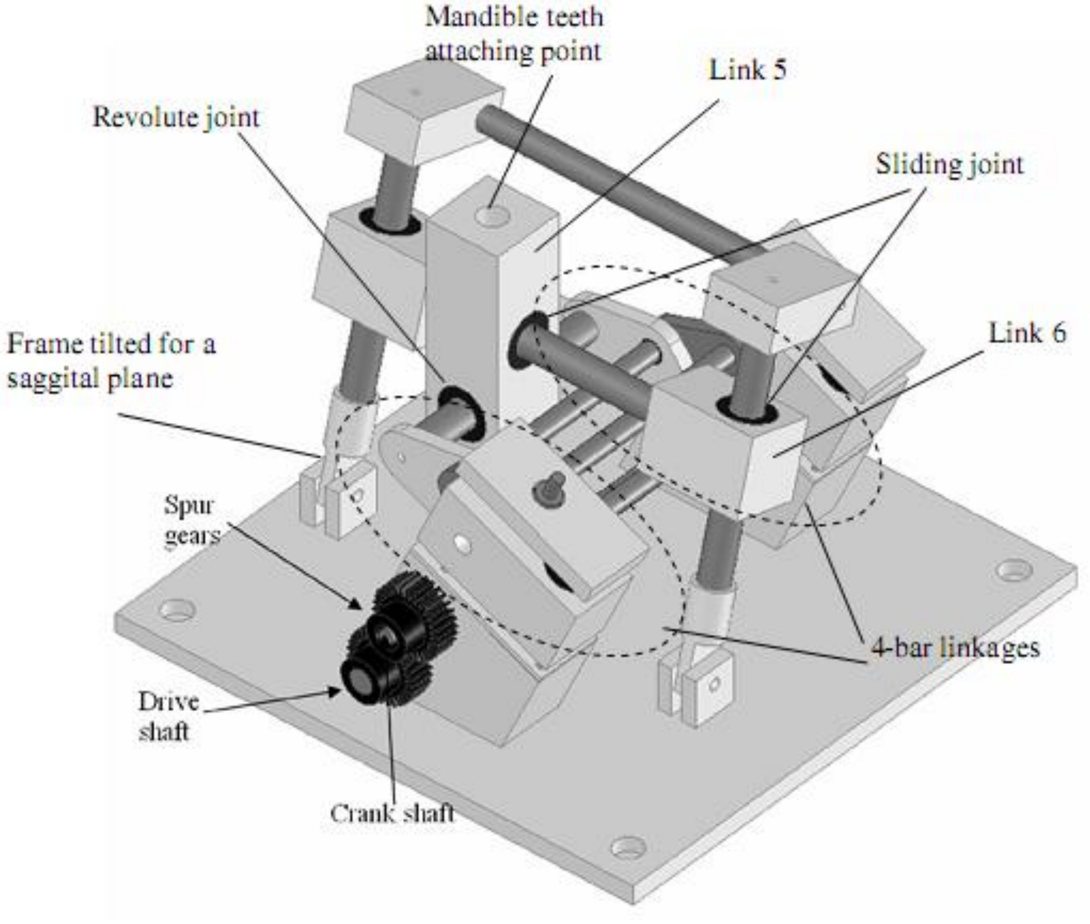

Figure 1.6 Design of a six-bar linkage mechanism (Xu et al., 2008)

While the six-bar linkage was being constructed, anatomical teeth with attachment mechanism, maxilla teeth repositioning table, a shock absorber which prevents excessive impact force and a simple food retention mechanism collecting chewed food particles are included. For the convenience of collecting chewed food particles, the linkage is inverted with mandible teeth up and the maxilla teeth down, as shown in Figure 1.7.

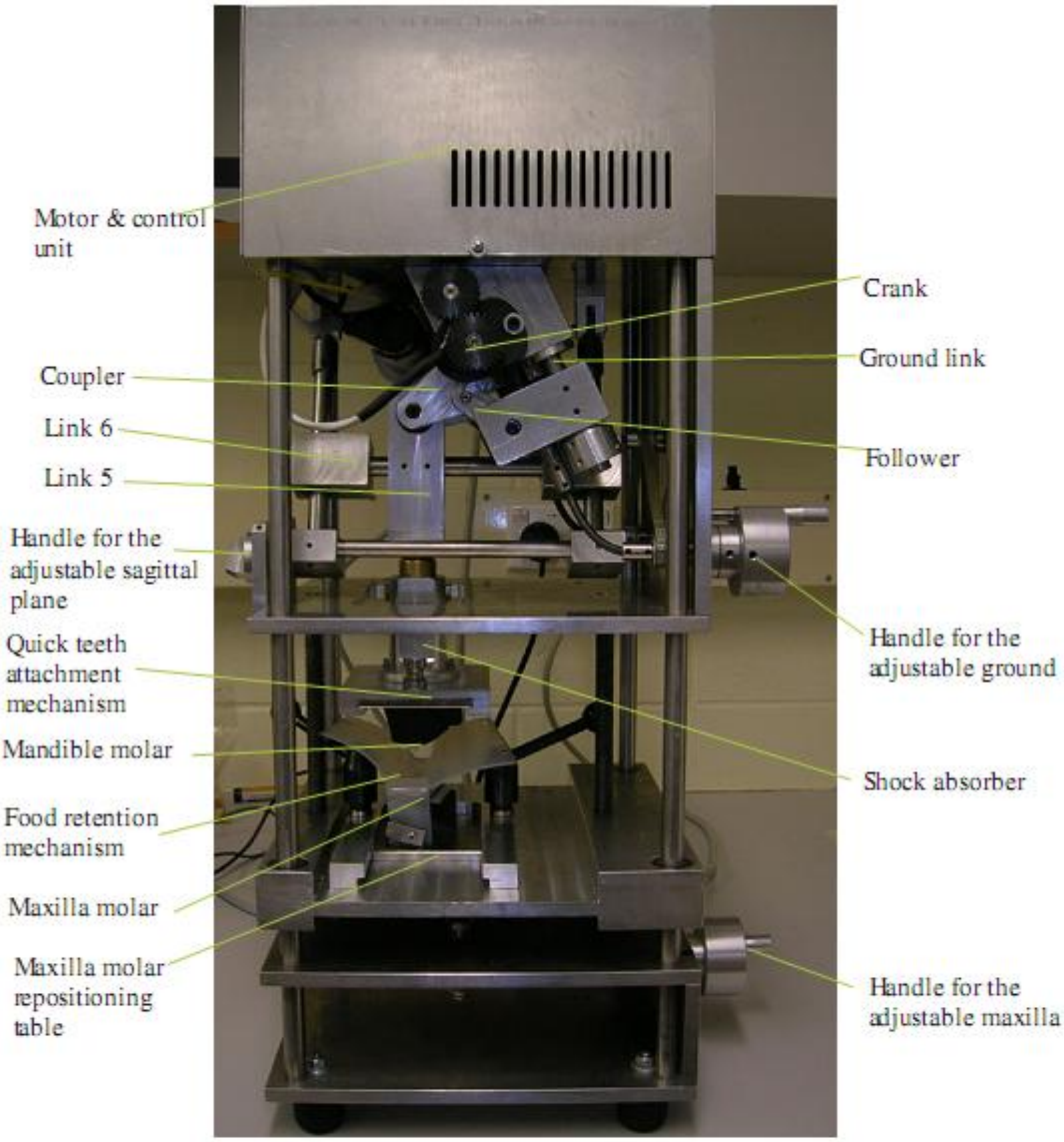

Figure 1.7 The original chewing machine (Xu et al., 2008)

### 1.2.3. *Motion Planning*

With regard to the chewing trajectory (Figure 1.4), the molar teeth moves at constant velocity during the occlusion phase, and speeds up from occlusal velocity to a maximum velocity and back down to occlusal velocity in a specified time. The occlusion starting and ending positions was found by a horizontal line of 0.5mm down from the maximum intercuspal position (Ogawa et al., 2001). 36° turn of crank shaft was found during entire occlusal phase with the help of simulation model in SolidWorks. As the occlusal time is 0.12s (Table 1-1), the occlusal velocity of the crank is 300°/s. The start angle and final angle of crank are found 18° and 342° (Figure 1.8a). Considering a 1:42 gear reduction between the motor and the crank, the occlusal velocity, start angle and final angle of the motor shaft are 12600°/s, 756° and 14364°, respectively. The opening/closing time is 0.65s (Table 1-1). Thus, a cubic trajectory of the motor shaft is found as (Hiiemae & Palmer, 1999)

$$\theta(t) = 756 + 12{,}600t + 38{,}471t^2 - 39{,}457t^3 \tag{1}$$

$$\dot{\theta}(t) = 12{,}600 + 76{,}942t - 118.371t^2 \tag{2}$$

$$\ddot{\theta}(t) = 76{,}942 - 236{,}742t \tag{3}$$

The above planned trajectory is for the lateral chewing only. The actual planned trajectory is decided by occlusal angle, occlusal time and opening/closing time (Figure 1.8b), which can be set up in the motion control GUI described in the following section.

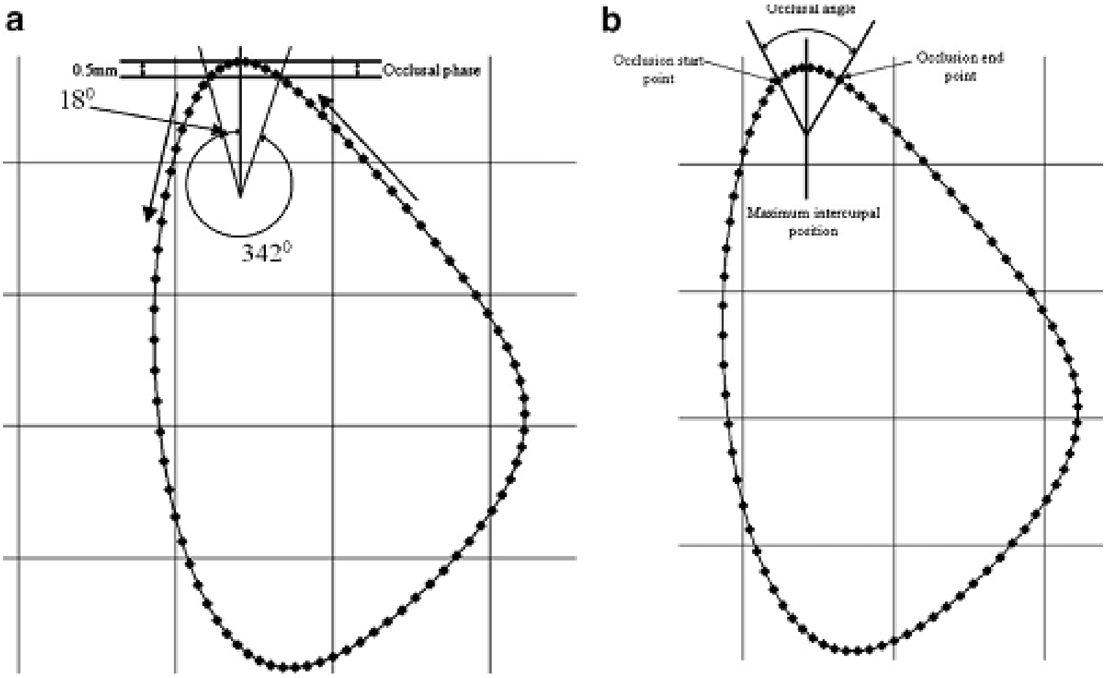

Figure 1.8 Definition of the occlusal phase (Ogawa et al., 2001)

### 1.2.4. *Control System and Software*

A GUI in LabView is made to allow the users to operate the device (Figure 1.9). A Maxon motor control card (4-Q-EC Servoamplifier DES 50/5) that could easily be interfaced with LabView was chosen to control the motor. The control card was connected to the computer through a RS-232 serial cable. The software also allows the operator to specify different velocity profiles for different foods by varying the parameters (Figure 1.10).

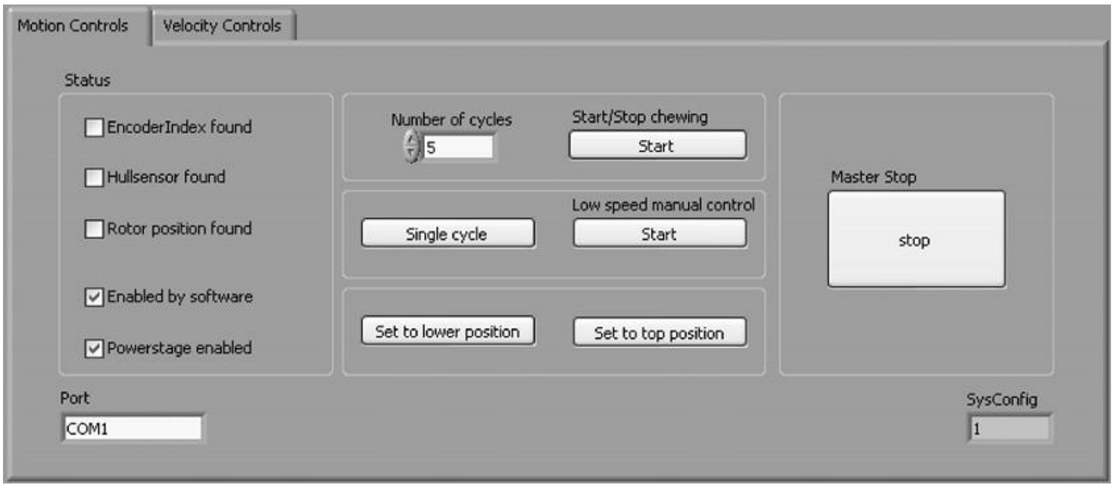

☐ EncoderIndex found
☐ Hullsensor found
☐ Rotor position found
☑ Enabled by software
☑ Powerstage enabled

Number of cycles: 5

Port: COM1

SysConfig: 1

Figure 1.9 GUI implementing the operational functions (Xu et al., 2008)

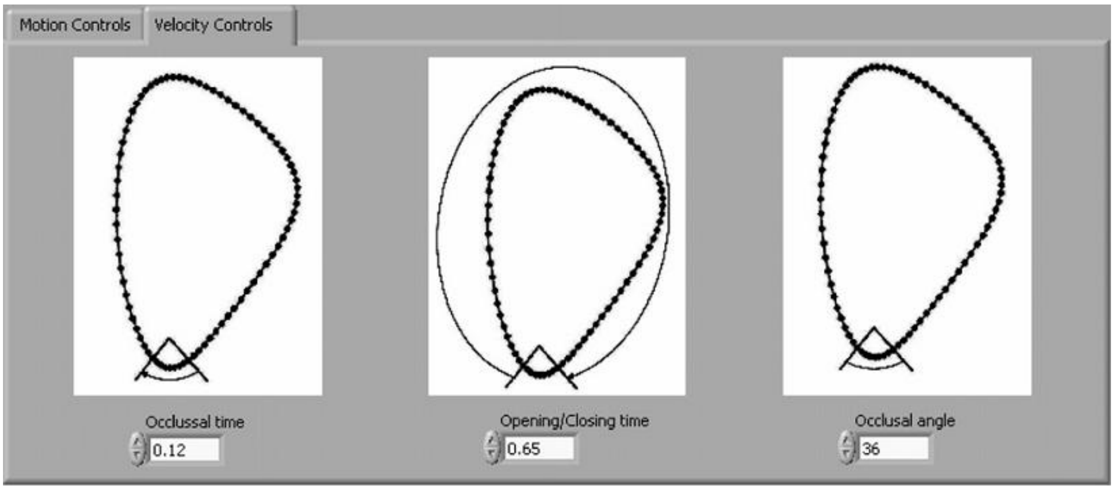

Occlussal time: 0.12

Opening/Closing time: 0.65

Occlusal angle: 36

Figure 1.10 GUI for specifying the velocity profile (Xu et al., 2008)

### 1.2.5. *Preliminary Experiment and Results*

A cereal bar was tested in the chewing machine and the results in particle size distribution were compared with those by human subjects. 1g slice was placed on the lower teeth. Proper amount of artificial saliva was added after the machine runs for the first two cycles. Then the food particles were repositioned on the teeth every five cycles, until the total number of cycles reached that in human chewing. The bolus was then collected and washed through 1.4mm and 0.25mm sieves and dried. The results in the fraction of particles passing through 1.4mm sieve were compared between the chewing machine and human (with 2g and 4g samples) (Figure 1.11). It can be found that the result by chewing machine has similar magnitude with that by humans.

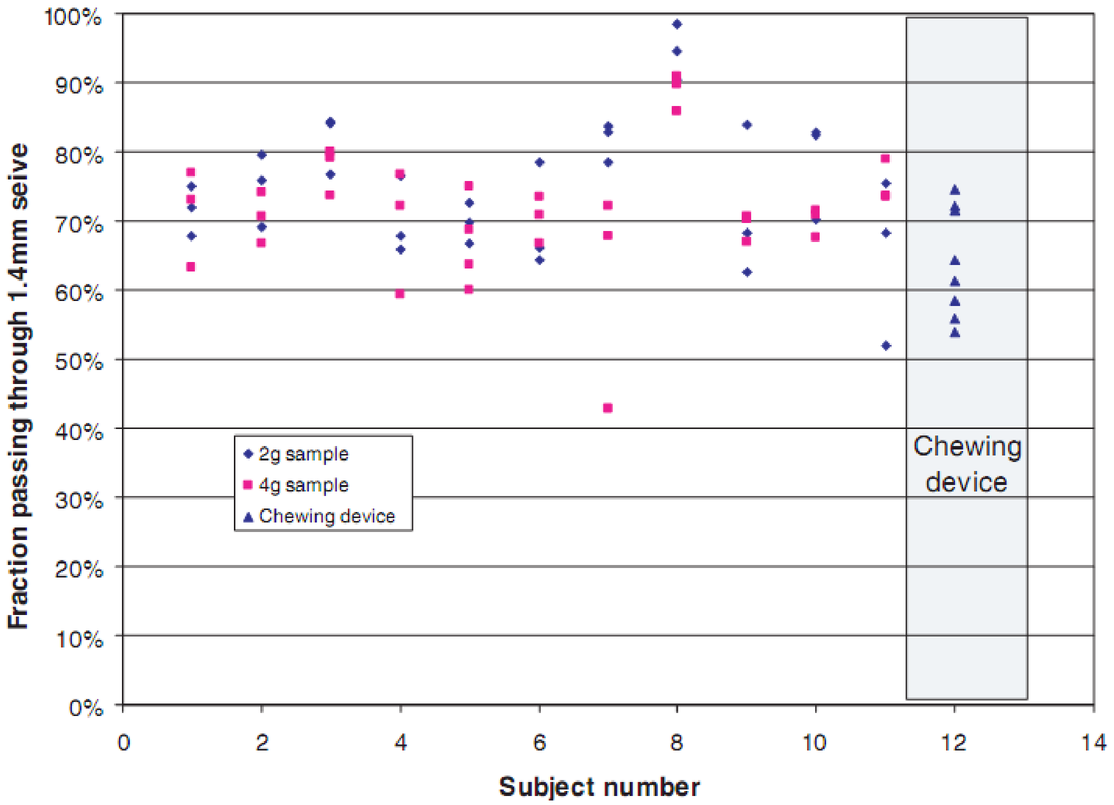

Figure 1.11 Comparison of chewing results between human (2g and 4g samples) and chewing machine (Xu et al., 2008)

### 1.2.6. ***Problems and Conclusions***

The six-bar linkage mechanism generates some play which is caused by the slackness from four linear bushes. The slackness directly affects the movement of the upper teeth during occlusion and possibly influences the chewing results. The current shock absorber generates the force profile during occlusion which is just a sudden high force, followed by a rapid reduction. This will not achieve the specified occlusal force profile in the future. The anatomically correct teeth cannot perform a perfect occlusion during chewing, which may result in inefficient chewing. The current food retention system cannot keep all the food particles on the teeth during chewing process. The operator has to stop the machine every a few chewing cycles to reposition the falling particles.

More validations of chewing are required before it becomes a routine laboratory apparatus for the purposes of pre-processing foods. The chewing device will be a useful tool to quantify texture in foods and provide standardised sample preparation for nutritional analysis.

## 1.3. Aim and Objectives

The aim of the research is to design a compliant force control on the current chewing robot to simulate human chewing behaviour and to enhance to a standard for food bolus preparation and texture analysis.

The aims will be achieved by division into four core objectives:

1. *Improvement on the chewing robot for the compliant force control*
2. *Dynamics modelling and experimental validation of chewing robotic system*
3. *Compliance control system design*
4. *Evaluation of chewing robot through the experiments with real food*

Each objective consists of a number of sub-tasks as outlined below.

## 1.4. Outline

This thesis outlines the process for the design and validation of compliant force control on the chewing robot. Chapter 2 includes the literature review for the background of human mastication system and food knowledge required. Chapter 3 contains the improvement required on the existing chewing robot to implement the compliant force control. Passive compliant force control was realized by implementing a spring-mass system in the upper teeth. The design of a food manipulation system was included in this chapter for food bolus preparation and texture analysis. Chapter 4 includes the kinematics and dynamics analysis of chewing robot, the development of the simulation model and food models in MATLAB. Chapter 5 includes the development of adaptive fuzzy control system and implementation in the simulation model of chewing robot in MATLAB. Chapter 6 contains the evaluation of chewing robot in real experiment and the analysis of chewing results in terms of food aspect. Chapter 7 concludes the thesis with the contributions presented within.

## 1.5. Major Contributions

There are four major contributions made in this thesis. The first contribution is to enhance the original chewing robot to a potential device where the entire mastication process can be continuously reproduced so that the masticatory efficiency and food dynamics are assessed quantitatively. This is achieved by installing a force sensor under the lower teeth to measure 3D chewing forces in real time, developing a food manipulation system based on the functionality of the human tongue to allow continuous chewing, designing a 3D carved teeth based on 3D modelled human teeth and developing a spring-mass system to achieve passive compliance control for desirable chewing force profiles of foods with different texture. The improvement on the chewing robot is essential for the implementation of compliance force control.

The second contribution is to develop the dynamic model of the chewing robotic system, which is composed of the linkage mechanism in the chewing robot, DC motor and food models of marshmallow and peanuts, and validate the simulation model of the chewing robot by comparing the simulated torques and the experimental torques. The chewing robotic system model is used for validating the compliance force control algorithms developed for the chewing robot.

The third contribution is to design the adaptive fuzzy force control algorithms to achieve the compliance force control for the chewing robot and validate through the chewing experiments by comparing the chewing results in particle size distributions between human and chewing robot. The adaptive fuzzy control is proposed to simulate human chewing behaviour on foods with different texture.

The last contribution is to carry out large amounts of chewing experiments of the chewing robot with real food to prove the usefulness of the chewing robot in food evaluation by analysing and comparing the chewing results between the chewing robot and humans in particle size distributions. An effective method to measure particle size distributions through image analysis has been investigated. The results prove the potential use of the chewing robot for the evaluation of food properties and bolus preparation.

# 2. LITERATURE REVIEW

## 2.1. Introduction

This chapter reviews available literature on the human mastication process, what elements are required to be replicated, and what is currently the state of the art in robotic chewing devices.

Before carrying on this project to make the chewing robot prepare the food bolus like human does, the human masticatory system has to be reviewed. To reproduce the chewing results which are similar to human, the masticatory performance which affect the chewing results is reviewed. Force control methods have been reviewed to help build the occlusal force control system in the simulation model and then implemented in the real machine. Therefore, the roles of the human masticatory system in the digestion process, factors influencing the masticatory performance and force control methods will be described.

## 2.2. Human Mastication System

### 2.2.1. *Biomechanical Principle*

The human jaw consists of an upper (maxilla) and lower (mandible) jaw. The upper jaw is fixed to the skull. The lower jaw is attached to the skull by muscles. Theses muscles are divided into five muscle groups (Figure 2.1 and Figure 2.2) (Lucas, 2004):

1) *Temporalis* – These muscles are attached from the side of the skull to the top of the lower jaw and help the lower jaw close and move forward and backward.

2) *Masseter* – The masseter muscles are attached between the cheek and the lower back section of the lower jaw and are used to close the mouth and help the lower jaw move laterally.

3) *Medial pterygoid* – The medial pterygoid muscles are attached on the inside of the skull and the lower jaw. They are used to move the lower jaw laterally from side to side and help the mouth close.

4) *Lateral pterygoid* – The lateral pterygoid muscles are attached between the skull and the lower jaw. They are used to move the lower jaw forward and backward.

5) *Digastric* – The digastric muscle which is attached between the chin and the bottom of the skull is used to open the mouth.

The mandible consists of a horizontal part called body and two vertical parts called the rami (Figure 2.3). The mandible is moved by the muscles and pivots around a point on each ramus called condyle. The chewing movement begins when the mandible opens to create a space between the teeth on both jaws.

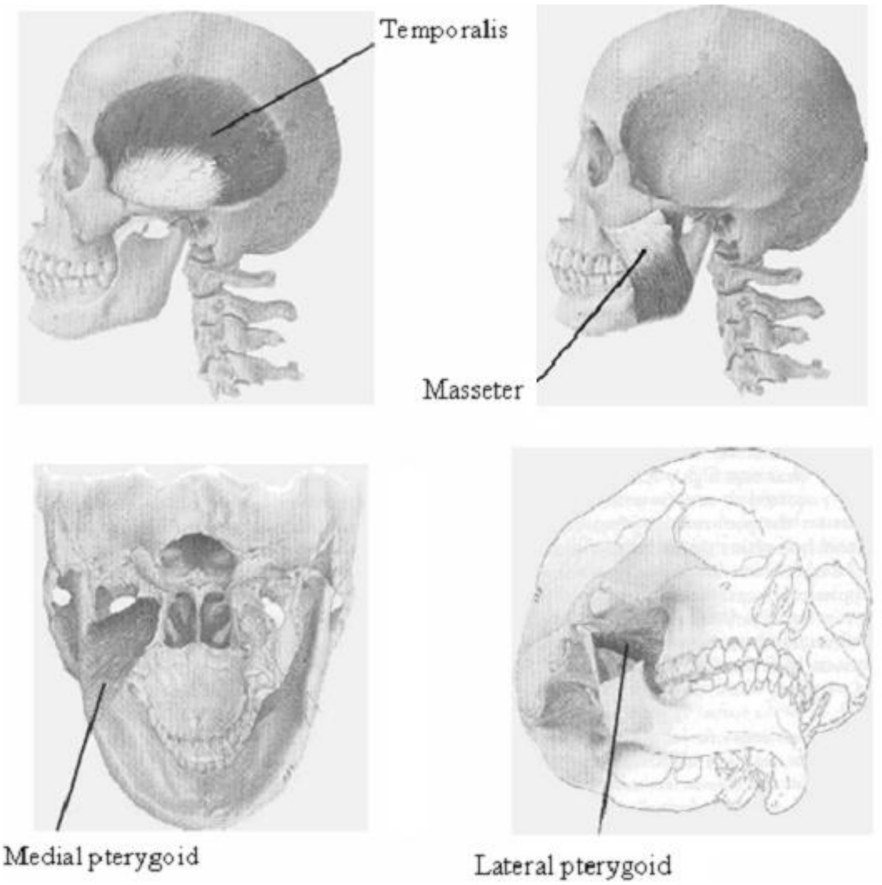

Figure 2.1 Chewing muscle groups (Hannam, 1997)

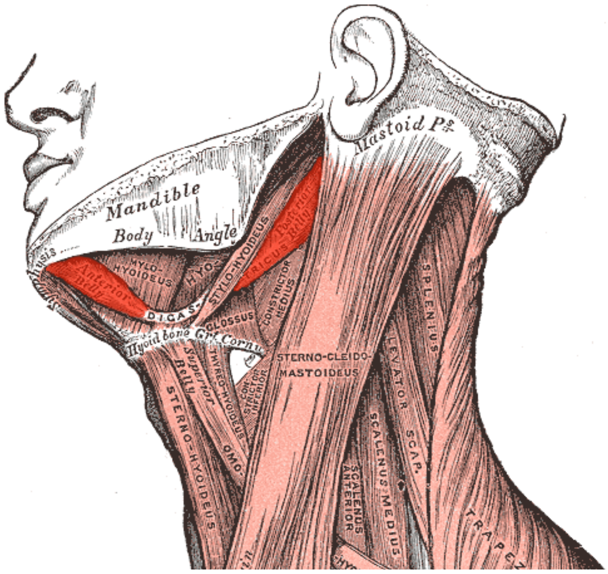

Figure 2.2 Digastric muscle of the neck (red) (Wikipedia, 2012)

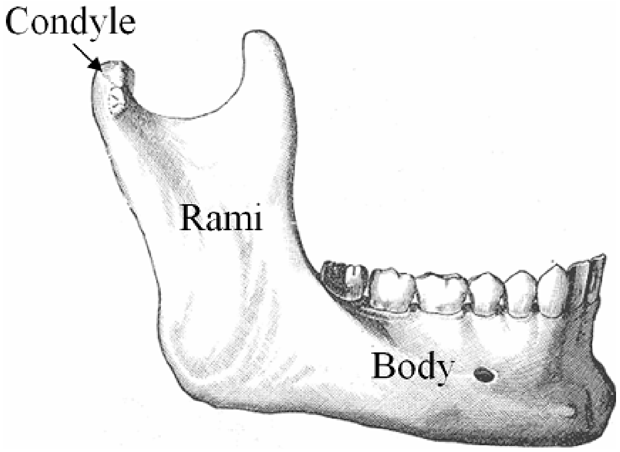

Figure 2.3 The human mandible (Abd-El-Malek, 1955)

### 2.2.2. ***The Chewing Process***

Mastication refers to a very complex process that occurs as the food is chewed and brought into a condition ready to be swallowed. Bourne (2002) described its complexity as a biting-chewing-swallowing action that is a complex stimulation-motor feedback process in which a constant stream of stimuli travels from mouth to brain and a corresponding stream of instructions travels from the brain to the mouth instructing it how to proceed. The masticatory sequence can be divided into three phases (M. R. Heath & Prinz, 1999):

1) Ingestion – transfer of food to between the teeth by the tongue

2) Main sequence – the food is chewed to a bolus through rhythmic chewing

3) Clearance and swallowing

*Chewing cycl*e

Ogawa (2001) divided the masticatory cycle into three separate phases: opening, closing and occlusal phases (Figure 2.4). The occlusal phase is defined as an area below the maximum intercuspation (MI) 0.5mm. The opening phase is from the 0.5mm off MI to the most inferior point of the cycle. The closing phase is from the most inferior point to 0.5mm to the MI.

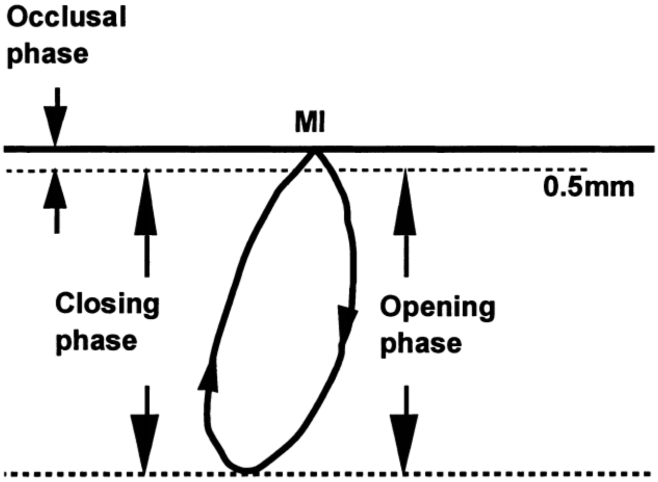

Figure 2.4 Opening, closing and occlusal phase of a chewing cycle (Ogawa et al., 2001)

The cycle shape can be measured in three-dimensional coordinates for different reasons. For example, the chewing cycle shape is recorded to analyse the effect of bolus hardness on masticatory kinematics by Optotrak cameras in Figure 2.5 (K. Anderson et al., 2002). The results show that chewing harder food results in an enlarged overall cycle, but the shape is not changed.

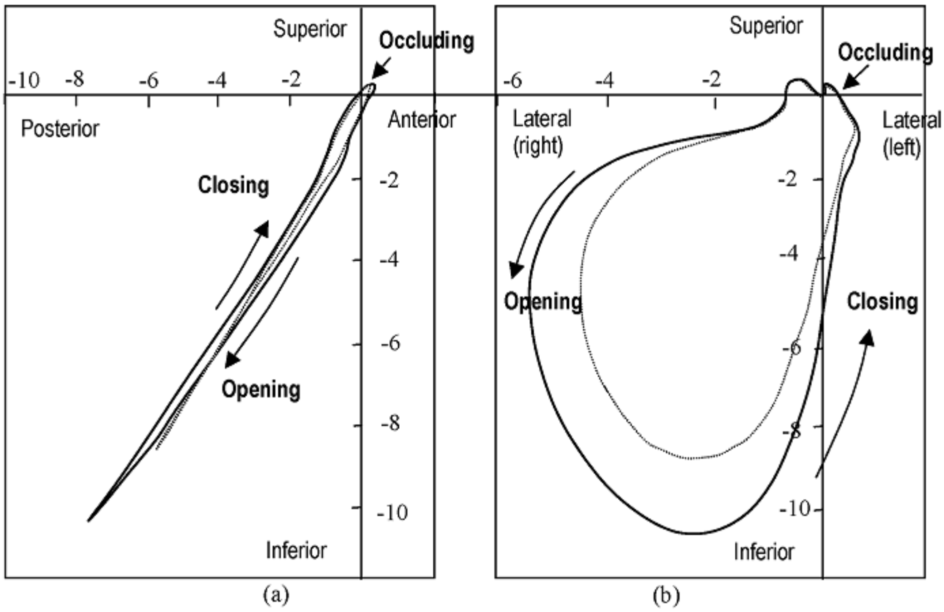

Figure 2.5 Chewing trajectories in sagittal plane (a) and frontal plane (b) on soft and hard chewing gum (K. Anderson et al., 2002)

*Chewing forces*

A few groups have studied forces during chewing. Several studies have used the transducers positioned on the cusp, bridges, crowns and removable prostheses. Anderson (1956) measured the chewing force on a molar tooth during the chewing of three foods: biscuits, raw carrots and cooked meat. The measured force range is 70-150N. Fields (1986) investigated the vertical interocclusal force during simulated chewing in 21 young adults. Their study found that the mean vertical occlusal force is 160N. Kawata and his team (Palmer et al., 1997) measured the tensile and compressive forces exerted on a molar in 3D in vivo during chewing of caramel and peanuts and maximum voluntary clenching (MVC). As shown in Figure 2.6a, during MVC, the compressive force applied on the molar increased dramatically from the start of clenching and reached a plateau. The maximum force was 173.29±15.32N, and the rate of increase was 0.144±0.034Nms$^{-1}$. As shown in Figure 2.6b, during CaC, the force increased and decreased rhythmically. The maximum force was 146.3±14.7N, and the rate of increase was 0.977±0.168Nms$^{-1}$. As shown in Figure 2.6c, during PeC, the force also increased and decreased rhythmically, the same as during CaC. The maximum force was 57.7±35.7N, and the rate of increase was 0.363±0.145Nms$^{-1}$.

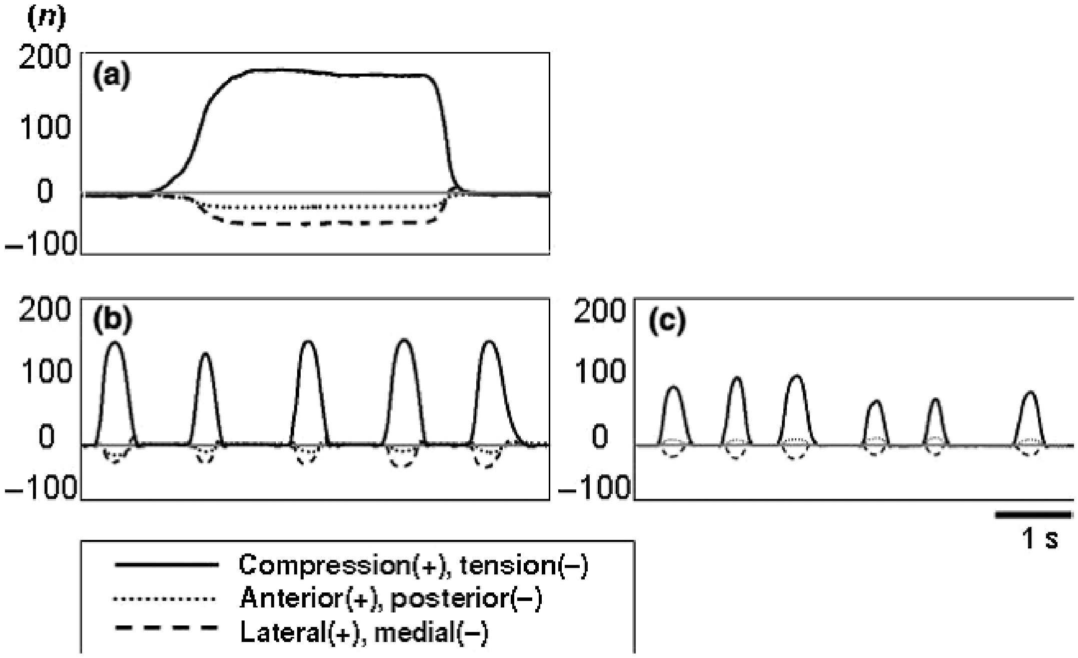

Figure 2.6 Example of calculated 3D force data for (a) MVC, (b) caramel chewing (CaC), (c) peanut chewing (PeC) (Palmer et al., 1997)

Because of different types of food used, measured chewing forces vary among the food types. Studies have found that several properties of food samples influence the chewing forces of humans. Kohyama and Hatakeyama (Kohyama, Hatakeyama, Sasaki, Azuma, et al., 2004; Kohyama, Hatakeyama, Sasaki, Dan, et al., 2004) have clarify both the effects of sample hardness and thickness on human chewing force using silicone rubber as a food model. Using a JIS-A tester that indents sample rubber (Association, 1997), JIS number 10, 30 or 70 represents degrees of mechanical resistance corresponding to hardness in the indention. The highest JIS number corresponds to hard rubber. The chewing force became significantly higher, as the sample hardness increased (Figure 2.7). The chewing force was also related to the food thickness, as shown in Figure 2.8. The chewing force was maximum at 2mm thickness in molar chewing and decreased as the sample thickness increased. The results may be caused due to the narrower jaw opening in the posterior position (Kohyama, Hatakeyama, Sasaki, Azuma, et al., 2004).

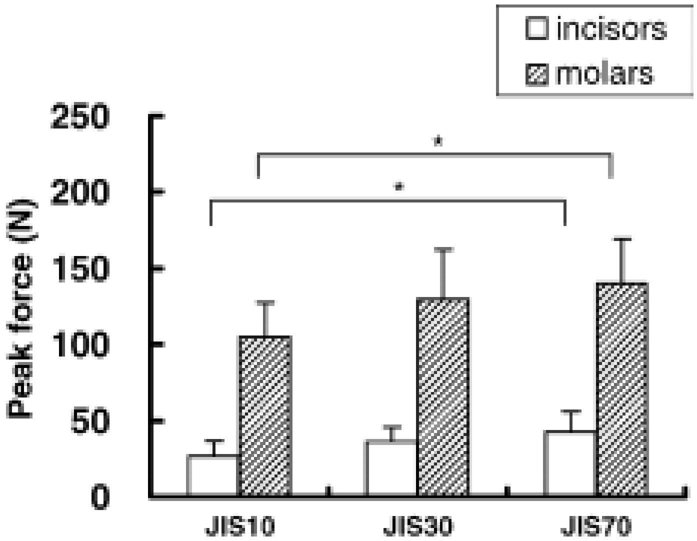

Figure 2.7 Peak force measured for silicone rubber samples of three hardnesses (Kohyama, Hatakeyama, Sasaki, Dan, et al., 2004)

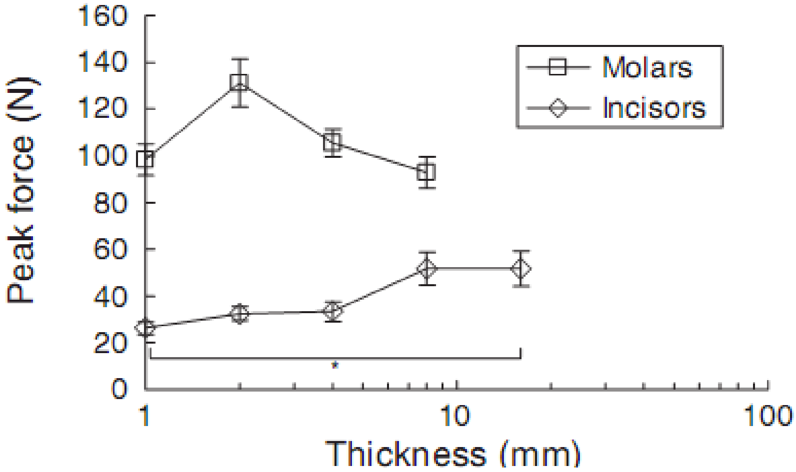

Figure 2.8 Peak force measured for silicone rubber samples of various thicknesses (Kohyama, Hatakeyama, Sasaki, Azuma, et al., 2004)

### 2.2.3. *Teeth*

Teeth are the main part for chewing foods and fracturing them into small particles. They can be categorized according to their shapes and functions. The teeth at the centre front of the mouth are called incisor. They are wedge-shaped and have a very sharp edge for cutting foods. The teeth, which are behind the incisors, located at the corners of the mouth are called cuspid. They are also called canines and are used to tear foods. Both the incisors and canines are known as the anterior teeth. Behind these teeth are the postcannines or posterior teeth, which are used for mastication.

The posterior teeth consist of two types of teeth: premolars or bicuspids and molars. The premolars located behind the canines are used to tear and break food. The molars located at the back of the mouth are used to fracture and grind food into fine particles. The permanent teeth diagram is shown below in Figure 2.9.

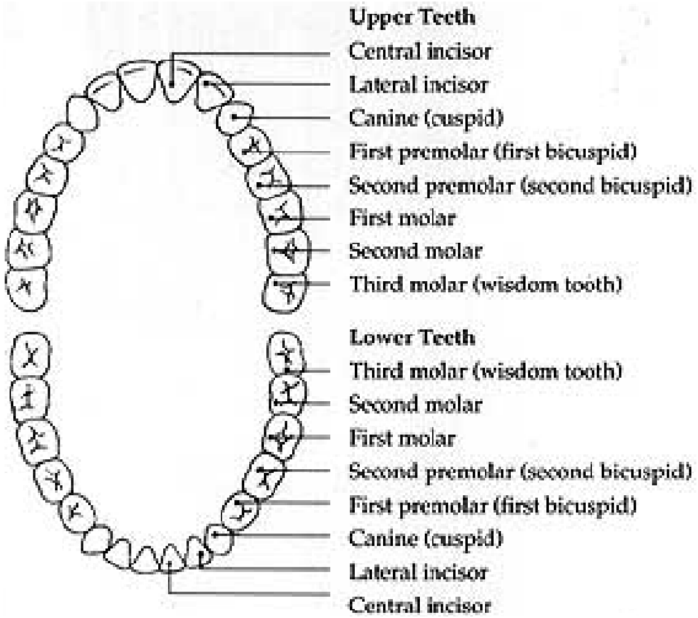

Figure 2.9 Teeth diagram of human (Oral-B website, 2005)

The pointed features of tooth crowns are called cusps. The cusps are used to start cracks in the food particle. However, the cusps on the posterior teeth are blunt rather than sharp. This is because sharp cusps are likely to suppress cracking and plastically deform food particles rather than fracturing them. Therefore, the shape of cusps is spherical in Figure 2.10. The fracture load that results in cracking is proportional to the radius of the spherical cusp (Lucas, 2004).

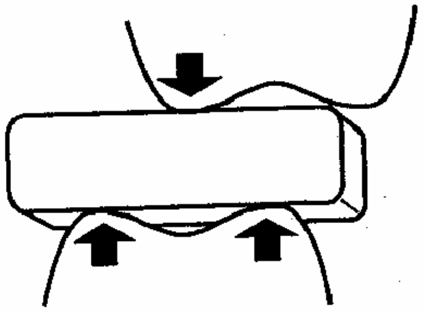

Figure 2.10 Three point bending of a food particle (Lucas, 2004)

### 2.2.4. *Tongue Movements during Mastication*

The tongue has very important functions: It plays a key role in ingestion, as in licking, lapping and browsing; and it moves food through the oral cavity from the incisors to the post canines for chewing, and then to the pharynx for bolus formation and swallowing (Lucas & Luke, 1986). The tongue movements during mastication are described in the process model of feeding (Hiiemae & Palmer, 1999; Palmer et al., 1997) which contains four main sequential stages: 1) Stage I transport, 2) Processing, 3) Stage II transport, and 4) Bolus formation and deglutition.

*(1) Stage I transport* (Figure 2.11)

As the food is bitten, the 'bite' is deposited on the anterior-middle tongue surface, and the posterior oral tongue rises. The tongue surface is quickly lowered to the level of the mandibular occlusal plane as the hyoid and tongue are pulled backward. As the jaws start closing, the tongue starts to rise. The food is then carried forward and upward to the first upper molars. Finally, the food is positioned on the occlusal surface plane by a twisting tongue movement about its posteroanterior long axis. The movement of tongue in this stage can be described as '*pull back*'.

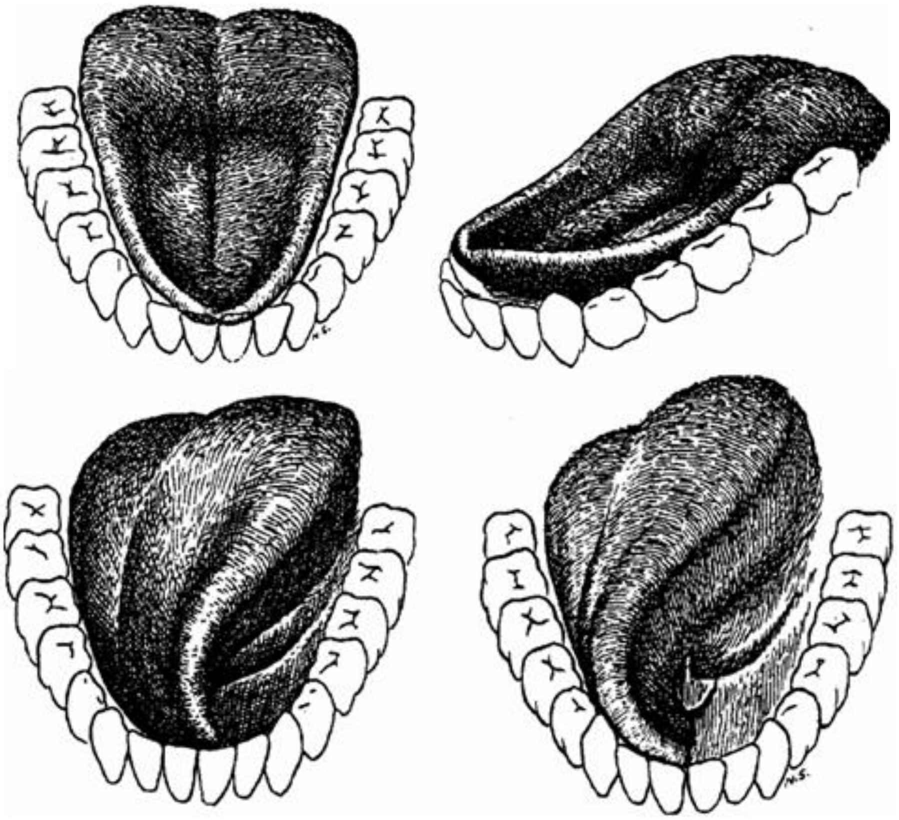

Figure 2.11 Tongue shapes change during Stage I transport (Abd-El-Malek, 1955). The upper pair of drawings shows the shape of the tongue when food is going to the mouth. The lower pair of drawings illustrates the twisting movements of tongue.

*(2) Processing*

During chewing, tongue movements occur in both the sagittal and coronal planes. In the sagittal plane, the tongue performs cycle movements. The tongue moves from a downward position at maximum jaw opening, upward and backward as the jaw closes. The tongue reaches its most backward position during closing, continuing to rise to reach the palate just after the teeth occlude. During the intercuspal phase and as the jaws start to open, the tongue continues to cycle forward and then downward. As processing proceeds, the tongue surface is brought sequentially closer to the palate, until contact the palate. This cycling moves chewed food progressively anteriorly. And then the tongue tip rises to collect and return the food from the anterior surface of the hard palate to the molar region by the *pull back* movement as the jaw reaches maximum opening.

Tongue movements in the coronal plane are very important. At the end of Stage I, the food is placed onto the occlusal surface of the posterior teeth by the tongue twisting about its antero-posterior axis. As processing proceeds, the tongue continues to collect insufficiently chewed food on the occlusal table and reposition it during late opening and early closing. Mioche et al. (2002) showed that as the tongue maintains the food by pushing it on the occlusal table, it also pushes it progressively into the cheek. The cheek pushes the food back toward the midline about every three cycles. The food then is moved across midline by the tongue rotating longitudinally away from the teeth on the active side during jaw opening.

*(3) Stage II transport*

Stage II transport involves the movement of food through the pillars of the fauces (Hutchings & Lillford, 1988). This movement indicates the beginning of the liquid swallow and bolus formation in the oropharynx (Thexton & Crompton, 1998). The anterior surface of the tongue first rises to contact the anterior hard palate. The tongue then moves upward sequentially ‘squeezing’ the food posteriorly, like fingers compress on a toothpaste tube. This movement can be called ‘*squeeze back*’. This action gradually accumulates the triturated food particles on the anterior hard palate.

*(4) Bolus formation and deglutition*

Toward the end of the Stage II period, the ‘*squeeze back*’ movement exaggeratedly occurs. Residual food particles are accumulated on the anterior hard palate. The tongue tip rises upward to contact the distal surface of the incisors, then the anterior hard palate while collecting the accumulated food particles on its surface. As the tongue surface continues to move upward, its contact with the hard palate expands posteriorly as the jaw continues to open. The accumulated food particles are then pushed backward from the anterior oral cavity to the pharyngeal surface of the tongue to form a bolus. The total accumulation time could be as long as 8-10 seconds for the hard foods. When the swallow is triggered, the tongue surface squeezes the bolus toward the pharynx, and the back of the tongue drops to eliminate the posterior oral seal to allow swallowing.

### 2.2.5. *Masticatory Performance*

Masticatory performance, evaluating the quality of chewing, is determined as the capacity of the food particle size reduction (Pedersen et al., 2002). Masticatory performance can also be considered as the number of chewing cycles required for food breakdown ready for swallowing (Chauncey et al., 1984). There are many factors to affect masticatory performance, such as the occlusal contact area of posterior teeth, bite force, sensory feedback, saliva (Van der Bilt et al., 2006). Among these factors, the key factors of masticatory performance are number of occlusal tooth units and bite force (Hatch et al., 2001).

*Occlusal factors*

Many different occlusal factors are considered to influence the masticatory performance, such as the total occlusal surface, the occlusal contact area, and the number of occluding pairs of teeth. 47 dentate subjects were selected to attend the study on measuring and comparing the masticatory performance (Julien et al., 1996). The analyses of the results demonstrated that the occlusal contact area of the posterior teeth is closely associated with masticatory performance. Participants with greater contact areas performed significantly better than the participants of same sex and weight with smaller contact areas. Another study revealed that the amount of occlusal contact area of molar and premolar teeth, which is one fifth of the total occlusal surface on average, are proved to be more important factor determining the masticatory performance of people with natural teeth (Luke & Lucas, 1985). Similarly, the number of occlusal units and the distribution of occlusal units are used to be a good predictor of masticatory performance (Hatch et al., 2001; Kayser, 1981). The occlusal units consist of the molar pairs and the premolar pairs, where an occluding molar pair is considered as two occlusal units and a premolar pair is considered as one occlusal pair.

*Bite force*

Significant correlations were found between maximum bite force and chewing efficiency (Fontijn-Tekamp, 2000). Chewing efficiency and bite force were measured with the same method in 143 female subjects divided into seven groups: two over denture groups, two full-denture groups, and three groups with natural dentitions. In this study, chewing efficiency is considered as the number of chewing strokes required to achieve a certain particle size reduction, such as to the median particle size. The study proved that chewing efficiency significantly increased when higher bite forces were applied. A higher bite force results in a better fragmentation of the food particles.

*Sensory feedback*

Many sensory receptors exist in the mouth. These receptors can be divided into two categories – those that supply information about jaw displacement and those that monitor stress (Figure 2.12) (Lucas, 2004). The tongue and cheeks manipulating food particles play an important role in the selection of food. The tongue and cheeks pick out large food particles and put them on the occlusal area of the teeth for further reduction. Therefore, if there is not enough number of coarse particles on the occlusal areas, a chewing stroke will be ineffective for particle reduction. There is a study showing that local anaesthesia weakens masticatory performance (Kapur et al., 1990). Ten subjects with complete natural dentitions chewed on standardized amounts of peanuts on their preferred chewing side. The subjects require an average of 40 chewing cycles after unilateral anaesthesia to achieve similar results achieved with 20 strokes before anaesthesia. Therefore, chewing efficiency is negatively influenced by sensory weakening. The tongue motor skill and masticatory performance were also significantly correlated (Koshino et al., 1997). 30 normal adult dentates, 10 normal elderly dentates and 20 complete denture wearers were chosen to examine the tongue motor skills by an ultrasound system. The tongue motor skills of adult dentates were statistically higher than those of elderly dentates and complete denture wearers. Moreover, the correlation coefficient was statistically significant between tongue motor skill and masticatory performance.

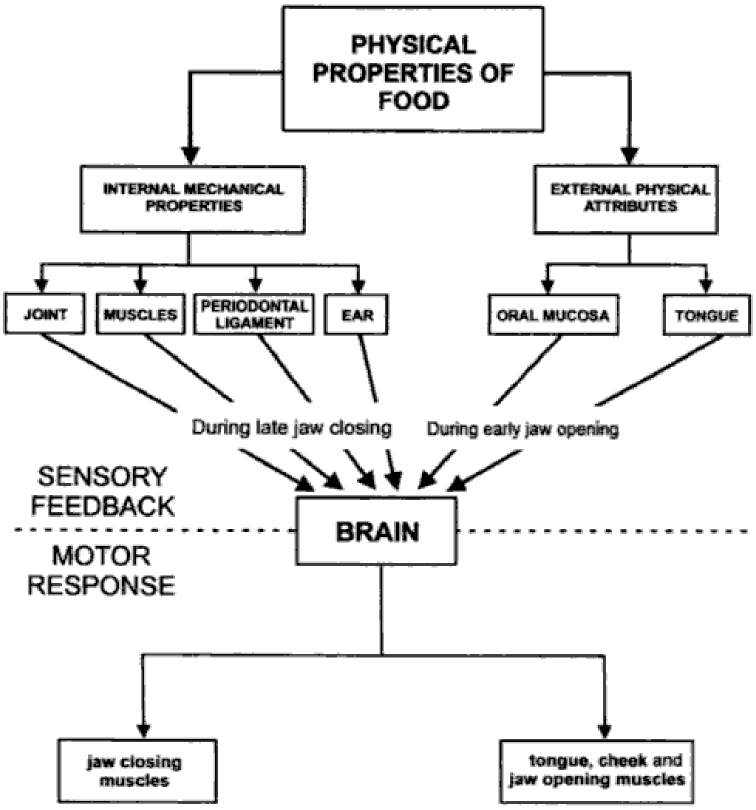

Figure 2.12 The sources of sensory information in the mouth related to food properties and the motor responses (Lucas, 2004)

*Saliva*

Saliva is generated by the salivary glands. It helps lubricate the food bolus for swallowing, soften dry food particles for food breakdown, flush away small food particles, absorb juices, dissolve and release food taste and odour chemicals, and deglutition (Bourne, 2002; Mandel, 1987). In a study on the relationship between the salivary secretion rate and masticatory efficiency in 10 healthy fully dentates, it was found that the masticatory efficiency in the dentates with hypo-salivation after atropine sulphate medication was significantly lower than that before (Ishijima et al., 2004). However, the increase in salivary secretion by pilocarpine hydrochloride medication did not achieve a better masticatory efficiency.

## 2.3. *Food Rheological Model*

Rheological models have been a useful tool for the evaluation and prediction of the mechanical response of foods to force-deformation (or stress-strain) history (Sahoo et al., 1988). The rheological properties of many solid foods have been evaluated, usually by tests involving creep, relaxation, compression and extension (Sherman, 1974). The rheological behaviour of a food is related to the physical structure and the biochemical composition which define its textural properties. Since a “textual property” is a very complex term in terms of mechanical aspect, it needs to be described by a very large number of parameters (Bourne, 1975). From a mechanical behaviour point of view, approximated models can be reached with a relatively small number of rheological elements. More elements or combinations can be required to obtain better accuracy for the fitting of the experimental behaviour.

### 2.3.1. ***Contact and Fracture Elements***

The basic elements of most rheological models are the elastic and viscous components and their primary combinations, the Maxwell and Voigt (Kelvin) elements (Mohsenin, 1986; Shama & Sherman, 1968). Many models which have been suggested (usually built of 3-10 basic elements) can be considered as an acceptable approximation of the food’s behaviour only within a limited range of conditions. One of the basic reasons for the limitations is the fact that the classic elastic and viscous elements cannot represent failure phenomena. To overcome such a problem, a fracture element has been introduced by which force peaks followed by instantaneous force drops can be anticipated (Drake, 1971).

The general element and its positions are shown in Figure 2.13. Basically, the element is a Maxwell body in which two restrictions have been incorporated in the form of fracture elements (Drake, 1971). The first critical force $F_{c1}$ is parallel to the viscous element. Once $F_{c1}$ failed, the viscous element will become effective. Until the first critical force level is reached, the element is purely elastic. The second critical force $F_{c2}$ is in series with the fracture element. Once $F_{c2}$ is reached, the general element unit as a whole is broken and eliminated from the general model array.

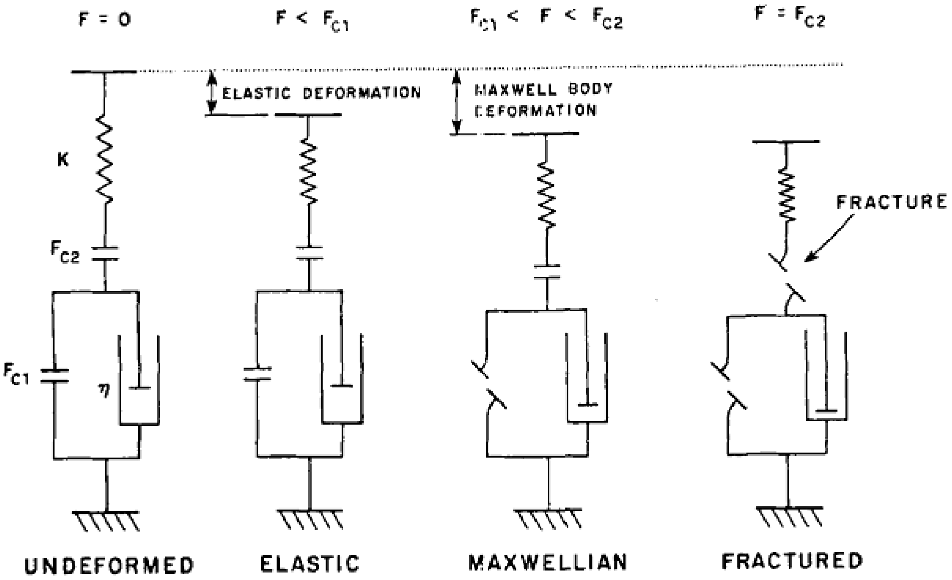

Figure 2.13 The general element and its possible positions (Sahoo et al., 1988)

The behaviour of the element under a general deformation pattern, constant rate of deformation, relaxation and creep can be described as follows:

Table 2-1 The behaviour of the element under different patterns (Sahoo et al., 1988)

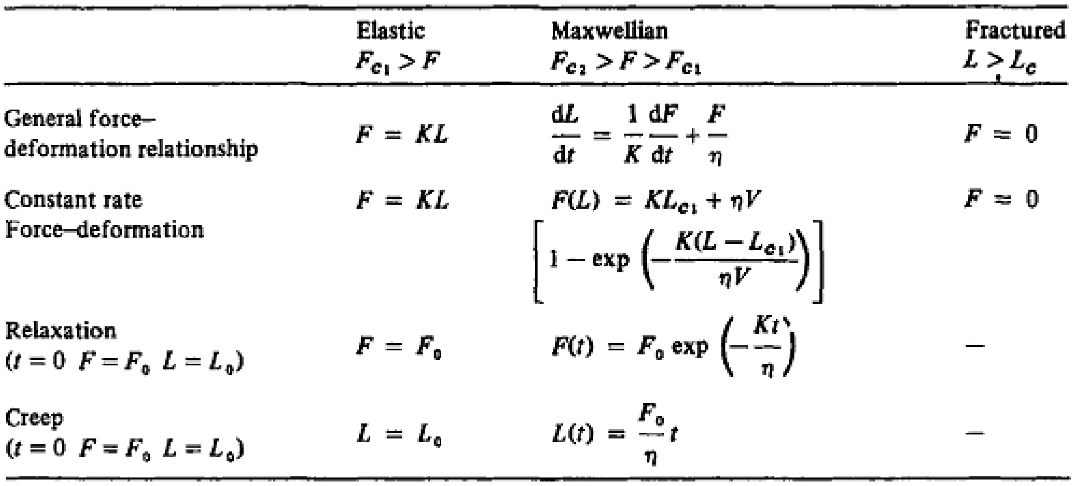

| | Elastic<br>$F_{c_1} > F$ | Maxwellian<br>$F_{c_2} > F > F_{c_1}$ | Fractured<br>$L > L_c$ |
|---|---|---|---|
| General force–deformation relationship | $F = KL$ | $\frac{dL}{dt} = \frac{1}{K}\frac{dF}{dt} + \frac{F}{\eta}$ | $F = 0$ |
| Constant rate Force–deformation | $F = KL$ | $F(L) = KL_{c_1} + \eta V \left[1 - \exp\left(-\frac{K(L - L_{c_1})}{\eta V}\right)\right]$ | $F = 0$ |
| Relaxation ($t = 0$ $F = F_0$ $L = L_0$) | $F = F_0$ | $F(t) = F_0 \exp\left(-\frac{Kt}{\eta}\right)$ | – |
| Creep ($t = 0$ $F = F_0$ $L = L_0$) | $L = L_0$ | $L(t) = \frac{F_0}{\eta}t$ | – |

Where $F$ is the force, $L$ is the deformation, $K$ is the spring modulus, $\eta$ is the viscosity, $V$ is the deformation rate, $t$ is the time, $L_{c1}$ and $L_{c2}$ are the deformations at $F_{c1}$ and $F_{c2}$, respectively, and $F_0$ and $L_0$ are the initial force and deformation for the relaxation and creep tests. Figure 2.14 shows the various conditions and patterns of force-deformation curves. The effect of the deformation rate on the force deformation curve of the general element is shown in Figure 2.15.

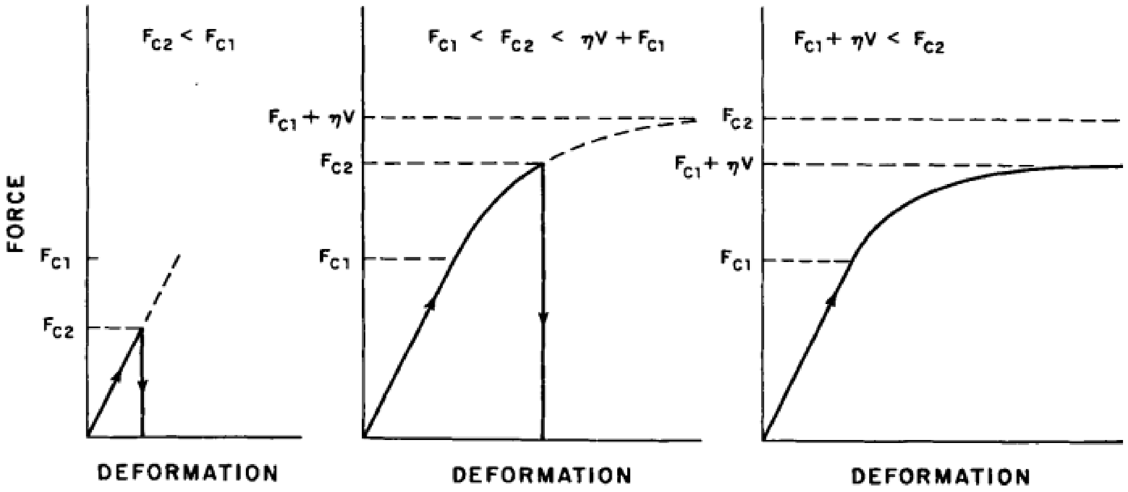

Figure 2.14 Types of force-deformation curves of the general element (Sahoo et al., 1988)

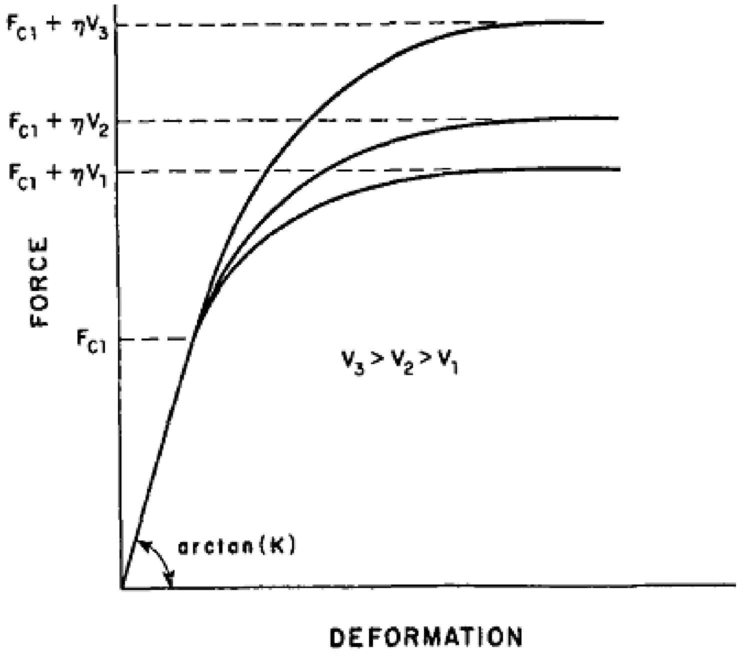

Figure 2.15 The effect of the deformation rate on the force deformation curve of a general element (Sahoo et al., 1988)

### 2.3.2. *The General Model*

Basically, the general model is a generalized Maxwell body (a parallel array of Maxwell elements) in which the units are the modified general elements. The number of the elements must be very large and have their individual parameters $K$, $\eta, F_{c1}$ and $F_{c2}$. Distributions and magnitudes of these parameters are characteristic of the material to which the model relates. Once the deformation occurs, the total force is the sum of forces acting on each element. Each individual element reaches its different stages of response or failure according to its own constants $F_{c1}$ and $F_{c2}$. Thus, at any given deformation there might be elements in three positions: the elastic stage, the Maxwellian stage, and fracture (Figure 2.16).

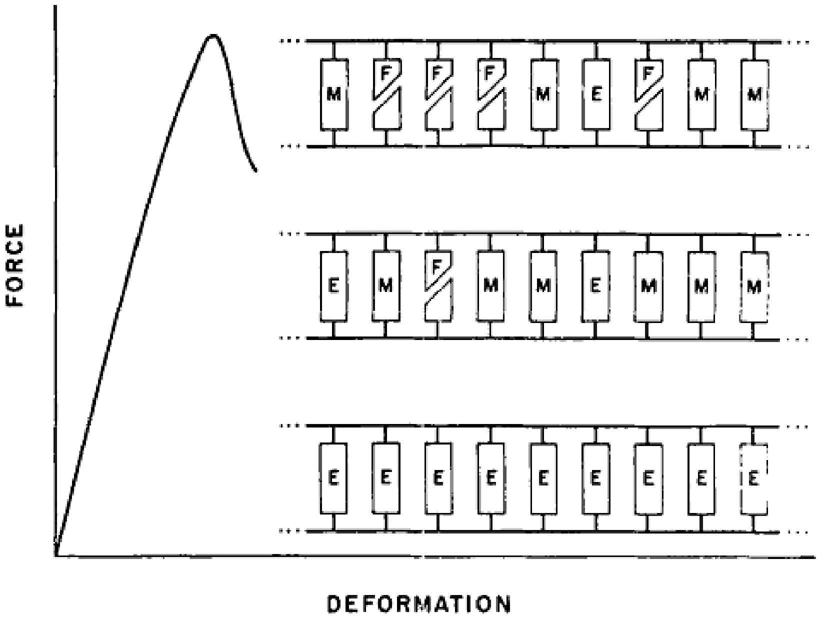

Figure 2.16 Schematic view of the general model at various deformation stages; E – elastic; M – Maxwellian; F – fractured elements (Sahoo et al., 1988)

Examples of force-deformation curves and their similarity to the published behaviour of real materials are shown in Figure 2.17. A, B, C and D are representative general elements. Their force-deformation curves are shown in the two bottom figures. The force-deformation curves of their combinations are shown in the upper apart. (Bourne, 1975; Olkku & Rha, 1975)

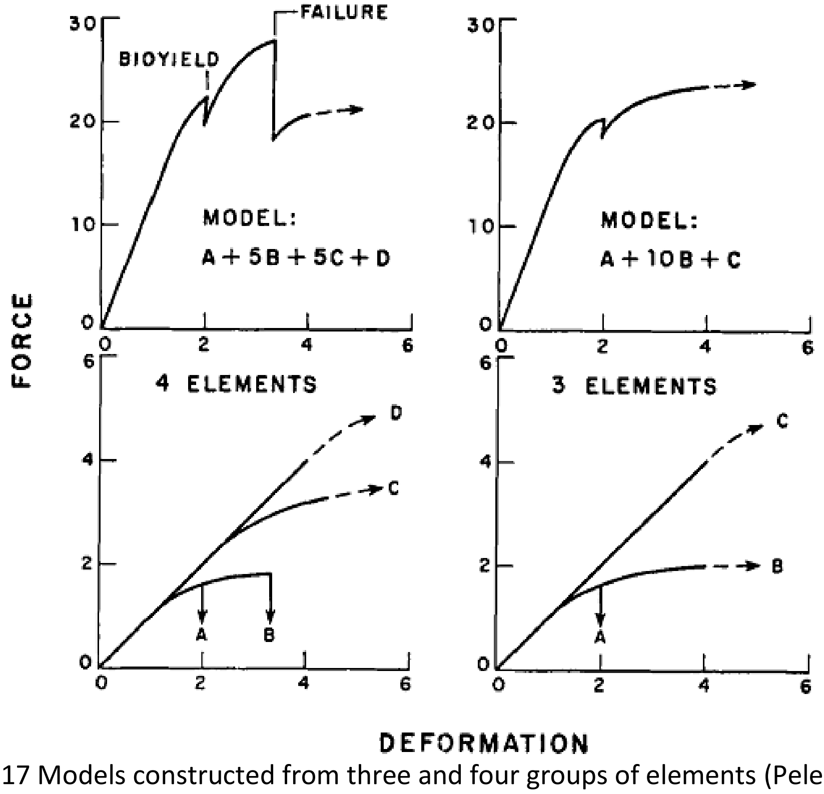

Figure 2.17 Models constructed from three and four groups of elements (Peleg, 1976)

### 2.3.3. *Mathematical Models for Force-Deformation Curves*

The most rational model to describe the force (F) - deformation ($\Delta H$) relationship is a single power law term, of the general form (Peleg & Campanella, 1989; ROY et al., 1989):

$$F = K(\Delta H)^n \tag{4}$$

or

$$\Delta H = \left(\frac{F}{K}\right)^{\frac{1}{n}} \tag{5}$$

The advantage of the model expressed by Equation 4 is that K represents a measure of stiffness (in force/(deformation$^n$)units) and n the deviation from linearity and the type and degree of concavity, (n = 1 indicates a linear relationship, n > 1 upward and n < 1 downward concavity) (Swyngedau, Normand, et al., 1991).

The disadvantage of Equation 4 and 5 for predicting the behaviour of a double layer array from the behaviour of its components is the mathematical format of the relationship:

$$\Delta H_T = \Delta H_1 + \Delta H_2 = \left(\frac{F}{K_1}\right)^{\frac{1}{n_1}} + \left(\frac{F}{K_2}\right)^{\frac{1}{n_2}} \tag{6}$$

where $\Delta H_T$ is the array's total deformation, $\Delta H_1$ and $\Delta H_2$ the deformation of layers 1 and 2 in the array and the K's and n's the corresponding constants. This relationship cannot be transformed in to an explicit algebraic function in the form of $F = K(\Delta H)$ (Swyngedau, Normand, et al., 1991).

This problem can be eliminated if the force-deformation curves of each component are expressed in terms of the following two parameter models (Nussinovitch et al., 1991; Swyngedau, Nussinovitch, et al., 1991). For a concave upward curve:

$$F = \frac{a\Delta H}{c-\Delta \mathrm{H}} (0 \leq \Delta H < C < H_o) \tag{7}$$

and for a concave downward curve:

$$F = \frac{a\Delta H}{c+\Delta \mathrm{H}} \tag{8}$$

where *a*, *c* are constants and $H_o$ is the layer's thickness. The constant *a* has force units and *c* deformation units. Their fit to experimental data was found comparable to that of the power law model (see below). These relationships can be reversed to $\Delta H = \Delta H(F)$ relationships by the rearrangement (Nussinovitch et al., 1991):

$$\Delta H = \frac{cF}{a+\mathrm{F}} \tag{9}$$

and

$$\Delta H = \frac{cF}{a-\mathrm{F}} \tag{10}$$

The deformation of a double layered array in terms of these models is

$$\Delta H_T = \Delta H_1 + \Delta H_2 = \frac{c_1F}{a_1 \pm \mathrm{F}} + \frac{c_2F}{a_2 \pm \mathrm{F}} \tag{11}$$

The fit of the two models in their original and linearized forms to experimental compression data is demonstrated in Figure 2.18-2.20. $F$ is the force and $\Delta H$ is the deformation.

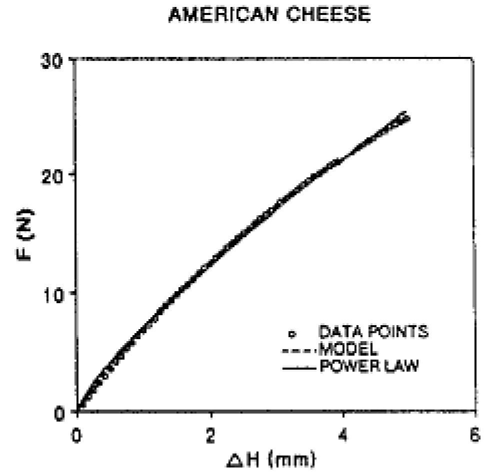

Figure 2.18 A compressive force deformation curve of American process cheese and the fit of equation 4 and 8 determined by nonlinear regression (Swyngedau, Normand, et al., 1991)

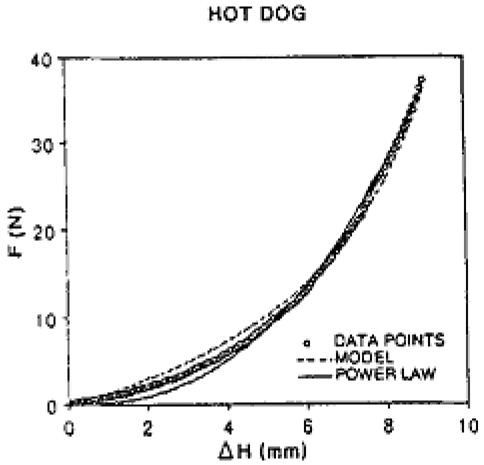

Figure 2.19 A compressive force deformation curve of Hot dog and the fit of equation 4 and 8 determined by nonlinear regression (Swyngedau, Normand, et al., 1991)

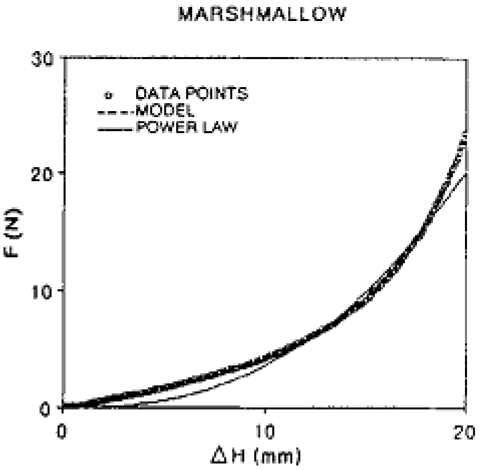

Figure 2.20 A compressive force deformation curve of marshmallow and the fit of equation 4 and 8 determined by nonlinear regression (Swyngedau, Normand, et al., 1991)

## *2.4. The State of the Art of Masticatory Robots*

There have been several robotic devices developed that aim to replicate aspects of the human mastication system. This section reviews the most relevant robots and summarises their key features.

### 2.4.1. *The Dental Training Robot*

*A. WY-5 series robots – the mouth training robot*

The WY (Waseda-Yamanashi) series of robots were developed as the mouth opening-closing training robot as a doctor model for the patient who have disorders on their jaw joints (Takanobu et al., 2002). The doctors' hand motion during a mouth opening training session was simulated by the robot. The WY-5 robot that has parallel mechanism, as shown in Figure 2.21, is used to manipulate the patient's mandible in 6-DOF space. The robot is able to reproduce the same movable range and forces as the human's jaw. The most advanced version is WY-5RVI in 2004 (Figure 2.22).

The 6-DOF robot consists of ball screws actuated by six linear actuators. The patient's upper jaw is held by the upper mouthpiece of the robot and the patient's lower jaw is manipulated by the movement of the mechanism. The mechanism is more effective than the conventional method which only performs 1-DOF movement which is opening and closing the mouth.

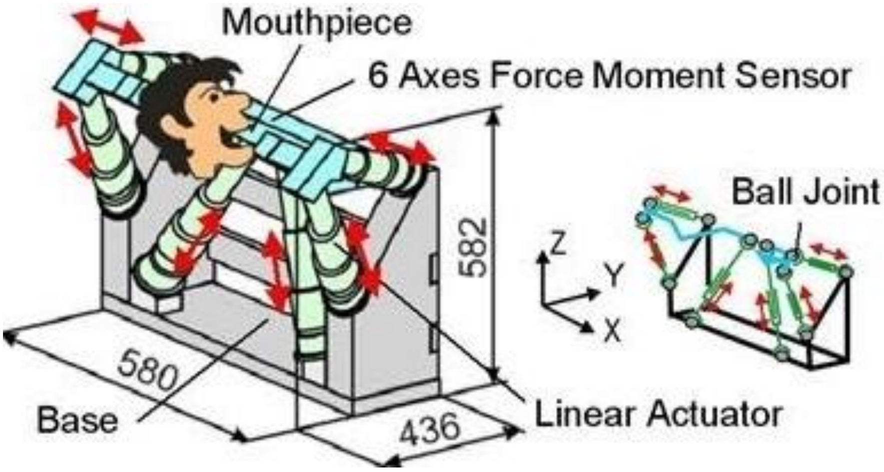

Figure 2.21 Patient Manipulator with 6-DOF mechanism

(www.takanishi.mech.waseda.ac.jp/research/index.htm)

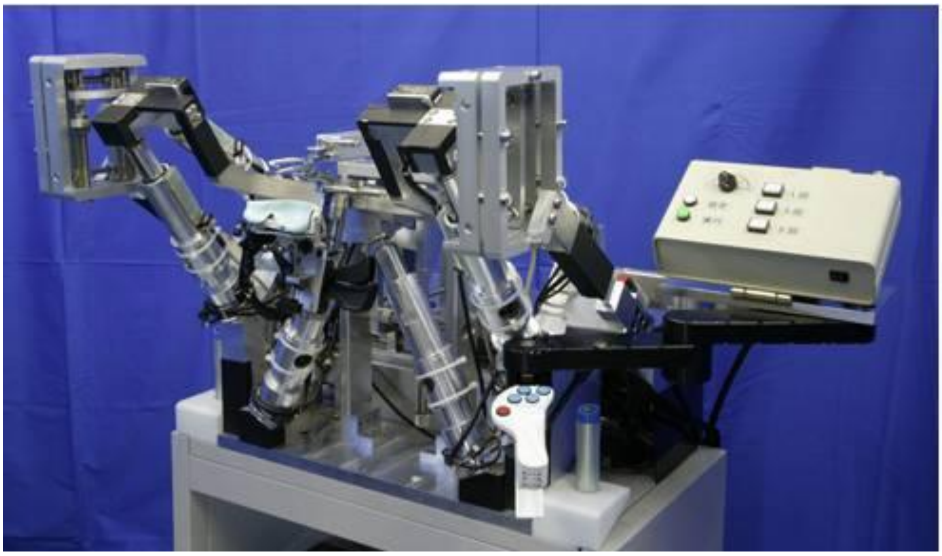

Figure 2.22 Treatment Robot WY-5RVI (www.takanishi.mech.waseda.ac.jp/research/index.htm)

The biting force acting on the patient via the mouth opening gag is the most important factor during therapy. Force sensors have been implemented to measure the mouth opening, forward and grinding directions' forces. The WY-5 is a typical force feedback type, master-slave system as shown in Figure 2.23. The mouth opening/closing angle, forward/backward and right/left displacements are sent from the doctor's manipulator to the patient manipulator (Takanobu et al., 2000). An EMG feedback signal measurement system has been developed to allow the doctor to monitor any change on patient's jaw muscle.

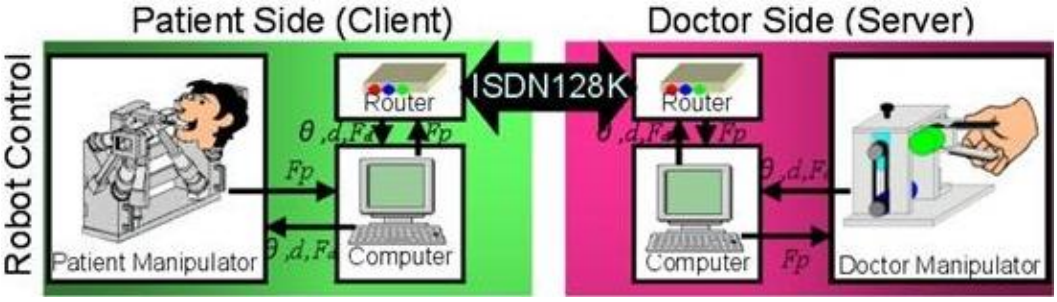

Figure 2.23 Total system configuration of WY-5

(www.takanishi.mech.waseda.ac.jp/research/index.htm)

The WY-5 was also modified as a food texture measurement robot called WWT-1 (WWT for Waseda Wayo Texturobot) as shown in Figure 2.24. The advantage of WWT-1 is the ability to measure food texture by simulating the human's mastication movement in 6-DOF space. This robot moves precisely with an accuracy of 0.02mm and is able to detect minimum of 0.001N of force.

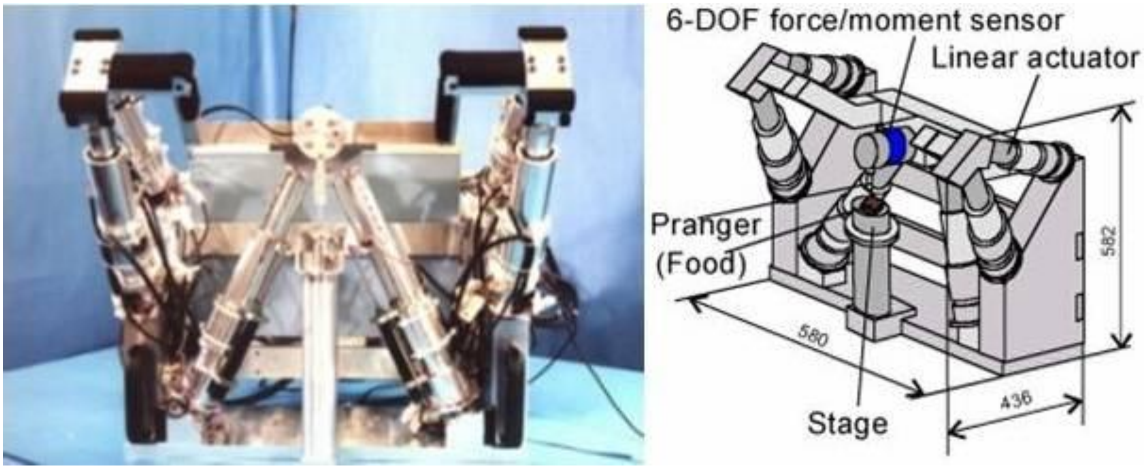

Figure 2.24 Food Texture Measurement Robot

(www.takanishi.mech.waseda.ac.jp/research/index.htm)

*B. WJ series robots – the mastication patient robot*

The WJ (Waseda Jaw) series robot was developed to replace human to work with the WY series robot for mouth training (Takanobu et al., 2002). The WJ robot is used to understand patient's jaw movement and resistance forces during mouth training. The WJ patient robot working with the WY robot is shown below in Figure 2.25.

Figure 2.25 A WJ robot is working on the WY robot (Takanobu et al., 2002)

The WJ robot has three degrees of freedom, which is open/close, forward/ backward and left/right (Takanobu et al., 2002), as shown in Figure 2.26. The robot simulates artificial trajectories for clenching and grinding. A carbon rod goes through the right and left condyles (jaw joint). This rod can only move forward and backward on a plane that is tilted 40 degree from the horizontal plane and consists of two TMJs. The robot contains eleven artificial muscle actuators (AMA). An AMA consists of a motor, an encoder, a tachogenerator, a tendon, and a force sensor (Figure 2.27). A tendon actuation method is used to simulate contraction forces. One end of the tendon attaching to the robot's mandible is the connecting point of the muscle, and the motor pulls the other end. Three biting force sensors that can measure the back and forth force are assigned on the right, centre and left part of the teeth. A control algorithm was developed for adaptive jaw movement using jaw position and biting force.

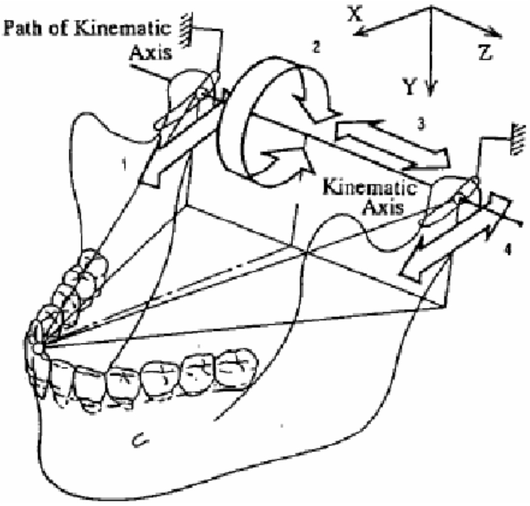

Figure 2.26 Jaw movements of 3 DOFs (Takanobu et al., 2002)

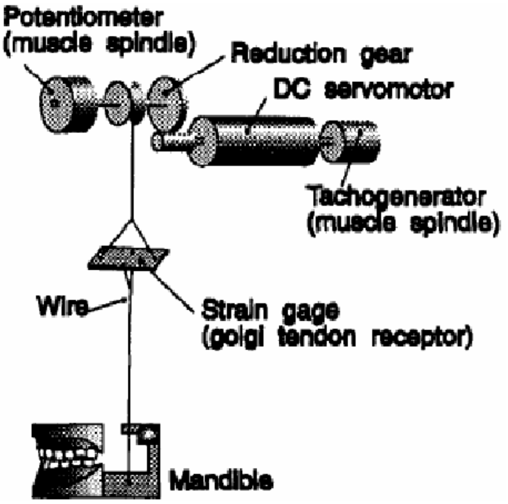

Figure 2.27 Artificial muscle actuator (Takanobu et al., 2002)

### 2.4.2. *The JSN Series of Jaw Simulators*

A JSN series of jaw simulators were developed to reproduce a chewing-like movement at Niigata University, Japan. The jaw simulator incorporated all muscle actuators and sensors under a physiological and adaptive control scheme. The simulator consists of five major parts as follows (Hayashi et al., 2000): 1) the upper and lower jaws with tooth-contact and bite-force sensors at the canines and first molars; 2) condylar housing, simulating TMJ; 3) wire-tendon DC-servo actuators including a rotary encoder and a cable-tension sensor, simulating dominant chewing muscles; 4) control units consisting of sensing and motor-driving circuits; 5) a computer controlling all actuators and analyzing all sensor outputs.

JSN/2A is the most advanced JSN jaw simulator, which involves 6 DOFs and 6 muscle actuators (Figure 2.28). The impedance control algorithm was used in the control system of the actuator, where the outputs of muscular position and bite force sensors are fed back and compared with the driving signal (Figure 2.29).

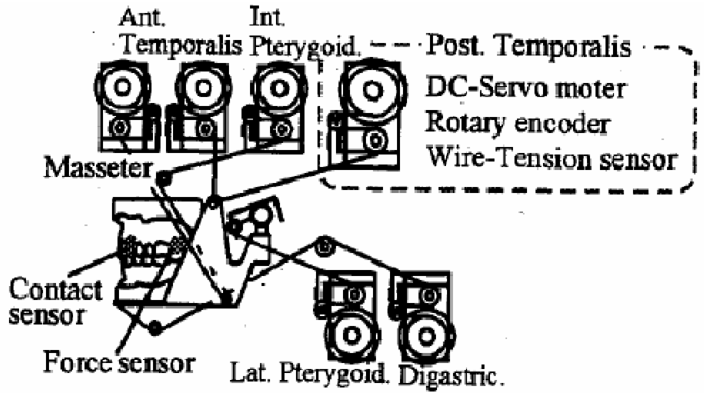

Figure 2.28 Jaw simulator JSN/2A with 6 muscular actuators and periodontal sensors (Hayashi et al., 2000)

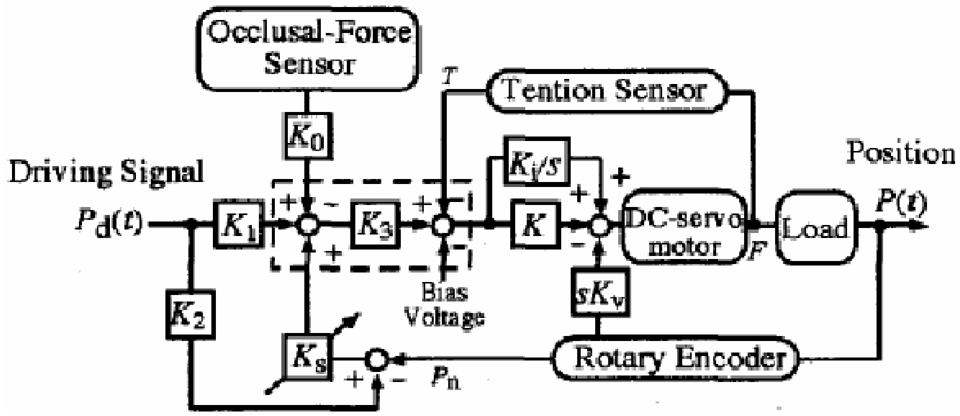

Figure 2.29 Impedance control system of muscular actuator (Hayashi et al., 2000)

### 2.4.3. ***The Robotic Jaw of 6RSS Parallel Mechanism***

The robotic jaw research program at Massey University started in 2002 focusing on the analytical food texture characterization (Xu et al., 2007). The robot simulating human chewing behaviour chews foods and prepares the food for food property evaluation. The robotic jaw of 6RSS parallel mechanism was built in 2005 with 6 RSS linkages representing 6 major mouth-closing muscles (two temporalis, two masseter and two pterygoid) in Figure 2.30. Each RSS linkage is actuated by a DC motor and consists of a crank and a coupler. The crank is pivoted to the ground and the coupler is connected to the crank and the mandible by a ball-socket joint.

The motion control system includes a six-axis motion control card, DMC-1860 by Galil, and two amplifiers. The Galil DMC Smart Terminal program integrates PID control programmes to the control card. The robot was controlled under PID control to reproduce the chewing.

The robot has been tested both its ability to follow a trajectory and to reproduce those movements when chewing on a hard food. A 6mm thick aluminium plate as a hard model food was inserted between the upper and lower jaws. The inverse kinematics was performed and the torque was limited to 55mNm at the motor. A torque of 3.6Nm is limited at the crank, approximately 250N of force at the link attaching to the jaw.

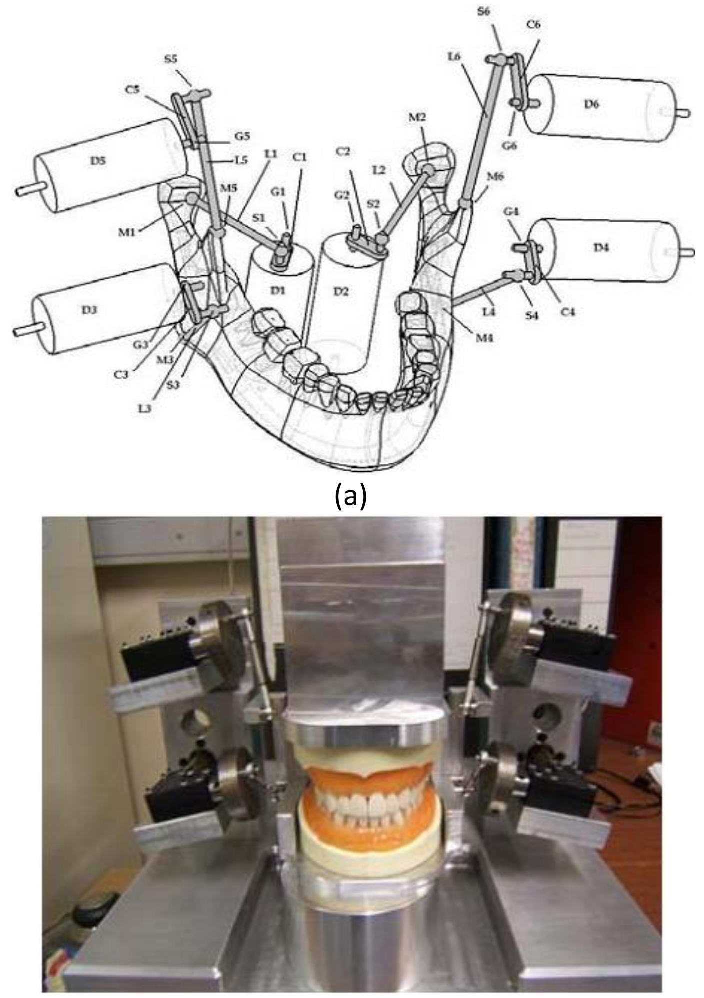

(a)

(b)

Figure 2.30 The concept (a) and the photo (b) of 6 RSS parallel mechanism (Torrance et al., 2006)

### 2.4.4. ***The Chewing Simulator***

The chewing simulator is developed for food breakdown and the analysis of in vitro flavour compound release in a mouth environment at University de Bourgogne, France (Salles et al., 2007). The chewing simulator is able to reproduce the similar principal phenomena occurring in the mouth during chewing, such as controlled compressive and shear forces, continuous saliva flow, same speed and frequency.

The system consists of an actuated cell, an electronic control box, a computer to monitor and tune each parameter. The cell consists of several parts: an actuated lower mandible, an actuated tongue and a fixed upper mandible (Figure 2.31). Both upper and lower mandibles are made of the 3D designed first molar teeth (Figure 2.32) tooled in a ring-shaped polytheretherketone (PEEK) cylinder. Two motors are used to actuate the lower mandible to allow the vertical translation and rotation. A third motor is used to actuate the tongue, which made of a full PEEK cylinder of 4.5cm diameter. The system is able to reproduce shear and compression forces together up to 250N. The force can be measured through the DC current of the brushless motors. The movement of the jaw is measured by an optical rotary encoder.

The control system of the chewing simulator consists of two National Instruments (NI) cards connecting to a NI signal conditioning system (SC-2345) (Figure 2.33). One card (PCI-7344) drives three DC motors and is used to measure the motor currents and their position. The second card (PCI-6014) is used for the measurement of temperature or carrier gas flow rate and to setup the carrier gas flow rate.

A preliminary experiment was carried out on peanuts to test and validate the food breakdown functionalities of the system. The results show that the peanut breakdown process and related inter-individual differences could be reproduced by the chewing simulator.

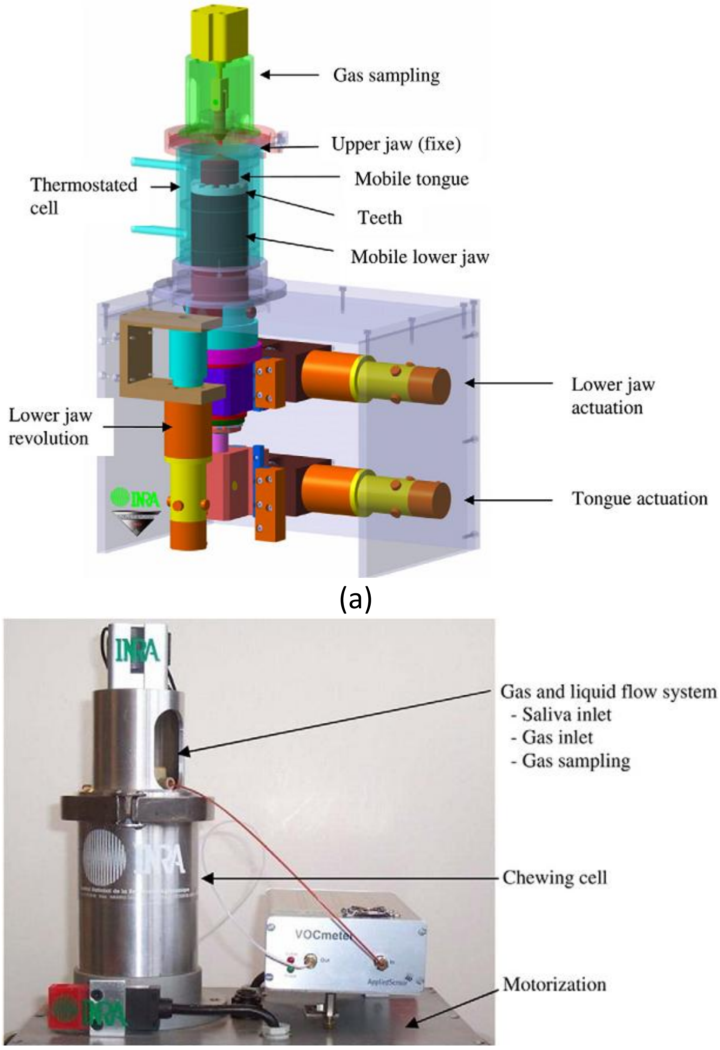

(a)

(b)

Figure 2.31 Diagram showing mechanical parts (a) and photo (b) of the chewing simulator

(Salles et al., 2007)

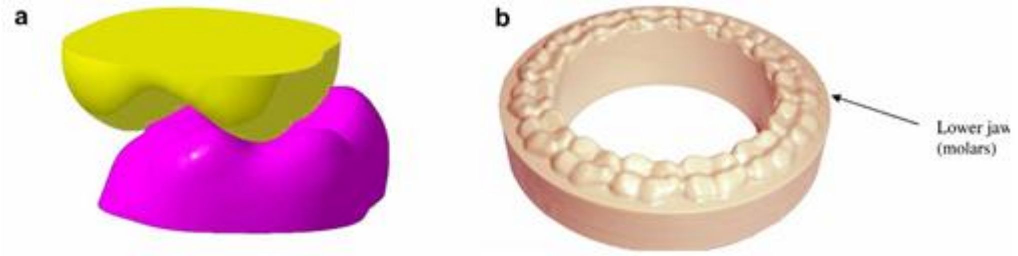

Figure 2.32 Designed teeth and jaw: (a) occlusion of molars and (b) lower jaw (Salles et al., 2007)

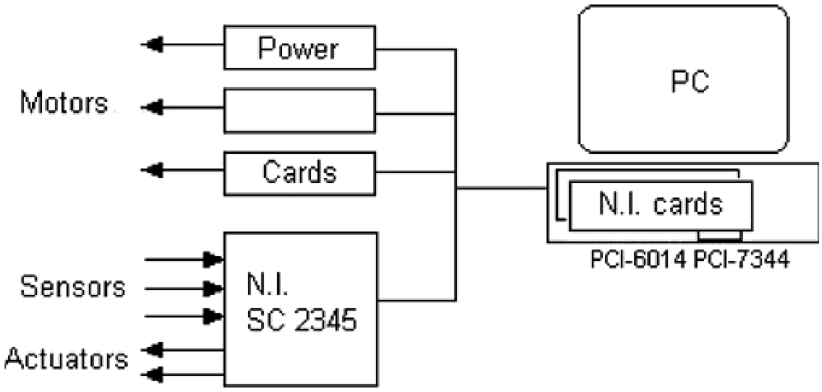

Figure 2.33 Automation of the system (Salles et al., 2007)

### 2.4.5. *Dento-Munch Robo-Simulator*

The Dento-Munch Robo-Simulator based on the Stewart Platform which has 6 DOF is developed for dental testing by the University of Britol, UK (Alemzadeh & Raabe, 2007). The robot simulator is used to replicate accurate human chewing patterns in 6 DOF with force and position feedback control to simulate the wear of dental materials on dental components.

The robot consists of six electrical actuators that can vary their length to achieve movement in 6- DOF (Figure 2.34). The complete robot periphery components are shown in Figure 2.35 and 2.36. The upper and lower jaws were reverse engineered integrated with artificial teeth. The accurate occlusion of the teeth is achieved by a dental teaching simulator. A strain gauge force sensor has been implemented under the second molars to allow the measurement of the axial biting forces. To prevent the fluctuating high bite forces during the occlusion that might damage the teeth, compliance module was built between the lower jaw and the platform. The compliance module is made of six spring mechanisms which compress when more than an axial force of 250N is applied. The module can support a maximum force of 575N.

The robot simulator employs the inner-outer loop force and position feedback control to match closely the human jaw's dynamics. The system includes current, speed, position and force control which achieved by the compliance module.

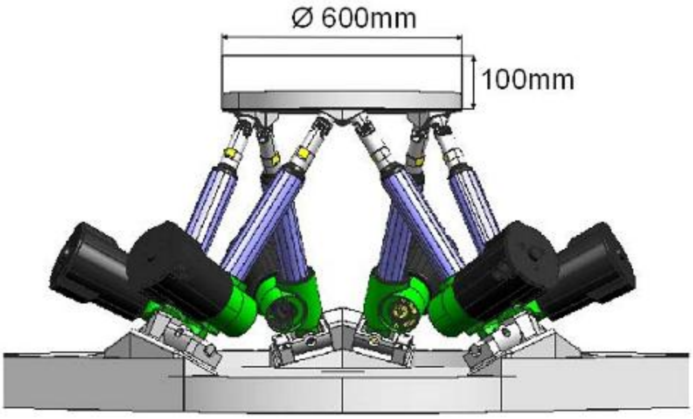

Figure 2.34 Robot simulator based on 6-DOF parallel robot (Alemzadeh & Raabe, 2007)

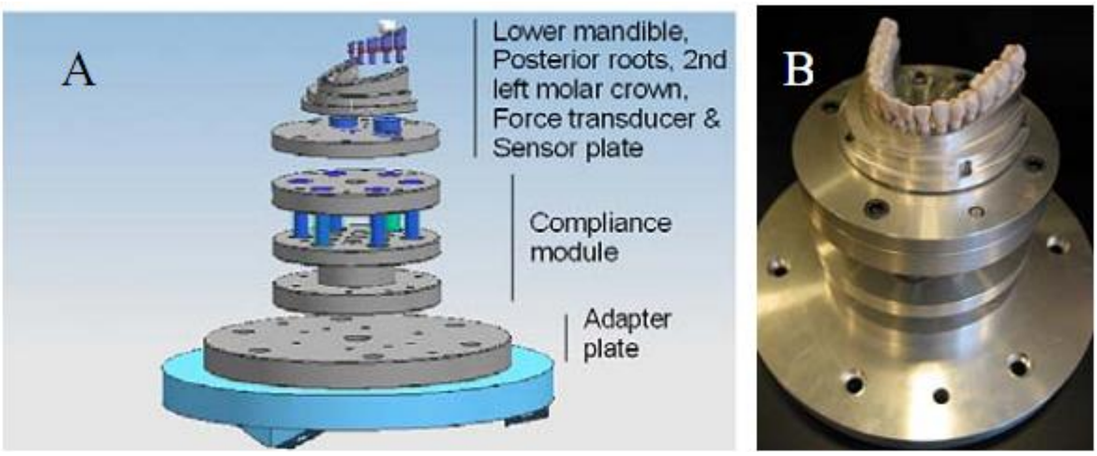

Figure 2.35 The upper assembly of all periphery components of the Robo-simulator

(Alemzadeh & Raabe, 2007)

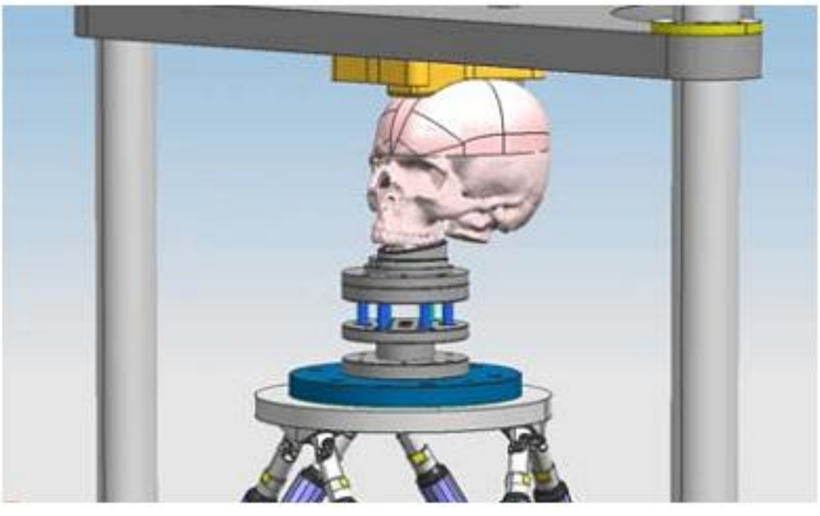

Figure 2.36 CAD model of complete periphery of Robo-simulator (Alemzadeh & Raabe, 2007)

## *2.5. Robot Force Control*

To find out the suitable force control algorithms for the chewing robot, an overview of robot force control algorithms is required. According to the paper (Zeng & Hemami, 1997), force control methods can be divided into fundamental robot force control algorithms and advanced robot force control algorithms. Different types of signal of the feedback (position, velocity and force) and different types of input signals determine different force control methods. In the following section, several fundamental force control methods and a few advanced force control methods are described.

### 2.5.1. *Fundamental Force Control*

Fundamental force control can be further categorized into four groups based on application of the relationship between position and force, or between velocity and force, or the application of direct force feedback, or their combinations (Zeng & Hemami, 1997):

1. Methods based on the relationship between position and force: stiffness control by only position feedback and stiffness control by force feedback correction;
2. Methods based on the relationship between velocity/position and force: impedance control and admittance control;
3. Methods applying directly position and applied force: hybrid position/force control and hybrid impedance control;
4. Methods that focus on force regulation: explicit force control and implicit force control.

#### *Stiffness Control*

In stiffness control, there are two types, passive stiffness control and active stiffness control. Passive stiffness control can be realized by equipping the robot end-effector with a mechanical device, such as springs or springs and dampers. While active stiffness control is achieved by changing the stiffness of the system through a force feedback signal (Spong & Vidyasagar, 2008). An example of active stiffness control is shown in Figure 2.37. In box 1, the stiffness controller includes a proportional force feedback and position feedback. $K_f$ is the compliance gain to modulate position input. The output of box 1 is the joint torque $\tau_p$ defined by the product of stiffness $K_p$ and joint angle displacement vector $\Delta\theta$. The unit of stiffness $K_p$ is force/displacement. Box 2 is the basic system containing a robot and the environment, the feedback of velocity and contacting force.

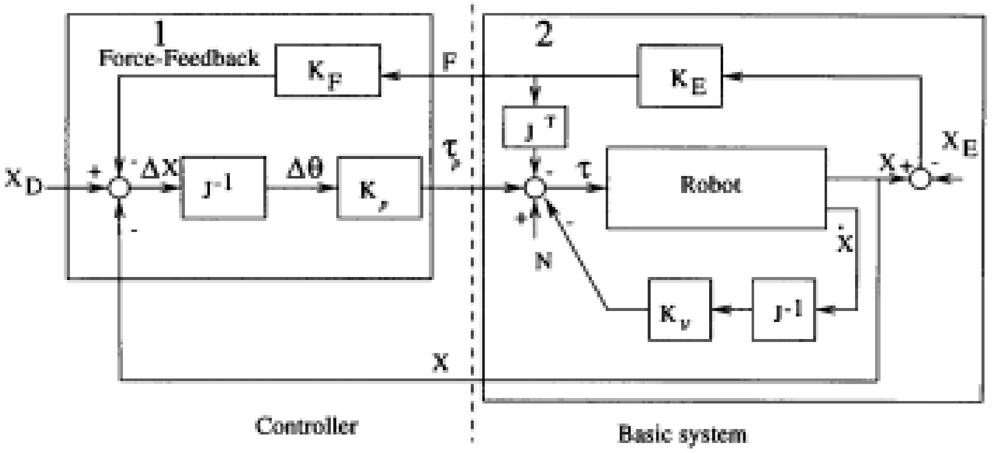

Figure 2.37 Active stiffness control(Zeng & Hemami, 1997)

Stiffness control is influenced by the combined stiffness of the environment, the robot and the sensor. Therefore, uncertainty in stiffness results in poor performance of force control (Yu, 2000). Many researches to overcome stiffness uncertainty are conducted involving adaptive, learning and other control strategies. Adaptive control was used with the stiffness controller to improve the performance in the presence of unknown parameters of the robot and the environment (Chiaverini et al., 1997; Pelletier & Daneshmend, 1990). A learning process was introduced to calculate the stiffness values of the end effector for repetitive tasks (Pelletier & Daneshmend, 1990).

### *Impedance Control and Admittance Control*

Impedance control is aiming not only to track a motion trajectory, but also to regulate the mechanical impedance of the manipulator (Hogan, 1984, 1985a). Compared with stiffness control using only one position feedback, impedance control can be implemented in different forms, depending on the feedback signals, i.e. position, velocity or force (Whitney, 1987). Figure 2.38 shows a basic impedance control diagram, which has position and velocity feedback loops. In this case, impedance control uses a proportional and derivative controller in which the sensed forces are generated from the modifications of the position and velocity (Zeng & Hemami, 1997). In the box 4.1 of Figure 2.38, the position modification is very similar to the one in active stiffness control. The sensed forces influence the position modification by multiplying the matrix $K_{F1}$. In the velocity modification (box 4.2), the results are also modified by the sensed force with a gain factor matrix of $K_{F2}$. The velocity feedback loop is able to modify the damping constant of the manipulator contacted with the environment. Thus, Impedance control is normally involved to satisfy the needs of adaptation to the damping characteristics of the environment (Zeng & Hemami, 1997).

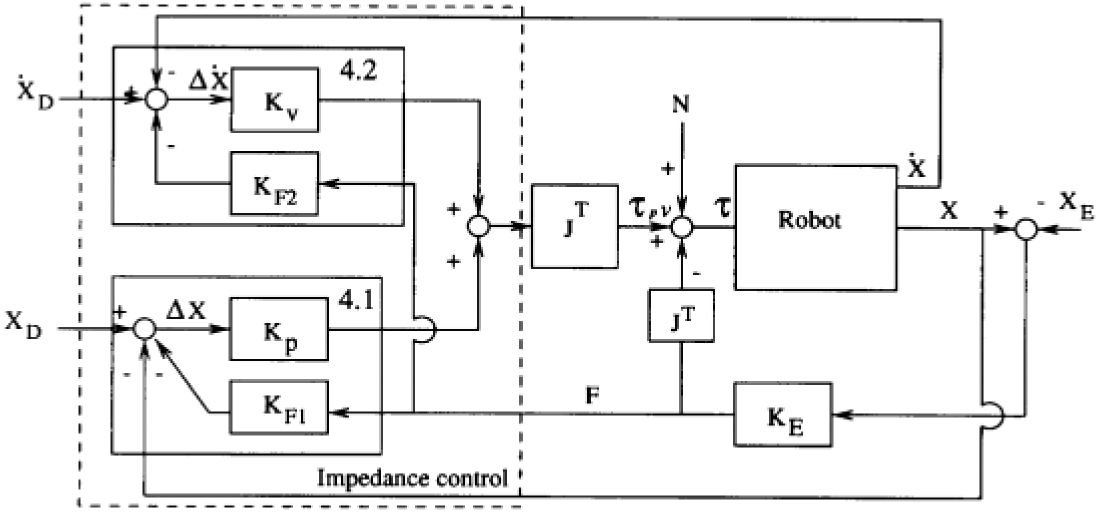

Figure 2.38 Basic impedance control (Zeng & Hemami, 1997)

The mechanical impedance $Z_m$ used to represent the relationship between the velocity $\dot{X}$ and the applied force *F* in the frequency domain, is expressed by

$$\frac{F(s)}{\dot{X}(s)} = Z_m(s) \tag{12}$$

In terms of position *X(s)*, it is expressed as

$$\frac{F(s)}{X(s)} = sZ_m(s) \tag{13}$$

Impedance control can also be implemented in another form, position-based impedance control as shown in Figure 2.39. $X_F$ represents the force-feedback trajectory. $X_I$ is the modified desired position input which is the solution to the following equation

$$M\ddot{X}_I + D\dot{X}_I + KX_I = -F + M\ddot{X}_D + D\dot{X}_D + KX_D \tag{14}$$

Where $X_I(0) = X_D(0), \dot{X}_I(0) = \dot{X}_D(0)$. *M, D* and *K* are the constant matrices of the desired inertia, damping and stiffness values, respectively. $X_I$ is a function of both the input $X_D$ and the sensed force *F*.

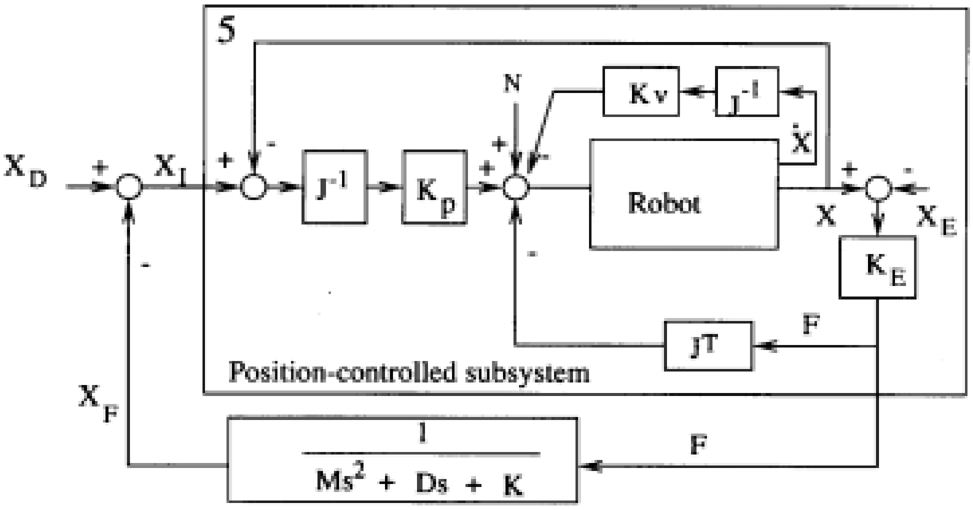

Figure 2.39 Position-based impedance control (Zeng & Hemami, 1997)

Impedance control is not suitable for applications where accurate force regulation is required (de Wit et al., 1996). Impedance control is limited to the contact tasks in which a specific contact force is required to apply on the surface. Poor position accuracy due to the wrong desired impedance may cause continuous oscillation (Heinrichs & Sepehri, 1999). Like stiffness control, the dynamic properties of the manipulator and its environment in impedance control need to be well known to control the contact force (Yu, 2000). Adaptive strategies were considered for controlling the mechanical impedance of robot manipulations (Colbaugh et al., 1991; Matko et al., 1997; Soitrov & Botev, 1993). Adaptive impedance control was implemented with inner position loop to improve position tracking accuracy (Lu & Meng, 1991).

In *admittance* control, the sensed contact force is used to adjust the motion, which can be a desired acceleration or a desired velocity. Figure 2.40 shows the structure of a common *admittance* control. Admittance control is widely used in robotic assembly where desired force tracking control is required.

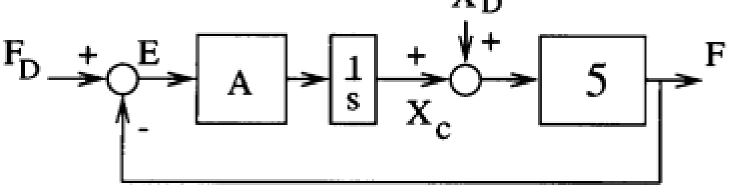

Figure 2.40 Admittance control (Zeng & Hemami, 1997)

The mechanical admittance is defined as the inverse of the impedance in equation 12, which is expressed as

$$A = \frac{\dot{X}}{F} \tag{15}$$

### *Hybrid Force/Position Control*

Another most common basic approach to force control is hybrid force/position control, besides impedance control. In hybrid control, motion and force are controlled separately. While impedance control, motion or force is not regulated directly, but instead the ratio of force to motion (or the mechanical impedance) is regulated (Hogan, 1985b, 1985c).

In hybrid control, the implementation of pure force control is the goal (De Schutter et al., 1998). Figure 2.41 illustrates the implementation direct force control. The measured force errors are directly converted to actuator forces or torques applied. The robot has mass $m$. The compliant environment has stiffness $k_e$. $F_d$ is the desired force; $F$ is the actual force measured by a force sensor; $K_f$ is a proportional control gain; $K_d$ is damping factor from velocity feedback (Bruyninckx et al., 1995); $F_{act}$ is the actuator force; $F_{dist}$ is an external disturbance force; $x$ and $v$ represent the position and the velocity of the robot; $x_e$ represents the position of the environment; $\hat{m}$ is an estimate of the robot mass to account for the robot dynamics. In Figure 2.42, measured force errors are converted to desired motion, either desired position or desired velocity, which is executed by a position or velocity control loop. This implementation is called inner position (or velocity)/outer force control. The velocity controller includes a feedback gain $k_v$. Compared between Figure 2.41 and 2.42, the advantage of the inner/outer control is that the bandwidth of the inner motion control loop can be made faster than the bandwidth of the outer force control loop (Carinena & Ranada, 1993). Hence, if the inner and outer loops are tuned consecutively, force disturbances are rejected more efficiently in the inner/outer control (Chiaverini & Sciavicco, 1993).

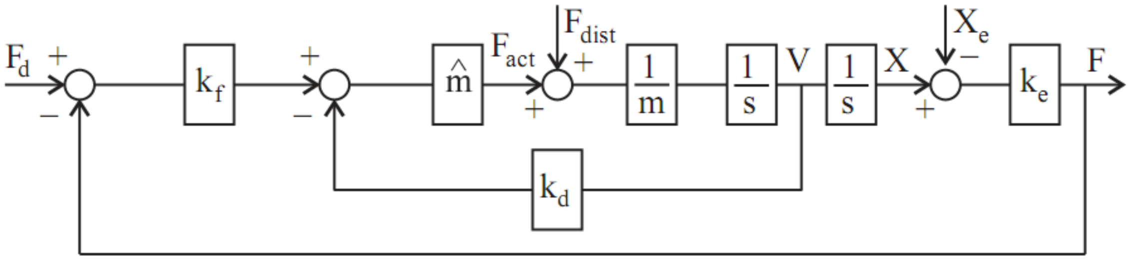

Figure 2.41 Direct force control (De Schutter et al., 1998)

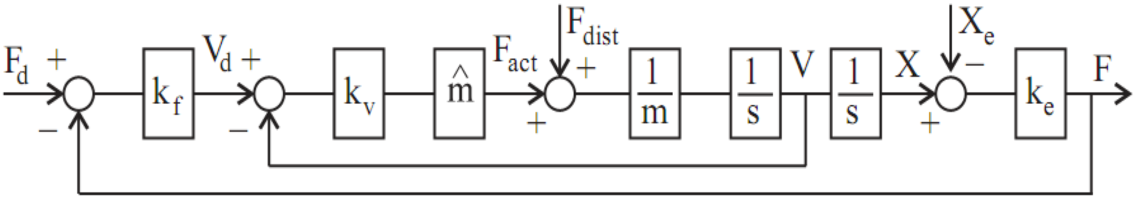

Figure 2.42 Force control with inner position/velocity control loop (De Schutter et al., 1998)

Hybrid force/position control has been widely used with other advanced controllers, such as adaptive, learning, fuzzy controllers and etc. For example, adaptive model-based schemes were introduced into the hybrid force/position control for geometrically constrained robot arms (Arimoto et al., 1993; Slotine & Li, 1987; Whitcomb et al., 1997). Learning control was used to improve the tracking error based on the operation data of repetitive tasks (Guglielmo & Sadegh, 1993; Jeon & Tomizuka, 1993; Lucibello, 1993). Fuzzy control was implemented in hybrid force/position control to improve model uncertainty (Hsu & Fu, 1996).

Anderson and Spong (1988) proposed hybrid impedance control combing impedance control and hybrid force/position control into one control scheme. This allows that the desired impedance of the robots can be selected by user to increase more flexibility. In Figure 2.43, $Z_{mp}\ and\ Z_{mf}$ are the customized impedance terms, which can be diagonal matrices to represent the impedance along every degree of freedom. $S$ is the compliance matrix. The modified desired trajectory $X_i$ is the sum of the modified position trajectory $X_{pi}$ and the modified force trajectory $X_{fi}$.

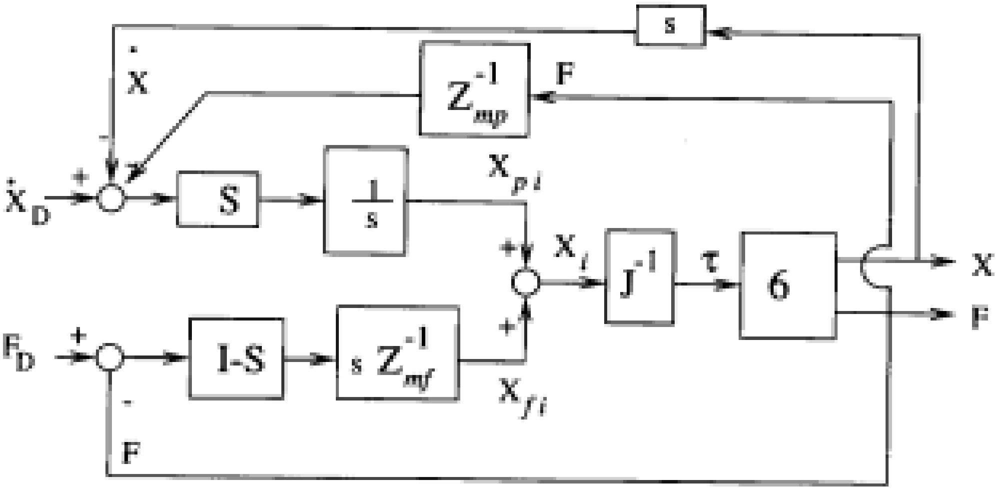

Figure 2.43 Hybrid impedance control (Zeng & Hemami, 1997)

### *Explicit and Implicit Force Control*

Explicit and implicit force control are both focus on force regulation (Chiaverini et al., 1999). In explicit force control, the measured force is directly used for the feedback to generate the force error (Figure 2.44). Typically, one of the subsets of PID control law is selected (Zeng & Hemami, 1997).

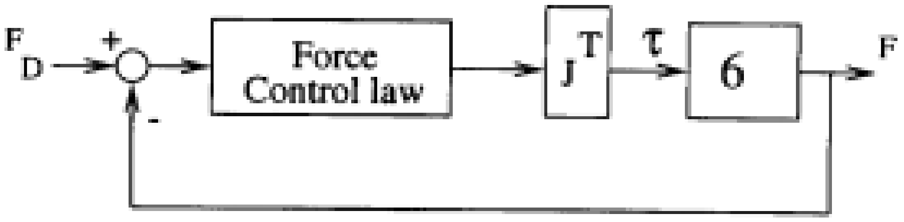

Figure 2.44 Explicit force control (Zeng & Hemami, 1997)

### 2.5.2. *Advanced Force Control*

Complex tasks involving unknown parameters, unstructured environments, external disturbances and etc. are real challenging problems for the robot (Zeng & Hemami, 1997). Many advanced force control algorithms are studied to achieve a better control performance in the presence of uncertain dynamics, sensor noise and external disturbances to the robot. Based on the fundamental force control strategies in section 2.5.1, advanced force control methods including adaptive control, learning control and fuzzy control are described here.

#### *Adaptive Force Control*

The basic goal of adaptive control is to maintain consistent performance of a control system in the presence of unknown parameters in robot and environment (Zeng & Hemami, 1997). Therefore, an adaptive force controller integrate certain adaptive strategy into a controller to maintain the desired force, impedance, admittance and so forth with unknown parameters of robot or in an unknown environment. An adaptive controller is a controller with adjustable parameters and a system for adjusting the parameters (Astrom & Wittenmark, 1994). In Figure 2.45, the inner loop (solid line) is an ordinary feedback control loop around the planet. The outer loop (dashed line) adjusts the parameters of the controller.

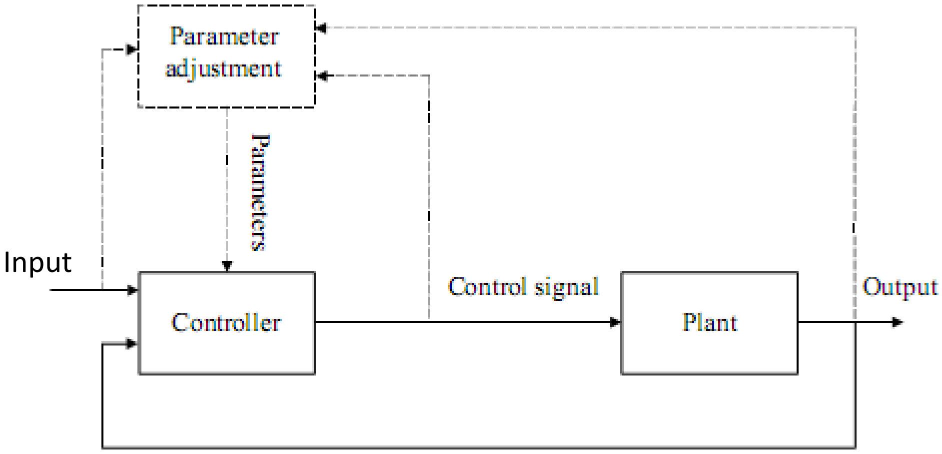

Figure 2.45 Adaptive control system (Jantzen, 2002)

***Learning Control***

Learning control has been introduced into different robot control, such as robot position control (Arimoto et al., 1984) and hybrid force/position control (Jeon & Tomizuka, 1993; Lucibello, 1993; Pandian & Kawamura, 1996). For example, learning control implemented in hybrid force/position control is suitable for the robot performing repeated tasks. The performance of the robot can be improved significantly. To learn the command input, the errors of position, velocity, acceleration or force are utilized. Figure 2.46 shows the learning control principle for robot force control.

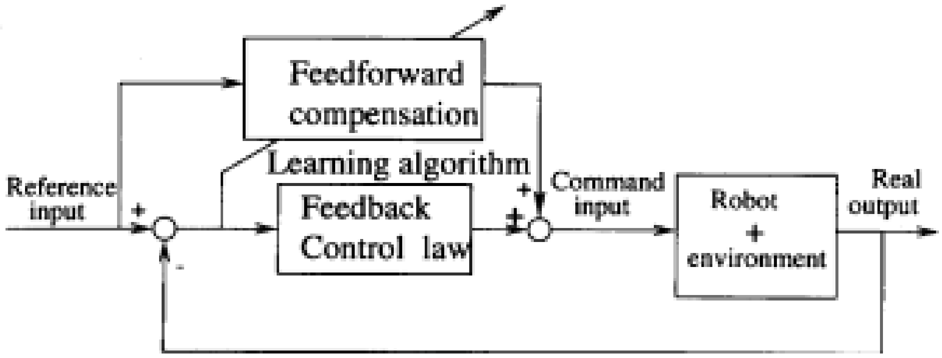

Figure 2.46 Learning algorithms in robot force control (Zeng & Hemami, 1997)

***Fuzzy Logic Control***

Fuzzy logic can be described as 'computing with words rather than numbers', fuzzy control can be described as 'control with sentences rather than equations' (Jantzen, 2002). Fuzzy logic is a method of rule-based decision making used for expert systems and process control that emulates the rule-of-thumb thought process used by human beings (Klir & Yuan, 1995). It is based on the Fuzzy set theory, which is defined quantitatively by linguistic terms called membership functions. The membership function specifically defines degrees of membership, which might be any value between 0 and 1.

With membership functions defined for system inputs and outputs, a rule base of IF-THEN type conditional rules, can be formulated. Such a rule base and the corresponding membership functions are employed to analyze controller inputs and determine controller outputs by the process of fuzzy logic inference.

The primary building block of fuzzy logic systems is the linguistic variable. This variable is one with a value that is a language expression, referring to some quantity of interest, related to the system of interest. It translates real values into linguistic values. Linguistic terms represent possible values of a linguistic variable. Each linguistic term is represented by a fuzzy set defined by a membership function. The defuzzification step translates the linguistic result back into a real value representing the current value of the control variable. Figure 2.47 shows the architecture of fuzzy adaptive controller.

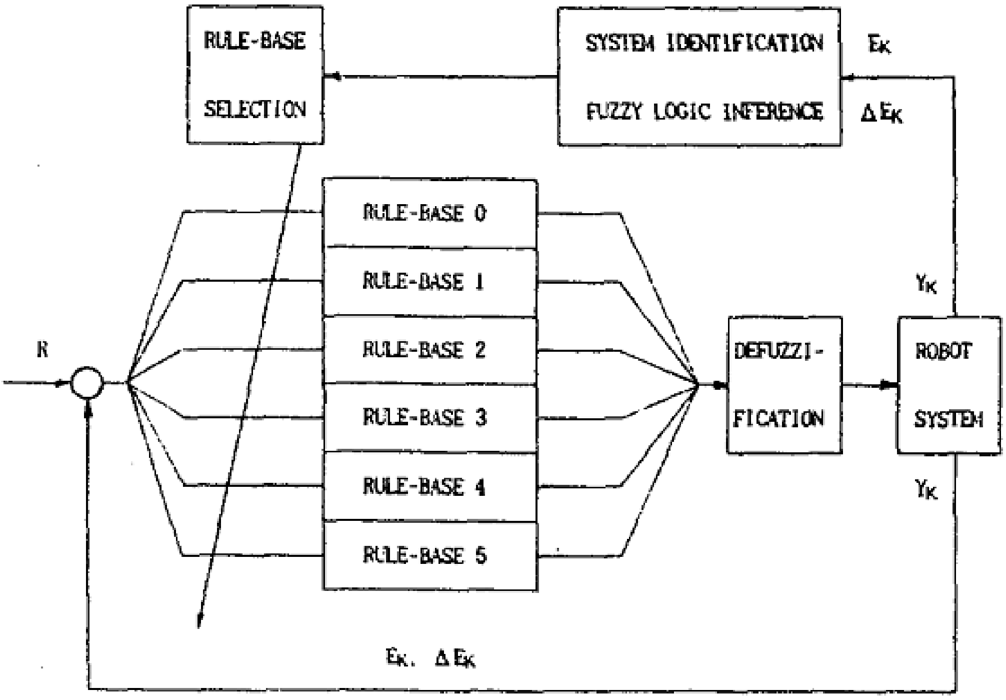

Figure 2.47 Architecture of fuzzy adaptive controller (Kim & Park, 1991)

## *2.6. Analysis of Literature*

The literature review covers four topics including the state of the art of chewing robots, human masticatory system, food rheological model and robot force control. Most chewing robots reviewed in the literatures are six degree freedom robots, which are WY-5 series robots, JSN series of jaw simulators, robotic jaw of 6RSS parallel mechanism and Dento-Munch Robo-Simulator. Compare to the linkage chewing robot, although these robots allow better flexibility, they involve more complex control systems. On the other hand, the linkage chewing robot is much simpler in structure and motion control and more reliable in operation. The chewing simulator involving two degree freedom is developed for the similar purpose with the chewing robot, which is used for food breakdown. However, the chewing simulator only performs simple crushing and grinding movement, rather than simulates the human chewing trajectory profiles. Therefore, the chewing simulator cannot simulate human chewing behaviour to perform chewing. The literature shows that the linkage chewing robot is unique, simple and easy to use.

In the literature, the tongue and occlusal surfaces show their importance in masticatory performance. The tongue plays a crucial role to push the food particles on the teeth during chewing so that the food could be chewed efficiently. The occlusal surfaces where the teeth occlude with each other directly affect the chewing performance. Both factors are required in the chewing robot so that the chewing robot could perform continuous chewing and reproduce human chewing results. Therefore, 3D designed molar teeth based on 3D scanned human teeth will be used for perfect occlusion to match what occurs in human in the chewing robot for better fragmentation. A practical food manipulation system mimicking the tongue and cheek will be developed to allow continuous chewing in the chewing process.

The literature of the food rheological model shows that the food can be expressed in mechanical elements to present their rheological behaviour. This is very useful to develop simulation models of food as a part of the chewing robotic system in Chapter 4.

Proper force application during chewing is required to replace the shock absorber to generate controllable force profile. Passive force control such as a spring mass system will be investigated. Force sensor is required to allow force data collection from the teeth and provide feedback for the compliance force control system to simulate human chewing behaviour on different foods.

In the literature, among all the force control algorithms, adaptive control is suitable to perform in the presence of unknown parameters in robot and environment. The chewing robot needs to adapt different foods with different texture. The chewing robot also needs to adapt to the change of food texture due to the fracture of the food during the chewing process. Therefore, an adaptive controller with adjustable parameters to comply with different textures of foods is desirable.

The literature shows no evidence about how the chewing force profile of any food should be specified. However, a few researches were conducted to find out the effects of food hardness on chewing forces and masticatory kinematics (K. Anderson et al., 2002; Kohyama, Hatakeyama, Sasaki, Dan, et al., 2004). It was found that the harder the food texture, the higher the chewing velocity which results in the larger chewing force. Based on this general concept, in order to control the chewing force, fuzzy control based on linguistic rules is proper for the task.

# 3. *IMPROVEMENT OF THE CHEWING ROBOT FOR COMPLIANCE CONTROL*

## *3.1. Introduction*

In order to implement adaptive fuzzy control system and enable the chewing robot to chew food like human, a few improvements, including implementing force sensor and DAQ card, design and development of spring-mass system and food manipulation system, have been made and described as follows.

## *3.2. Implementation of Force Sensor and DAQ card*

A force sensor sensing the chewing force in real time is required to provide feedback force to complete the closed-loop force control system. This force sensor also provides the 3D occlusal force profile on teeth for analysing the food texture. This task involves selecting a three dimensional force sensor, installing the force sensor under the lower teeth and interfacing the force sensor with the existing software, LabView. The selection of the force sensor includes the justification and comparisons to other sensors. An analogue to digital converter capable of rapid communication is also required to allow data collection.

### 3.2.1. *The Selection of Force Sensor*

In order to apply the appropriate force profile on the food during chewing for texture analysis, real time force measurement during chewing process is required. The selection of the force sensor is mainly determined from four factors: 1) force sensing range, 2) physical properties, 3) accuracy, and 4) data acquisition (DAQ) card, software supported by LabView. First, the force sensing range should be higher than the maximum chewing force applied from the machine, which is 150N. Second, the sensor would have to be appropriately sized to fit under the lower teeth, which means that the diameter of the force sensor should be smaller than 52mm. The thickness of the force sensor should be smaller than 20mm. Furthermore, most force sensors have 0.1% accuracy, which means the accuracy is equal to 0.1% of the total force sensing range. Therefore, the force sensing range should not be too much higher than 150N to give a better accuracy. Finally, DAQ card is required to processing the signal from the force sensor to give a meaningful result. Since the control software of the chewing machine is programmed by LabView, the driver of the DAQ card should be supported by LabView. The DAQ card should also include spare analogue and digital input ports for acquiring the encoder signal, current signal and any future requirements.

Through all these considerations, ATI Mini40 force sensor was selected and installed under the lower teeth (Figure 3.1). The transducer senses applied loading with six degrees of freedom. Mini40 also has a compact design with diameter of 40mm and thickness of only 12.2mm, which is small enough to fit under the lower teeth. The parameters of the force sensor are listed in Table 3-1. A National Instruments PCI-6036E DAQ card for acquisition of the data from the sensor was used (Figure 3.2). The specifications of PCI-6036E DAQ are listed in Table 3-2. Real time data recording function has been added into the LabView control programme of the chewing machine (Figure 3.4). The data recording function has the ability to acquire the signal from the force transducer, the incremental encoder and current from the motor. And then these signals are recorded into one spreadsheet. The force data programme was created to convert the force transducer data to real force data by multiplying the calibration matrix from ATI.

Figure 3.1 ATI Mini40 force sensor

Table 3-1 Parameters of Mini40 force sensor

| Axes | Sensing Ranges | Resolution | Overload |
|---|---|---|---|
| $F_x, F_y$ $(\pm N)$ | 80 | 1/200 | 870 |
| $F_z$ $(\pm N)$ | 240 | 1/100 | 2700 |
| $T_x, T_y$ $(\pm Nm)$ | 4 | 1/8000 | 22 |
| $T_z$ $(\pm Nm)$ | 4 | 1/8000 | 21 |

Figure 3.2 National Instruments PCI-6036E DAQ

Table 3-2 Specifications of PCI-6036E

| | Channels | Resolution | Sample Rate |
|---|---|---|---|
| Analog Input | 16 | 16 bits | 200 kS/s |
| Analog Output | 2 | 16 bits | 10 kS/s |
| Digital I/O | 8 | --- | --- |
| Counter/Timers | 2 | 24 bits | 10 ns |

### 3.2.2. *Interfacing the Force Sensor with LabView*

The hardware configuration of the force sensor ATI Mini40 interfacing with the DAQ card is shown in Figure 3.3. The force sensor powered by the power supply electronics transmits the transducer load information (analogue voltages) to the interface electronics first. The interface electronics conditions the transducer signals to be used with the data acquisition system, and then sends the amplified signal to the PCI-6036E DAQ through a robust cable with NI connector.

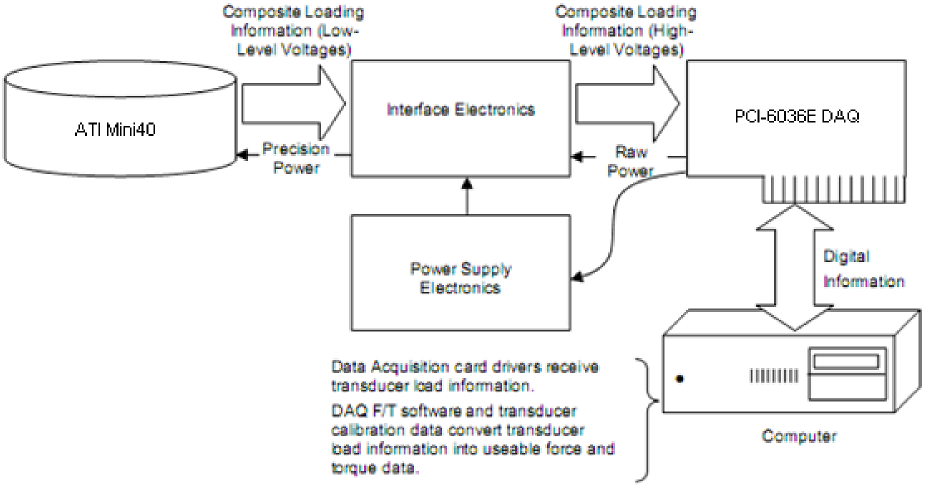

Figure 3.3 Hardware configuration of the force sensor ATI Mini40

Since the signal obtained from the force sensor is not the final force and torque values (only analog voltages), a real-time converting program in LabView is used to convert the transducer signals from analog voltages into real force and torque data. A LabView code of force data acquisition is shown in Figure 3.4. The part on the left is used for acquiring analogue signals. The range of the input analogue signal is set between -10 and 10 volts. The sample rate is selected to be 1 KHz for best performance, since it does not only provide sufficient force data to generate the force profile, but also not generate too much data to make the timing lag. The part included in the dashed block on the top right in Figure 3.4 is the force calibration matrix. The real force and torque data is the product of the transducer analogue signals and the calibration matrix. The part below the dashed block on the bottom right exports the force and torque data to a spreadsheet.

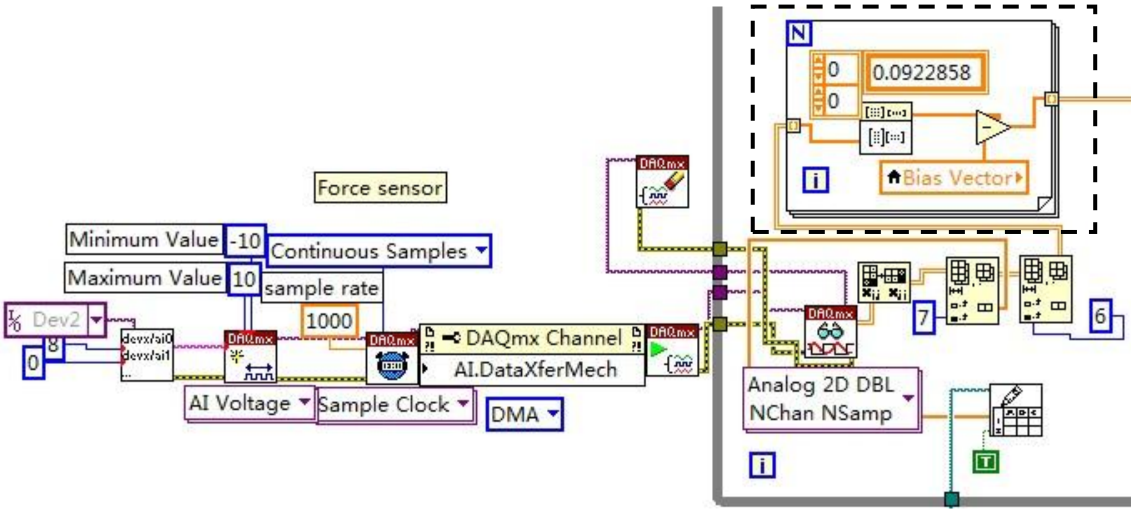

Minimum Value -10
Maximum Value 10
sample rate 1000
Continuous Samples
AI Voltage
Sample Clock
DMA
DAQmx Channel AI.DataXferMech
Analog 2D DBL NChan NSamp

Figure 3.4 LabView code of force data acquisition

Force and torque acquired by the force sensor during chewing have different coordinate system from the one on the teeth. Therefore, the transformation of the force and torque vector from the sensor frame to the teeth frame is required. The output of the sensor is a 6 x 1 vector, ${}^{S}F$, composed of three forces and three torques in the sensor frame S. The transformation from the sensor frame to teeth frame can be written in Eq. (16) (Craig, 1989).

$$ {}^{T}F_{T} = {}^{T}_{S}T_{f} \cdot {}^{S}F_{S} \tag{16} $$

Where $ {}^{T}_{S}T_{f} = \begin{bmatrix} {}^{T}_{S}R & 0 \\ {}^{T}P_{SORG} \times {}^{T}_{S}R & {}^{T}_{S}R \end{bmatrix} $

As it is known that

$$ {}^{T}P_{SORG} = \begin{bmatrix} 0 \\ -0.0005 \\ -0.04 \end{bmatrix} \qquad {}^{T}_{S}R = \begin{bmatrix} 1 & 0 & 0 \\ 0 & 1 & 0 \\ 0 & 0 & 1 \end{bmatrix} $$

Substituting ${}^{T}P_{SORG}$ and ${}^{T}_{S}R$ , ${}^{T}_{S}T_{f}$ can be obtained.

$$ {}^{T}_{S}T_{f} = \begin{bmatrix} 1 & 0 & 0 & 0 & 0 & 0 \\ 0 & 1 & 0 & 0 & 0 & 0 \\ 0 & 0 & 1 & 0 & 0 & 0 \\ 0 & 0.04 & -0.0005 & 1 & 0 & 0 \\ -0.04 & 0 & 0 & 0 & 1 & 0 \\ 0.0005 & 0 & 0 & 0 & 0 & 1 \end{bmatrix} $$

## 3.3. *Passive Compliant Force Control*

The original resulting force profile during occlusion was just a sudden high force, followed by a rapid reduction. In order to improve food particle size reduction to a distribution which closely matches that produced by human, passive compliant force control, such as a spring-mass system, instead of the shock absorber should be installed to apply specified human occlusal chewing force profile. The spring-mass system will be built according to the simulation model in the above objective.

### 3.3.1. *Design of Spring-Mass System*

The original shock absorber MA150 installed in the chewing robot uses spring and hydraulic liquid damping system (only 6.9N return force from spring). According to the datasheet of the shock absorber, the effective velocity is from 0.15m/s to 3.66m/s. The response of the shock absorber when compressed at different velocities, which is from 3mm/s to 10mm/s, the reaction force is from 10N to 30N. According to the literature (Ogawa et al., 2001), the displacement in the occlusal phase is 0.5mm and the time to complete this occlusal phase is 0.12s (that is 8.33mm/s in velocity). The required chewing force is from 70N to 150N (D. J. Anderson, 1956). Therefore, the movement of the shock absorber quickly reaches its limit (10mm), which is stopped by the guidance pins, the force profile changes in a sudden (see Figure 3.5).

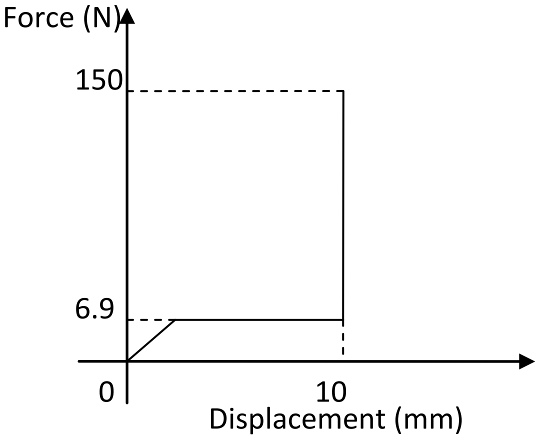

Figure 3.5 The force profile of original shock absorber in the chewing robot

When the teeth are not under the force, the spring is compressed to a shorter length, which is the initial pretightening force, such as 70N, the compressed length of the spring is 10.5mm. Changing the maximum movement of the brass bush (used to block the spring inside the aluminium sleeve) from 10mm to 12mm, thus, the force from the spring is 12mm x 6.69 N/mm = 80N. Since the initial pretightening force is 70N, when the brass bush is stopped by the guidance pins, the force applied is 70N + 80N = 150N. Compared to the shock absorber, the force applied changes more steadily (see Figure 3.6).

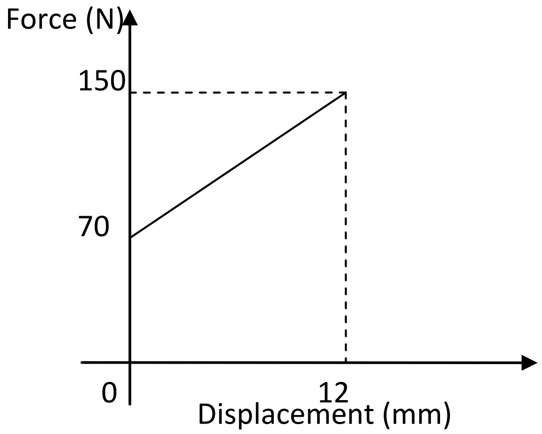

Figure 3.6 The force profile of the spring mass system with a pretightening force of 70N to reach the maximum force of 150N

According to the energy conservation, the energy stored in the compressed spring and the energy produced by the gravity of lower teeth mechanism is equal to the kinetic energy produced by the lower teeth mechanism. Therefore, the formula is:

$$\frac{1}{2}mv^2 = \frac{1}{2}kx_f^2 - \frac{1}{2}kx_i^2 + mg\left(x_f - x_i\right)$$

$$m = 0.66kg$$

$$k = 6.69N/mm$$

$$x_i = 0 \sim 20mm$$

$x_f = x_i +$ Spring compression displacement

Spring recovery time: $t = \dfrac{x_f - x_i}{v}$

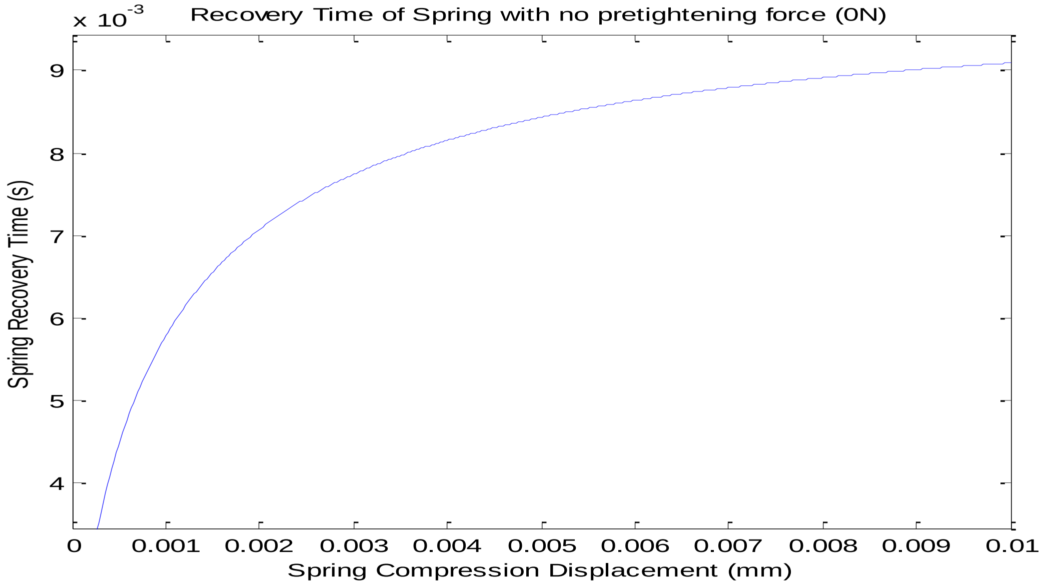

Figure 3.7 Spring recovery time with zero pretightening force (xi=0mm)

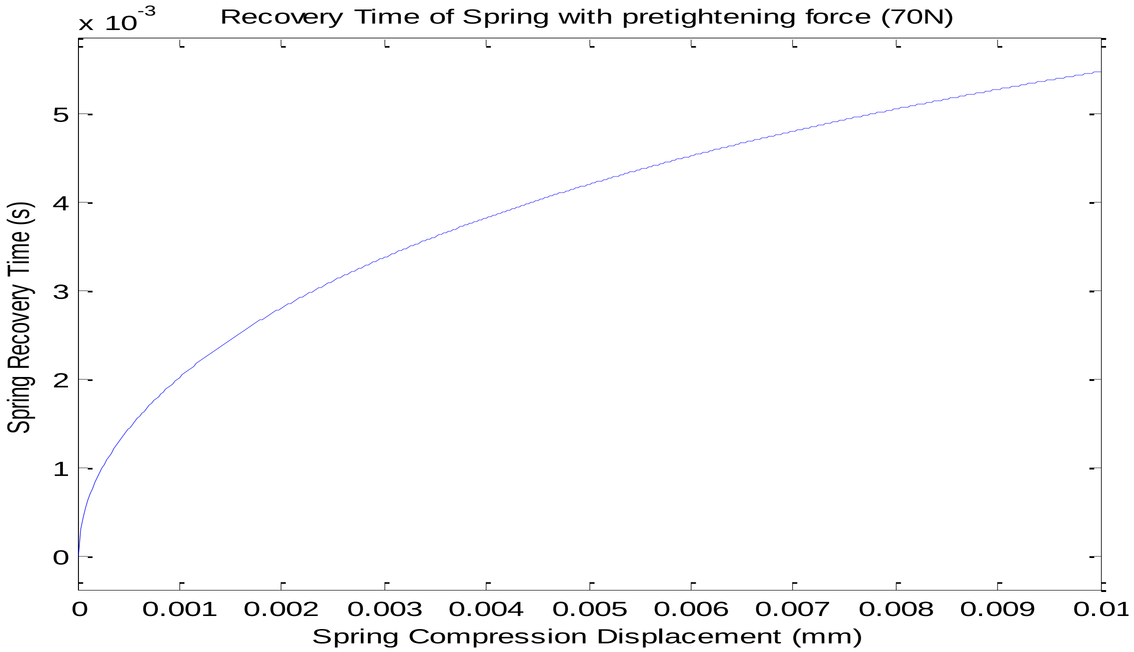

Figure 3.8 Spring recovery time with pretightening force of 70N (xi = 10.5mm)

From Figure 3.7 and Figure 3.8, it is found that the spring recovery time is related to the spring pretightening force and the spring compression displacement during chewing. When there is no pretightening force and the spring is compressed at maximum displacement (10mm), the spring recovery time is found to be the slowest, 0.0091s. The more the pretightening force, the less the recovery time is. The more the compression displacement, the more the recovery time is. Since the time for one chewing cycle is between 0.6 and 1 second, the spring recovery time is short enough for recovering before the next chewing cycle. Therefore, the spring rate is suitable for the chewing application.

A spring-mass system was designed to replace the shock absorber. The spring-mass system consists of five parts (Figure 3.9): 1) hard stop, 2) guidance pins, 3) pretightening plate, 4) spring, and 5) aluminium sleeve. The slot together with the guidance pins in the hard stop allows the spring compressed for 12mm, and also provides a high damping function to largely reduce the oscillation of the spring which may affect the chewing force profile. The pretightening plate is used to adjust the initial spring compression displacement to provide different initial force. Thus, the spring-mass system is very adaptable to any desirable force profile during occlusion required for different foods.

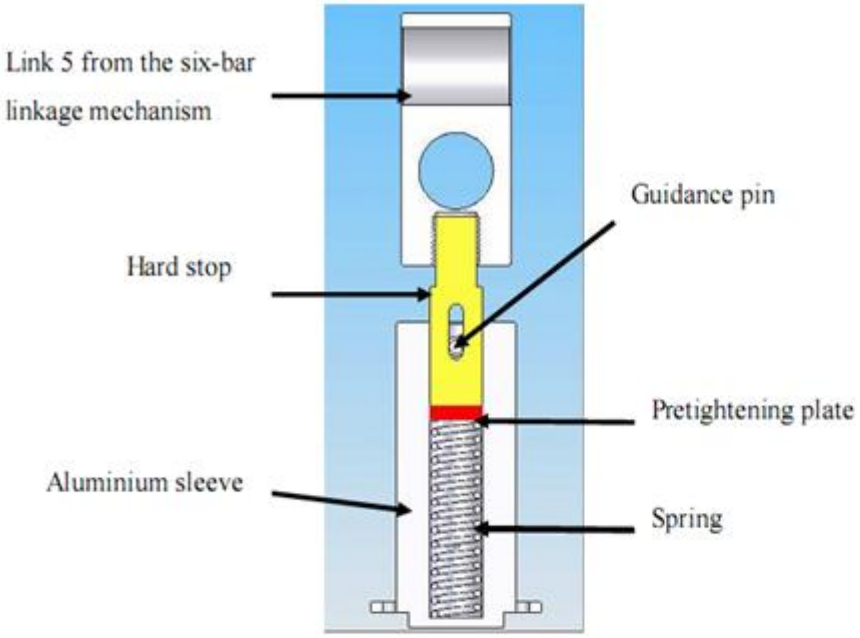

Figure 3.9 SolidWorks model of the spring-mass system

### 3.3.2. *Simulation Model*

The spring-mass system is simulated in SimScape in MATLAB (Figure 3.10). The input of the simulation model is the velocity in the direction of the spring force. The output is the force generated by the spring-mass system. The model consists of one translational spring, two translational hard-stop blocks, two ideal force sensors, one ideal motion sensor and one velocity source. The spring is in series with two hard-stop blocks. The translational hard-stop block 1 in Figure 3.10 is used for holding the spring in place, like the aluminum sleeve in Figure 3.9. The translational hard-stop block 2 in Figure 3.10 is to simulate the hard-stop mechanism in Figure 3.9.

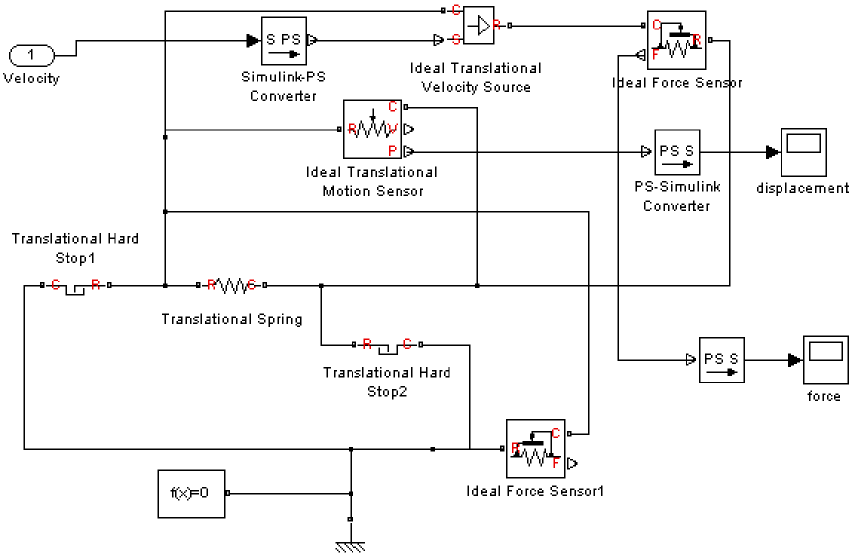

Figure 3.10 MATLAB simulation model of spring-mass system

A ramp signal is selected to be the velocity input to the spring-mass system, as shown in Figure 3.11. The compression force exerted from the spring is calculated based on the displacement which the spring is compressed (Figure 3.12).

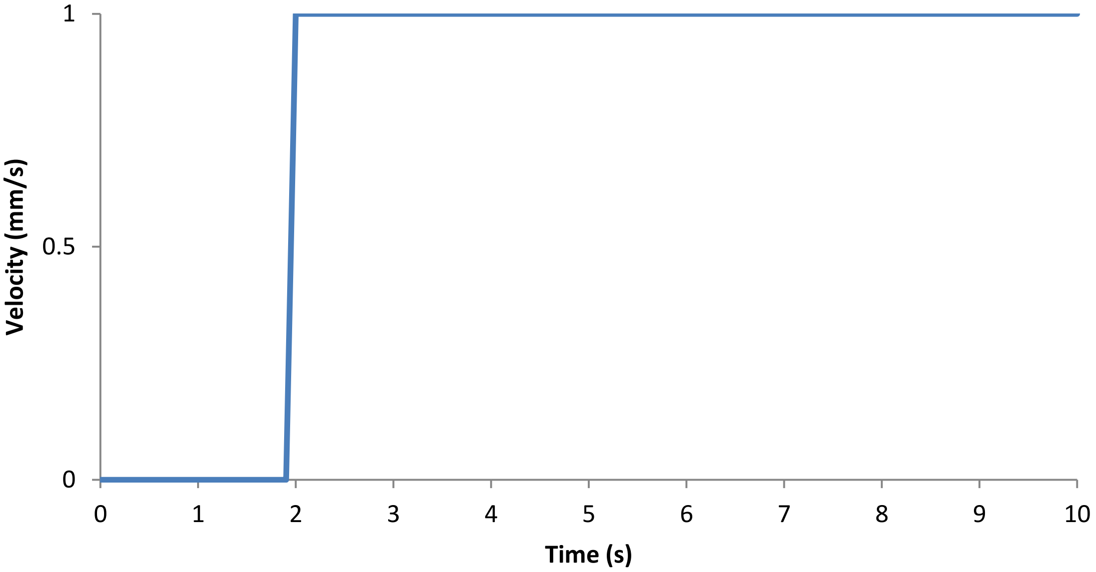

Figure 3.11 Ramp signal of velocity input to the spring-mass system

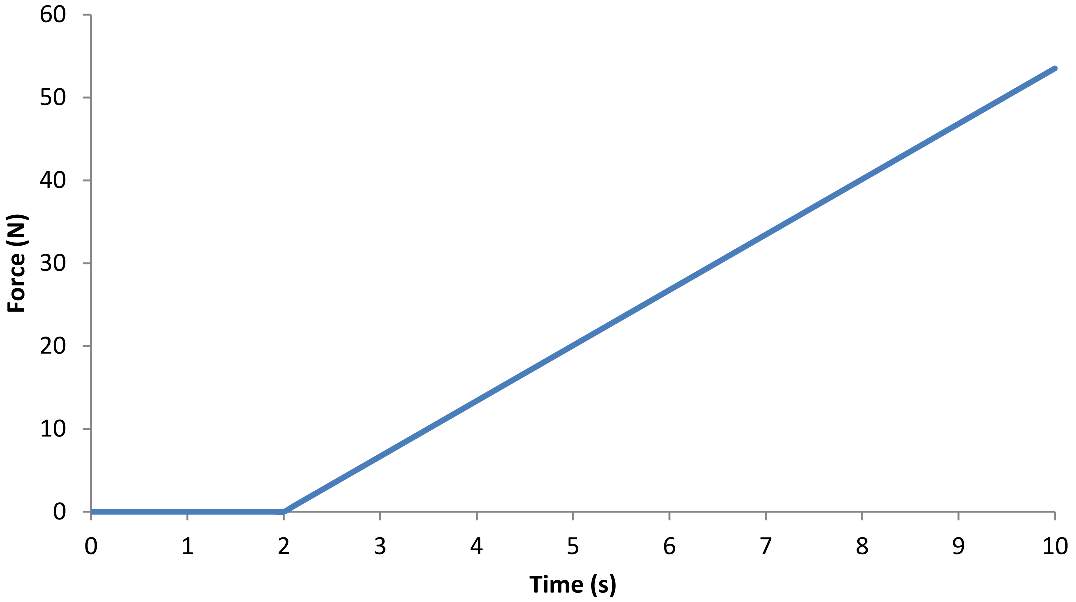

Figure 3.12 Compression force of the spring-mass system

## *3.4. Design and Development of Food Manipulation System*

Existing food retention system was a passive system which could not prevent particles falling out of the teeth. A new active food manipulation system together with a new set of teeth is critical for the chewing robot during continuous chewing. The designs of the new teeth and the food manipulation system are presented below.

### 3.4.1. ***Design of 3D Carved Teeth***

Original anatomically correct teeth attached in the chewing machine were made according to a teeth model for dental study. The teeth cannot occlude perfectly and chew food effectively. Therefore, a new set of teeth for chewing is designed according to a 3D scanned teeth model of human. The new upper and lower teeth will make perfect alignment with each other to chew food efficiently.

The teeth used in the original chewing machine consisted of four teeth including canine, pre-molar, first molar and second molar. Through the chewing experiment with the original teeth, it is found that the canine and pre-molar teeth could not hold food particles during chewing. Most particles chewed by the canine and premolar fell off the teeth and stuck between the gaps of the teeth. These particles would not be chewed again in the chewing process. This strongly affects the chewing results in particle size distributions. In human chewing, these particles were collected by our tongue and pushed back onto the teeth so that they could be chewed again.

The new set of teeth was designed to overcome the problems occurring during chewing experiment with the original teeth. The teeth were 3D tooled and based on 3D scans of the first human molars, after 3D modelling and rendering (SolidWorks 2010) for both the upper and lower teeth (Figure 3.13). The new upper and lower teeth both aligned in one straight line (Figure 3.13b). The upper and lower teeth are adjusted to ensure that they can occlude perfectly to allow an efficient crushing effect similar to that which occurs with human jaws (Figure 3.13a). The teeth only have the occlusal surface area of the molars rather than the whole teeth shape. There are only small gaps between the teeth, where only fine particles could be stuck and possibly not be chewed. The material of the teeth is selected to be brass so that it could not easily wear out. The shape of the bottom teeth block (left in Figure 3.13b) is part of the food manipulation system (which is described in 3.3.2).

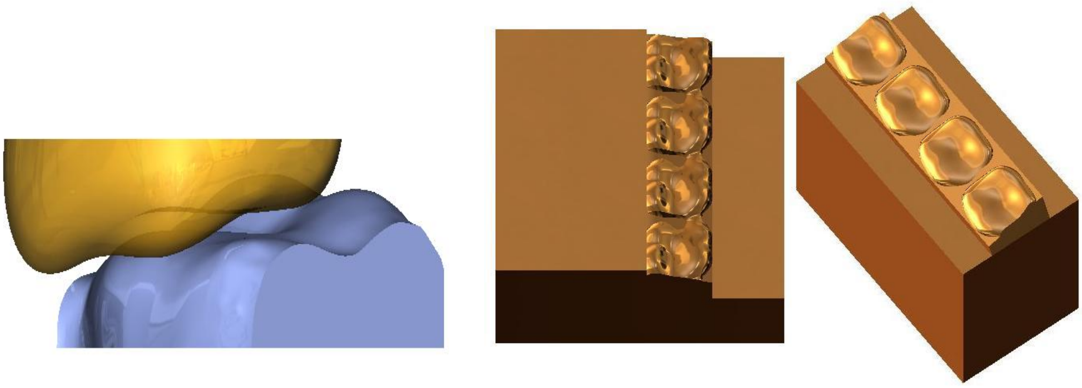

(a) (b)

Figure 3.13 Teeth designed for the robot: (a) Arrangement of upper and lower molar (b) Upper teeth (right) and lower teeth (left)

### 3.4.2. *Design of Food Manipulation System*

The tongue plays a crucial role throughout the complete food oral processing sequence and one of its key roles is as a mechanical device for food manipulations (M.R. Heath, 2002). According to the literature, in *Stage I transport* of chewing process, the function of the tongue is to transport the food particles from the anterior part the mouth onto the occlusal surface of the first molar after the first bite. Since the chewing robot does not have this stage of chewing process, the food is manually put onto the occlusal surface of teeth at the beginning of the chewing experiment. In *processing* stage, the function of the tongue is to collect insufficiently chewed food on the occlusal table and reposition it back on the occlusal surface by pushing.

Based on the functions of the tongue during chewing, three solenoids were used to achieve the purpose of repositioning food particles on the teeth (Figure 3.14). The left medium-sized solenoid is to mimic the pushing function of the cheek. The right large-sized solenoid is to mimic the pushing function of the tongue. The middle small-sized solenoid is to lower the occlusal table during occlusion, which is to avoid the contact with the upper teeth. When selecting the solenoids, the pushing force, linear displacement, size and recovery time are considered. The specifications of three solenoids are listed in Table 3-3. The pushing force needs to big enough to push the food on the teeth. The linear displacement needs to be long enough to avoid the chewing trajectory of the upper teeth. The size needs to be small enough to fit into the existing structure of the chewing robot. Especially, the small solenoid needs to fit under the occlusal table. The recovery time needs to be short enough to avoid the contact of the upper teeth during chewing. Based on the above considerations, the specifications of the selected solenoids are listed in Table.

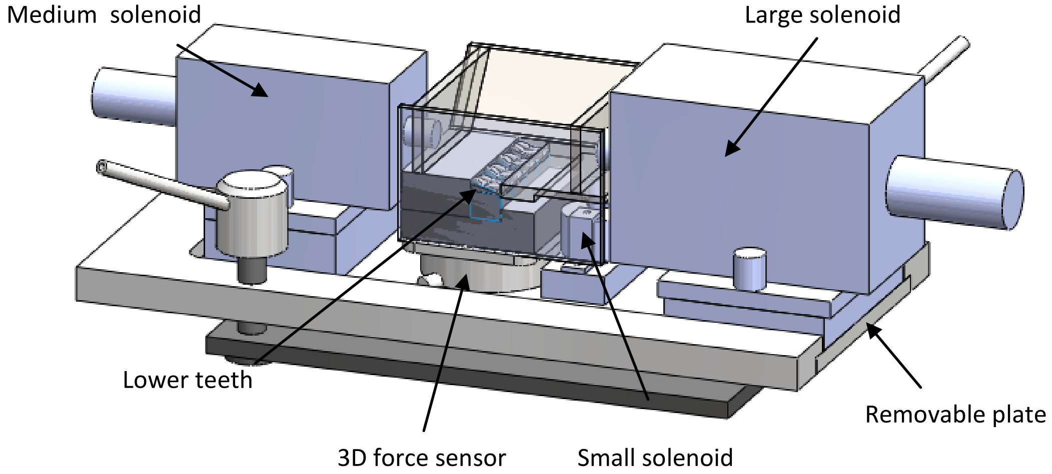

Figure 3.14 Food manipulation system in the chewing robot

Table 3-3 Specifications of solenoids

|  | Pushing force | Displacement | current (A) |
|---|---|---|---|
| Large Solenoid | 10kg | 20mm | 1 |
| Medium Solenoid | 7kg | 15mm | 0.52 |
| Small Solenoid | 200g | 2mm | 0.33 |

Since the chewed food particles will be collected for analysis, the food manipulation system is built on a removable plate which can be detached from the chewing robot for collecting the food particles. Two of the solenoids on the left and right side of the teeth are also easily detachable from the system for the convenience of particle collection.

### 3.4.3. *Control of Food Manipulation System*

The three solenoids are controlled by three digital outputs from the DAQ card through three Panasonic PhotoMos relay AQV252. The PhotoMos relay can drive up to 1A of continuous current, which is sufficient for the solenoids. The PhotoMos relay isolates the digital input signal on the side of the DAQ card from the relay circuit. This prevents any noise from the relay that could interfere with the controller. The solenoid control circuit is shown in Figure 3.15.

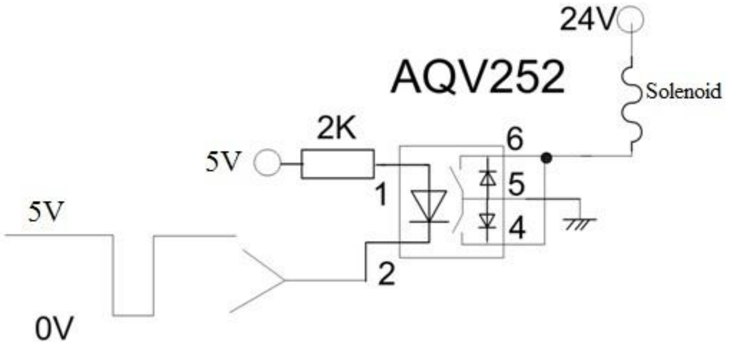

Figure 3.15 The solenoid control circuit using PhotoMos Relay AQV252.

#### *Implementation in LabView*

The solenoids are controlled by the digital output ports through LabView control software. The solenoids are triggered according to the upper teeth position which is converted from the crank angular position sensed by the encoder. After the occlusion, the small solenoid first pushes the food particles up to the occlusal surface. The pushing plates attached to the two big solenoids push the food particles towards the lower teeth and quickly returns back without contacting the moving upper teeth. After a few trials, the start positions for the small, medium and big solenoids are set to 250 degree, 300 degree and 300 degree from the max open position of the teeth, respectively. The stop positions for the small, medium and big solenoids are all set to 360 degree. Figure 3.16 shows the position control of the solenoids. The solenoids pushing rate, which is the food manipulation frequency, can also be configured as required by the operator. All the above configurations can be accessed through the

GUI setup page for the food manipulation system, as shown in Figure 3.17. The chewing robot with the food manipulation system and new teeth is shown in Figure 3.18.

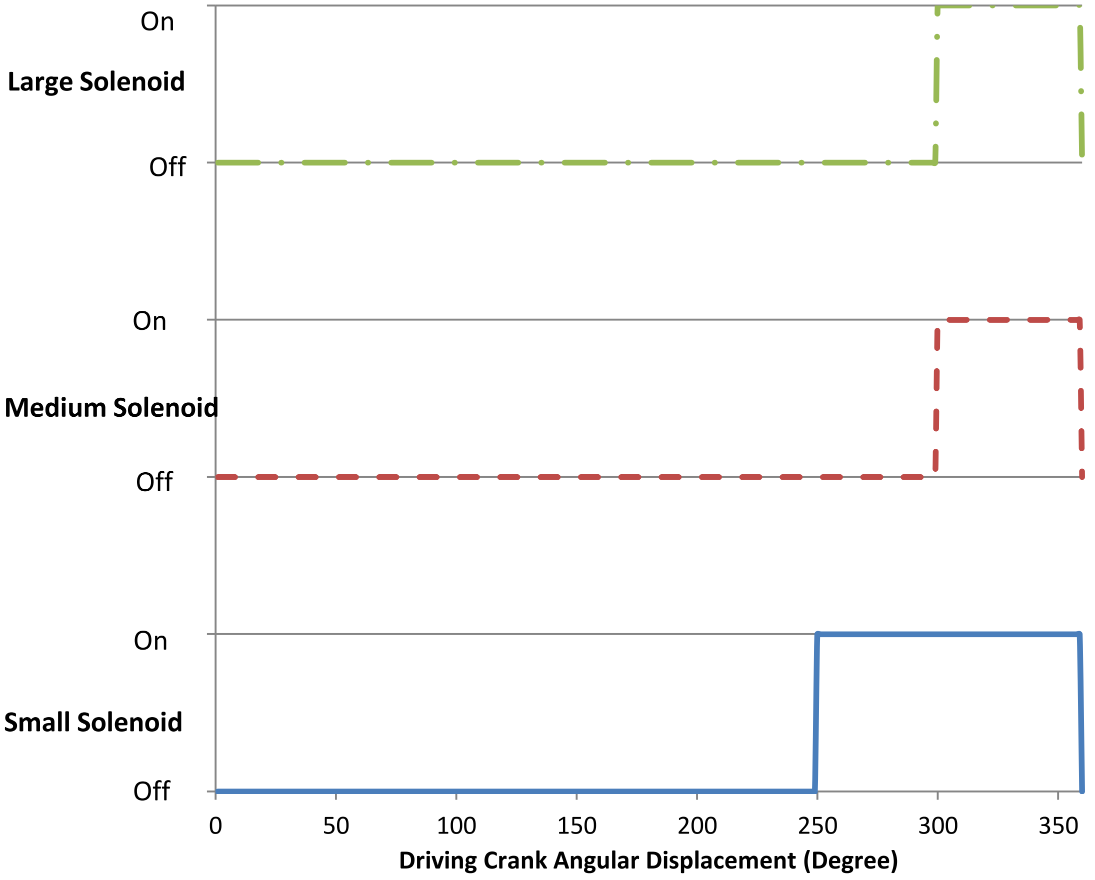

Figure 3.16 Position control of the solenoids

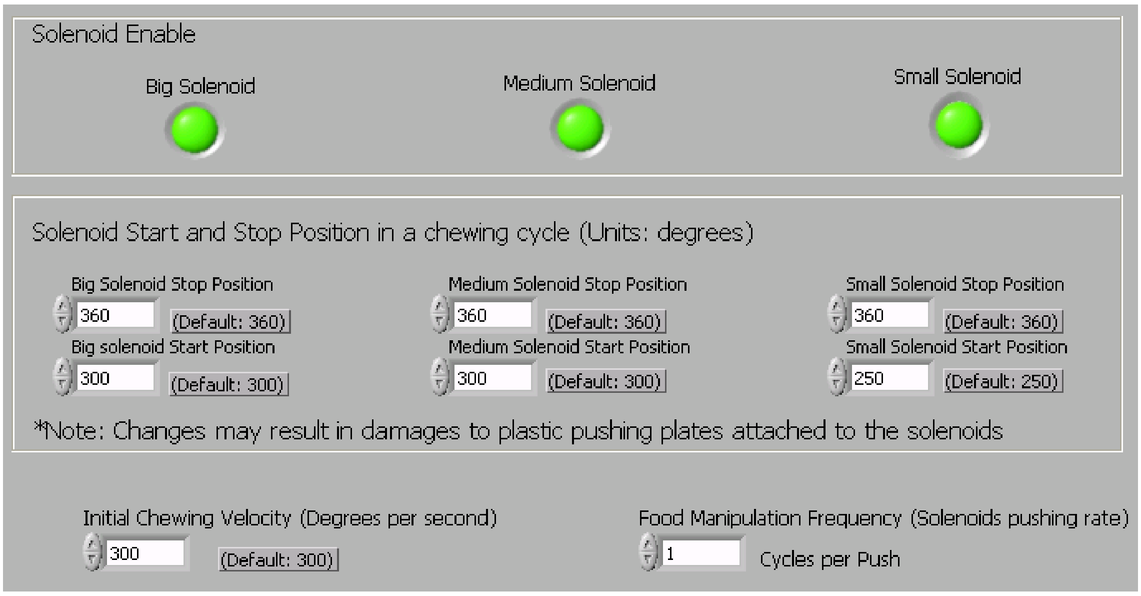

Solenoid Enable

Big Solenoid ●
Medium Solenoid ●
Small Solenoid ●

Solenoid Start and Stop Position in a chewing cycle (Units: degrees)

Big Solenoid Stop Position: 360 (Default: 360)
Big solenoid Start Position: 300 (Default: 300)
Medium Solenoid Stop Position: 360 (Default: 360)
Medium Solenoid Start Position: 300 (Default: 300)
Small Solenoid Stop Position: 360 (Default: 360)
Small Solenoid Start Position: 250 (Default: 250)

*Note: Changes may result in damages to plastic pushing plates attached to the solenoids

Initial Chewing Velocity (Degrees per second): 300 (Default: 300)
Food Manipulation Frequency (Solenoids pushing rate): 1 Cycles per Push

Figure 3.17 GUI setup for the food manipulation system

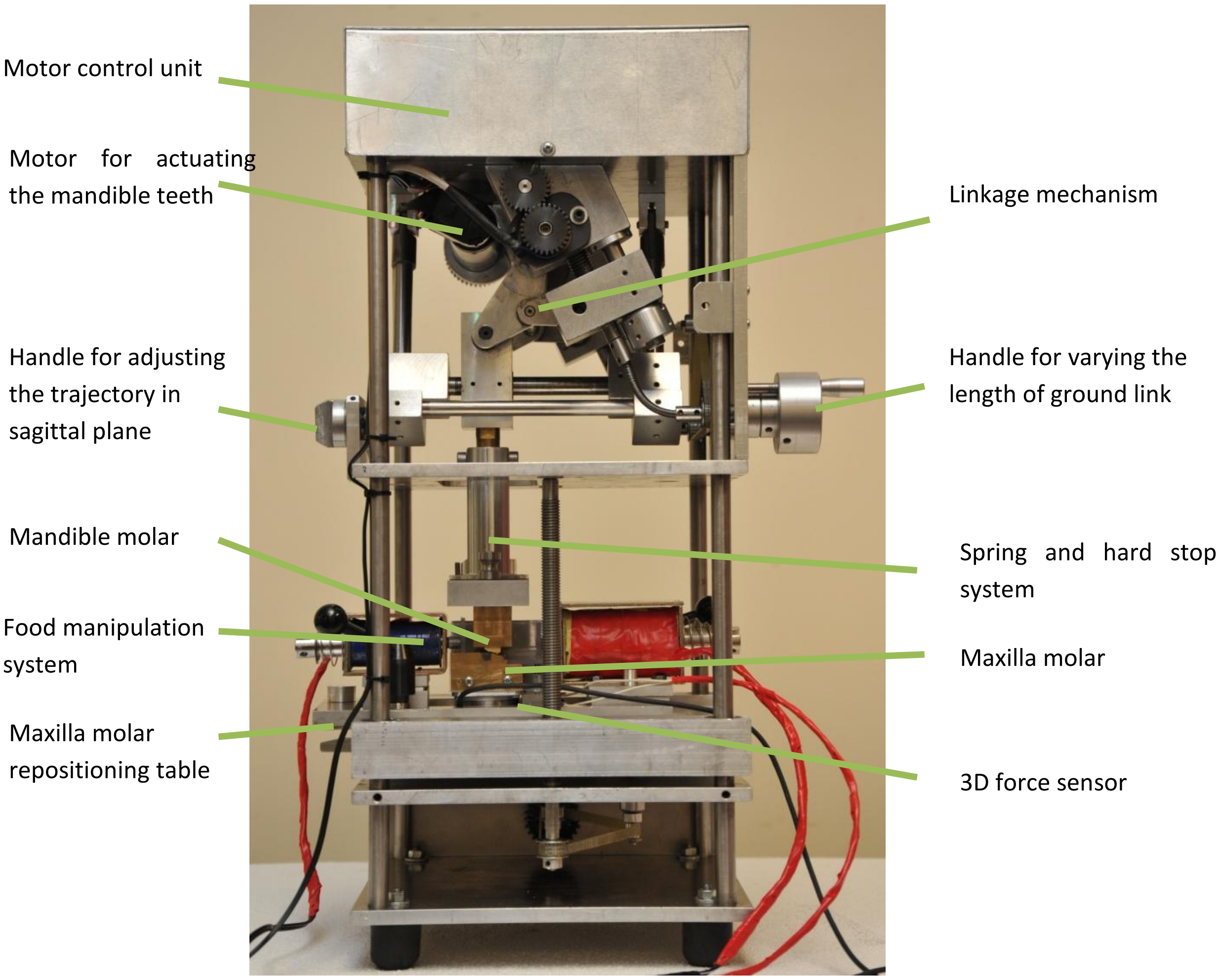

Figure 3.18 The linkage chewing robot with food manipulation system

## 3.5. *Chapter Conclusion*

In this chapter, a few improvements have been achieved to enhance the chewing robot so that the compliant force control can be implemented and the evaluation of the chewing robot with real food chewing experiment can be carried out. First, a 3D force sensor and correlated data collection hardware have been installed in the chewing robot. The force sensor allows the real-time force data to be collected during chewing. Moreover, the shock absorber attached to the upper teeth has been replaced with a properly designed spring-mass system for passive compliant force control. The spring and hard stop mechanism is able to generate an adjustable force profile during the chewing experiment. The adjustable force profile is realized by varying the pretightening force in the spring. Thus, the chewing robot can produce a proper force profile for the foods with different texture. Furthermore, an automatic food manipulation system and a new set of teeth have been developed and installed in the chewing robot. The food manipulation system utilized three solenoids to simulate the movements and functionality of human’s tongue by pushing the food particles onto the occlusal surface of the teeth during each cycle. The new teeth are 3D modelling designed and carved out of brass by 3D milling machine. The food manipulation system with the new teeth will improve the masticatory performance of the chewing robot to be close to the one of humans. The chewing robot now has a huge potential to be a useful tool for food evaluation.

# 4. *DYNAMICS MODELLING AND VALIDATION OF THE CHEWING ROBOTIC SYSTEM*

## *4.1. Introduction*

The chewing robotic system consists of the linkage chewing mechanism, DC motor control system and food models. Dynamics modelling of the chewing robotic system enables the compliant force control to be implemented and validated. Kinematics and dynamics of the linkage mechanism in the chewing robot are required to be analysed. An analytical model of the linkage mechanism will be created and validated through the comparison of simulation results with the ones from SolidWorks model of the linkage mechanism and the ones from chewing robot experiment. SimMechanics model of the linkage mechanism in Matlab will be developed. A simulation model of the Maxon DC motor in the chewing robot will be built. The dynamics of the spur gear in the chewing robot and the gear box in the DC motor are considered. The motor control algorithms in the Maxon motor control card will be built in Simulink and integrated with the DC motor model. The PI parameters in the motor control will be tuned to give the optimized performance. In order to validate the adaptive fuzzy control, food models of marshmallow and peanut will be designed. The food models will generate force profiles against deformation.

## *4.2. Analysis and Simulation of Linkage Mechanism*

The simulation model of linkage mechanism is useful for designing the compliance control to achieve human chewing force profile. The dynamics of the mechanism – the torque applied by the motor to achieve the specified chewing motion, is analyzed. The analytical model of chewing mechanism consists of linkage mechanism model and gear system model. The linkage mechanism consists of two identical parallel four-bar linkage mechanism and two slider links. In order to simplify the complexity of the actual model and still reflect the physical characteristic of the real robot, a conceptual model of chewing mechanism is created based on the following assumptions.

1. Assuming that the real 3D model can be considered as a 2D planar model. Because the dual four bar mechanisms are symmetric and slider link moves in Z direction will not affect the torque driving the crank around Z-axis.
2. No friction between links and gears

To prove the assumption for the conceptual model, the simulation results of the conceptual model are compared with the simulation results from the SolidWorks model of original dual four bar linkage mechanism which is built with the same physical characteristics.

### 4.2.1. ***Kinematics of Linkage Mechanism***

A block diagram of a planar chewing mechanism in Figure 4.1 is used to write the kinematic equations of motion. Note that "$\theta_1$" is the rotation angle of crank link and it is the input to the mechanism for the kinematic analysis. In order to develop the differential equation of motion in the dynamic analysis, angular position, velocity and acceleration of links 2, 3, 4 and 5 are expressed as a function of independent quantities crank velocity $\dot{\theta}_1$ and crank acceleration $\ddot{\theta}_1$. The link symbols in block diagram of linkage mechanism are listed in Table 4-1.

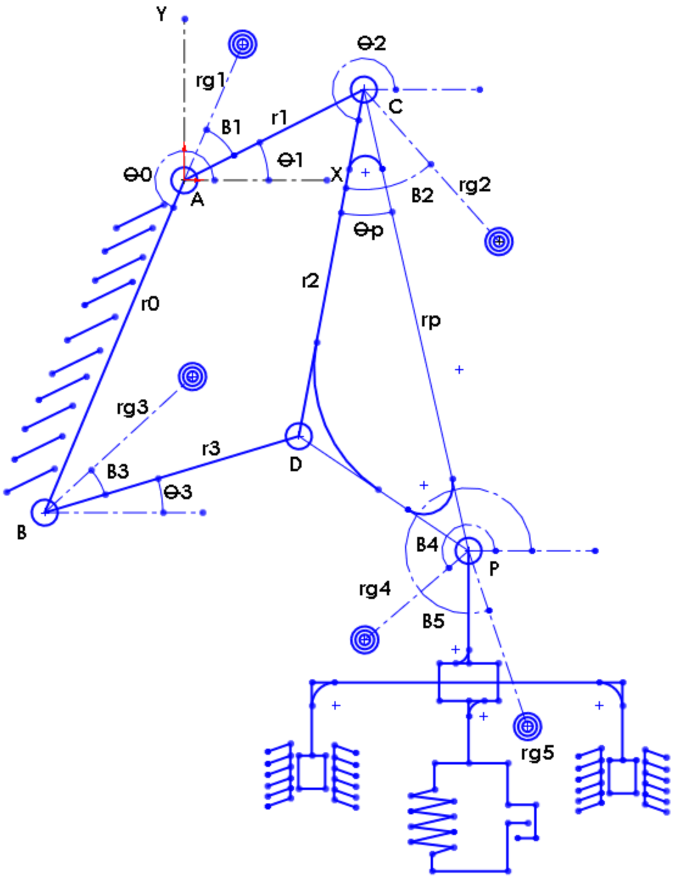

Figure 4.1 Block diagram of planar linkage mechanism

Table 4-1 Representation of link symbols in block diagram of linkage mechanism

| Link | Angular or linear displacement | Length | Mass | Moment Inertia | Center of mass position | Center of mass angle (rad) |
|---|---|---|---|---|---|---|
| Ground | $\theta_0$ | $r_0$ | N/A | N/A | N/A | N/A |
| Crank | $\theta_1$ | $r_1$ | $m_1$ | $I_{g1}$ | $r_{g1}$ | $\beta_1 + \theta_1$ |
| Coupler | $\theta_2$ | $r_2$ | $m_2$ | $I_{g2}$ | $r_{g2}$ | $\beta_2 + \theta_2$ |
| Follower | $\theta_3$ | $r_3$ | $m_3$ | $I_{g3}$ | $r_{g3}$ | $\beta_3 + \theta_3$ |
| Coupler P | $\theta_p$ | $r_p$ | N/A | N/A | N/A | N/A |

| | | | | | | |
|---|---|---|---|---|---|---|
| Slider Link 4 | $d_4$ | N/A | $m_4$ | $I_{g4}$ | $r_{g4}$ | $\beta_4$ |
| Slider Link 5 | $d_5$ | N/A | $m_5$ | $I_{g5}$ | $r_{g5}$ | $\beta_5$ |

**Position analysis:**

Position analysis of four bar linkage begins with formulating the loop-closure equation for the four-bar mechanism shown below.

$$\mathbf{r_2} + \mathbf{r_3} = \mathbf{r_1} + \mathbf{r_4} \tag{17}$$

After incorporating complex numbers,

$$r_2 * e^{i\theta 2} + r_3 * e^{i\theta 3} = r_1 * e^{i\theta 1} + r_4 * e^{i\theta 4} \tag{18}$$

Note link lengths r1, r2, r3 and r4 with $\theta_1$ are constants. Let $\theta_2$ be the input, and $\theta_3$ and $\theta_4$ be the output. Rearranging the equation (18),

$$r_3 * e^{i\theta 3} - r_4 * e^{i\theta 4} = r_1 * e^{i\theta 1} - r_2 * e^{i\theta 2} \tag{19}$$

Angular positions $\theta_3$ and $\theta_4$ can now be solved from equation (19)

$$\cos(\theta_3) = (A + r_4 * \cos(\theta_4))/r_3 \tag{20}$$

$$\sin(\theta_3) = (B + r_4 * \sin(\theta_4))/r_3 \tag{21}$$

Where

$$A = r_1 * \cos(\theta_1) - r_2 * \cos(\theta_2) \tag{22}$$

$$B = r_1 * \sin(\theta_1) - r_2 * \sin(\theta_2) \tag{23}$$

Substituting these results into $\sin^2(\theta_3) + \cos^2(\theta_3) = 1$ and simplifying,

$$B * \sin(\theta_4) + A * \cos(\theta_4) = (A^2 + B^2 + {r_4}^2 - {r_3}^2)/(-2 * r_4) \tag{24}$$

From equation (24), the formulas for $\theta_3$ and $\theta_4$ can be obtained

$$\theta_4 = atan2(B, A) \pm \operatorname{acos}\left((A^2 + B^2 + {r_4}^2 - {r_3}^2)/\left(-2 * r_4 * \sqrt[2]{A^2 + B^2}\right)\right) \tag{25}$$

$$\theta_3 = atan2((B + r_4 * \sin(\theta_4))/r_3\,, (A + r_4 * \cos(\theta_4))/r_3) \tag{26}$$

By analyzing the position of Point P on the coupler link 2, the positions of horizontal and vertical slider links 4 and 5 are obtained. First, the loop-closure equation is formulated as follows

$$\mathbf{r_1} + \mathbf{r_p} = \mathbf{AP} \tag{27}$$

Where $\mathbf{AP}$ is the position vector from the base of the input link (A) to point P.

And then incorporating complex numbers,

$$r_1 * e^{i\theta 1} + r_p * e^{i(\theta 2 + \theta p)} = AP \tag{28}$$

Separate the real and imaginary parts of Eq. (28), the position $d_4$ for horizontal slider link 4 and the position $d_5$ for vertical slider link 5 can be obtained

$$d_4 = r_1 * \cos(\theta_1) + r_p * \cos(\theta_2 + \theta_p) \tag{29}$$

$$d_5 = r_1 * \sin(\theta_1) + r_p * \sin(\theta_2 + \theta_p) \tag{30}$$

**Velocity analysis:**

The velocity analysis of four bar linkage is performed by differentiating the position equation (18), and the velocity equation is

$$\dot{\theta}_1 * r_1 * i * e^{i\theta 1} + \dot{\theta}_2 * r_2 * i * e^{i\theta 2} = \dot{\theta}_3 * r_3 * i * e^{i\theta 3} \tag{31}$$

Then angular velocity $\dot{\theta}_3$ and $\dot{\theta}_4$ by rearranging equation (31) can be obtained

$$\dot{\theta}_2 = \dot{\theta}_1 * r_1 * \sin(\theta_3 - \theta_1)/(r_2 * \sin(\theta_2 - \theta_3)) \tag{32}$$

$$\dot{\theta}_3 = \dot{\theta}_1 * r_1 * \sin(\theta_2 - \theta_1)/(r_3 * \sin(\theta_2 - \theta_3)) \tag{33}$$

The velocity analysis of horizontal slider link 4 and vertical slider link 5 is performed by differentiating the Point P position equation (28). The derivatives of position equation will yield the horizontal and vertical velocities of point P, which are also the velocities of horizontal slider link 4 and vertical slider link 5.

$$\dot{\theta}_1 * r_1 * i * e^{i\theta 1} + \dot{\theta}_2 * r_p * i * e^{i(\theta 2 + \theta p)} = \dot{d} * e^{i\theta} \tag{34}$$

The real part of equation (23) is the velocity of horizontal slider link 4.

$$\dot{d}_4 = -\dot{\theta}_1 * r_1 * \sin(\theta_1) - \dot{\theta}_2 * r_p * \sin(\theta_2 + \theta_p) \tag{35}$$

The imaginary part of equation (23) is the velocity of vertical slider link 5.

$$\dot{d}_5 = \dot{\theta}_1 * r_1 * \cos(\theta_1) + \dot{\theta}_2 * r_p * \cos(\theta_2 + \theta_p) \tag{36}$$

**Acceleration analysis:**

The acceleration analysis of four bar linkage is performed by differentiating the velocity equation (31)

$$i\ddot{\theta}_1 r_1 * e^{i\theta 1} - \dot{\theta}_1^2 r_1 * e^{i\theta 1} + i\ddot{\theta}_2 r_2 * e^{i\theta 2} - \dot{\theta}_2^2 r_2 * e^{i\theta 2} = i\ddot{\theta}_3 r_3 * e^{i\theta 3} - \dot{\theta}_3^2 r_3 * e^{i\theta 3} \quad (37)$$

Then the analytical solutions for $\ddot{\theta}_3$ and $\ddot{\theta}_4$ can be derived

$$\ddot{\theta}_2 = \begin{pmatrix} \ddot{\theta}_1 r_1 * \sin(\theta_3 - \theta_1) \\ -\dot{\theta}_1^2 r_1 * \cos(\theta_3 - \theta_1) - \dot{\theta}_2^2 r_2 * \cos(\theta_3 - \theta_2) + \dot{\theta}_3^2 r_3 \end{pmatrix} / r_2 * sin(\theta_2 - \theta_3) \quad (38)$$

$$\ddot{\theta}_3 = \begin{pmatrix} \ddot{\theta}_1 r_1 * \sin(\theta_2 - \theta_1) - \\ \dot{\theta}_1^2 r_1 * \cos(\theta_2 - \theta_1) + \dot{\theta}_3^2 r_3 * \cos(\theta_2 - \theta_3) - \dot{\theta}_2^2 r_2 \end{pmatrix} / r_3 * \sin(\theta_2 - \theta_3) \quad (39)$$

The acceleration analysis of horizontal and vertical slider is performed by differentiating the slider velocity equation (34).

$$i\ddot{\theta}_1 r_1 * e^{i\theta 1} - \dot{\theta}_1^2 r_1 * e^{i\theta 1} + i\ddot{\theta}_2 r_p * e^{i(\theta 2 + \theta p)} - \dot{\theta}_2^2 r_p * e^{i(\theta 2 + \theta p)} = \ddot{d} * e^{i\theta} \quad (40)$$

The real part of equation (40) is the acceleration of horizontal slider link 4.

$$\ddot{d}_4 = -\ddot{\theta}_1 r_1 * \sin(\theta_1) - \dot{\theta}_1^2 r_1 * \cos(\theta_1) - \ddot{\theta}_2 r_p * \sin(\theta_2 + \theta_p) - \dot{\theta}_2^2 r_p * \cos(\theta_2 + \theta_p) \quad (41)$$

The imaginary part of equation (40) is the acceleration of vertical slider link 5.

$$\ddot{d}_5 = \ddot{\theta}_1 r_1 * \cos(\theta_1) - \dot{\theta}_1^2 r_1 * \sin(\theta_1) + \ddot{\theta}_2 r_p * \cos(\theta_2 + \theta_p) - \dot{\theta}_2^2 r_p * \sin(\theta_2 + \theta_p) \quad (42)$$

### 4.2.2. ***Dynamics of Linkage Mechanism***

Lagrangian dynamic formulation is used to develop the equations of motion for the mechanism. The equations of motion for the mechanism are then given by

$$\frac{d}{dt}\frac{\partial T}{\partial \dot{\theta}_i} - \frac{\partial T}{\partial \theta_i} + \frac{\partial u}{\partial \theta_i} = Q_i \quad (43)$$

Where $T$ is the total kinetic energy; $u$ is the potential energy; $\theta_i$ and $\dot{\theta}_i$ are the generalized coordinates and velocities; $Q_i$ is the generalized force corresponding to the coordinate $\theta_i$ .

The total kinetic energy is the sum of the kinetic energy in the individual link (i) and can be expressed as

$$T = \sum_{i=1}^{n} \frac{1}{2} m_i (\dot{x}_{gi}^2 + \dot{y}_{gi}^2) + \sum_{i=1}^{n} \frac{1}{2} I_{gi} \dot{\theta}_i^2 \quad (44)$$

Where $(x_{gi}, y_{gi})$ are the coordinates of the center of mass of link i in the mechanism

The Lagrange’s equation of motion of the chewing mechanism, where $\theta_1$ is the generalized coordinate, is

$$\tau \ = \sum_{i=1}^{5} \left\{ m_i \left( \ddot{x}_{gi} \frac{\partial \dot{x}_{gi}}{\partial \dot{\theta}_1} + \ddot{y}_{gi} \frac{\partial \dot{y}_{gi}}{\partial \dot{\theta}_1} + g \frac{\partial \dot{y}_{gi}}{\partial \dot{\theta}_1} \right) + I_{gi} \ddot{\theta}_i \frac{\partial \dot{\theta}_i}{\partial \dot{\theta}_1} - F_i \frac{\partial \dot{r}_i}{\partial \dot{\theta}_1} \right\} \tag{45}$$

Where $F_i$ is the external force acting on link i and $r_i$ is the radius vector of $F_i$ measured from the origin of the global coordinate system.

Therefore, the equation of driving torque of chewing mechanism is presented into two phases.

- Open/Close phase

$$\tau \ = \sum_{i=1}^{5} \left\{ m_i \left( \ddot{x}_{gi} \frac{\partial \dot{x}_{gi}}{\partial \dot{\theta}_1} + \ddot{y}_{gi} \frac{\partial \dot{y}_{gi}}{\partial \dot{\theta}_1} + g \frac{\partial \dot{y}_{gi}}{\partial \dot{\theta}_1} \right) + I_{gi} \ddot{\theta}_i \frac{\partial \dot{\theta}_i}{\partial \dot{\theta}_1} \right\} \tag{46}$$

- Occlusal phase

$$\tau \ = \sum_{i=1}^{5} \left\{ m_i \left( \ddot{x}_{gi} \frac{\partial \dot{x}_{gi}}{\partial \dot{\theta}_1} + \ddot{y}_{gi} \frac{\partial \dot{y}_{gi}}{\partial \dot{\theta}_1} + g \frac{\partial \dot{y}_{gi}}{\partial \dot{\theta}_1} \right) + I_{gi} \ddot{\theta}_i \frac{\partial \dot{\theta}_i}{\partial \dot{\theta}_1} - F_i \frac{\partial \dot{d}_i}{\partial \dot{\theta}_1} \right\} + \frac{\partial V}{\partial \theta_1} \tag{47}$$

Where V is the potential energy of spring and $F_i$ is the food resistance force on link i. The potential energy of spring can be expressed as

$$V = \frac{1}{2} k (n + x)^2 \tag{48}$$

Where k is the spring constant, n is the pretightening spring displacement and x is the changing spring displacement due to food resistance. The food must be hard enough to compress the spring. V is only valid if x is a positive number. The changing spring displacement is expressed as

$$x = h - |p_{bottom} - d_5| \tag{49}$$

Where x must be positive, h is the food thickness which can be constant or a variable, $p_{bottom}$ is the bottom occlusal position in Y axis in the base coordinate$(\theta_i)$ and $d_5$ is vertical slider displacement which can be expressed as

$$d_5 = r_1 * \sin(\theta_1) + r_p * \sin(\theta_2 + \theta_p) \tag{50}$$

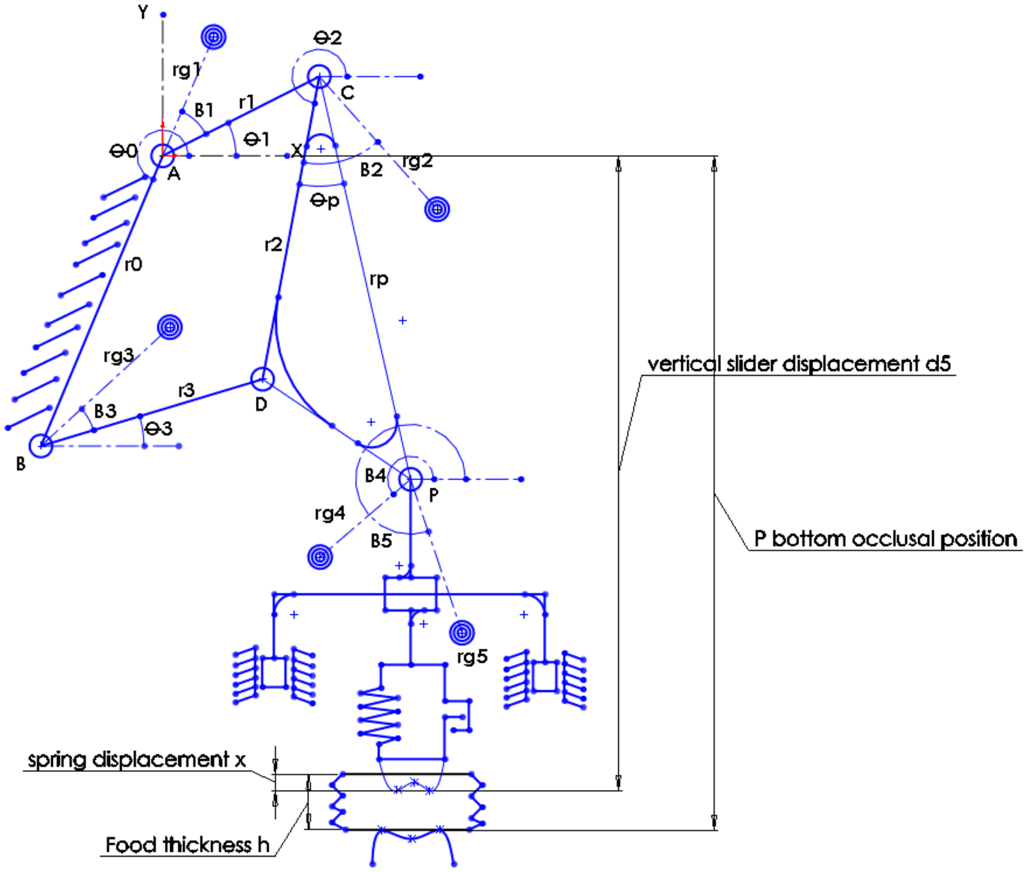

Figure 4.2 Block diagram demonstrating the variables related with changing spring displacement

The mass centre accelerations, which are using the same method described above, are given by

$$\ddot{x}_{g1} = -\ddot{\theta}_1 r_{g1} * \sin(\theta_1 + \beta_1) - \dot{\theta}_1^2 r_{g1} * \cos(\theta_1 + \beta_1) \tag{51}$$

$$\ddot{y}_{g1} = \ddot{\theta}_1 r_{g1} * \cos(\theta_1 + \beta_1) - \dot{\theta}_1^2 r_{g1} * \sin(\theta_1 + \beta_1) \tag{52}$$

$$\ddot{x}_{g2} = -\ddot{\theta}_1 r_1 * \sin(\theta_1) - \dot{\theta}_1^2 r_1 * \cos(\theta_1) - \ddot{\theta}_2 r_{g2} * \sin(\theta_2 + \beta_2) - \dot{\theta}_2^2 r_{g2} * \cos(\theta_2 + \beta_2) \tag{53}$$

$$\ddot{y}_{g2} = \ddot{\theta}_1 r_1 * \cos(\theta_1) - \dot{\theta}_1^2 r_1 * \sin(\theta_1) + \ddot{\theta}_2 r_{g2} * \cos(\theta_2 + \beta_2) - \dot{\theta}_2^2 r_{g2} * \sin(\theta_2 + \beta_2) \tag{54}$$

$$\ddot{x}_{g3} = -\ddot{\theta}_3 r_{g3} * \sin(\theta_3 + \beta_3) - \dot{\theta}_3^2 r_{g3} * \cos(\theta_3 + \beta_3) \tag{55}$$

$$\ddot{y}_{g3} = \ddot{\theta}_3 r_{g3} * \cos(\theta_3 + \beta_3) - \dot{\theta}_3^2 r_{g3} * \sin(\theta_3 + \beta_3) \tag{56}$$

$$\ddot{d}_{g4} = -\ddot{\theta}_1 r_1 * \sin(\theta_1) - \dot{\theta}_1^2 r_1 * \cos(\theta_1) - \ddot{\theta}_2 r_p * \sin\left(\theta_2 + \theta_p\right) - \dot{\theta}_2^2 r_p * \cos\left(\theta_2 + \theta_p\right) - \ddot{d}_4 r_{g4} * \sin(\beta_4) - \dot{d}_4^2 r_{g4} * \cos(\beta_4) \tag{57}$$

$$\ddot{d}_{g5} = \ddot{\theta}_1 r_1 * \cos(\theta_1) - \dot{\theta}_1^2 r_1 * \sin(\theta_1) + \ddot{\theta}_2 r_p * \cos\left(\theta_2 + \theta_p\right) - \dot{\theta}_2^2 r_p * \sin\left(\theta_2 + \theta_p\right) + \ddot{d}_5 r_{g5} * \cos(\beta_5) - \dot{d}_5^2 r_{g5} * \sin(\beta_5) \tag{58}$$

The partial derivative terms are

$$\frac{\partial \dot{\theta}_2}{\partial \dot{\theta}_1} = r_1 * \sin(\theta_3 - \theta_1)/(r_2 * \sin(\theta_2 - \theta_3)) \tag{59}$$

$$\frac{\partial \dot{\theta}_3}{\partial \dot{\theta}_1} = r_1 * \sin(\theta_2 - \theta_1)/(r_3 * \sin(\theta_2 - \theta_3)) \tag{60}$$

$$\frac{\partial \dot{d}_4}{\partial \dot{\theta}_1} = -r_1 * \sin(\theta_1) - \frac{\partial \dot{\theta}_2}{\partial \dot{\theta}_1} * r_p * \sin\left(\theta_2 + \theta_p\right) \tag{61}$$

$$\frac{\partial \dot{d}_5}{\partial \dot{\theta}_1} = r_1 * \cos(\theta_1) + \frac{\partial \dot{\theta}_2}{\partial \dot{\theta}_1} * r_p * \cos\left(\theta_2 + \theta_p\right) \tag{62}$$

$$\frac{\partial \dot{x}_{g1}}{\partial \dot{\theta}_1} = -r_{g1} * \sin(\theta_1 + \beta_1) \tag{63}$$

$$\frac{\partial \dot{y}_{g1}}{\partial \dot{\theta}_1} = r_{g1} * \cos(\theta_1 + \beta_1) \tag{64}$$

$$\frac{\partial \dot{x}_{g2}}{\partial \dot{\theta}_1} = -r_1 * \sin(\theta_1) - r_{g2} * \frac{\partial \dot{\theta}_2}{\partial \dot{\theta}_1} * \sin(\theta_2 + \beta_2) \tag{65}$$

$$\frac{\partial \dot{y}_{g2}}{\partial \dot{\theta}_1} = r_1 * \cos(\theta_1) + r_{g2} * \frac{\partial \dot{\theta}_2}{\partial \dot{\theta}_1} * \cos(\theta_2 + \beta_2) \tag{66}$$

$$\frac{\partial \dot{x}_{g3}}{\partial \dot{\theta}_1} = -r_{g3} * \frac{\partial \dot{\theta}_3}{\partial \dot{\theta}_1} * \sin(\theta_3 + \beta_3) \tag{67}$$

$$\frac{\partial \dot{y}_{g3}}{\partial \dot{\theta}_1} = r_{g3} * \frac{\partial \dot{\theta}_3}{\partial \dot{\theta}_1} * \cos(\theta_3 + \beta_3) \tag{68}$$

$$\frac{\partial \dot{d}_{g4}}{\partial \dot{\theta}_1} = -r_1 * \sin(\theta_1) - \frac{\partial \dot{\theta}_2}{\partial \dot{\theta}_1} * r_p * \sin\left(\theta_2 + \theta_p\right) - r_{g4} * \frac{\partial \dot{d}_4}{\partial \dot{\theta}_1} * \sin(\beta_4) \tag{69}$$

$$\frac{\partial \dot{d}_{g5}}{\partial \dot{\theta}_1} = r_1 * \cos(\theta_1) + \frac{\partial \dot{\theta}_2}{\partial \dot{\theta}_1} * r_p * \cos\left(\theta_2 + \theta_p\right) + r_{g5} * \frac{\partial \dot{d}_5}{\partial \dot{\theta}_1} * \cos(\beta_5) \tag{70}$$

$$\frac{\partial \dot{d}_4}{\partial \dot{\theta}_1} = -r_1 * \sin(\theta_1) - \frac{\partial \dot{\theta}_2}{\partial \dot{\theta}_1} * r_p * \sin\left(\theta_2 + \theta_p\right) \tag{71}$$

$$\frac{\partial \dot{d}_5}{\partial \dot{\theta}_1} = r_1 * \cos(\theta_1) + \frac{\partial \dot{\theta}_2}{\partial \dot{\theta}_1} * r_p * \cos\left(\theta_2 + \theta_p\right) \tag{72}$$

$$\frac{\partial V}{\partial \theta_1} = k * (n + x) * \frac{\partial \dot{d}_5}{\partial \dot{\theta}_1} \tag{73}$$

### 4.2.3. *Simulation Results Compared with SolidWorks*

In order to validate the simulation model under assumption 1, simulation results of 2D planar linkage mechanism were compared with the results of SolidWorks 3D model under the same condition. Both models used link parameters from SolidWorks model in Table 4-2 and same chewing velocity profile as the input crank velocity. For the analytical model, angular displacement, angular velocity and angular acceleration of crank were specified. For SolidWorks model, crank angular velocity was only specified. Crank angular displacement and angular acceleration were generated automatically by SolidWorks integrator solver.

In the following, results of displacement, velocity and acceleration of all moving links (crank, coupler, following, slider link 4 and slider link 5) were compared between two models. And then crank torque driving the linkage mechanism and also the driving torque with the simulated food resistance were also compared. Finally, comparison results of total torque driving through the gear were presented.

Table 4-2 Link parameters for linkage mechanism

| | i | $\theta_i$ (rad) | Length $r_i$ (m) | Mass $m_i$ (kg) | Moment Inertia $I_{gi}$ (kg*m$^2$) | $r_{gi}$ (m) | Center of mass angle (rad) |
|---|---|---|---|---|---|---|---|
| Ground | 0 | 4.276 | 0.05 | N/A | N/A | N/A | N/A |
| Crank | 1 | $\theta_1$ | 0.01 | 0.0259 | 7.7424e-5 | 0.0004 | $\theta_1$ |
| Coupler | 2 | $\theta_2$ | 0.035 | 0.1753 | 3.1914e-4 | 0.0411 | 0.3168+$\theta_2$ |
| Follower | 3 | $\theta_3$ | 0.03 | 0.0361 | 0.8290e-4 | 0.0086 | $\theta_3$ |
| Coupler P | p | 0.4793 | 0.0564 | N/A | N/A | N/A | N/A |
| Slider Link 4 | 4 | N/A | N/A | 0.9932 | 4.9558e-3 | 0.0113 | -1.5666 |
| Slider Link 5 | 5 | N/A | N/A | 1.2375 | 7.4746e-3 | 0.0970 | -1.5919 |

***Kinematics Simulation Results***

According to the chewing velocity profile for the chewing robot (Xu et al., 2008), crank angular velocity is expressed as follows and shown in Figure 4.3.

$$\dot{\theta}_1 = \begin{cases} 300 & t\ at\ other\ times \\ 300 + 1831.95t - 2818.36t^2 & 0.77 * n \le t \le 0.77 * n + 0.65 \end{cases} \tag{74}$$

Where n is from 1 to the number of cycles minus 1.

The chewing velocity first starts with constant velocity of 300 degrees per second from the top position of the chewing cycle to the beginning of the opening phase. The chewing velocity starts accelerating during the opening phase and decelerating during the closing phase until the beginning of the occlusal phase. During occlusal phase, the chewing velocity stays at constant velocity of 300 degrees per second.

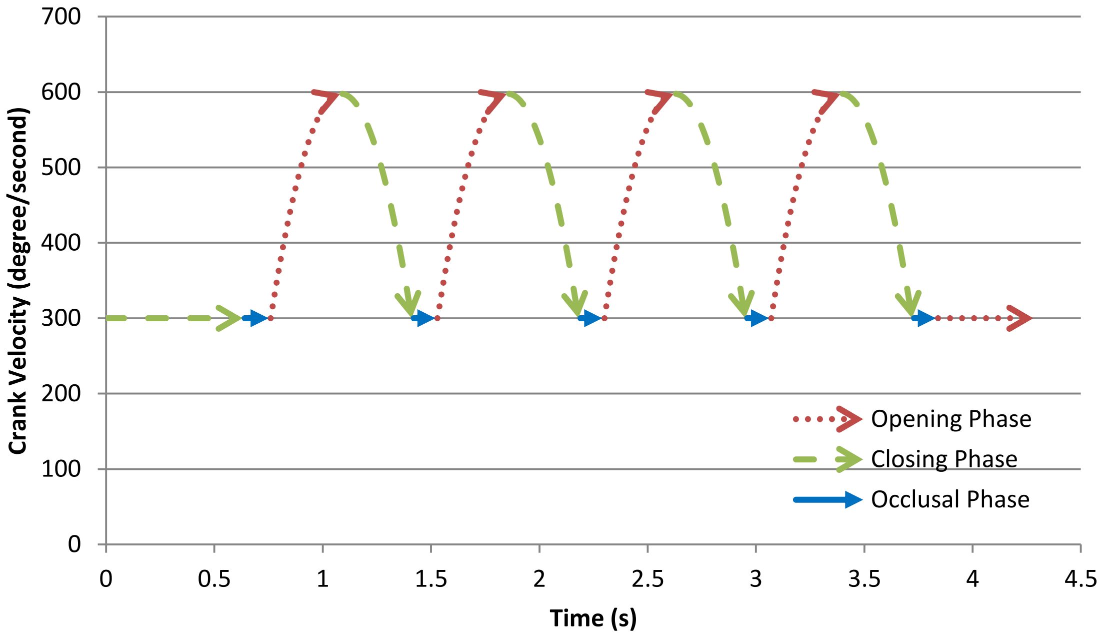

Figure 4.3 Input crank angular velocity for SolidWorks and Analytical model

Crank angular accelerations for SolidWorks and analytical model are plotted in Figure 4.4. The spikes difference in crank angular acceleration in Figure 4.5 between analytical and SolidWorks simulation model occur when the acceleration changes from 0 to the next value (around 1800). This is resulted from the integrator solver used by SolidWorks. Therefore, in order to compare the analytical model with the SolidWorks model under the same circumstance, two simulation results of analytical model for the angular accelerations of coupler, follower, horizontal slider link 4 and vertical slider link 5 with two input crank angular acceleration are plotted: one with the specified crank acceleration; the other with the simulated crank acceleration from SolidWorks, which is for the comparison between analytical and SolidWorks model under the same circumstance.

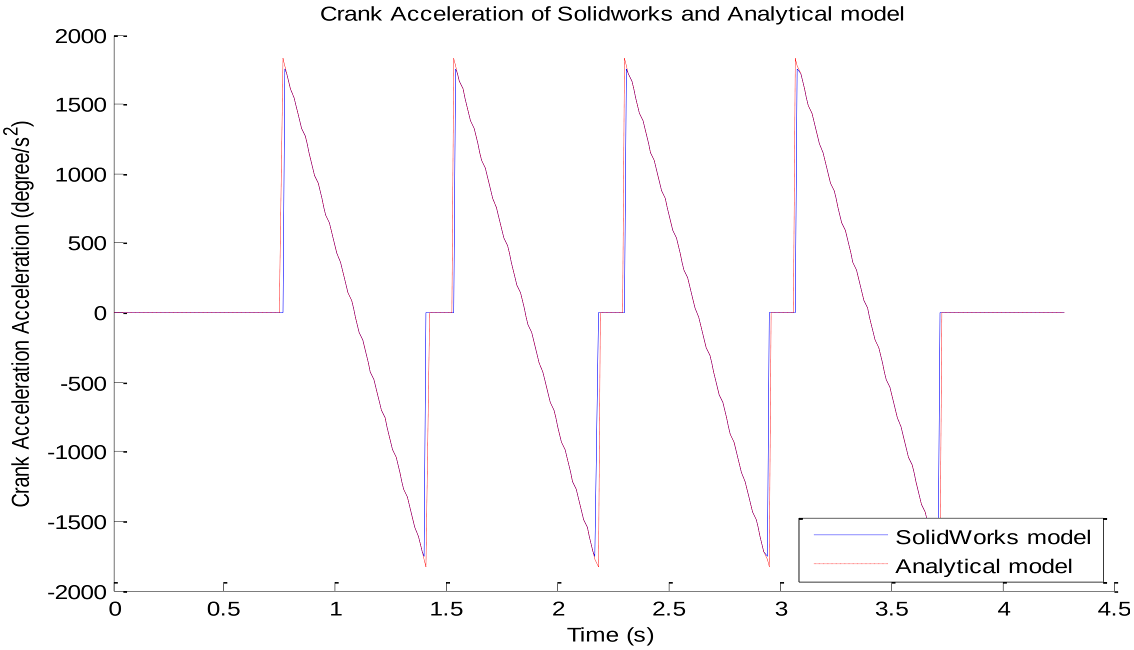

Figure 4.4 Input crank angular acceleration of SolidWorks and Analytical model

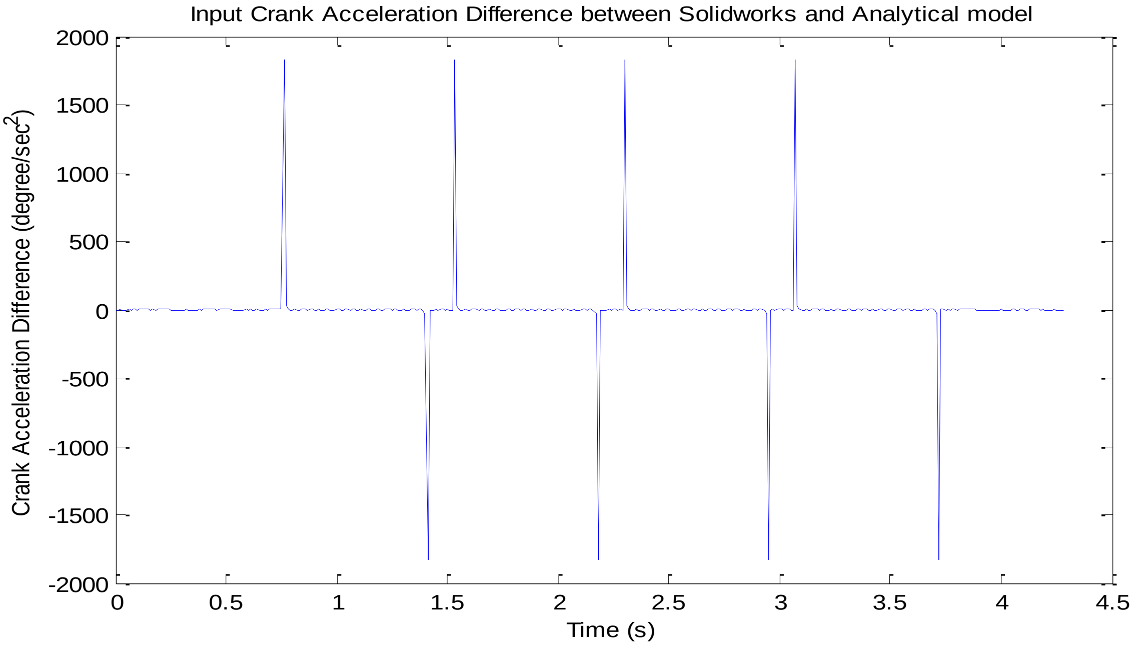

Figure 4.5 Input crank angular acceleration difference between Solidworks and Analytical model

In Figure 4.6 and 4.7, the coupler angular velocity and acceleration of analytical model quite perfectly match with the ones of SolidWorks model, if the same crank angular acceleration is used as input to both models.

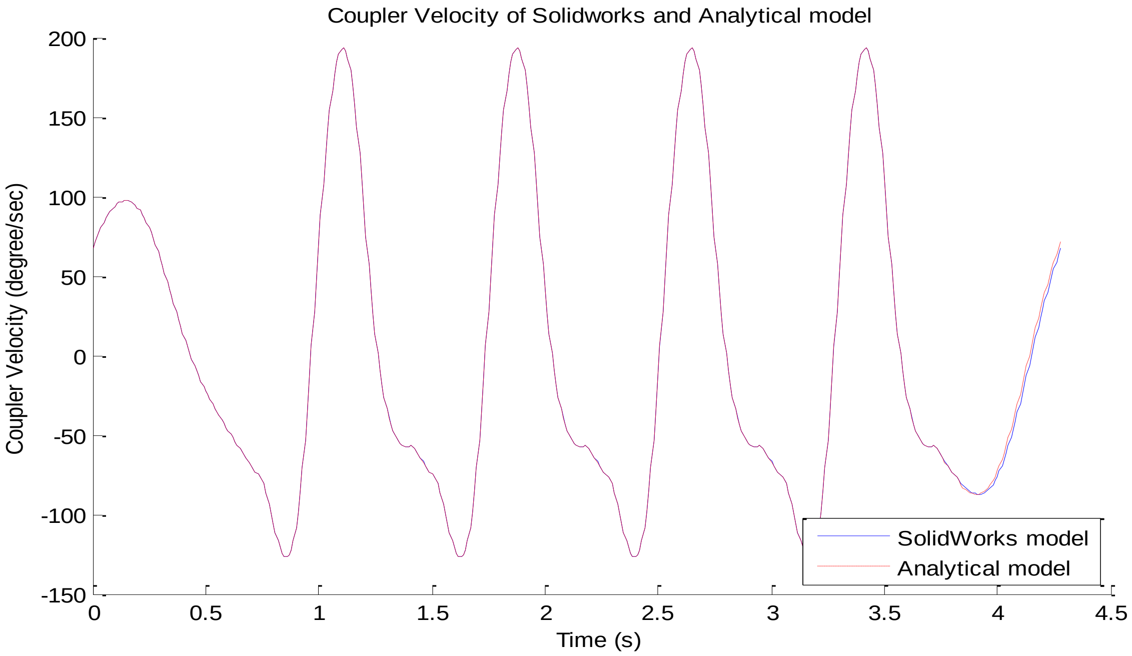

Figure 4.6 Coupler angular velocity of SolidWorks and Analytical model

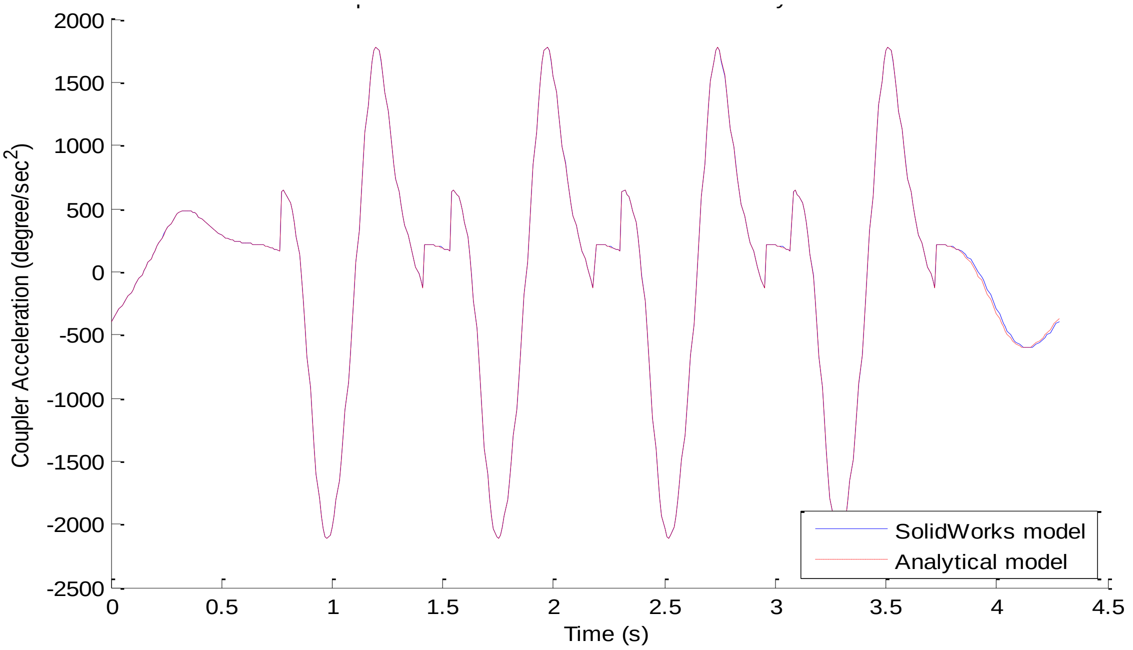

Figure 4.7 Coupler angular acceleration of SolidWorks and Analytical model using same input crank angular acceleration.

In Figure 4.8, the difference of coupler angular acceleration between SolidWorks and analytical model is caused by the spike difference of crank angular acceleration between SolidWorks and analytical model. In the following figures, angular accelerations of SolidWorks and analytical model are only compared using the same input crank angular acceleration.

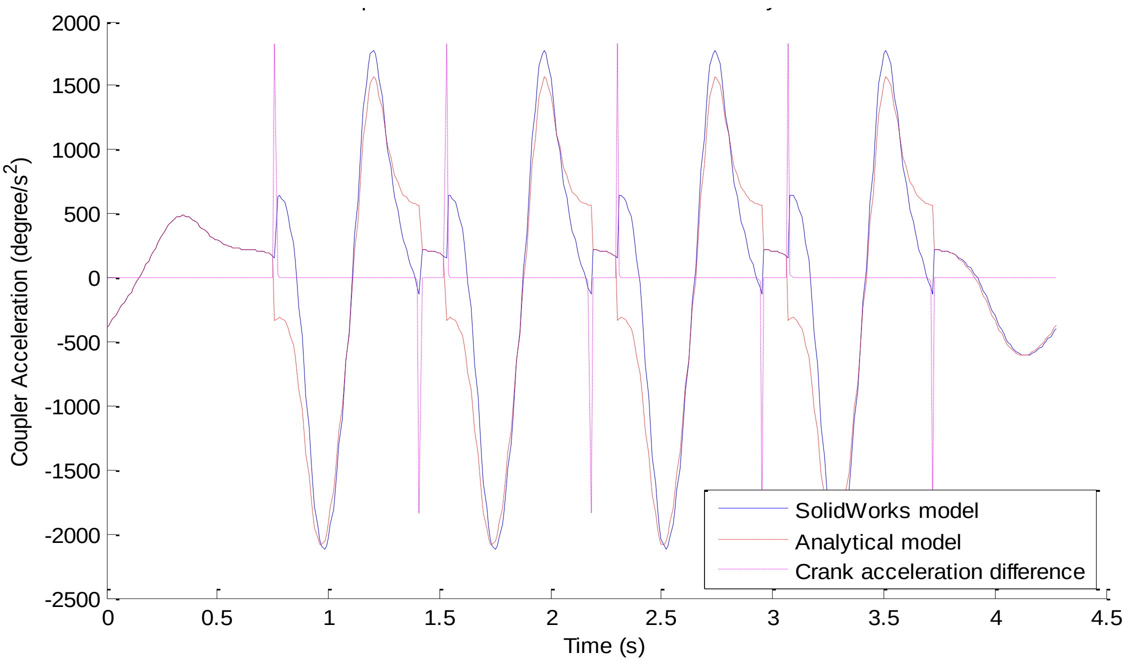

Figure 4.8 Coupler angular acceleration of SolidWorks and Analytical model using two input crank angular acceleration with spike difference

In Figure 4.9 and 4.10, there are no differences between the follower angular velocity and acceleration of Solidworks and analytical model.

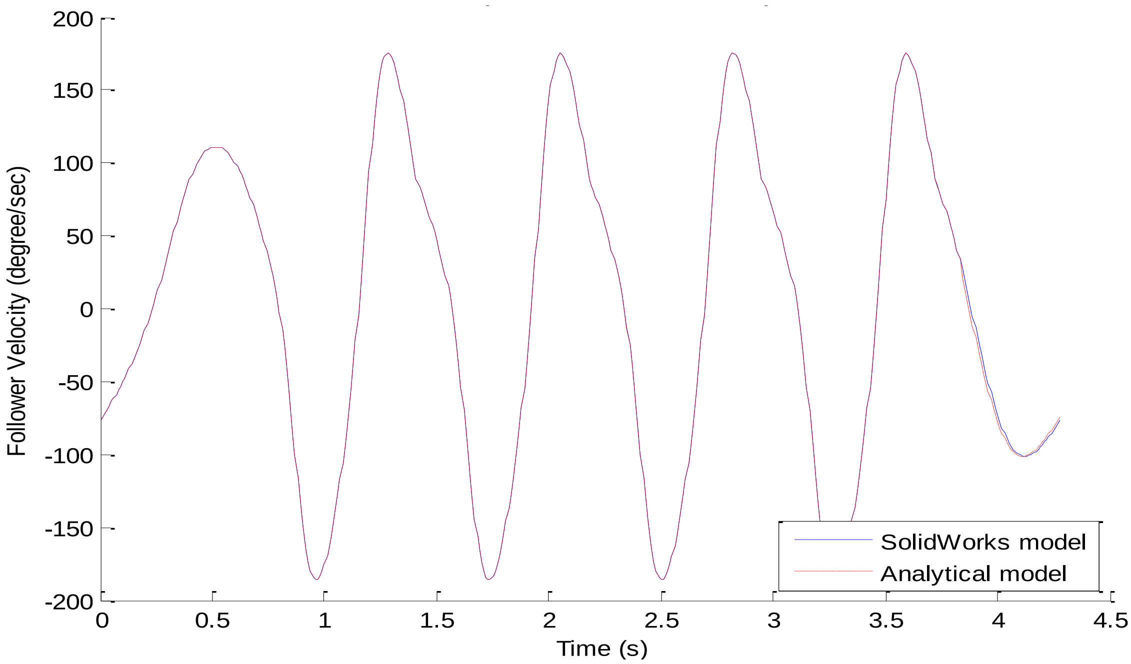

Figure 4.9 Follower angular velocity of SolidWorks and Analytical model

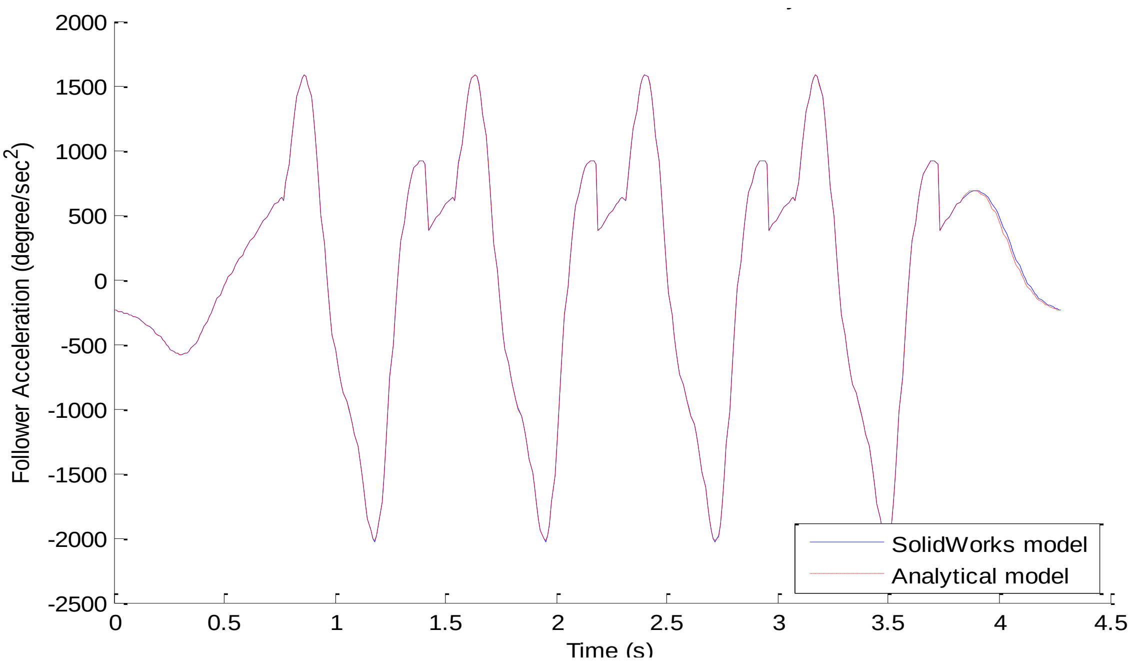

Figure 4.10 Follower angular acceleration of SolidWorks and Analytical model using same input crank angular acceleration

In Figure 4.11, 4.12 and 4.13, the horizontal slider link 4 linear displacements, velocity and acceleration of SolidWorks and analytical model are very consistent with each other.

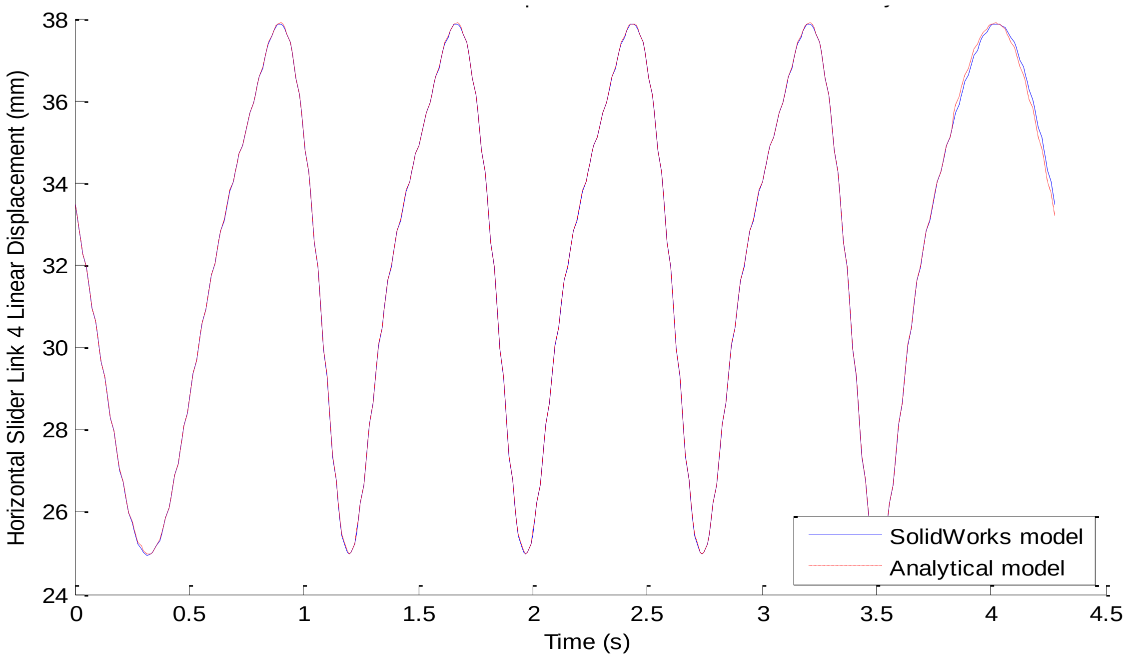

Figure 4.11 Horizontal slider link 4 linear displacement of SolidWorks and Analytical model

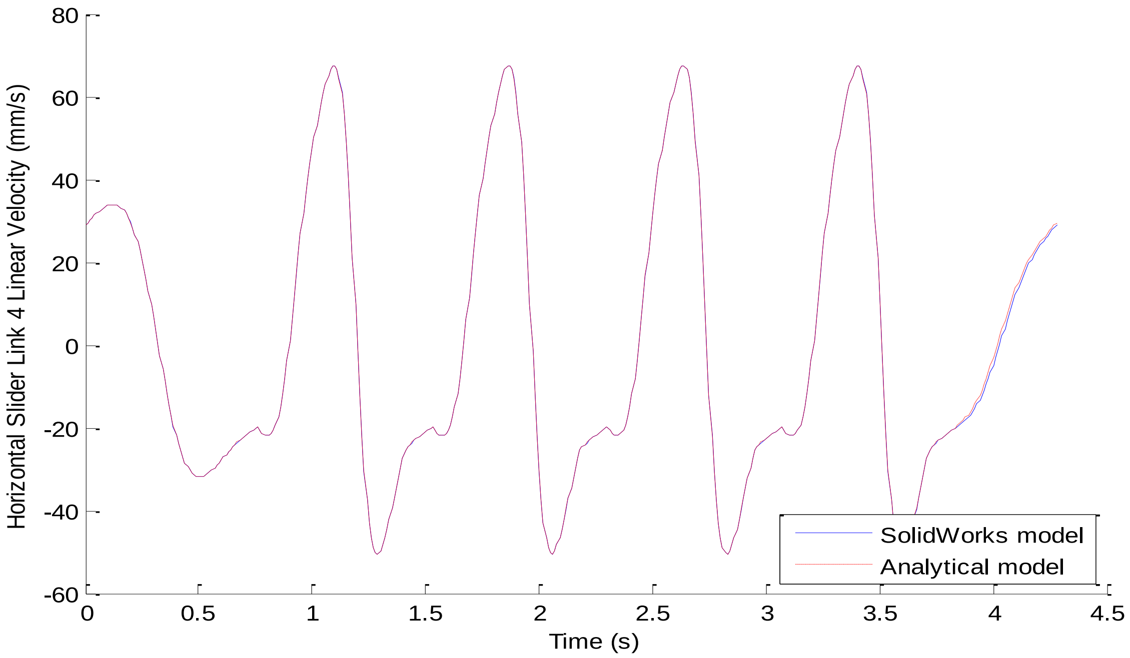

Figure 4.12 Horizontal slider link 4 linear velocity of SolidWorks and Analytical model

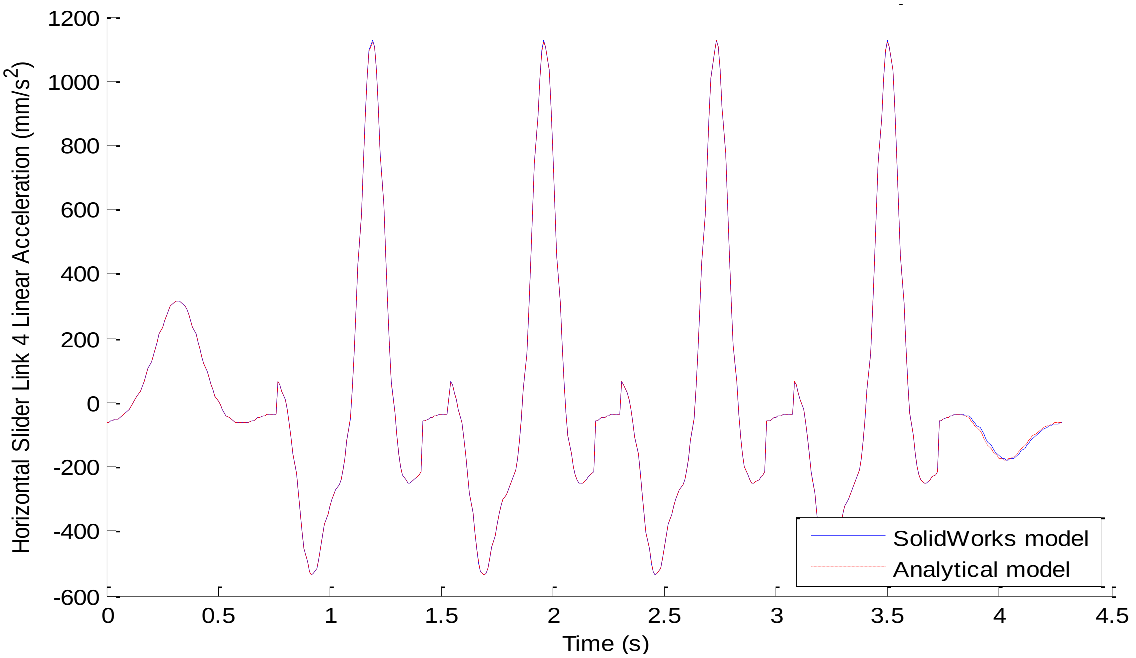

Figure 4.13 Horizontal slider link 4 linear acceleration of SolidWorks and Analytical model using same input crank angular acceleration

In Figure 4.14, 4.15 and 4.16, the vertical slider link 5 linear displacements, velocity and acceleration of SolidWorks and analytical model are very consistent with each other.

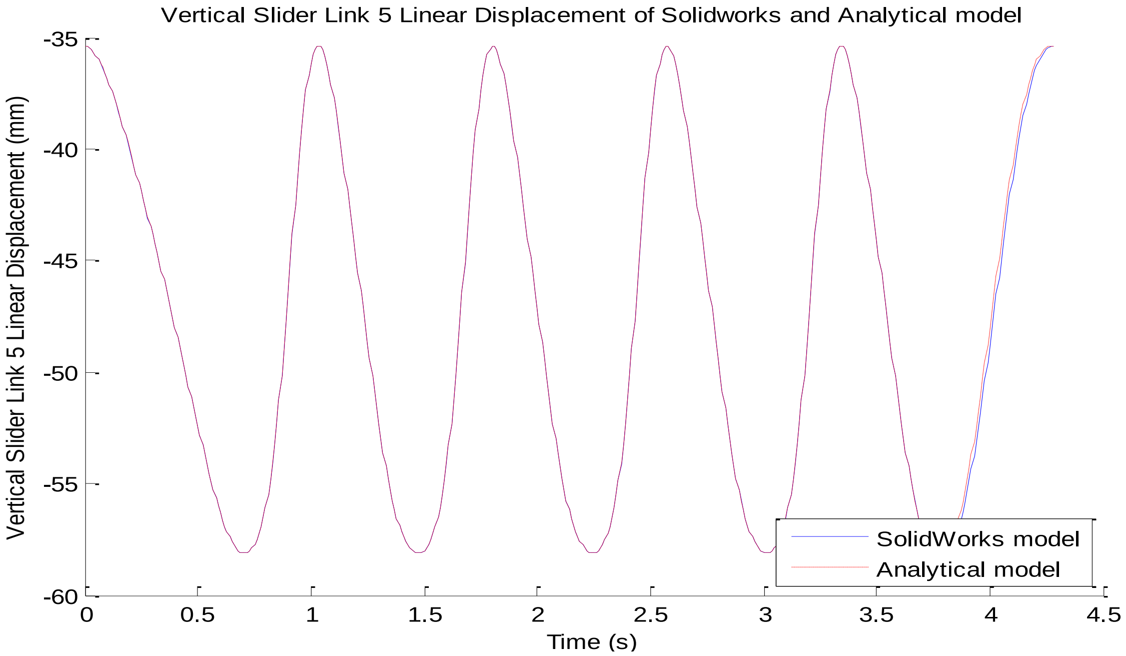

Figure 4.14 Vertical slider link 5 linear displacement of SolidWorks and Analytical model

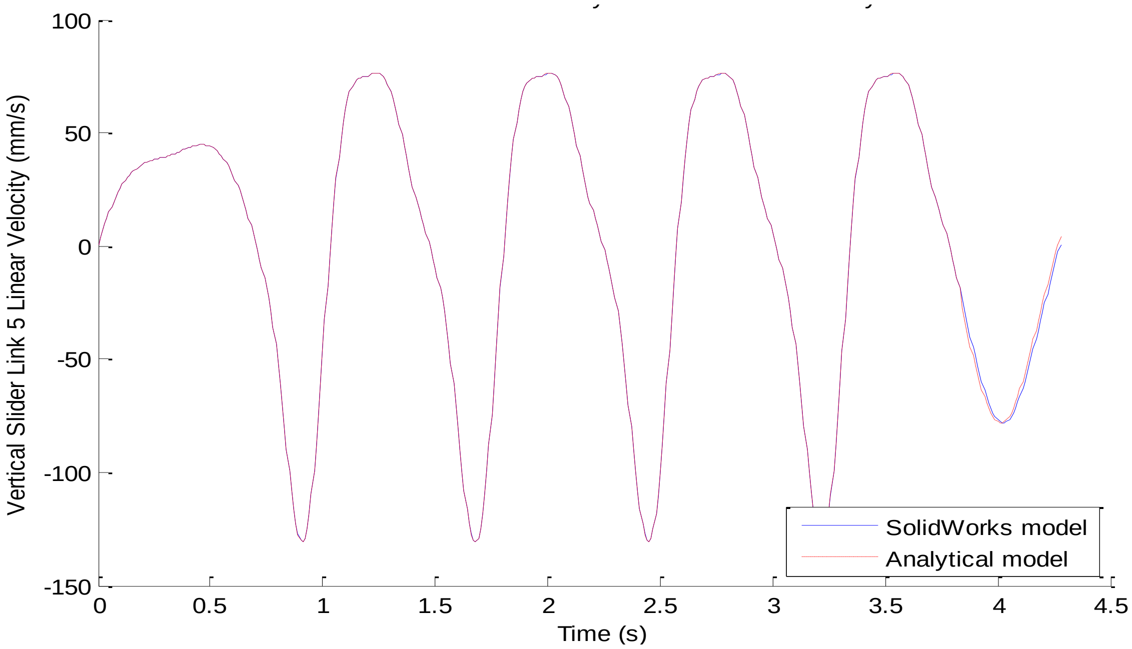

Figure 4.15 Vertical slider link 5 linear velocity of SolidWorks and Analytical model

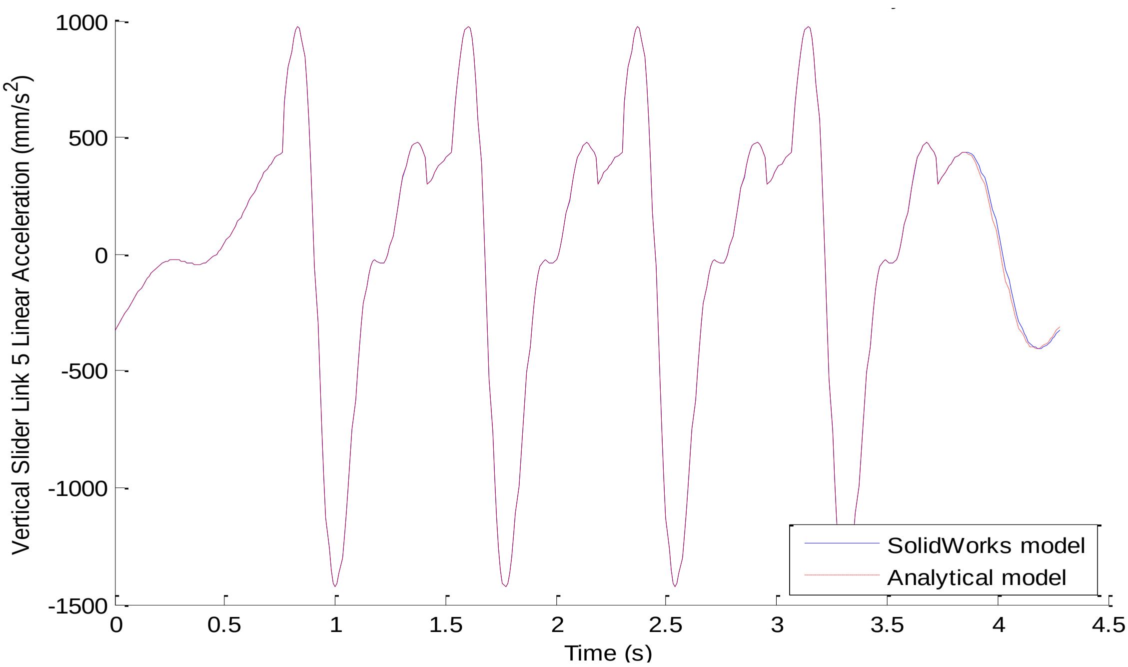

Figure 4.16 Vertical slider link 5 linear acceleration of SolidWorks and Analytical model using same input crank angular acceleration

From the above results, it is found that there is almost no difference of displacement and velocity of all moving links between the SolidWorks 3D model and analytical model of 2D planar chewing mechanism. For the acceleration of all moving links, the spike differences mentioned before are resulted from the spike difference between the input crank angular acceleration of both models. If the same crank angular acceleration is used as the input for both models, all the acceleration results of analytical model almost perfectly match the ones of the SolidWorks model.

***Dynamics Simulation Results***

In the following, the same angular acceleration is used as the input for the analytical model and SolidWorks model. The torque driving the crank to run at chewing velocity without force resistance on vertical slider link 5 for two models is first compared. The crank torque with different directions of force resistance on vertical slider link 5 is then compared. At last, the driving torque of two models through the gear system is also compared.

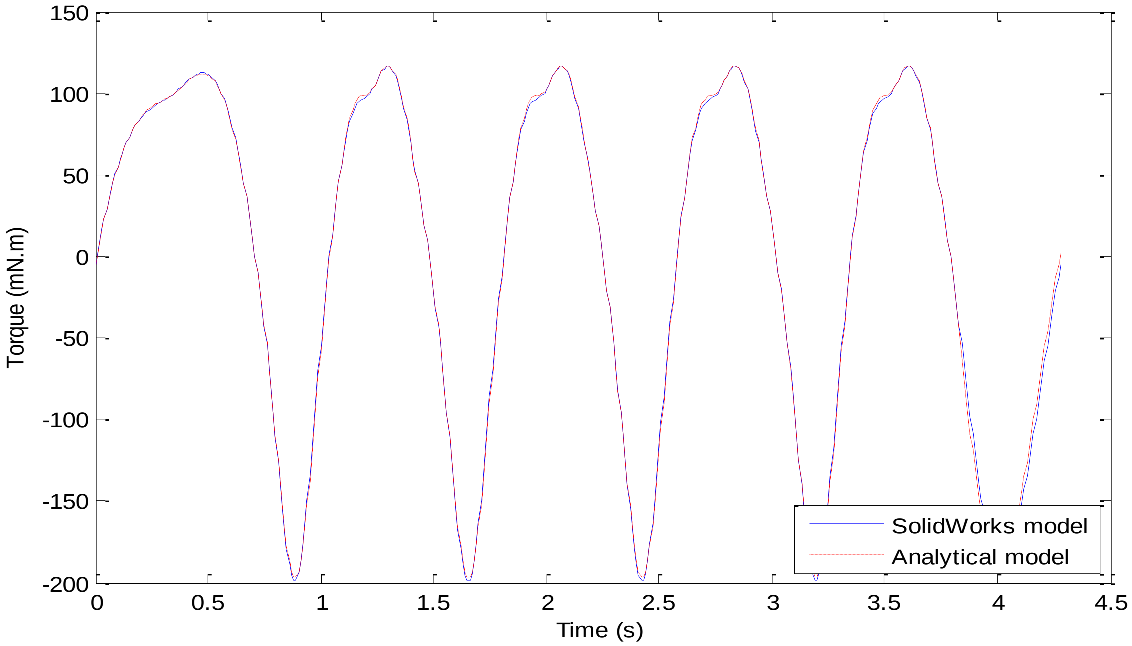

Figure 4.17 Applied crank torque of SolidWorks and Analytical model using same input crank angular acceleration. No food resistance is applied.

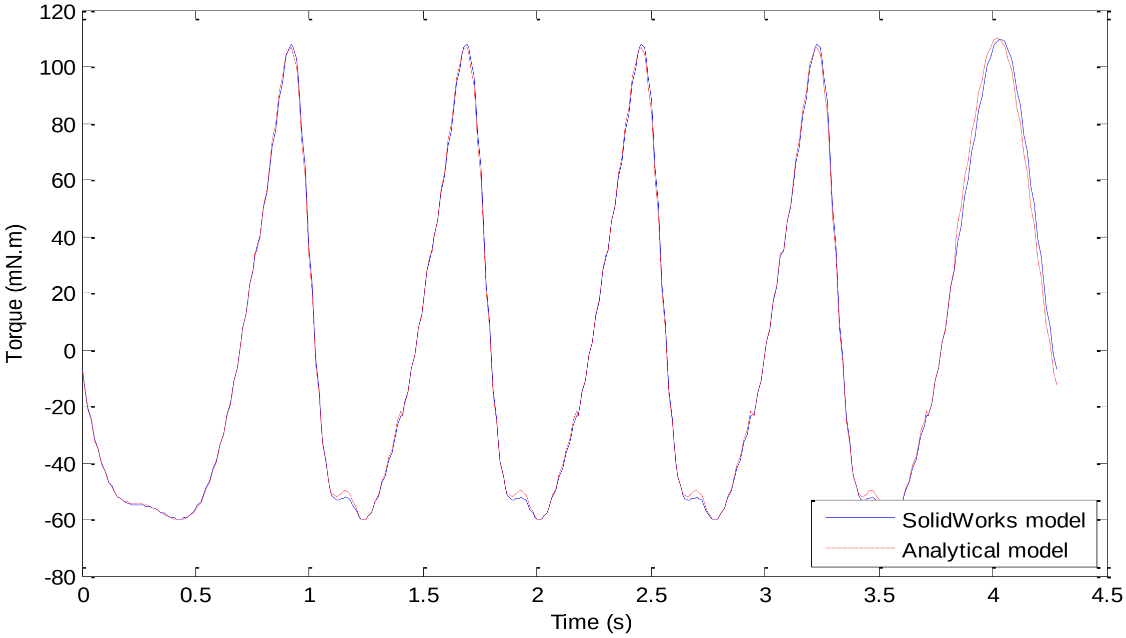

Figure 4.18 Crank torque of Solidworks and Analytical model using same input crank angular acceleration. Constant 20N is vertically applied on vertical slider link 5 as food resistance.

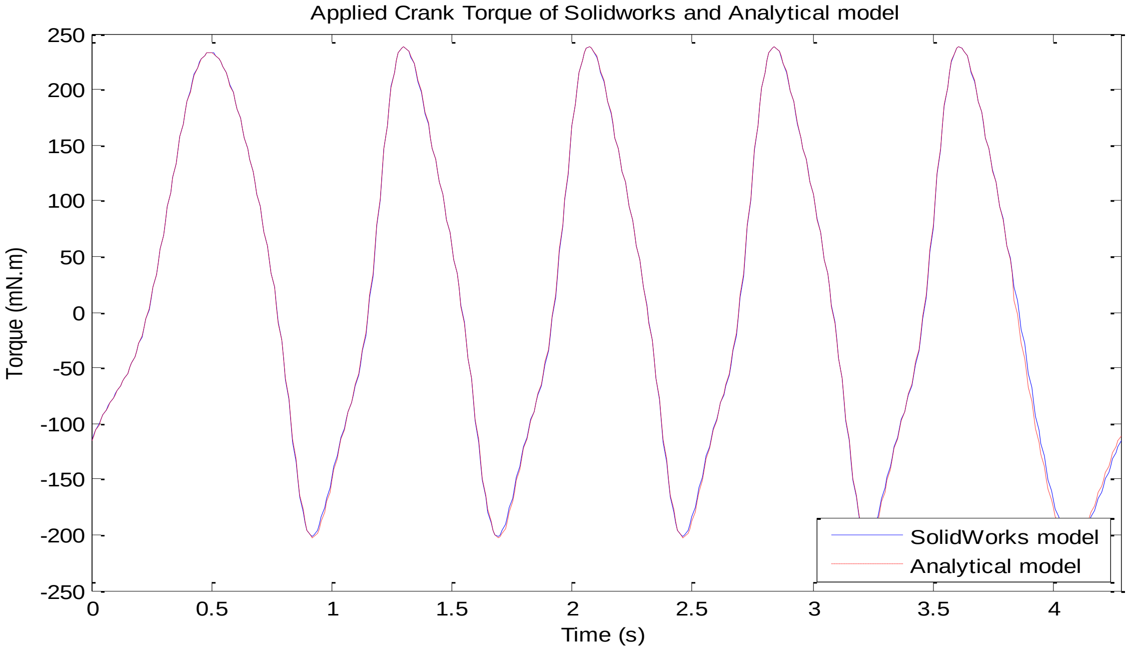

Figure 4.19 Crank torque of Solidworks and Analytical model using same input crank angular acceleration. Constant 20N is horizontally applied on horizontal slider link 4 as food resistance.

From Figure 4.17, 4.18 and 4.19, the crank torque of SolidWorks and analytical model are almost identical to each other.

Since a spring-mass mechanism is implemented between the upper teeth and vertical slider link 5 in the chewing machine, the food resistance in Y-axis can be considered as the force applied from the compressed spring, where the spring rate is selected to be 6.69N/mm from Chapter 3. The spring compression force is proportional to the spring displacement changed during occlusion. The food thickness is assumed to be constant 5mm during the simulation. Thus, the spring will compress when the upper teeth moves within 5mm from lower teeth. The compression force of spring as food resistance is shown in Figure 4.20, during chewing an imaginary unbreakable food with the thickness of 5mm. When the compression force reaches the maximum value, the upper teeth move into full contact with the lower teeth.

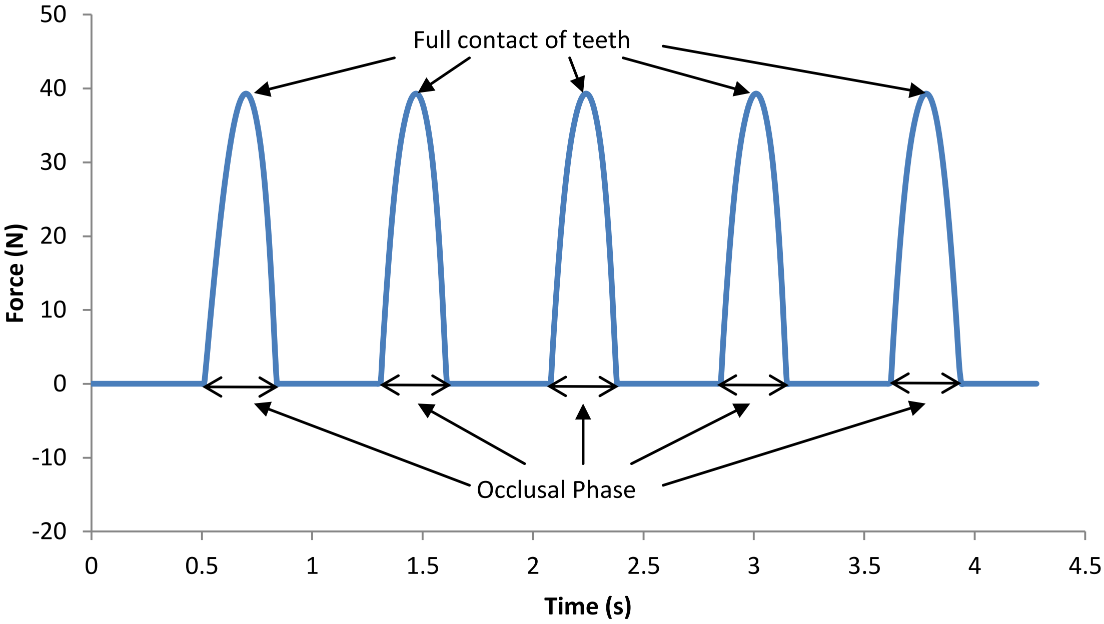

Figure 4.20 Y-axis compression force of spring as food resistance in Matlab model

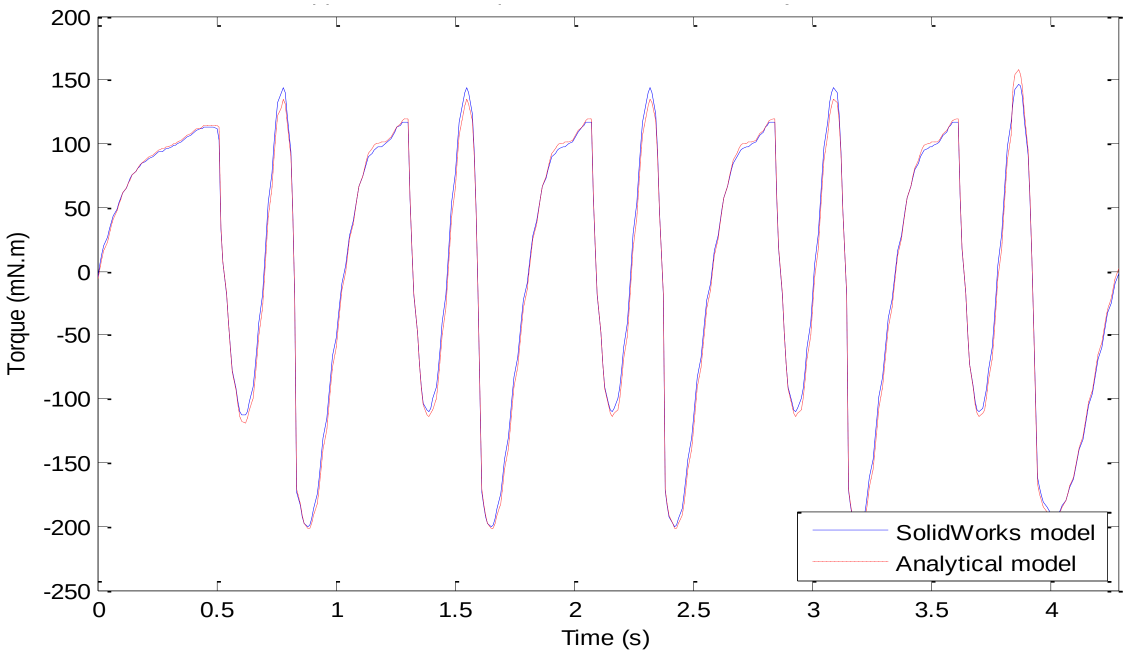

Figure 4.21 Applied crank torque of SolidWorks and Analytical model using same input crank angular acceleration. The food resistance is applied in Y axis on vertical slider link 5 due to spring compression.

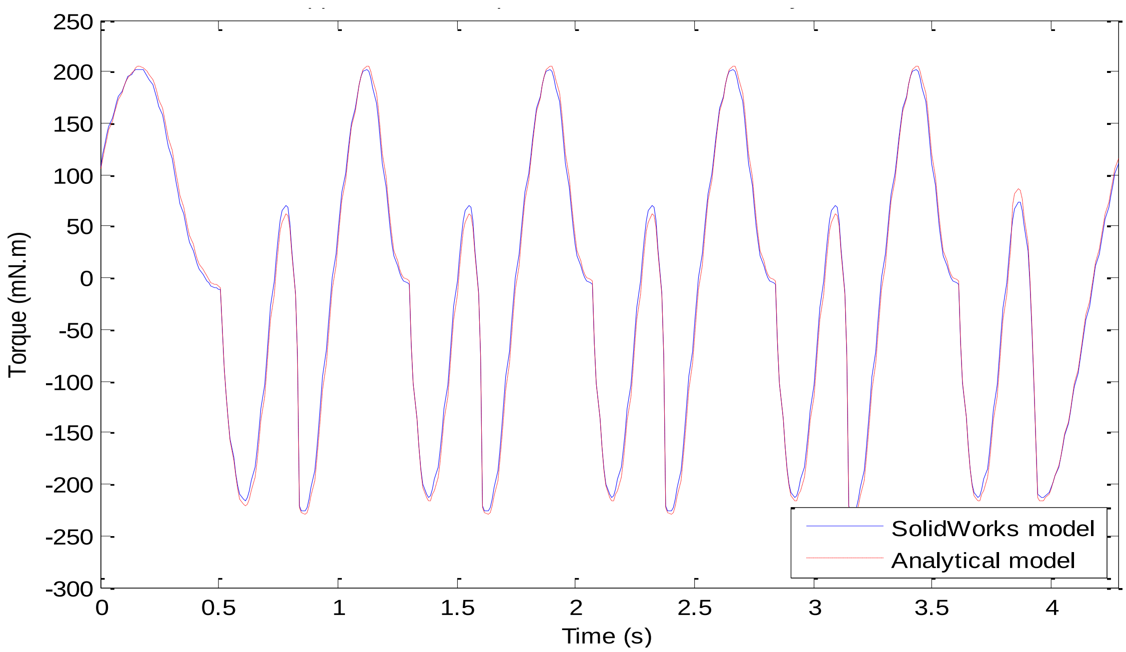

Figure 4.22 Applied crank torque of SolidWorks and Analytical model using same input crank angular acceleration. The food resistance is applied in Y axis on vertical slider link 5 due to spring compression and constant 20N is horizontally applied on horizontal slider link 4.

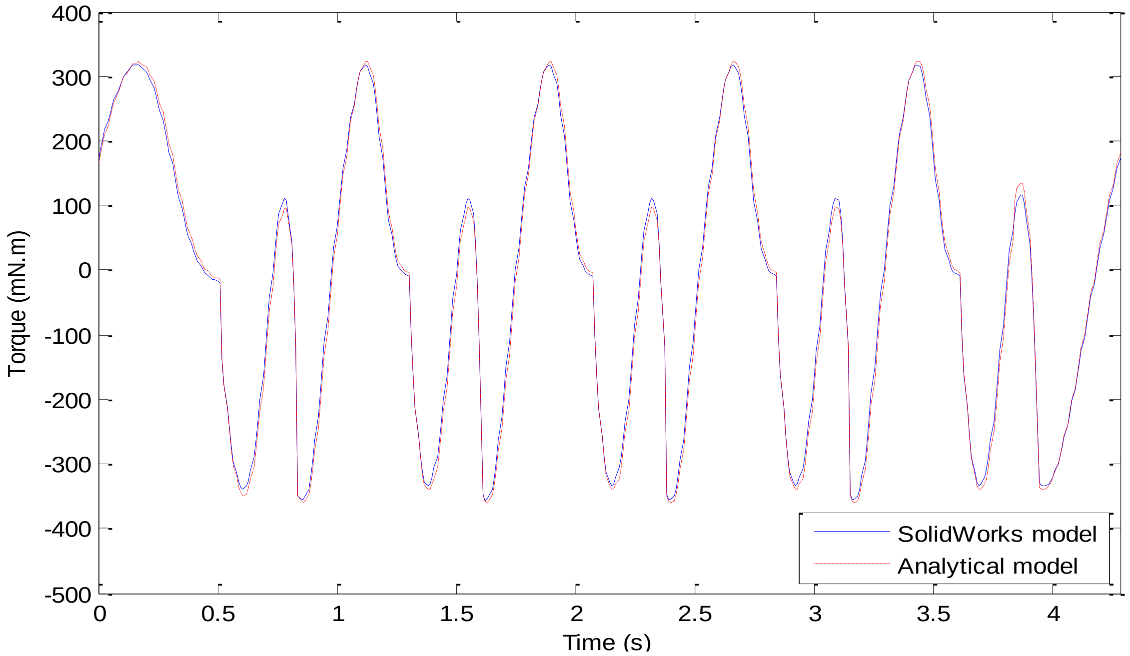

Figure 4.23 Total driving torque through gear system between SolidWorks and Analytical model using same input crank angular acceleration. The food resistance is applied in Y axis on vertical slider link 5 due to spring compression and constant 20N is horizontally applied on horizontal slider link 4.

From the above results of torque, other than the slight difference during occlusion, the results from the analytical model almost perfectly match with the ones of SolidWorks model. Therefore, the analytical model of 2D planar chewing mechanism can correctly simulate real chewing mechanism under assumption 1 and 2.

### 4.2.4. ***SimMechanics Model of Linkage Mechanism***

SimMechanics provides tools for building mechanical models such as 6-bar linkage mechanism model and spring mass system model. SimMechanics blocks can also be integrated with Simulink blocks, such as velocity control model and force control model. By simulating the SimMechanics model, it is possible to impose kinematic constraints, apply forces and torques, and measure the resulting motions and forces. Therefore, SimMechanics simulation will enable us to simulate the linkage chewing machine both the mechanism and control system. It helps validate the design of the spring-mass system that has been added to the device.

The SimMechanics model of the linkage mechanism is built based on the kinematics and dynamics analyzed in the previous section, as shown in Figure 4.24. This model takes angular position, angular velocity and angular acceleration motion signals as the input to drive the crank linkage of the linkage mechanism, as shown in Figure 4.25. The torque required at the crank to achieve the input motion is generated through the joint sensor and output as the counter torque to the DC motor model. The vertical displacement (mm) and velocity (mm/s) of the link attached to the upper teeth are measured by the body sensor in the model. The vertical displacement of the link can be converted to the deformation of the food in the simulation if the original thickness of the food is known. The forces generated during chewing the food act as a resistance force to the upper teeth link through the body actuator, as shown in Figure 4.26. Parameters of physical properties for linkage mechanism in SimMechanics model are listed in Table 4-3.

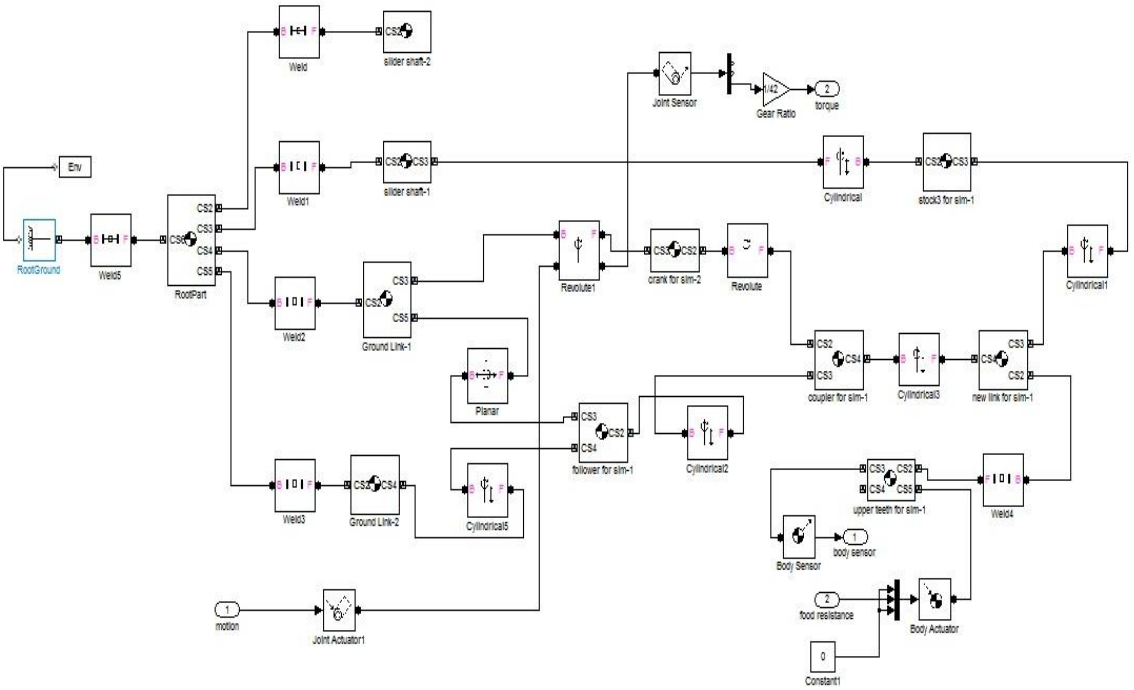

Figure 4.24 Simulation model of 6-bar linkage mechanism

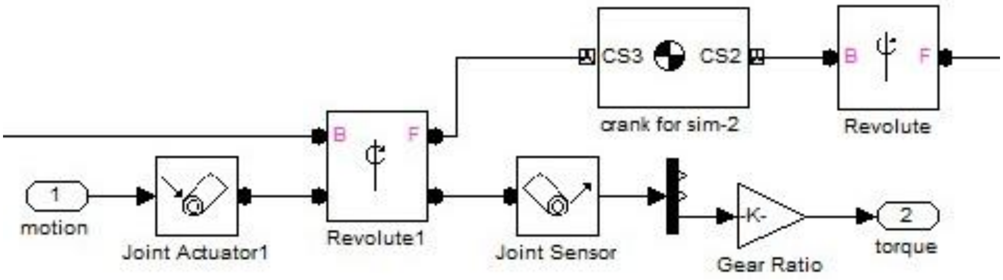

Figure 4.25 Motion input through the joint actuator and torque output through the join sensor in the SimMechanics model

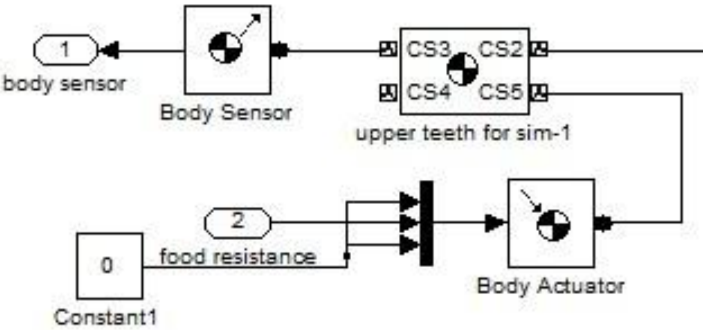

Figure 4.26 Vertical displacement and velocity output through the body sensor and food resistance input through the body actuator in the SimMechanics model

Table 4-3 Parameters of physical properties for linkage mechanism

| | Crank | Coupler | Coupler2 | Follower | Ground |
|---|---|---|---|---|---|
| **Length** | **10mm** | **35mm** | **57.7mm** | **30mm** | **50mm** |
| **Mass** | **40g** | **147.2g** | | **34.5g** | **N/A** |
| | **Bar** | **Bar2** | **Bar3** | **Bar4** | **Link** |
| **Length** | **100mm** | **100mm** | **100mm** | **100mm** | **40mm** |
| **Mass** | **14.57g** | **80.54g** | **14.57g** | **16.26g** | **41.17g** |

## *4.3. DC Motor Simulation and Control*

### 4.3.1. *DC Motor Simulation*

The model of the DC motor is shown in Figure 4.27, where *R* is the armature resistance, *L* is the armature inductance, *v* is the voltage applied to the motor, *i* is the current through the motor, $k_f$ is the back emf constant of the motor, *J* is the moment of inertia of the load, *b* is the viscous friction coefficient, *τ* is the torque generated by the motor, *Θ* is the angular position of the motor, *ω* is the angular velocity of the motor.

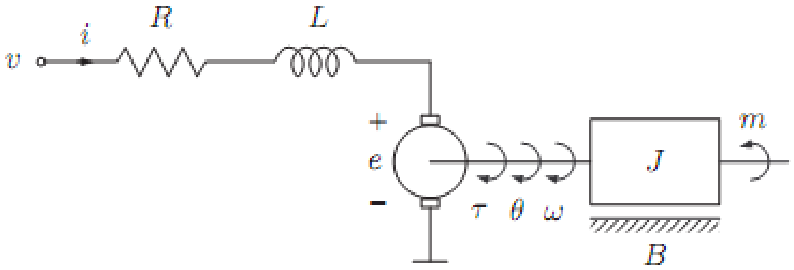

Figure 4.27 Schematic diagram of a simple DC motor

The back emf voltage *e* is proportional to the shaft angular velocity and can be expressed as

$$e = k_f \omega = k_f \frac{d\theta}{dt} \tag{75}$$

The motor torque is proportional to the armature current and can be expressed as

$$\tau = k_i i \tag{76}$$

Where $k_i$ is the torque constant of the motor. In SI units, the numerical values of $k_f$ and $k_i$ are the same.

From Figure 4.27, the following equations based on the Newton's law combined with the Kirchoff's law can be expressed as:

$$J \frac{d^2\theta}{dt^2} + b \frac{d\theta}{dt} = k_i i \tag{77}$$

$$L\frac{di}{dt} + Ri + k_f\frac{d\theta}{dt} = V \quad (78)$$

Using the Laplace transform, equation (77) and (78) can be written as:

$$Js^2\theta(s) + bs\theta(s) = k_i i(s) \quad (79)$$

$$Lsi(s) + Ri(s) + k_f s\theta(s) = V(s) \quad (80)$$

Therefore, the transfer function from the input *V(s)* to the output $\theta(s)$ is

$$\frac{\theta(s)}{V(s)} = \frac{k_i}{(Ls+R)(Js+b)+k_f k_i} \quad (81)$$

A block diagram of Simulink model representing the relationship between *V(s)* and $\theta(s)$ in equation (81) is shown in Figure 4.28. The parameters of Maxon EC 32 motor are given and listed in Table 4-4.

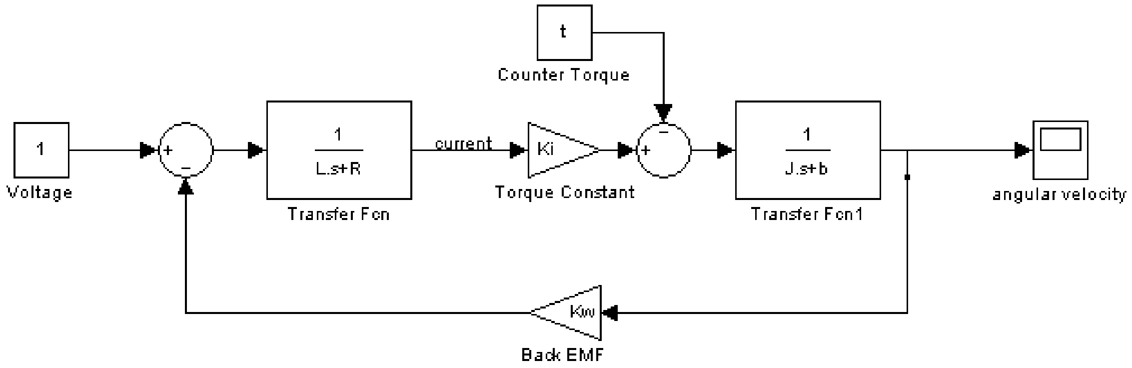

Figure 4.28 Simulink model of DC motor

Table 4-4 Parameters of Maxon EC 32 motor

| | |
|---|---|
| Resistance $\boldsymbol{R}$ | 1.39 Ω |
| Inductance $\boldsymbol{L}$ | 2.26e-4 H |
| Back EMF constant $\boldsymbol{k_\omega}$ | 0.0205 Vs/rad |
| Torque Constant $\boldsymbol{k_i}$ | 0.0205 Nm/A |
| Rotor Inertia $\boldsymbol{J}$ | 2e-6 Nms$^2$ |
| Mechanical Damping $\boldsymbol{b}$ | 3.035e-4 Nms |

### 4.3.2. ***Dynamics of Gear System***

In the chewing machine, the motor drives the linkage mechanism through a gear train system. The motor-load system through a gear train is shown below in Figure 4.29. The load $T_L$ represents the calculated driving torque of linkage mechanism. The load $T_m$ is the torque applied from the motor. $\theta_m$ is the motor shaft angular displacement. The parameters of motor and gear properties are listed in Table 4-6.

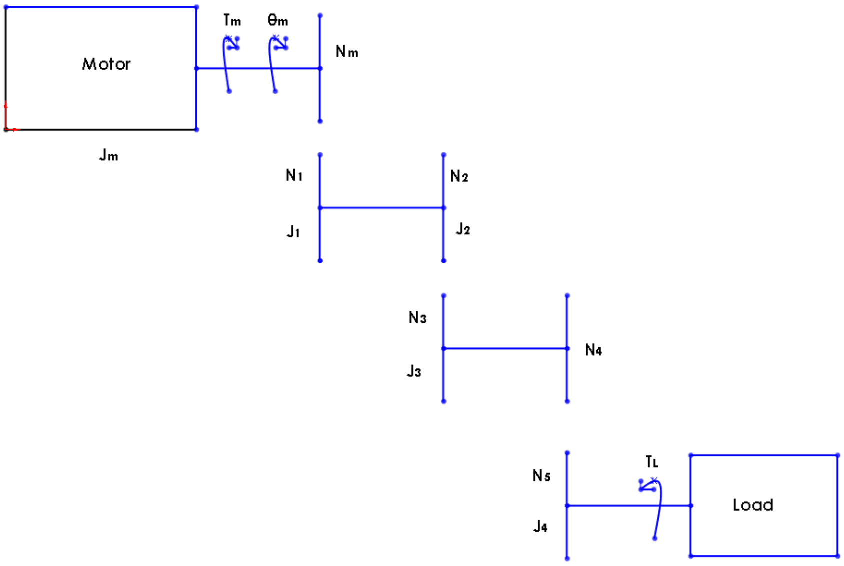

Figure 4.29 Motor-load system through a gear train with loss

Table 4-5 Parameters of motor and gear properties

| | $i$ | Inertia $J_i$ (kg*m$^2$) | Number of teeth of gear $N_i$ |
|---|---|---|---|
| Motor | $m$ | 0.2e-5 | 1 |
| Planetary Gear | 1 | 0.7e-7 | 66 |
| Spur gear | 2 | 0.2584e-4 | 44 |
| | 3 | 1.1542e-3 | 28 |
| | 4 | 1.0989e-3 | 28 |
| | 5 | N/A | 28 |

To simplify the motor-gear-load system, an equivalent system at the input is shown in Figure 4.30. $T_m$ can be expressed as

$$T_m = J_e * \ddot{\theta}_m + T_{reflect} \tag{82}$$

Where $\ddot{\theta}_m$ is the motor shaft angular acceleration and $J_e$ is the combined inertia. $\ddot{\theta}_m$, $J_e$ and $T_{reflect}$ can be expressed below

$$J_e = J_m + (J_1 + J_2)\left(\frac{N_m}{N_1}\right)^2 + J_3\left(\frac{N_m \cdot N_2}{N_1 \cdot N_3}\right)^2 + J_4\left(\frac{N_m \cdot N_2 \cdot N_4}{N_1 \cdot N_3 \cdot N_5}\right)^2 \tag{83}$$

$$\ddot{\theta}_m = \frac{N_1 \cdot N_3 \cdot N_5}{N_m \cdot N_2 \cdot N_4} * \ddot{\theta}_1 \tag{84}$$

$$T_{reflect} = \frac{N_m \cdot N_2 \cdot N_4}{N_1 \cdot N_3 \cdot N_5} * T_m \tag{85}$$

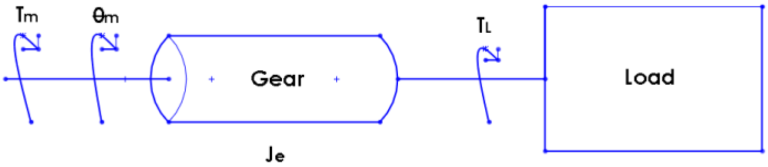

Figure 4.30 Equivalent motor-load system at the input

### 4.3.3. ***Motor Control Simulation***

The chewing robot is actuated through the motor control unit, Maxon Des 50/5 servo amplifier. The Maxon controller uses a PI cascade controller, which consists of an inner current PI controller and an outer velocity PI controller. The input of the current controller is the current error between the armature current of motor and the output demand current of velocity controller. The control system is simulated in Simulink (Figure 4.31). The parameters of current and velocity controllers are tuned by the Simulink Response Optimization toolbox. The block diagram of the velocity control model driving the linkage mechanism model is shown in Figure 4.32. The motor model first gets the chewing velocity profile in rpm as the input velocity and converts the velocity to current signal through the velocity PI controller. The current signal multiplies the torque constant to generate the torque. The torque will subtract the counter torque value generated from the linkage mechanism and input to the servomotor model. A rotational motion sensor block is used to measure the angular velocity produced by the input torque to the motor model. The angular velocity is then sent to the linkage mechanism model as a motion command. The electrical and mechanical parameters of the Maxon DC motor are used in the motor simulation model, as shown in Figure 4.33.

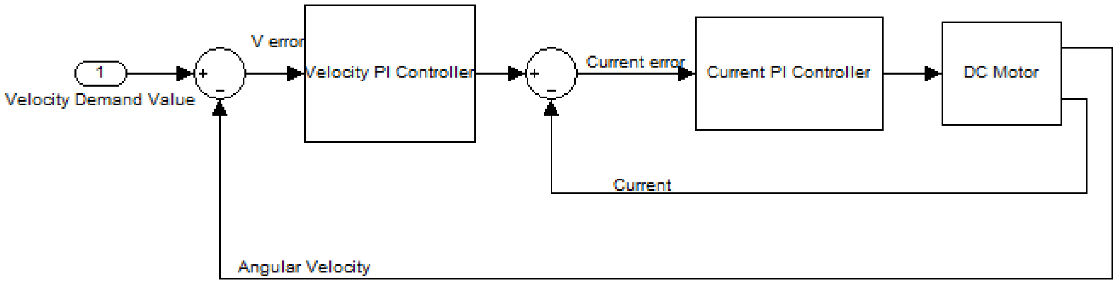

Figure 4.31 Cascade velocity control system

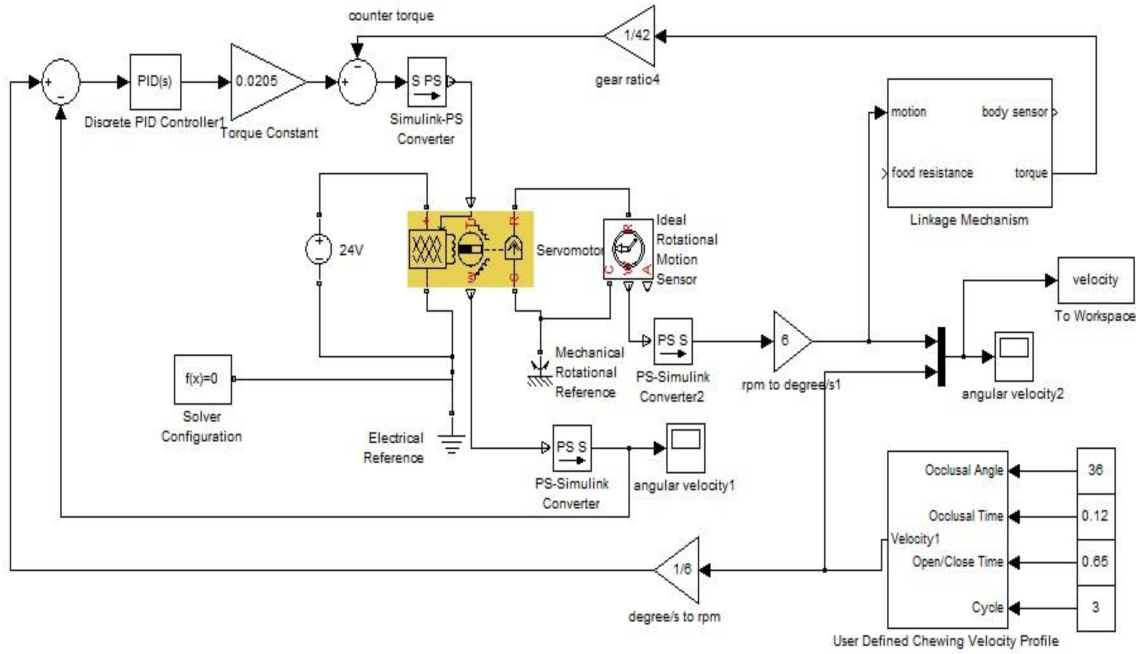

Figure 4.32 Block diagram of velocity control simulation model with linkage mechanism model

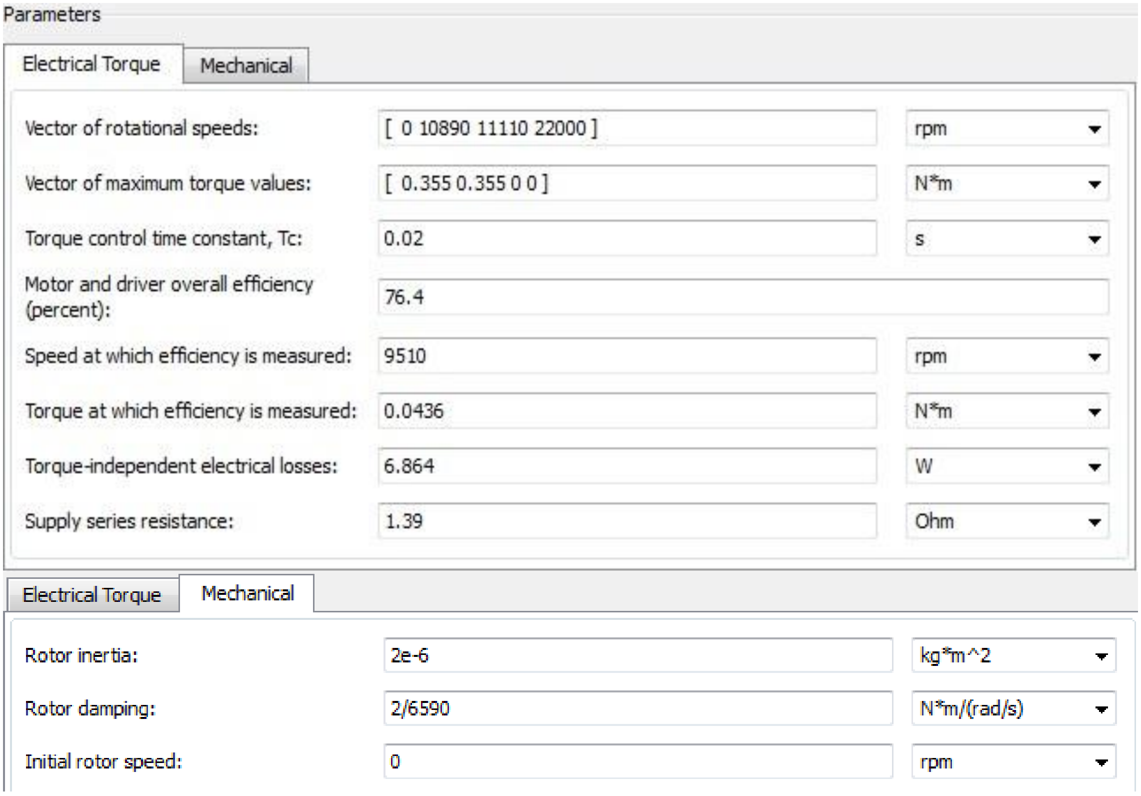
Parameters

Electrical Torque | Mechanical

| | | |
|---|---|---|
| Vector of rotational speeds: | [ 0 10890 11110 22000 ] | rpm |
| Vector of maximum torque values: | [ 0.355 0.355 0 0 ] | N*m |
| Torque control time constant, Tc: | 0.02 | s |
| Motor and driver overall efficiency (percent): | 76.4 | |
| Speed at which efficiency is measured: | 9510 | rpm |
| Torque at which efficiency is measured: | 0.0436 | N*m |
| Torque-independent electrical losses: | 6.864 | W |
| Supply series resistance: | 1.39 | Ohm |

Electrical Torque | Mechanical

| | | |
|---|---|---|
| Rotor inertia: | 2e-6 | kg*m^2 |
| Rotor damping: | 2/6590 | N*m/(rad/s) |
| Initial rotor speed: | 0 | rpm |

Figure 4.33 Electrical and mechanical parameters of Maxon motor used in the servomotor block of the simulation model

Since the simulation model of the chewing robot (including motor and linkage mechanism) has been created in Simulink, a Simulink PID Controller block was used to implement the PID motor control. To tune the PID, PID Tuner in Simulink was used to tune the PID parameters to achieve a robust design with the desired response time, shown in Figure 4.34. After launching the PID Tuner, the software automatically computed a linear plant model from the Simulink model and designs an initial controller, shown in Figure 4.35.

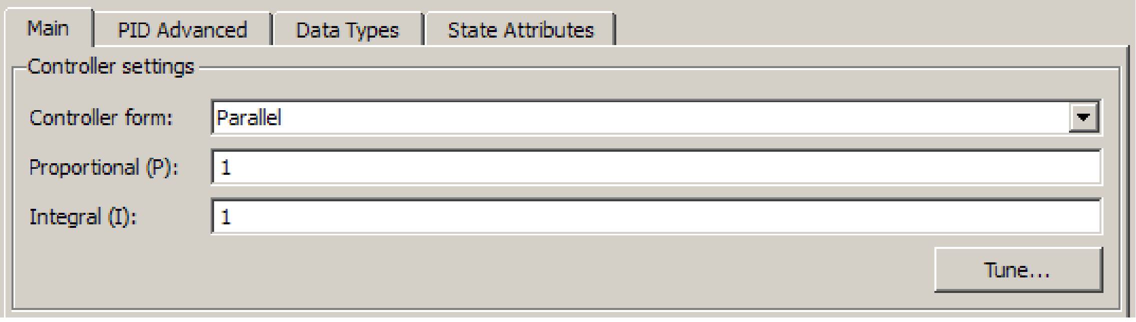

Controller settings

Controller form: Parallel

Proportional (P): 1

Integral (I): 1

Figure 4.34 PI controller block with auto tuner

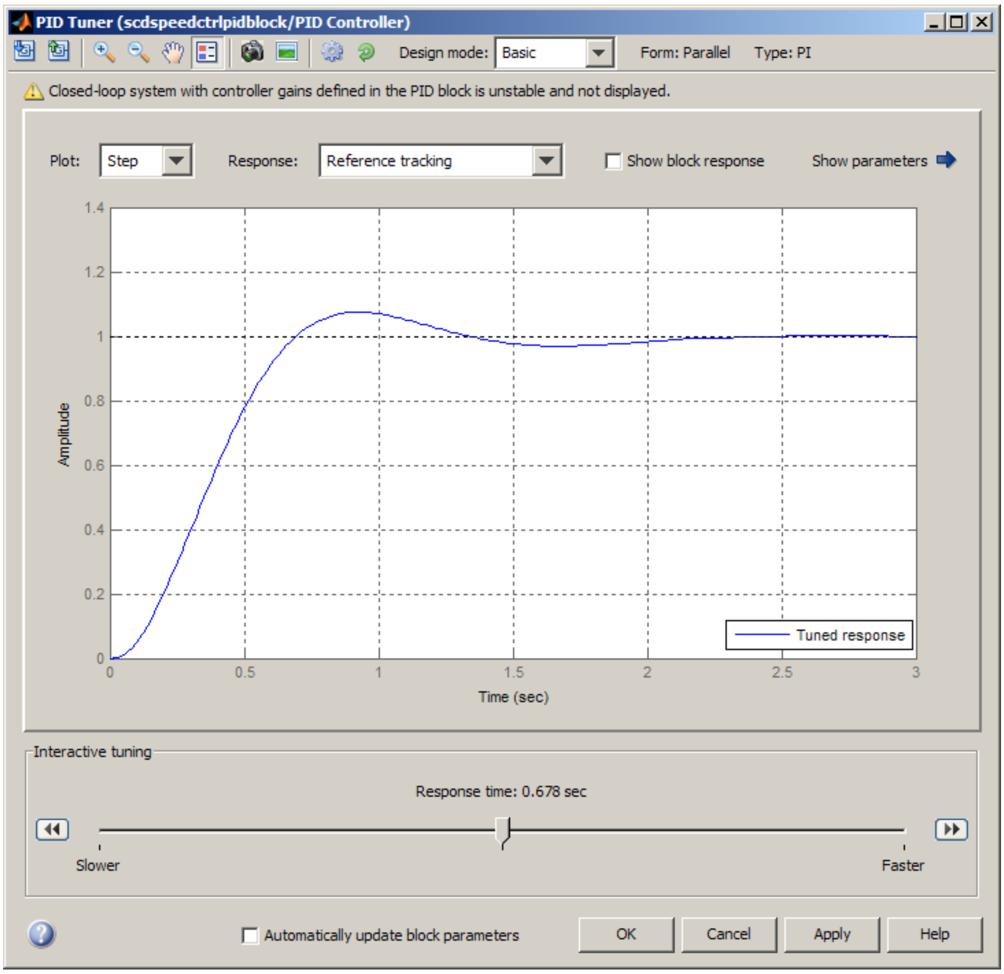

Design mode: Basic

Form: Parallel

Type: PI

Closed-loop system with controller gains defined in the PID block is unstable and not displayed.

Plot: Step

Response: Reference tracking

☐ Show block response

Response time: 0.678 sec

☐ Automatically update block parameters

Figure 4.35 The PID Tuner dialog with the initial design.

Figure 4.36 shows the tuning of PI parameters through the Simulink Control Design. After tuning the PI controller, the proportional gain is 0.0196 and the integral gain is 1.1076. The rise time of 0.02 second and the settling time of 0.0671 second are fast enough to deal with the human chewing velocity profile, where the average velocity is 0.77 second per chewing cycle. Figure 4.37 shows the responses of motor velocity output when the chewing robot runs at 400 degree/sec for a chewing cycle. It is found that the motor velocity output is very stable and controls the speed reaching to its reference speed rapidly. Figure 4.38 shows the simulated chewing velocity when Xu's chewing velocity profile (see section 1.2.4) is used for two cycles. The result shows the motor output velocity follows the Xu's chewing velocity profile reasonably well.

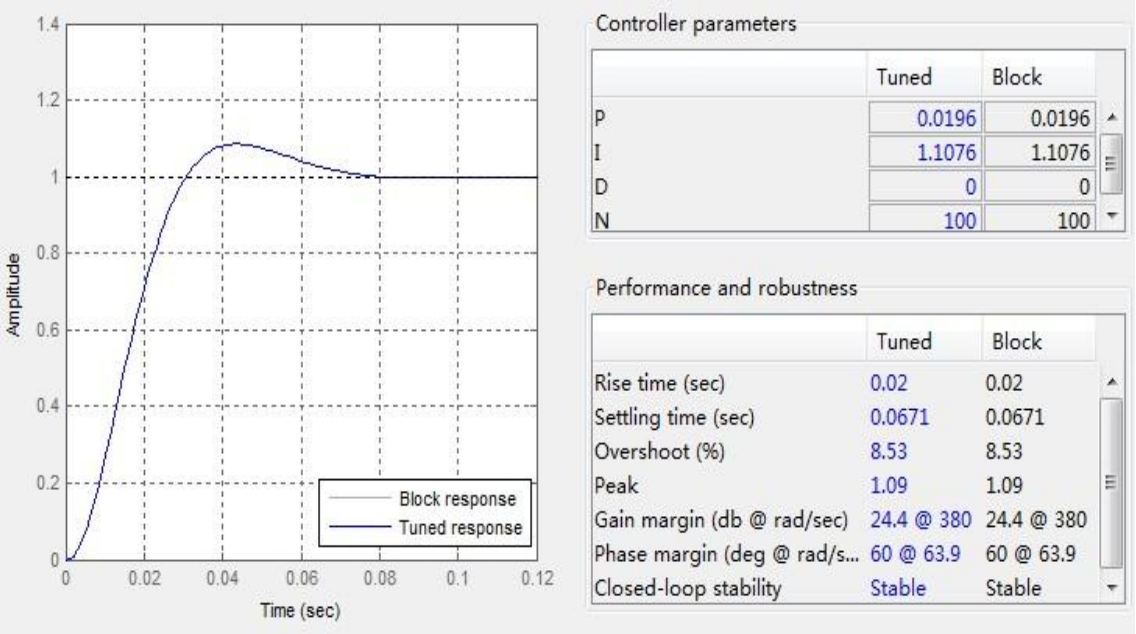

Controller parameters

| | Tuned | Block |
|---|---|---|
| P | 0.0196 | 0.0196 |
| I | 1.1076 | 1.1076 |
| D | 0 | 0 |
| N | 100 | 100 |

Performance and robustness

| | Tuned | Block |
|---|---|---|
| Rise time (sec) | 0.02 | 0.02 |
| Settling time (sec) | 0.0671 | 0.0671 |
| Overshoot (%) | 8.53 | 8.53 |
| Peak | 1.09 | 1.09 |
| Gain margin (db @ rad/sec) | 24.4 @ 380 | 24.4 @ 380 |
| Phase margin (deg @ rad/s... | 60 @ 63.9 | 60 @ 63.9 |
| Closed-loop stability | Stable | Stable |

Figure 4.36 PID tuning for better performance of motor

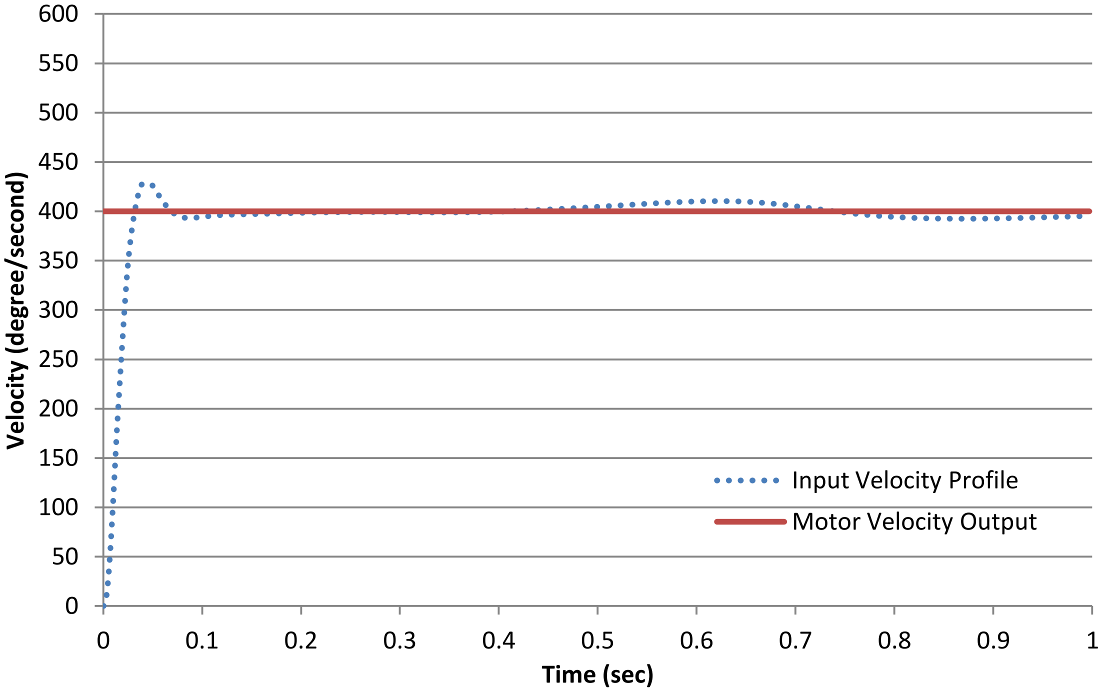

Figure 4.37 Comparison of simulated velocity output with the chewing velocity profile at constant 400 degree per second

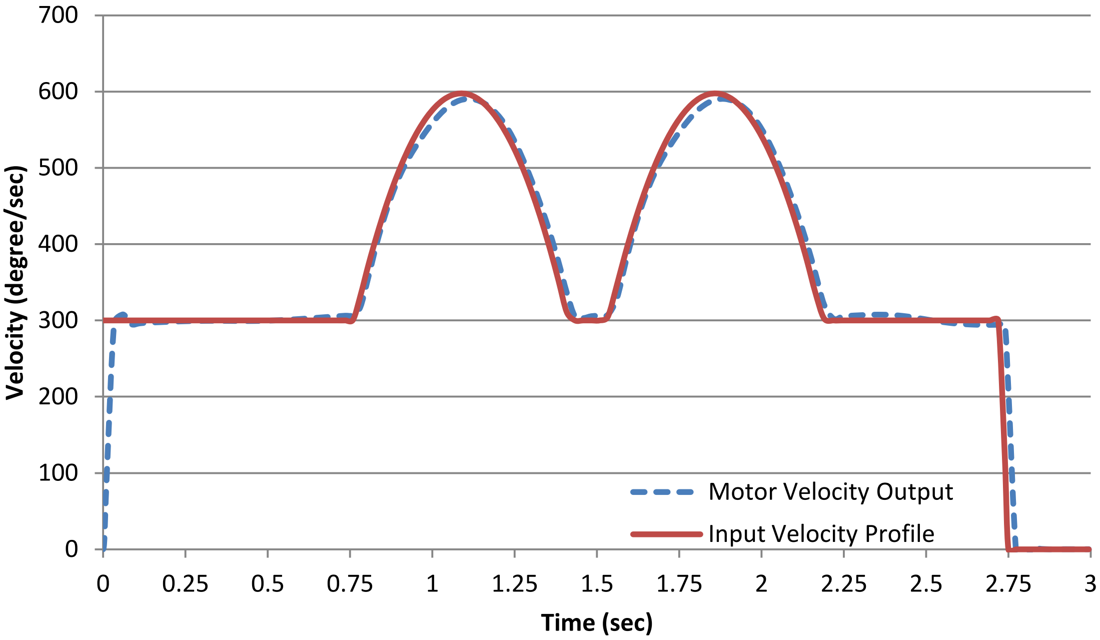

Figure 4.38 Comparison of simulated velocity output with input chewing velocity profile for two cycles

## *4.4. Chewing Experiment for Validation of the Chewing Robot*

The chewing experiment of chewing robot have carried out using bottom teeth and four real food, including Moro bar, Crunchy bar, Apricot & Pie bar, Fruits & Nuts bar. The bottom teeth can be considered as a simulated food with different thickness by rising up the bottom teeth for defined displacements, such as 1mm, 2mm and etc. To prepare the chewing experiment, the upper teeth are made sure to perfectly occlude with the bottom teeth by checking the force sensor showing almost no force (< 1N) applied from upper teeth. In this case, the bottom teeth are raised up from the reference position mentioned above. The food will has constant thickness during occlusion. Thus, the food resistance obtained from the force sensor is the same as the spring compression force. Each chewing experiment runs for five chewing cycles and two pretightened displacements of the spring in the upper teeth (0mm and 6mm). 6mm of pretighting displacement is selected so that when the spring is fully compressed (12mm) during chewing, the maximum force exerted from the spring can reach up to 150N, which is the maximum required force for chewing (D. J. Anderson, 1956). The chewing velocity profile used in the experiment was the one developed by Xu (Xu et al., 2008). Table 4-6 shows the chewing experiment data.

Table 4-6 Chewing experimental data

| Experiment | food | Food thickness (mm) | Spring pretightening displacement (mm) |
|---|---|---|---|
| #1 | Bottom teeth | 0 | 0 |
| #2 | Bottom teeth | 1 | 0 |
| #3 | | | 6 |
| #4 | Bottom teeth | 2 | 0 |
| #5 | | | 6 |
| #6 | Bottom teeth | 3 | 0 |
| #7 | | | 6 |
| #8 | Bottom teeth | 4 | 0 |
| #9 | | | 6 |
| #10 | Apricot Pie Bar | 15 | 0 |
| #11 | Crunchie Bar | 15 | |
| #12 | Fruit & Nuts bar | 15 | |
| #13 | Moro bar | 15 | |

During the chewing experiments, motor currents are measured to calculate motor torque. Real-time encoder data of crank link are recorded and converted into crank angular displacement, velocity and acceleration, which are input to the analytical model. 3D forces measured under the bottom teeth input to the analytical model to simulate food resistance and can be used to estimate the spring compression displacement during chewing.

### 4.4.1. *Validation of Spring-Mass System*

The chewing force profiles in Y-axis without pretightened spring and with the spring pretightened for 6mm are shown in Figure 4.39 and Figure 4.40. A comparison of different distances which the bottom teeth are raised up is shown in each figure. In general, when the bottom teeth are raised up higher, the chewing force in Y-axis is larger, since the spring is compressed more. The force profiles in each cycle are almost identical. This means that the chewing robot is able to reproduce the force profile. The average maximum force comparison between no pretightened and pretightened 6mm of spring is listed in Table 4-7.

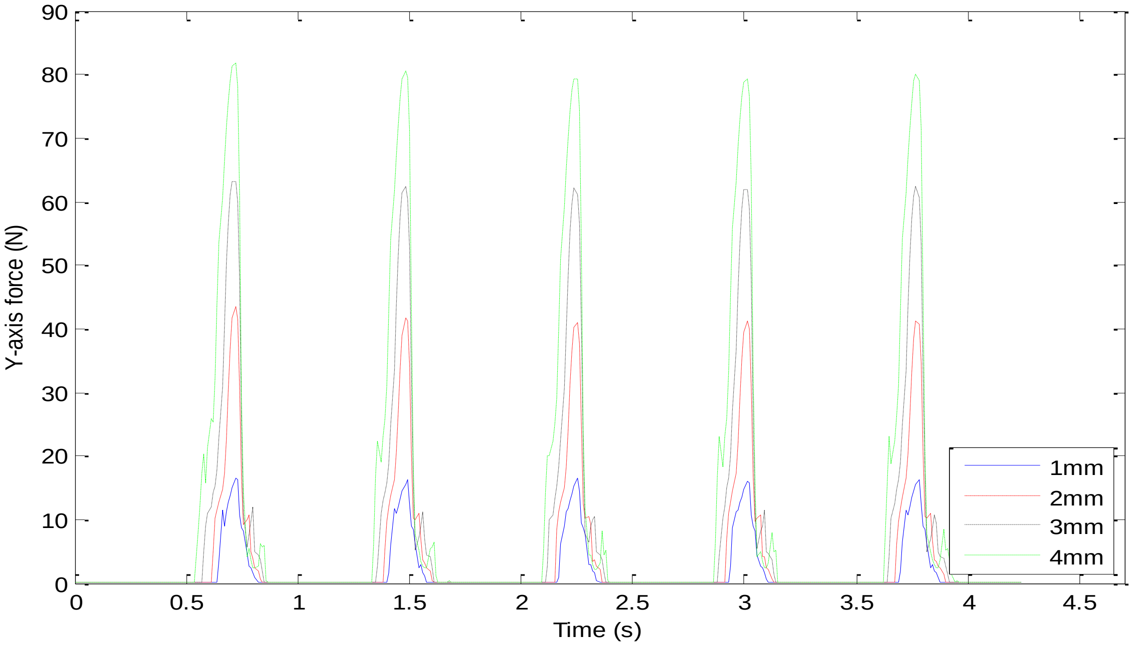

Figure 4.39 Chewing force profiles in Y-axis with no pretightening force. The bottom teeth are raised up 1mm, 2mm, 3mm and 4mm respectively.

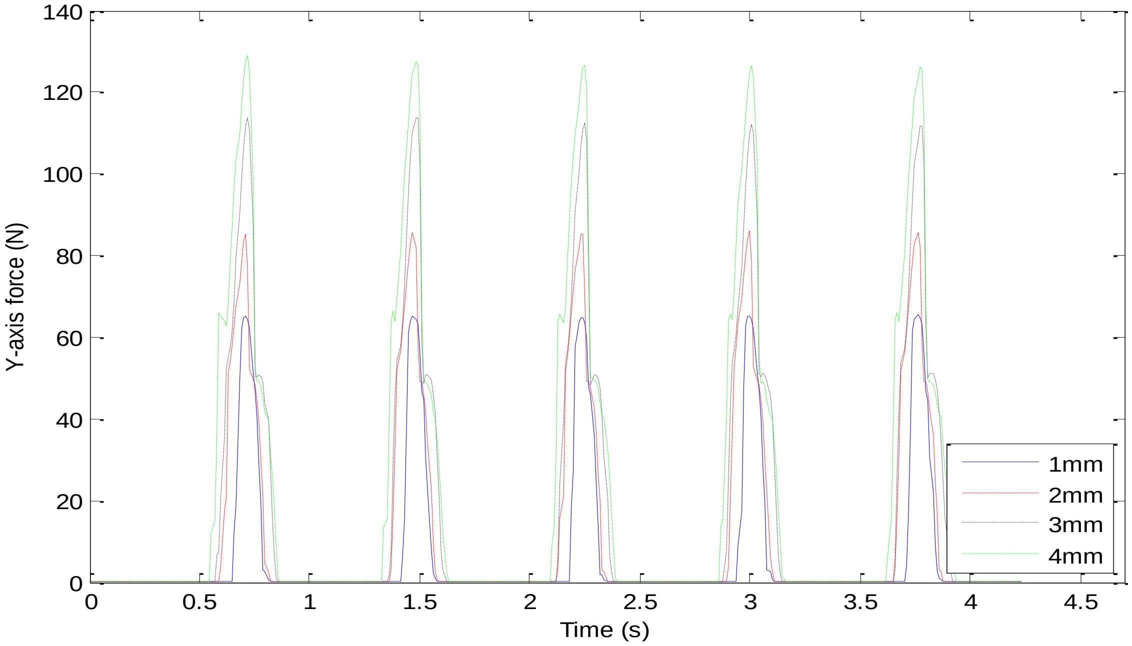

Figure 4.40 Chewing force profiles in Y-axis with spring pretightened 6mm. The bottom teeth are raised up 1mm, 2mm, 3mm and 4mm respectively.

Table 4-7 Average maximum force comparison between no pretightened and pretightened 6mm of spring

| Food thickness (spring displacement) (mm) | Average maximum force of five chewing cycles with spring pretightened 6mm(N) | Average maximum force of five chewing cycles without spring pretightened (N) | Average maximum force difference (N) |
|---|---|---|---|
| 1 | 65.5 | 16.7 | 48.8 |
| 2 | 86.2 | 41.8 | 44.4 |
| 3 | 113.3 | 62.4 | 50.9 |
| 4 | 127.7 | 80.2 | 47.5 |

From first four experiments in Table 4-7, it is found that the relationship between the force and spring displacement is

$$F = 20 * x \tag{86}$$

Where F is the y-axis force from force sensor under bottom teeth, and 20 is the corrected value to modify the relationship between force and spring displacement during chewing. The reason that the chewing force measured is not related to the given spring constant from the datasheet may be because that the upper teeth which contain the spring do not move vertically during chewing and also the occlusal surface is not flat.

From average maximum force difference in Table 4-7, it is found that the spring pretightening force (pretightening displacement x spring constant = 6 x 7.9 = 47.4) matches the experiment results. This proves the given spring constant is 7.9 N/mm.

### 4.4.2. *Simulation Results Compared with Chewing Robot*

The measured motor current in the experiment is used to calculate the real motor torque driving the chewing mechanism. And then the real motor torque in the experiment is compared with simulated motor torque in the analytical model. The motor torque of the experiment data is calculated by the following formula

$$T_m = \left(T_{motor} + T_{friction}\right) \cdot \eta \tag{87}$$

Where $T_m$ is the mechanical torque from the motor, $T_{motor}$ is the electrical motor torque, $T_{friction}$ is the internal friction torque in the bearings and commutation system and $\eta$ is the efficiency in percentage describing the relationship of mechanical power delivered to electrical power consumed. Since the efficiency of the motor for our application is a practical value obtained from the experiment, the efficiency is assumed to be 50% for the following comparisons.

The electrical motor torque $T_{motor}$ can be expressed as

$$T_{motor} = I \cdot k_t \tag{88}$$

Where $I$ is the measured motor current (A), $k_t$ is the torque constant (0.0205 Nm/A).

The internal friction torque $T_{friction}$ can be expressed as

$$T_{friction} = I_0 \cdot k_t \tag{89}$$

Where $I_0$ is the no-load current (0.286 A).

In Figure 4.41, the simulation result has the similar trend with the torque of experiment. The difference is likely mainly caused by the estimated constant efficiency (50%). Since the efficiency is proportional to the motor torque, current and voltage, the efficiency value should be a variable instead of a constant. However, the efficiency needs to be obtained through a set of experiments. Thus, for simplicity, the efficiency is estimated as 50% in the following experiments.

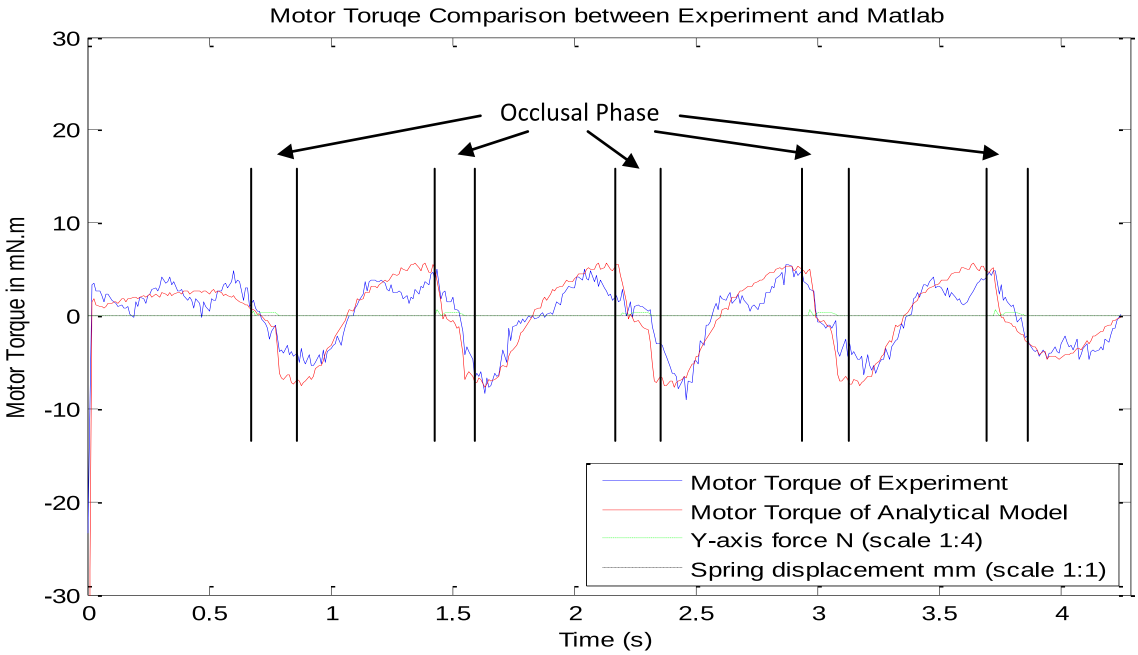

Figure 4.41 Motor torque compared between experiment #1 and analytical model. There is no food resistance during occlusion.

In Figure 4.42, the simulation result has the similar trend with the torque of experiment. During five occlusion periods (when green dash dotted line stick up), the simulated torque closely match the experimental torque for the second, third and fifth occlusion. The reason for not well matching the experimental torque during the other two occlusions may be due to the estimated efficiency of the motor.

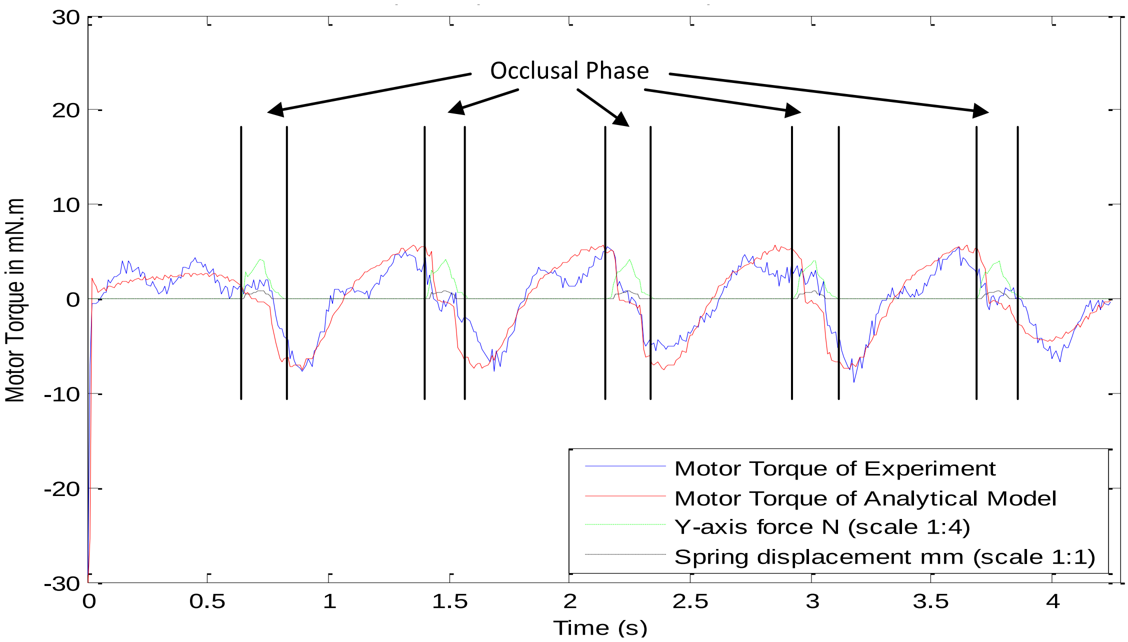

Figure 4.42 Motor torque compared between experiment #2 and analytical model. The bottom teeth are raised up for 1mm.

In Figure 4.43, during the occlusal phase, the simulated torque matches the experiment torque very well, especially from the second cycle to the fifth cycle.

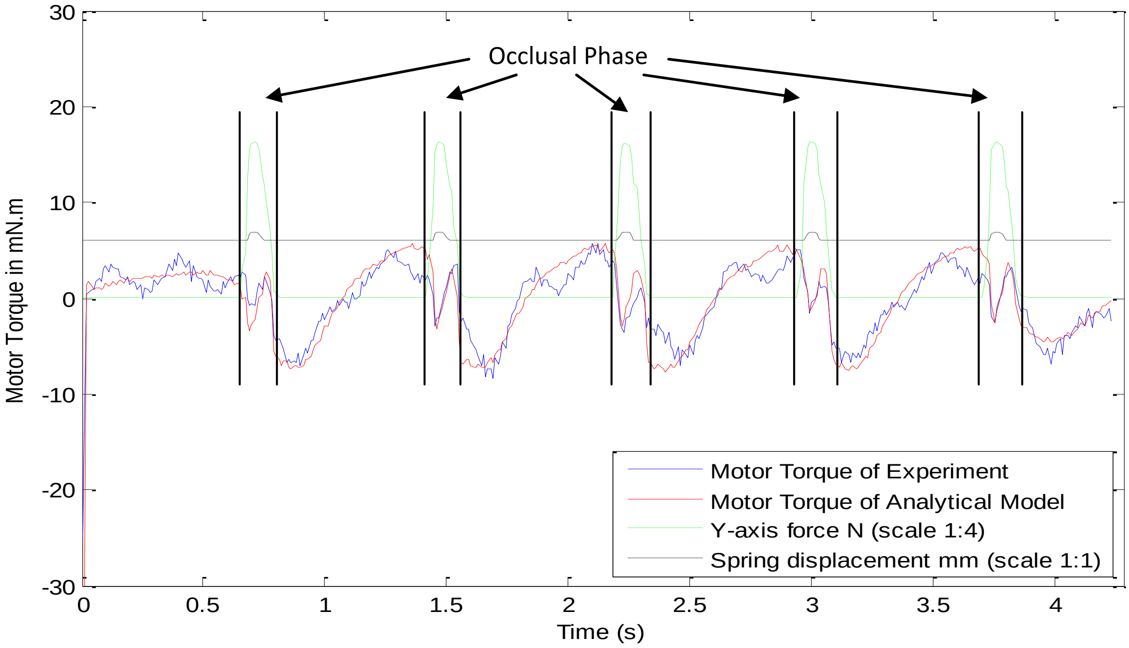

Figure 4.43 Motor torque compared between experiment #3 and analytical model. The bottom teeth are raised up for 1mm. The spring is pretightened for 6mm.

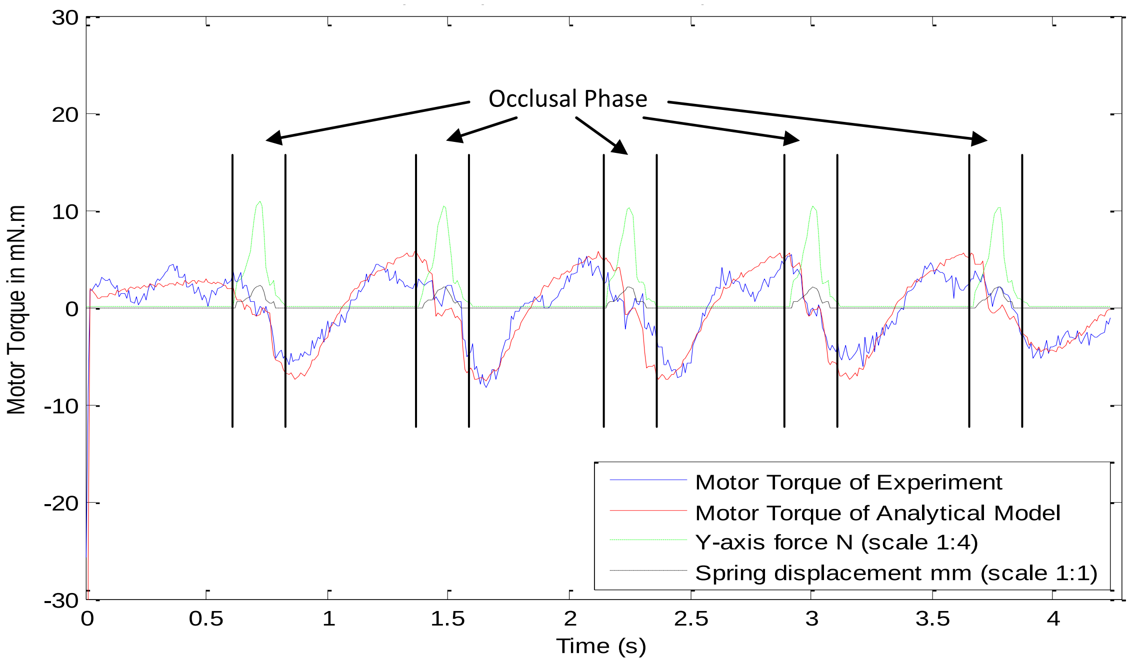

Figure 4.44 Motor torque compared between experiment #4 and analytical model. The bottom teeth are raised up for 2mm for constant food resistance.

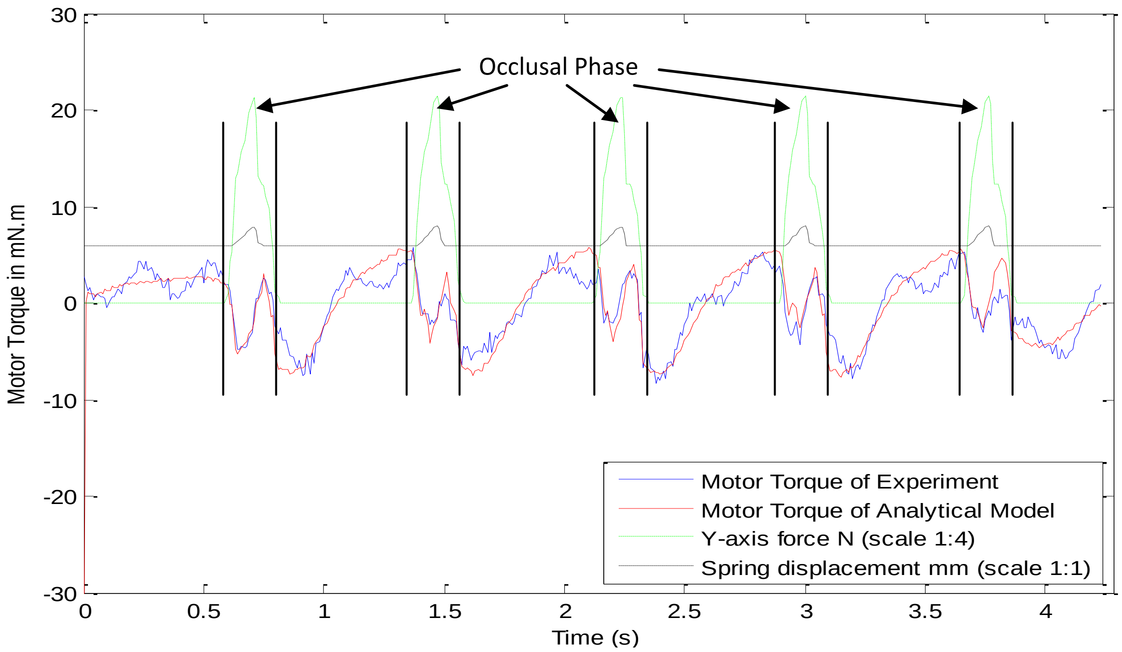

Figure 4.45 Motor torque compared between experiment #5 and analytical model. The bottom teeth are raised up for 2mm for food resistance. The spring is pretightened for 6mm.

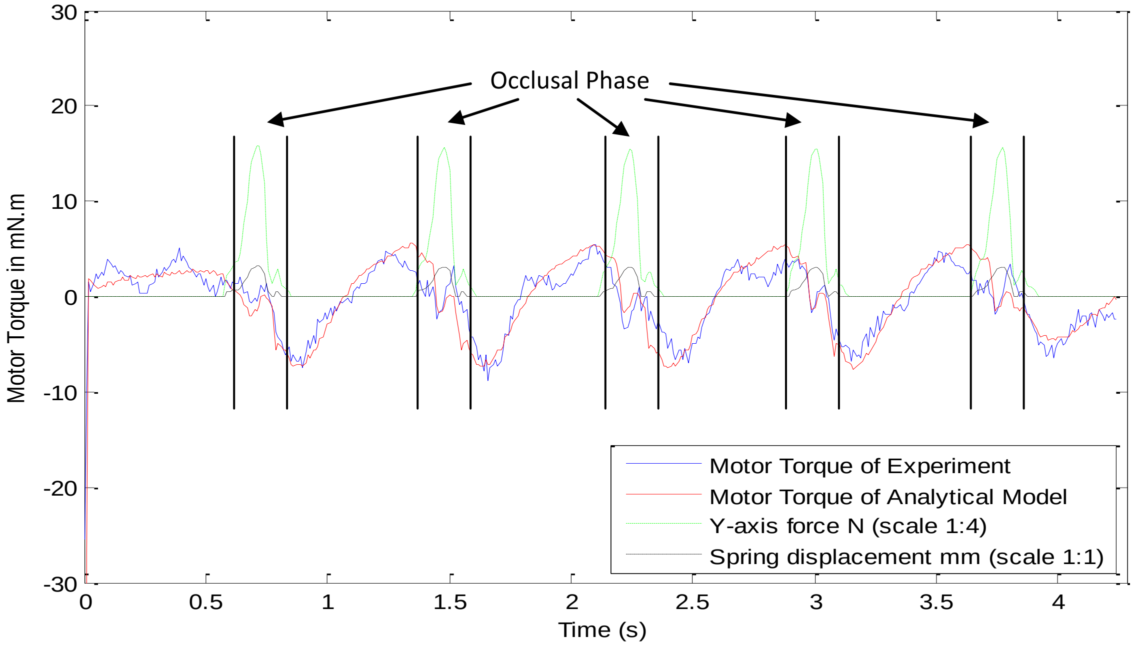

Figure 4.46 Motor torque compared between experiment #6 and analytical model. The bottom teeth are raised up for 3mm for food resistance.

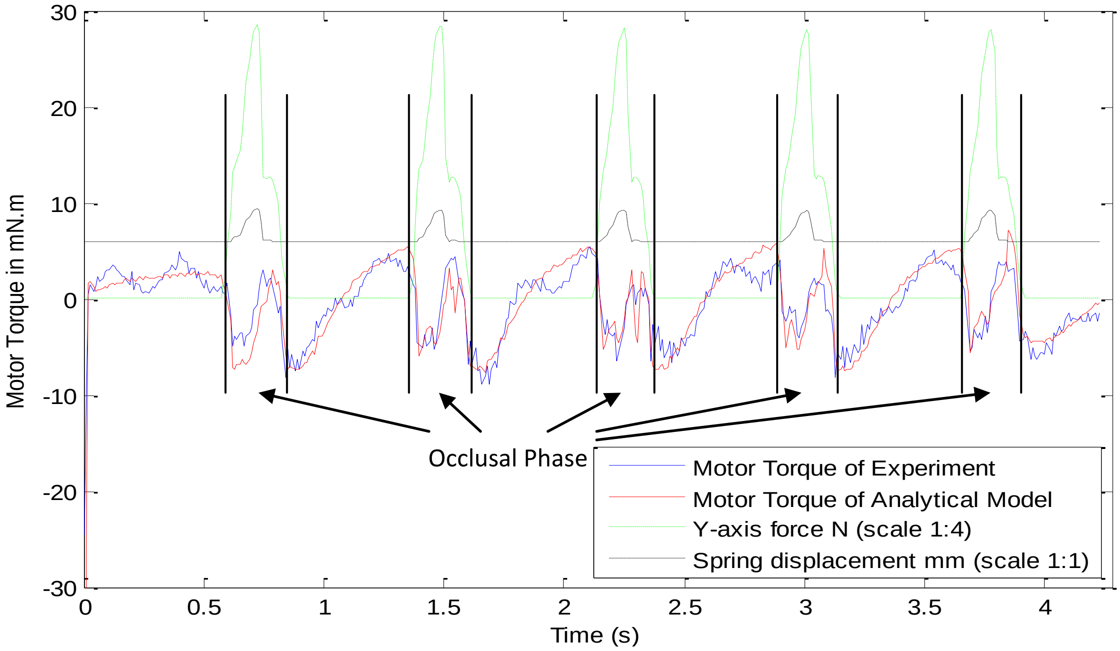

Figure 4.47 Motor torque compared between experiment #7 and analytical model. The bottom teeth are raised up for 3mm for food resistance. The spring is pretightened for 6mm.

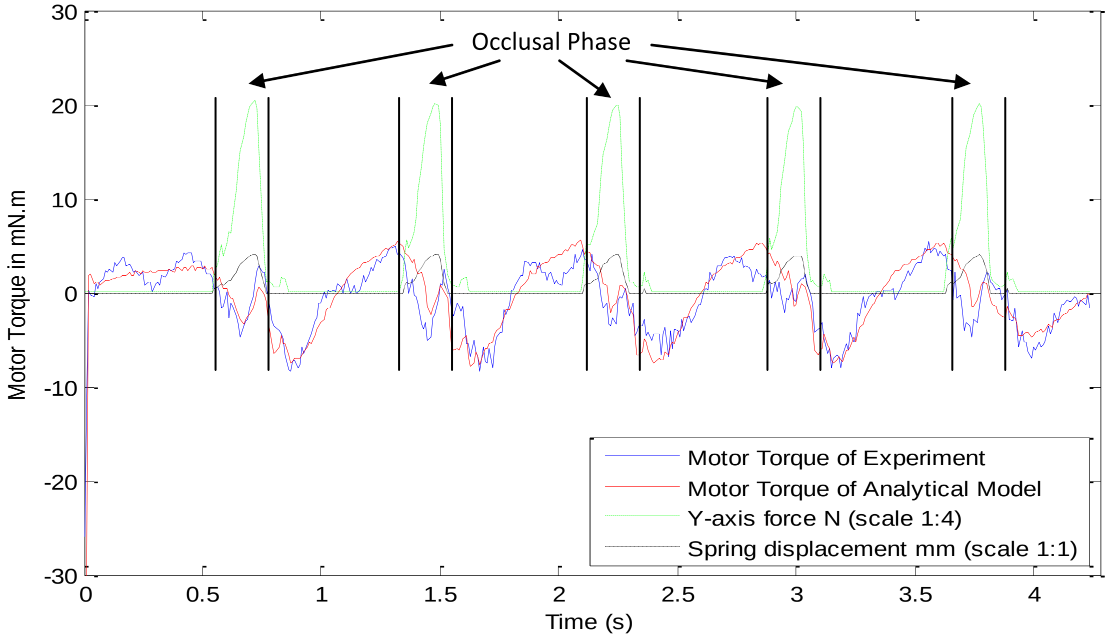

Figure 4.48 Motor torque compared between experiment #8 and analytical model. The bottom teeth are raised up for 4mm for food resistance.

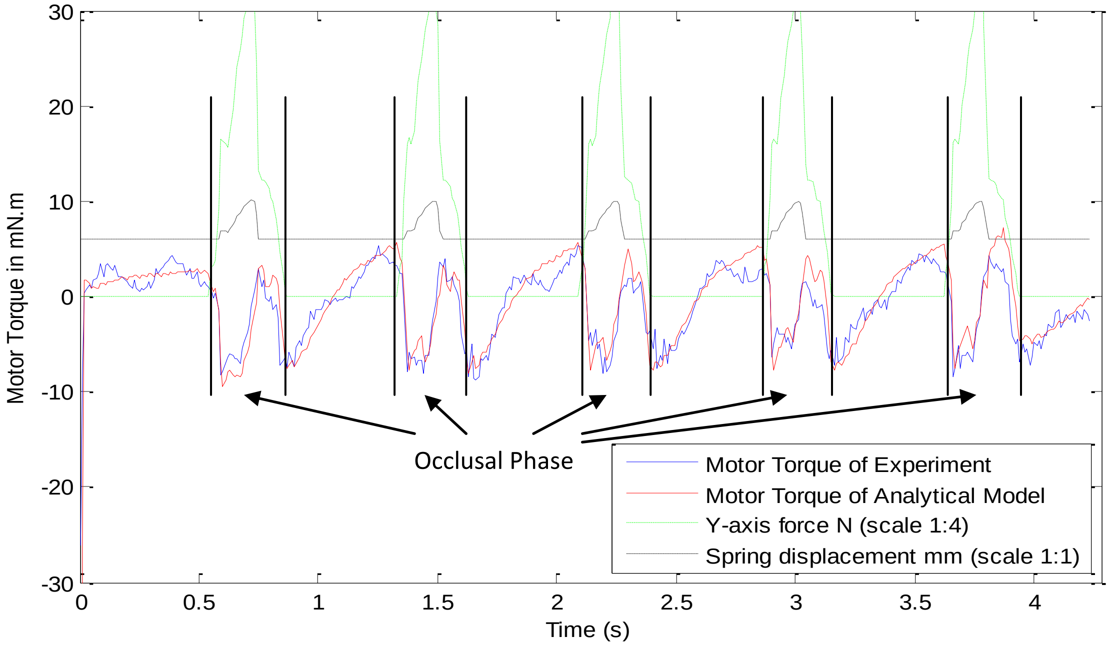

Figure 4.49 Motor torque compared between experiment #9 and analytical model. The bottom teeth are raised up for 4mm for food resistance. The spring is pretightened for 6mm.

From Figure 4.43 to Figure 4.49, most simulated torques closely match the experimental torques during occlusal phases. The reason for the simulated torques not well matching may be because the estimated motor efficiency and also the modified spring constant.

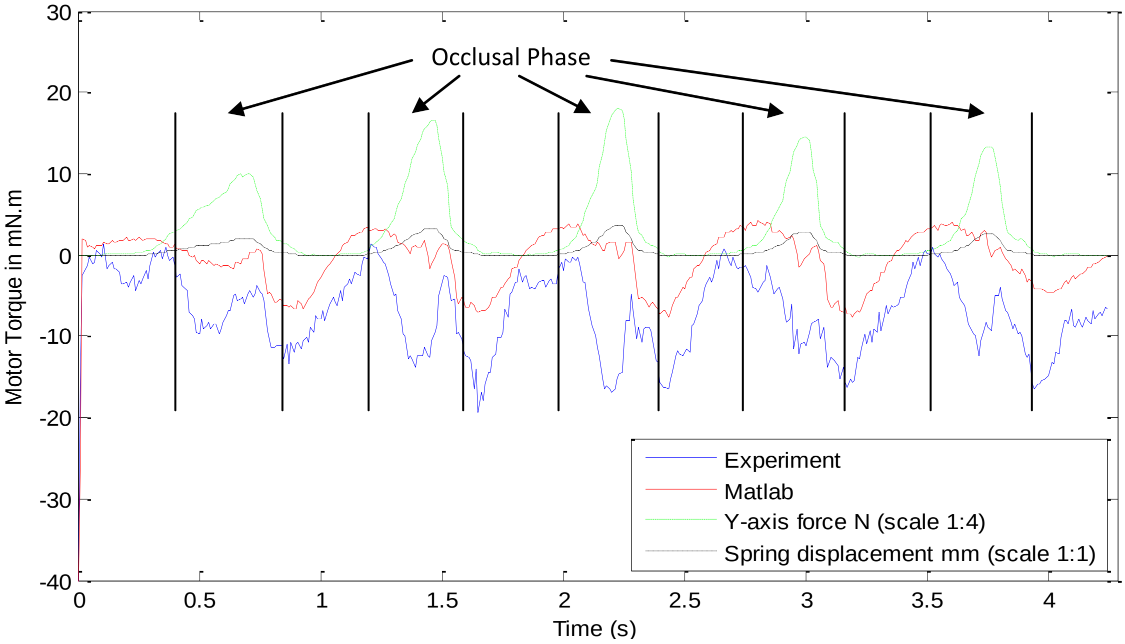

Figure 4.50 Motor torque compared between experiment #10 and analytical model. The Apricot & Pie bar is used as food resistance.

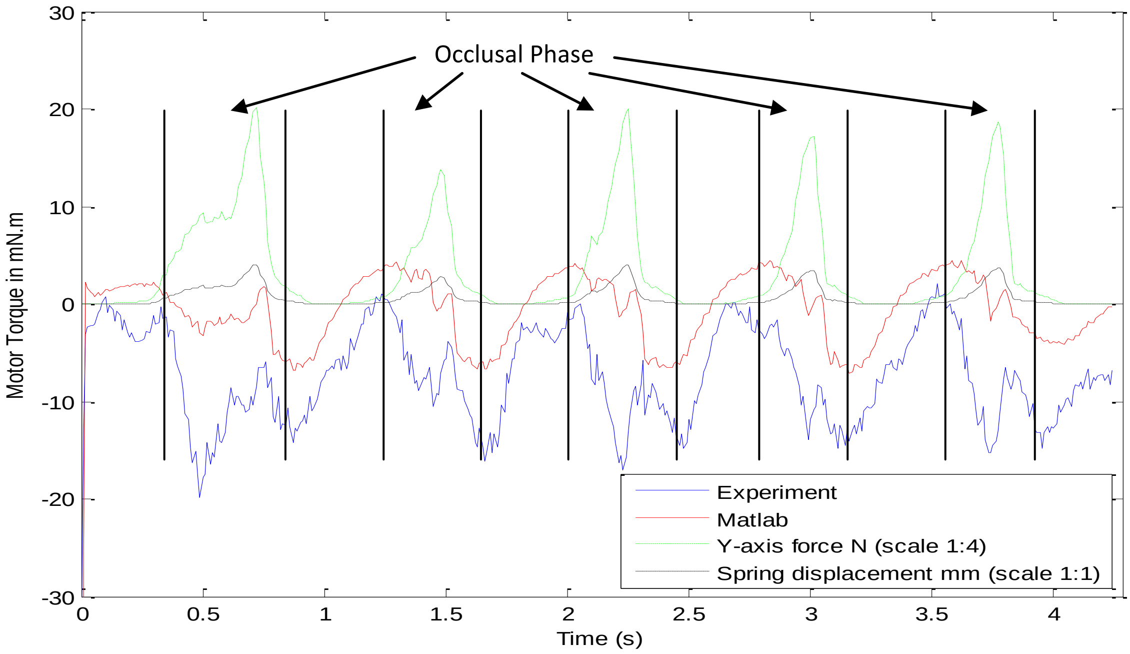

Figure 4.51 Motor torque compared between experiment #11 and analytical model. The Crunchie bar is used as food resistance.

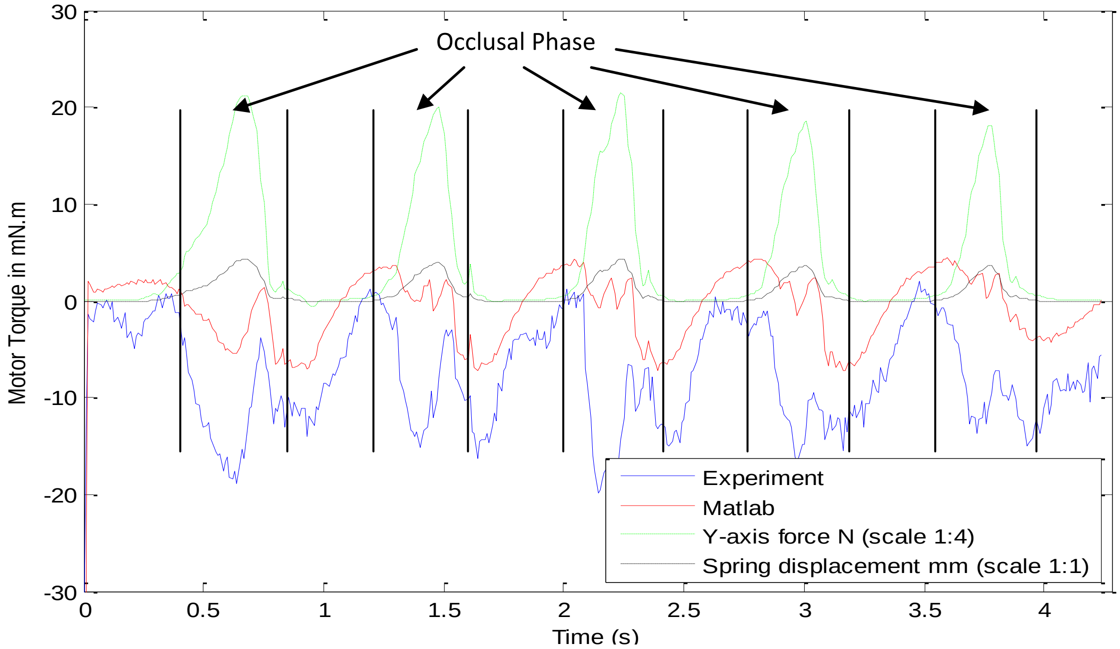

Figure 4.52 Motor torque compared between experiment #12 and analytical model. The Fruit & Nut bar is used as food resistance.

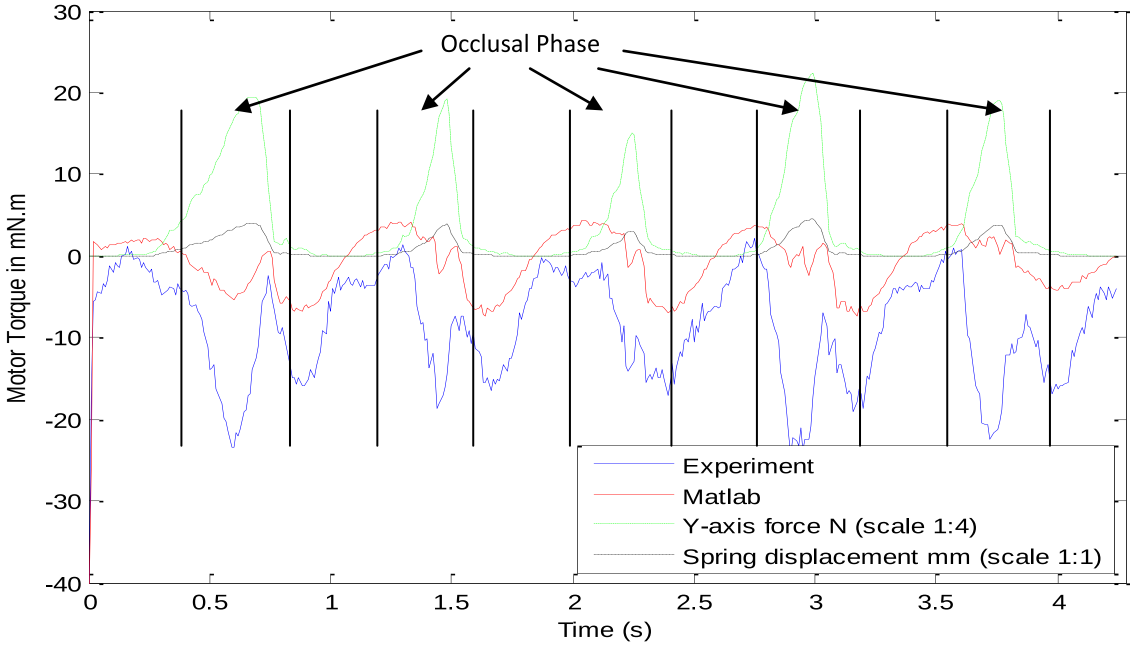

Figure 4.53 Motor torque compared between experiment #13 and analytical model. The Moro bar is used as food resistance.

From Figure 4.51 to 4.53, the simulated torque cannot match the torque of real food experiment during occlusion. The reason is because the calculated spring displacement according to the force sensor is not correct. The force sensed from the force sensor is not the total spring compression force. The food might absorb certain forces for its breakage during mastication. Therefore, the estimated total spring force might be equal to the force breaking the food and the force from the force sensor.

## *4.5. Food Model Simulation*

Food simulation models are required for validating the closed loop compliance control in MATLAB simulation. The food models will generate a force profile during chewing which is used as the feedback force for the compliance control. Therefore, commonly used force vs. deformation profiles of the foods in food industry need to be obtained. These profiles are generated by using the Instron Texture Analyzer. In this section, two types of food models, marshmallow and peanut, have been created to be used for the validation of the chewing robotic system. Marshmallow is a typical food representing the concave force-deformation curve types of food, which include hot dog, cheese and etc (Swyngedau, Normand, et al., 1991). Peanut is a good example to represent crunchy food which fractures during chewing.

### 4.5.1. *Marshmallow Modeling*

***Force-deformation profile***

Pascall-branded marshmallows have been selected, since their shapes are column-shaped and easy for the compression experiments. The marshmallows are chosen to have a height of 20mm and a diameter of 10mm. The compression head in the Instron Texture Analyser is selected to be a round flat-bottom plate with a diameter of 15mm. The compression speed is set to be constant 40mm/min. The flat side of the marshmallow is placed on the machine. The compression experiments have been repeated for 10 times. The force vs. deformation profiles of ten marshmallows have been plotted in Figure 4.54. From this figure, it is found that the marshmallows have similar force profiles. For example, before 12mm of deformation, the compression force in the profile is very small (less than 20N). From 12mm to 18mm of deformation, the compression force increases dramatically to 160N. An average force profile of the ten marshmallows has been generated to be the reference profile for the food model.

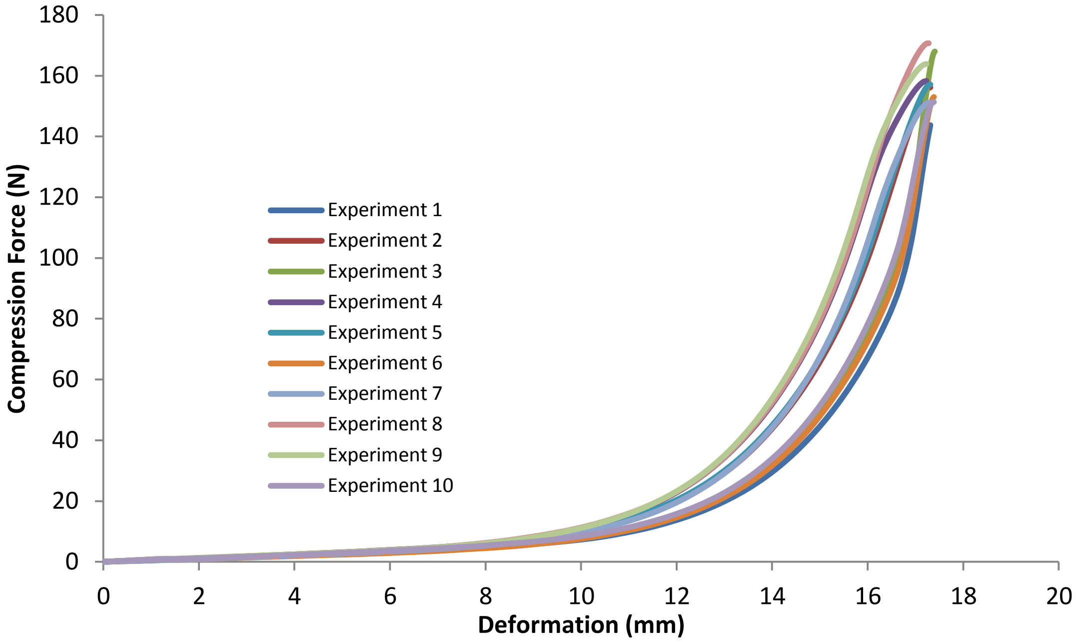

Figure 4.54 Force vs. deformation profile from Instron Texture Analyzer

### *Food Rheological Model*

A general mathematical model (Equation 4) has been given to represent the force vs. deformation profile of the visco-elastic foods, like marshmallows (Peleg & Campanella, 1989).

$$F = K(\Delta H)^n \tag{4}$$

Curve fitting method is used to find out the parameters in the equation. The reference force vs. deformation profile has been entered into the curve fitting toolbox in MATLAB. Least squares method in the MATLAB curve fitting toolbox was used to obtain the parameter K and n in (Equation 4). The mathematical model with known parameters is obtained from the curve fitting toolbox (Figure 4.55). The curve fitting result shows that the mathematical model fits the force profile of marshmallow very well with the R-square factor of 0.9976. Figure 4.56 shows that between 4mm and 10mm of deformation, the force profile from the mathematical model is slightly smaller (less than 4N) than the original profile from the experiment. From 12mm of deformation onwards, the predicted force profile from the model is almost identical to the real force profile. In the next section, the mathematical model from curve fitting is built in the MATLAB.

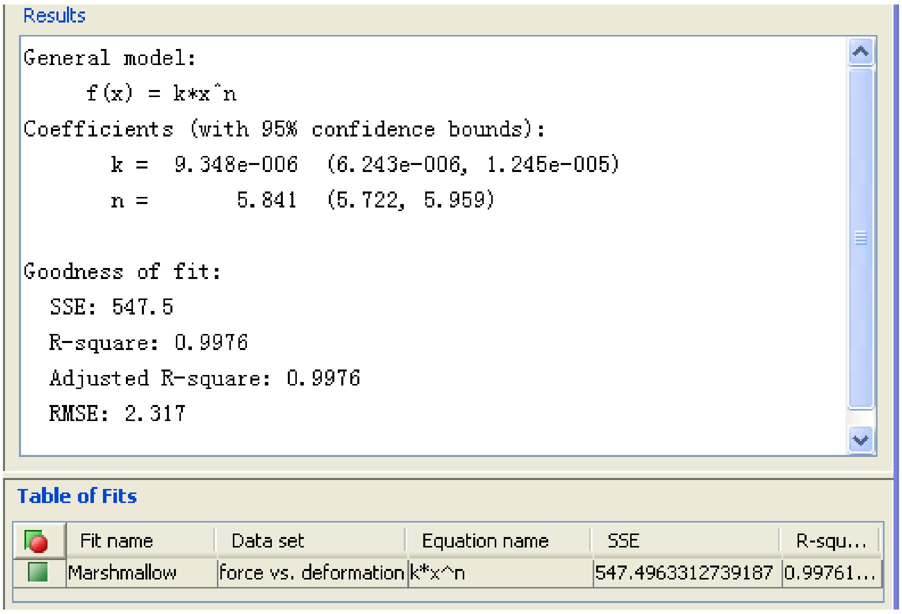
Results

```
General model:
     f(x) = k*x^n
Coefficients (with 95% confidence bounds):
       k =   9.348e-006  (6.243e-006, 1.245e-005)
       n =        5.841  (5.722, 5.959)

Goodness of fit:
  SSE: 547.5
  R-square: 0.9976
  Adjusted R-square: 0.9976
  RMSE: 2.317
```

Table of Fits

| | Fit name | Data set | Equation name | SSE | R-squ... |
|---|---|---|---|---|---|
| 🟩 | Marshmallow | force vs. deformation | k*x^n | 547.4963312739187 | 0.99761... |

Figure 4.55 Curve fitting results from Matlab Curve Fitting Toolbox

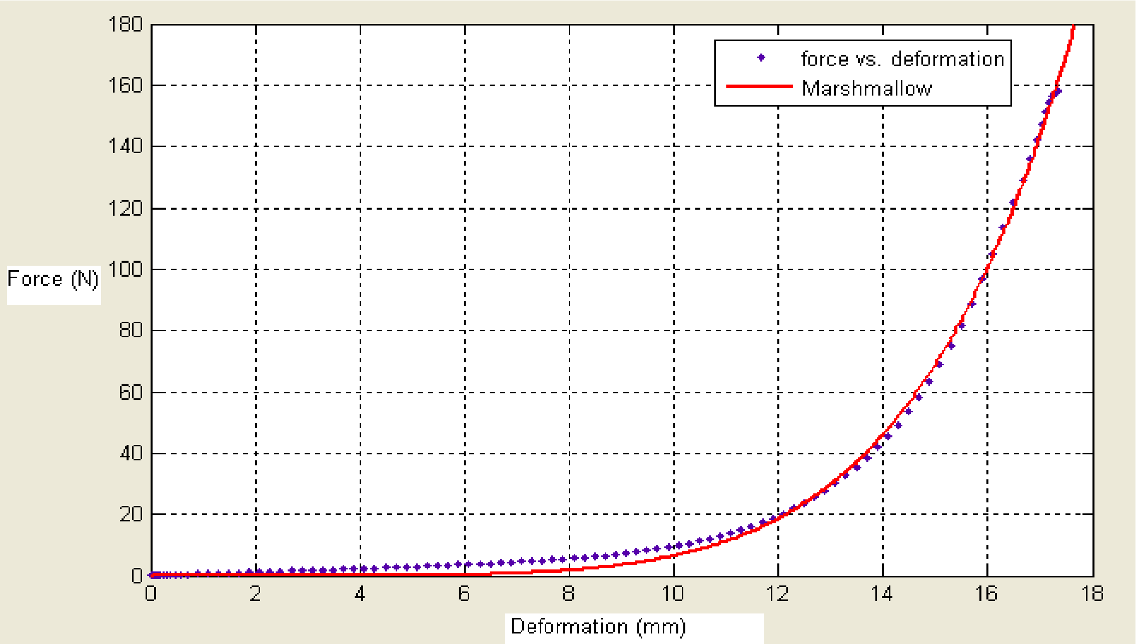

Figure 4.56 Curve fitting result for the force profile of Marshmallow

***Simulation Model***

The marshmallow simulation model of force vs. deformation profile is built in SIMULINK, as shown in Figure 4.57. This model is integrated and interacted with the spring-mass system in the chewing robot model. When the marshmallow is chewed in the chewing robot, the deformation of the spring in the upper teeth also varies with the force applied. Therefore, the total compressed deformation from the initial food contact location to the compressed distance is the product of the deformation of the food and the deformation of the spring. The deformation of the marshmallow is the subtraction of the spring deformation from the total. The simulation results of marshmallow is shown in Figure 4.58.

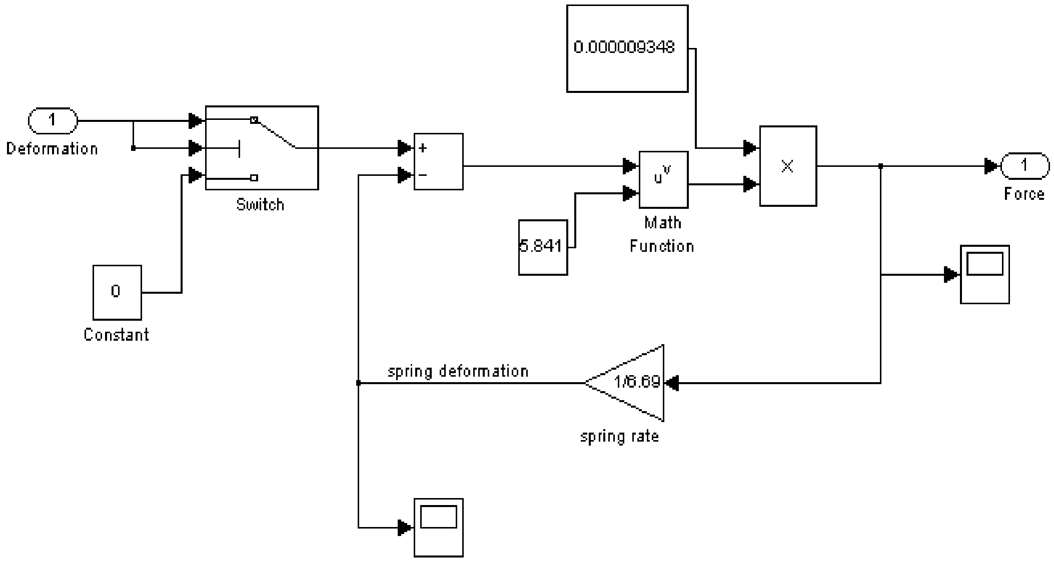

Figure 4.57 Marshmallow simulation model in Matlab

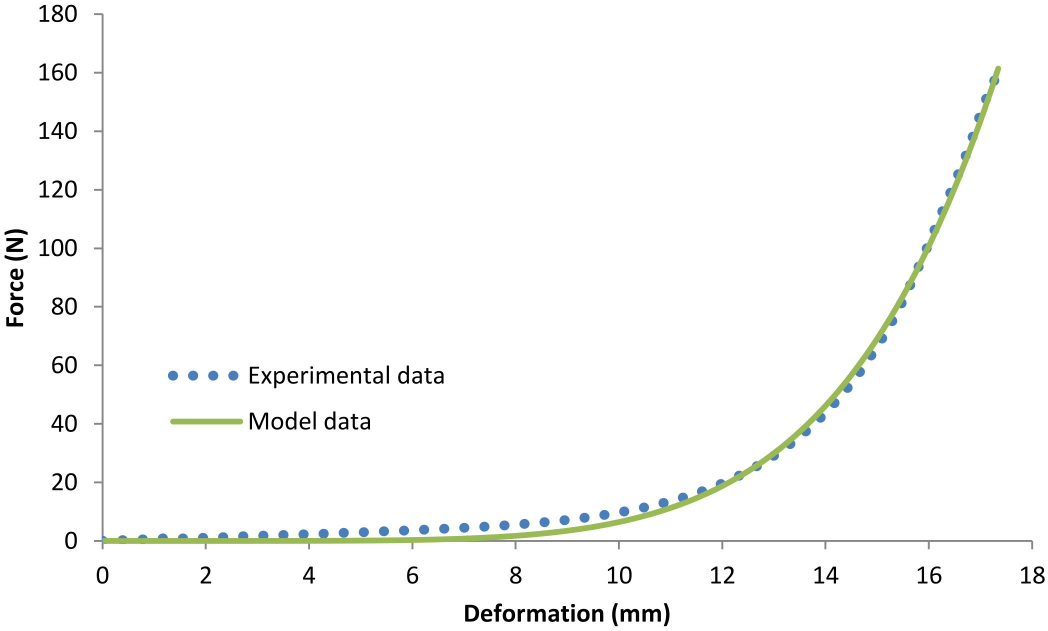

Figure 4.58 Marshmallow's force-displacement profile generated by the model (solid line) and the experiment (dotted line)

### 4.5.2. ***Peanuts Modeling***

***Force-deformation profile***

Several compression experiments on unsalted roasted peanuts (Parkin'Save, NZ) in Instron Texture Analyzer have been carried out to find out the force vs. deformation profile. One whole peanut with around 1g of weight has been selected to be the food sample. The compression head in the Instron Texture Analyser is selected to be a round flat-bottom plate with a diameter of 15mm. The compression speed is set to be constant 40mm/min. The compression experiments have been replicated for five peanuts. The experiment data of force and deformation were measured and plotted in the following five figures (Figure 4.59). From the compression results of the five different peanuts, it is found the five force profiles all have zigzag shapes due to the fracture occurring in peanuts. However, these fracture points are not at the same deformation, and actually randomly exist. This can be easily explained that no peanuts are identical. Therefore, a simulation model to reproduce the same force profile of one of the peanuts (first peanut in Figure 4.59) is created.

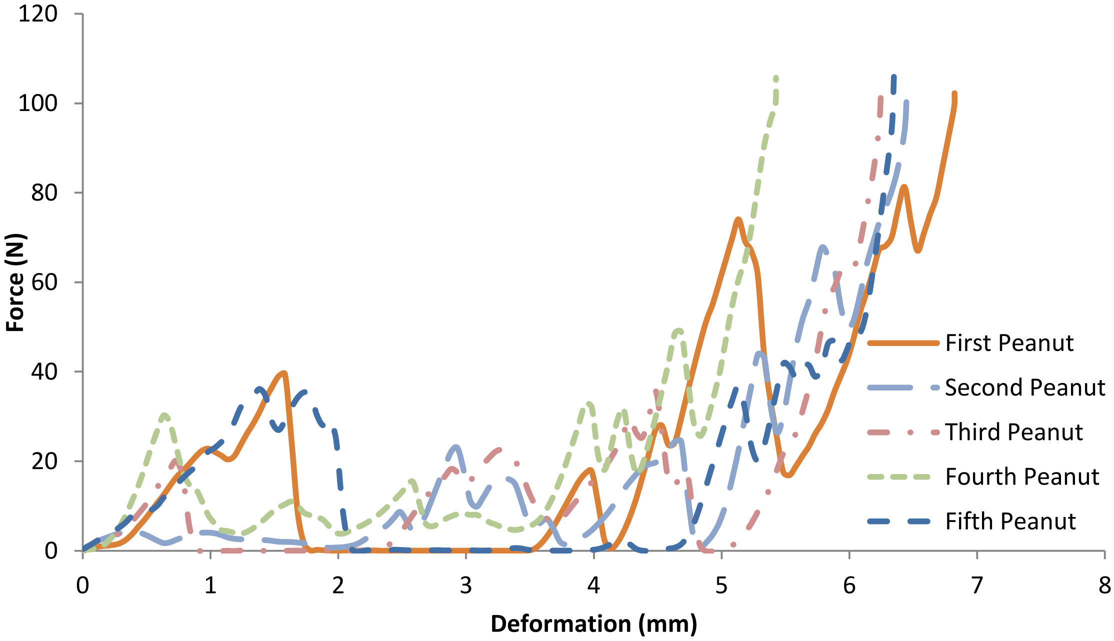

Figure 4.59 Force vs. deformation profiles from the compression experiments on five whole peanuts

### *Food Rheological Model*

In the literature, a general element including fracture element has been introduced to describe the behavior of solid food under compression. The general element is composed of one spring, one damper and two critical force points. The general element is elastic, when the force is smaller than the two critical forces. Once the smaller critical force is reached, the damper of the general element is activated and in series with the spring. This makes the general element viscous. After the bigger critical force is reached, the general element breaks. The force exerted from the general element will disappear.

### *Simulation Model*

The simulation model of a general element is created in Matlab and shown in Figure 4.60. The model consists of a spring and a damper. The two critical force thresholds are realized by using If…Then rules. The parameters of the spring, damper and two critical forces can be adjusted through the mask of the model (Figure 4.61). A total of thirteen general elements have been created to reproduce the force vs. deformation profile of the peanut in the first chewing cycle, as shown in Figure 4.62. Each general element determines whether it’s elastic or maxwellian by comparing the input force with its two critical force thresholds. The input force is determined by the product of the deformation and the spring rate in the general element. The output forces of all the general elements then merges together to generate the force profile of the peanut model. Figure 4.63 shows that the force profile generated by the simulation model matchs the force profile from the real experiment very well.

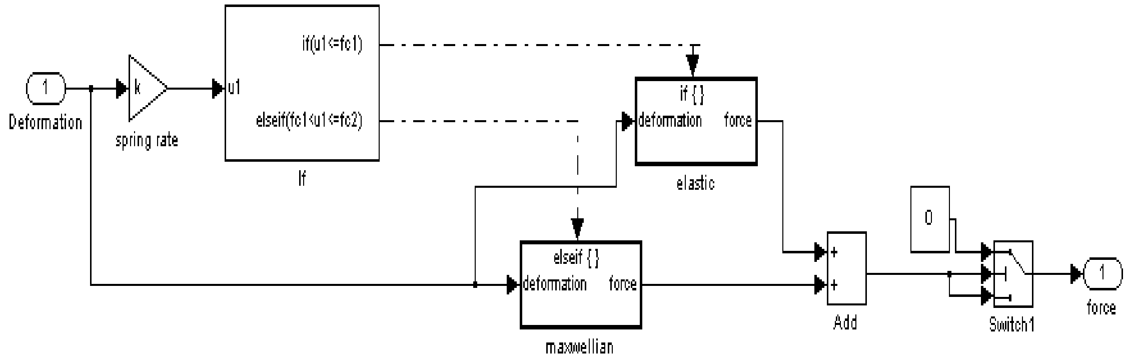

Figure 4.60 Simulation model of a general element

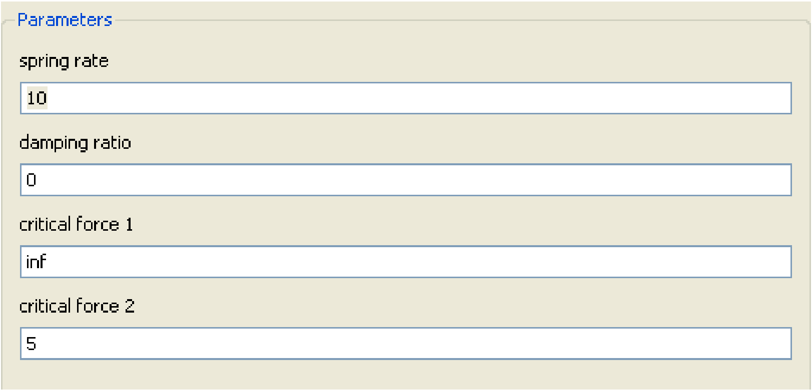
Parameters

spring rate

10

damping ratio

0

critical force 1

inf

critical force 2

5

Figure 4.61 Adjusted parameters for the general element

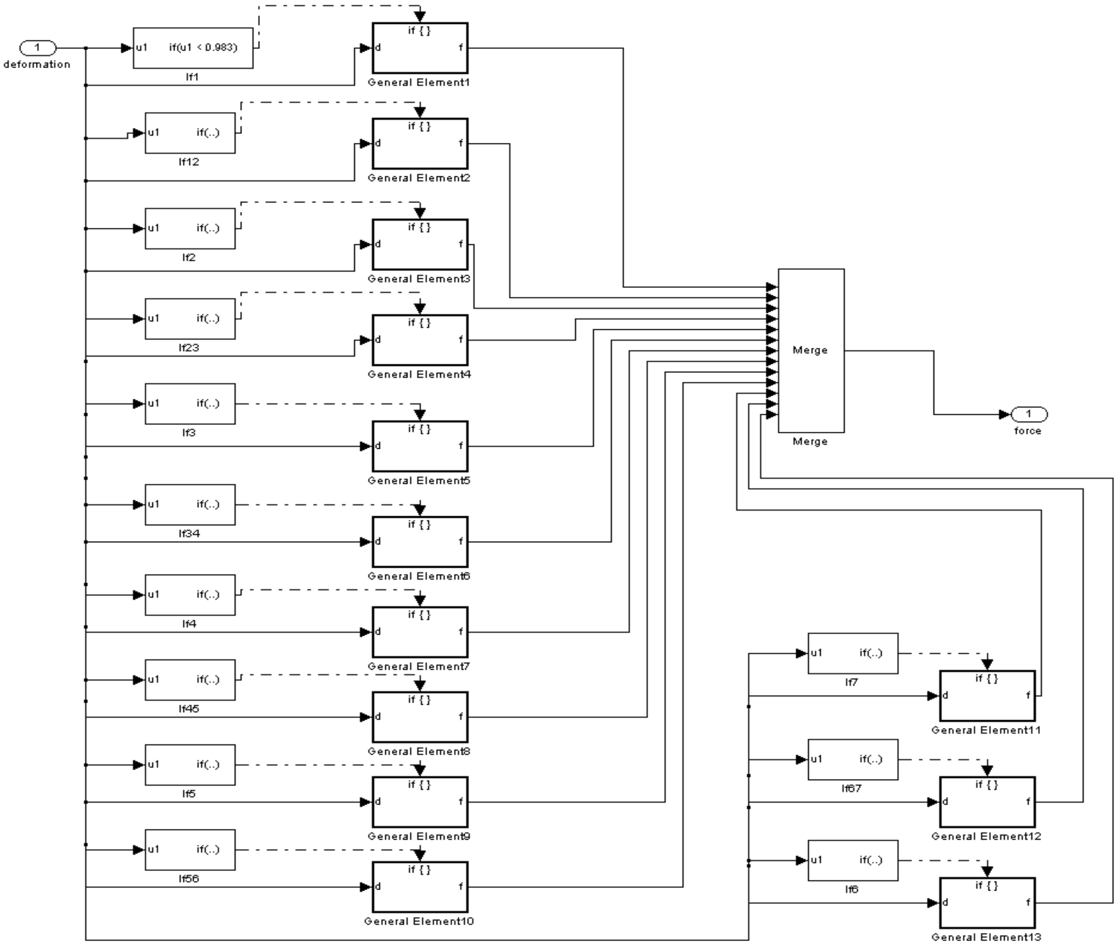

Figure 4.62 A complete model of peanut including 13 general elements

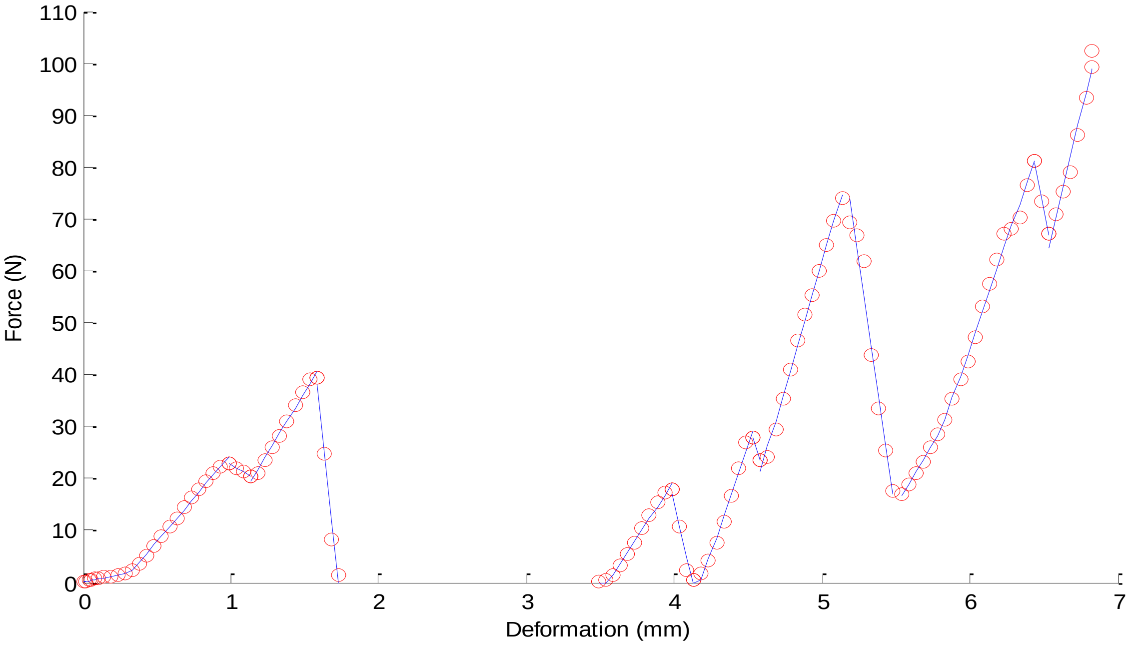

Figure 4.63 Peanut's force-displacement profile generated by the model (solid line) and the experiment (circled)

## *4.6. Chapter Conclusion*

The kinematics and dynamics of the simplified linkage mechanism of the chewing robot have been analyzed. To validate the simplified analytical model, the simulation results of the analytical model are compared with the results from the SolidWorks model of the original linkage mechanism. The comparison results show that the analytical model of chewing mechanism under the assumptions can correctly simulate the kinematics and dynamics of the real chewing mechanism. A SimMechanics model of the linkage mechanism based on the simplified analytical model has been developed. In order to modify the analytical model to simulate the chewing machine in real environment, the driving torques between the analytical model and experimental data are compared. The results show that the analytical model is possible to simulate the driving torque from the experimental data, especially when the food thickness is assumed constant (in the situation of raised bottom teeth as food resistance).

A simulation model of motor control in the chewing robot has been built in Matlab. The dynamics of the spur gear in the chewing robot and the gear box in the DC motor are analyzed. The motor control algorithms in the Maxon motor control card are built in Simulink. The PI parameters in the motor control are tuned to give the optimized performance.

The food simulation models of marshmallow and peanut are developed. The force vs. deformation profiles of both foods were obtained from the Instron Texture Analyser under compression experiments. The food models are able to produce the similar force profiles compared with the profiles from the real food. The food models will be integrated into the chewing robot models, which include motor model and linkage mechanism model, to create a complete chewing robot simulation environment. The complete integrated model will be used to validate the adaptive fuzzy control.

# *5. ADAPTIVE FUZZY CONTROL*

## *5.1. Introduction*

The chewing robot that was previously developed at Massey University used a fixed velocity profile regardless of the food being chewed. The velocity profile is composed of an open/close phase and an occlusion phase. However, according to the literature (K. Anderson et al., 2002), human chew food with a different velocity depends on the texture of the foods. In general, the harder the food texture, the larger the chewing velocity. Therefore, based on this point, a compliance control method to adapt the food texture changed during mastication based on the adaptive fuzzy controller is proposed and developed to control the chewing robot to chew food like human. In the following sections, the design of adaptive fuzzy control is described. The simulation model of adaptive fuzzy control is built in MATLAB and implemented into the complete model of chewing robot which is mentioned in the previous chapter. Simulation results with “chewing” the marshmallow model and peanuts model are given and analysed. The chewing control software in LabView has been upgraded with the adaptive fuzzy control integrated into the system.

## *5.2. Design of Adaptive Fuzzy Control*

### 5.2.1. *General Description*

The complete chewing robot control system consists of velocity control system, DC motor, linkage mechanism, spring system, food model and the adaptive fuzzy control system as shown in Figure 5.1. The fuzzy controller acquires the angular velocity of the crank link in the linkage mechanism and chewing force generated from the food model to output a desired chewing velocity through the fuzzy rules. The fuzzy adaptation mechanism acquires the vertical velocity of the link attached to the upper teeth in the linkage mechanism and the chewing force rate on the food model to generate the food texture index. The desired chewing velocity from the fuzzy controller adapts to the texture of the food by multiplying the food texture index to create the adapted chewing velocity.

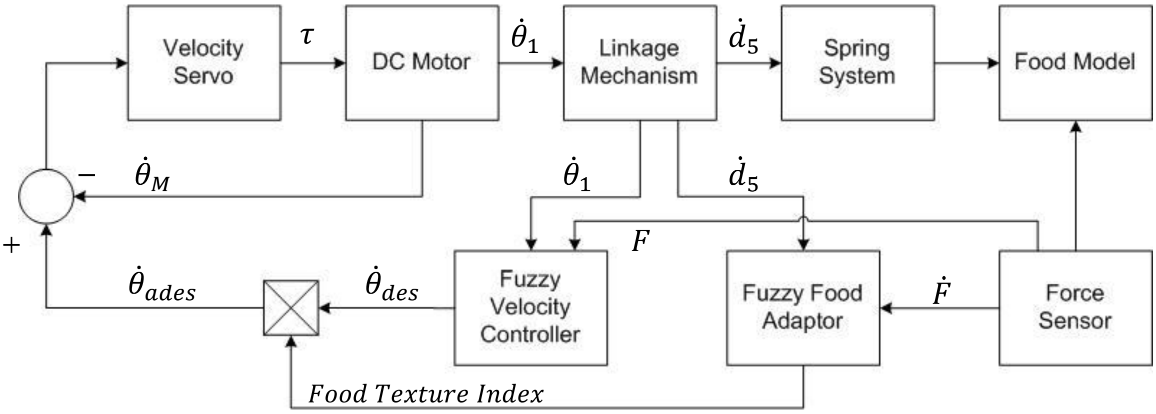

Figure 5.1 Compliance control system for the chewing robot

### 5.2.2. *Velocity Fuzzy Controller*

The fuzzy controller is developed to generate the desired velocity based on two inputs, the angular velocity and the chewing force applied on food. The range of the input variable ‘force’ is selected according to the range of the chewing forces applied by human. The ranges of the input variable ‘velocity’ and the output variable ‘desired velocity’ are determined by the actual velocity. The fuzzy rules and membership functions for the force, velocity and desired velocity are shown in Figure 5.2. In order to determine the desired velocity, If-Then clauses are used and converted into a table as given in Table 5-1.

The number of membership functions for each variable is five triangle subsets denoted as small (S), medium small (MS), medium (M), medium big (MB), and big (B). The range of chewing force input is between 0N and 150N (Figure 5.2a). This covers the force range on a molar teeth measured by Anderson (1956). The range of the human chewing velocity is from 0.6 seconds per cycle to 1.2 seconds per cycle depends on the chewed food. Therefore, the range of velocity input for the crank link of linkage mechanism is selected between 200 degree/sec and 600 degree/sec (Figure 5.2b). The range of velocity output is between 200 degree/sec and 600 degree/sec (Figure 5.2c). The fuzzy interference system is mamdani. Fuzzy inference methods are “min” for AND, “max” for OR, “min” for fuzzy implication, “max” for fuzzy aggregation, and “centroid” for defuzzification.

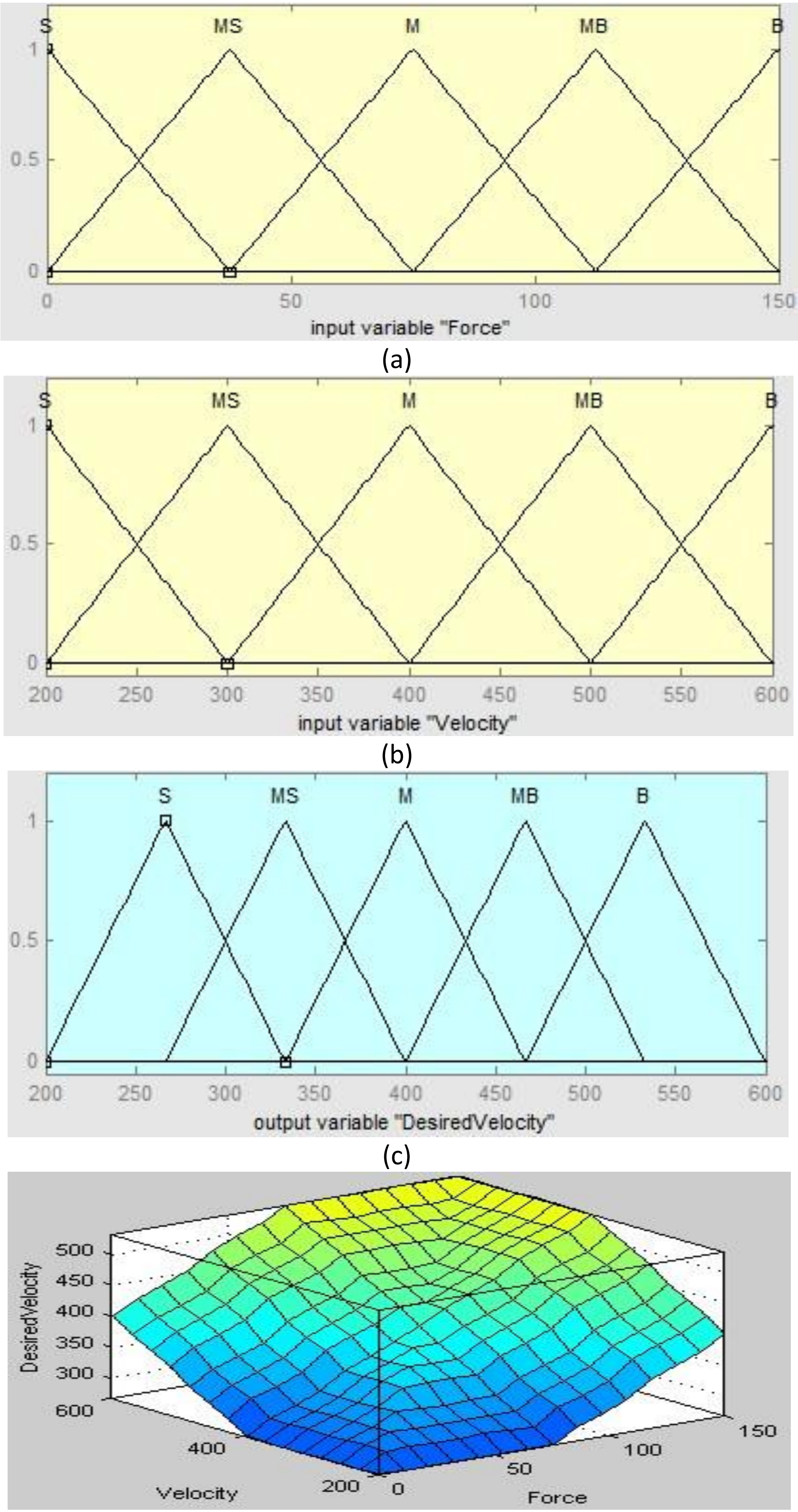

(a)

(b)

(c)

(d)

Figure 5.2 Fuzzy rules membership functions of force (a), velocity (b) and desired velocity (c) and surface view (d)

In the fuzzy rules of the fuzzy velocity controller, the higher the chewing force, the higher the desired velocity compared with the current velocity. The smaller the force, the smaller the desired velocity compared with the current velocity. When the force is medium, the desired velocity remains in the same range of the current velocity.

Table 5-1 Fuzzy rule assignment table for fuzzy velocity controller

| **Velocity** | **Force** | | | | |
|---|---|---|---|---|---|
| | S | MS | M | MB | B |
| S | S | S | S | MS | M |
| MS | S | MS | MS | M | MB |
| M | S | MS | M | MB | B |
| MB | MS | M | MB | MB | B |
| B | M | MB | B | B | B |

### 5.2.3. *Fuzzy Adaption Mechanism*

The fuzzy adaption mechanism is designed to determine the food texture index based on two inputs, the vertical velocity and the rate of force. The food texture index indicates the relative hardness of the food. For hard food, the food texture index will be a higher value (larger than 1) in the range defined in the membership function. For soft food, the food texture index will be a smaller value (smaller than 1). The food texture index will multiply the desired velocity from the fuzzy controller to give an adapted velocity. The fuzzy membership functions for the vertical velocity, force rate and food texture index and surface view are shown in Figure 5.3. If-Then clauses are displayed in a table as given in Table 5-2.

The number of membership functions for each variable is five triangle subsets denoted as small (S), medium small (MS), medium (M), medium big (MB), and big (B). The range of chewing velocity input is between 200 degree/sec and 600 degree/sec (Figure 5.3a). The range of force rate input is between 0 N/sec and 1000 N/sec (Figure 5.3b). The range of index output is between 0.75 and 1.25 (Figure 5.3c). The fuzzy interference system is mamdani. Fuzzy inference methods are “min” for AND, “max” for OR, “min” for fuzzy implication, “max” for fuzzy aggregation, and “centroid” for defuzzification.

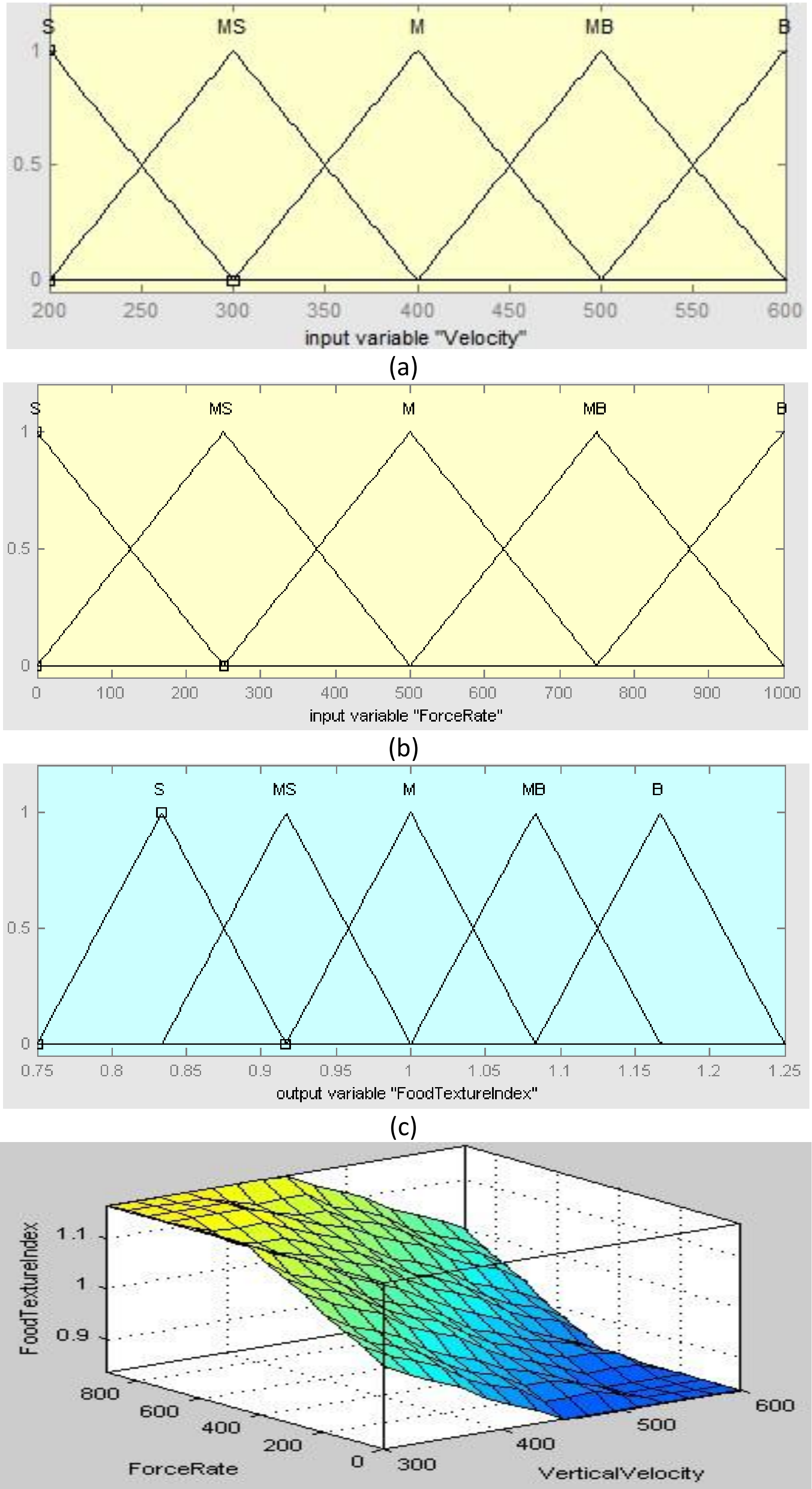

(a)

(b)

(c)

(d)

Figure 5.3 Fuzzy rules membership functions of vertical velocity (a), force rate (b) and food texture index (c) and surface view (d)

In the fuzzy rules of the fuzzy adaption mechanism, when the force rate is small, the higher the vertical velocity, the smaller the food texture index and the softer the food. When the force rate is large, the smaller the vertical velocity, the bigger the food texture index and the harder the food. When both the force rate and the vertical velocity are equally large or small, the food texture index is relatively medium.

Table 5-2 Fuzzy rule assignment table for fuzzy adaption mechanism

| **Force Rate** | **Vertical Velocity** | | | | |
|---|---|---|---|---|---|
| | S | MS | M | ML | L |
| S | M | MS | S | S | S |
| MS | ML | M | MS | S | S |
| M | L | ML | M | MS | S |
| ML | L | L | ML | M | MS |
| L | L | L | L | ML | M |

### 5.2.4. ***Simulation of Adaptive Fuzzy Control***

The complete model simulated in Matlab is shown in Figure 5.4. In the simulation, the adaptive fuzzy control system is disabled unless the chewing force is detected during chewing. The initial chewing velocity is set to constant 300 degree/sec. In the simulation model, the motor model subsystem consists of the DC motor model and the velocity control system. The motor model subsystem first acquires the velocity command from the fuzzy controller and outputs the motor velocity command to drive the linkage mechanism. The linkage mechanism model then output the velocity of the link attached to the upper teeth. The spring hard stop system and the food model are integrated into the food model subsystem. The food model subsystem generates the force, the force rate and the vertical velocity to feed into the fuzzy control system. The adapted fuzzy control subsystem includes the fuzzy velocity controller and fuzzy adaptation mechanism controller, as shown in Figure 5.5.

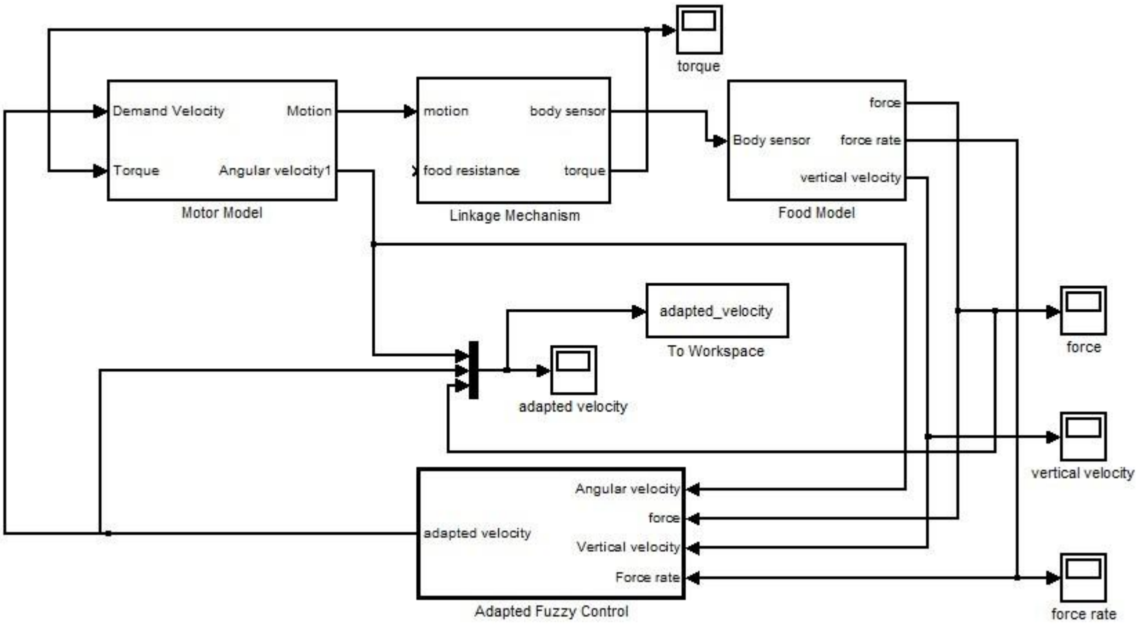

Figure 5.4 Complete simulation model of chewing robot in Matlab

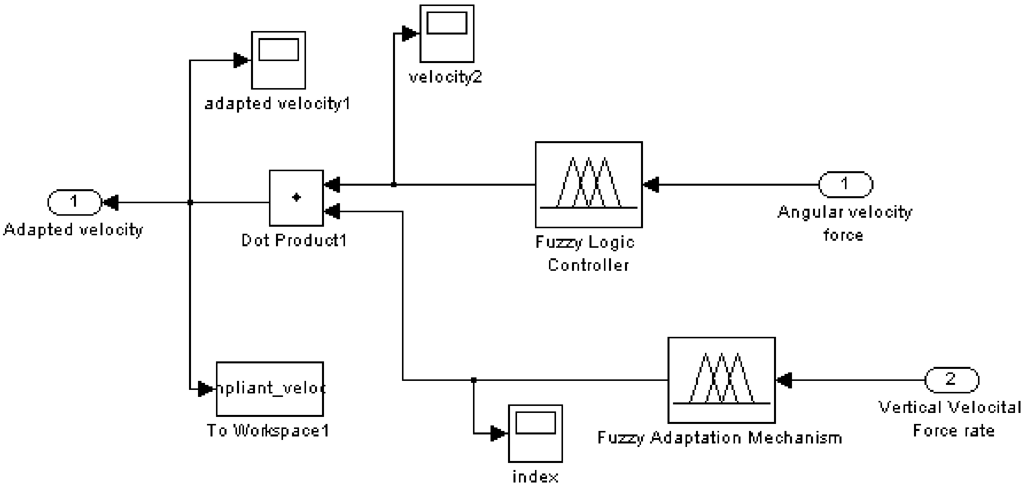

Figure 5.5 Adaptive fuzzy controller model in Matlab

Figure 5.6 shows the adapted desire velocity of the chewing machine with an initial velocity at 300 degree/second. As shown in Figure 5.6, the adapted velocity starts increasing just around 0.4s (after the chewing force occurred) and reaches the maximum value when the chewing force is at the maximum point. The adapted velocity stops changing after the chewing force disappears. The result shows the adaptive fuzzy control enables the chewing machine to adapt the chewing velocity to the change of food properties during chewing of marshmallow model. Figure 5.7 shows the chewing force rate profile with the chewing force. The chewing force rate first starts changing slowly in the beginning, when the marshmallow starts to be compressed (only a small amount of force is detected). As the chewing force increases, the force rate increases rapidly from around 100 N/s to about 500 N/s. This could be explained by the concave-up curve force-deformation profile of the marshmallow. The force rate starts dropping to zero at the maximum chewing force, since the chewing velocity is zero when the teeth occlude with each other. After the occlusion of the teeth, the force rate becomes negative due to the change of the moving direction of the upper teeth. Figure 5.8 shows the chewing velocity and force profile during the mastication of peanut. Figure 5.9 shows the chewing force rate during the mastication of peanut.

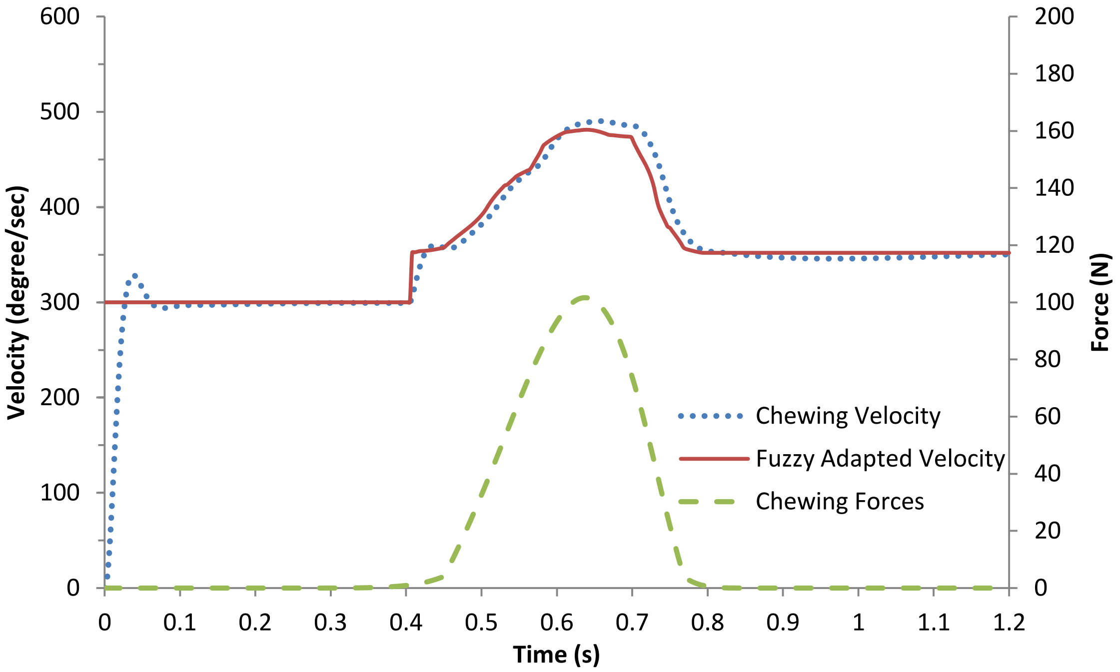

Figure 5.6 Fuzzy adapted velocity of chewing robot with initial velocity 300deg/sec during mastication of marshmallow

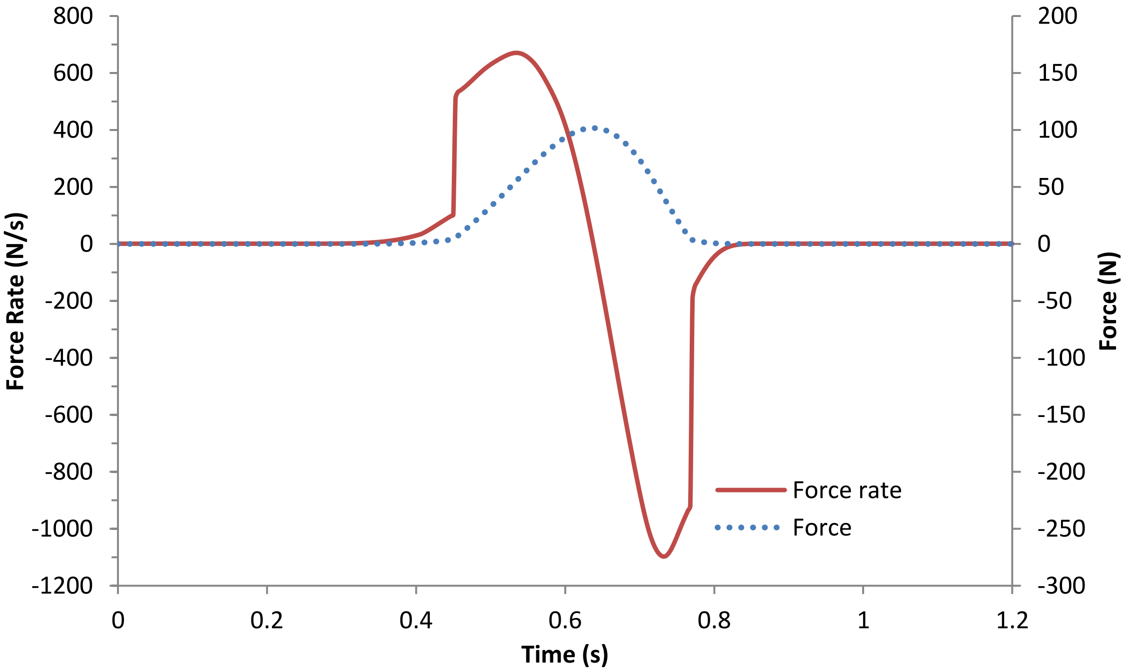

Figure 5.7 Chewing force rate during mastication of marshmallow

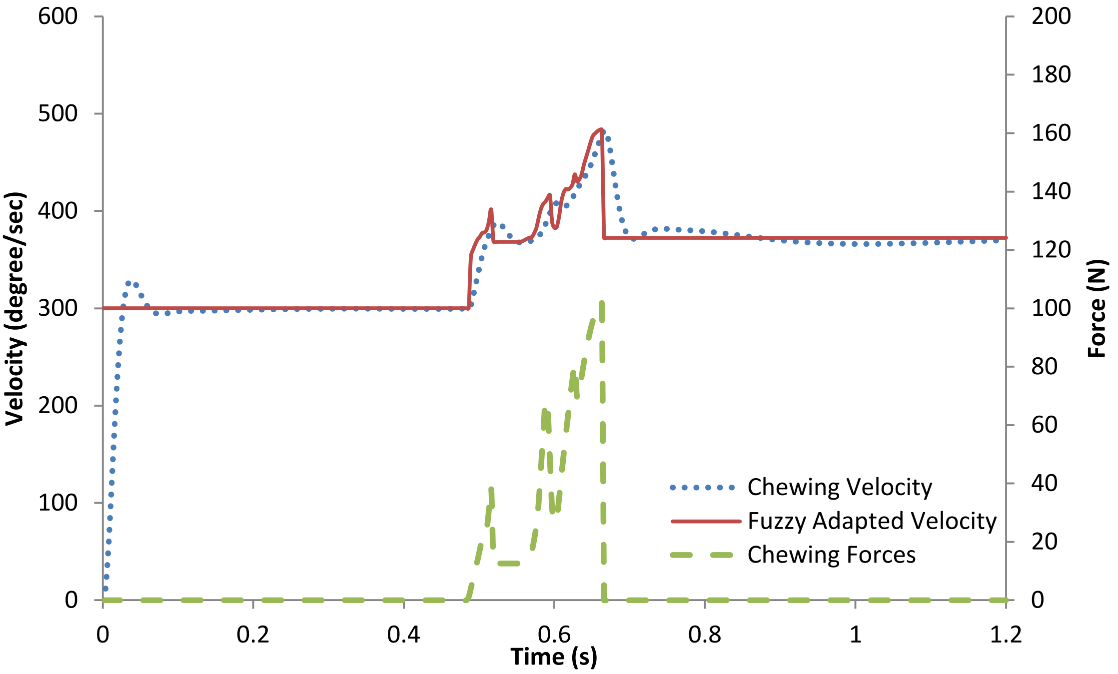

Figure 5.8 Fuzzy adapted velocity of chewing robot with initial velocity 300deg/sec during chewing of peanut

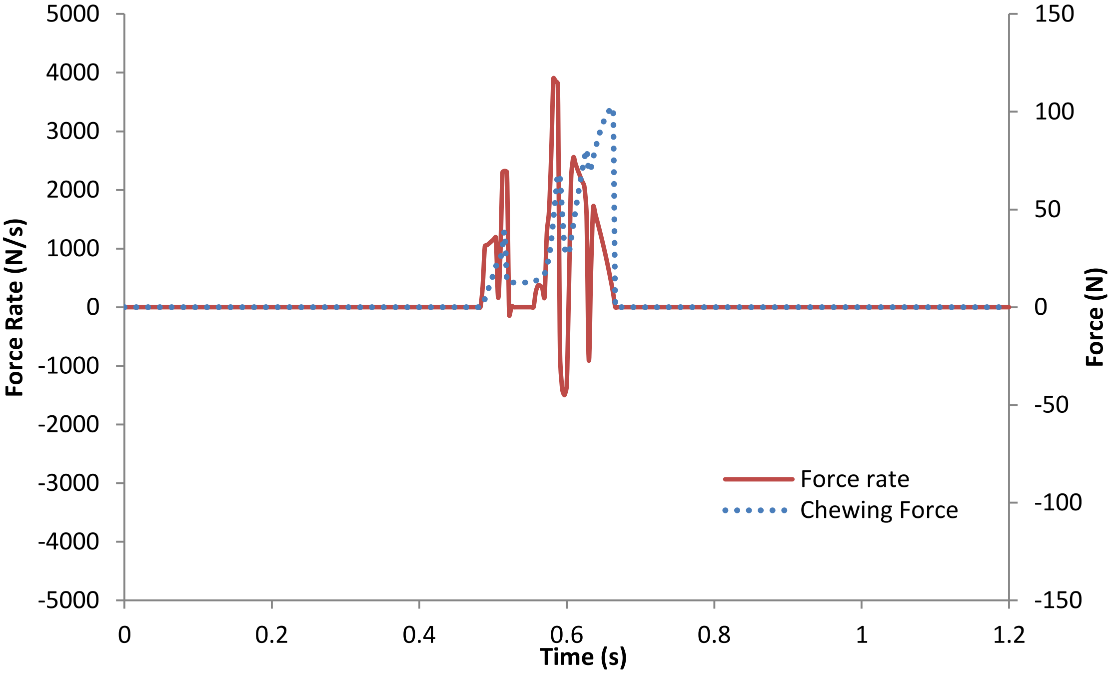

Figure 5.9 Chewing force rate during mastication of marshmallow

## *5.3. Implementation in LabView*

Fuzzy velocity controller and fuzzy adaptation mechanism are implemented by fuzzy system designer in LabView. The membership functions of fuzzy velocity controller are shown in Figure 5.10. The membership functions of fuzzy adaptation mechanism are shown in Figure 5.11.

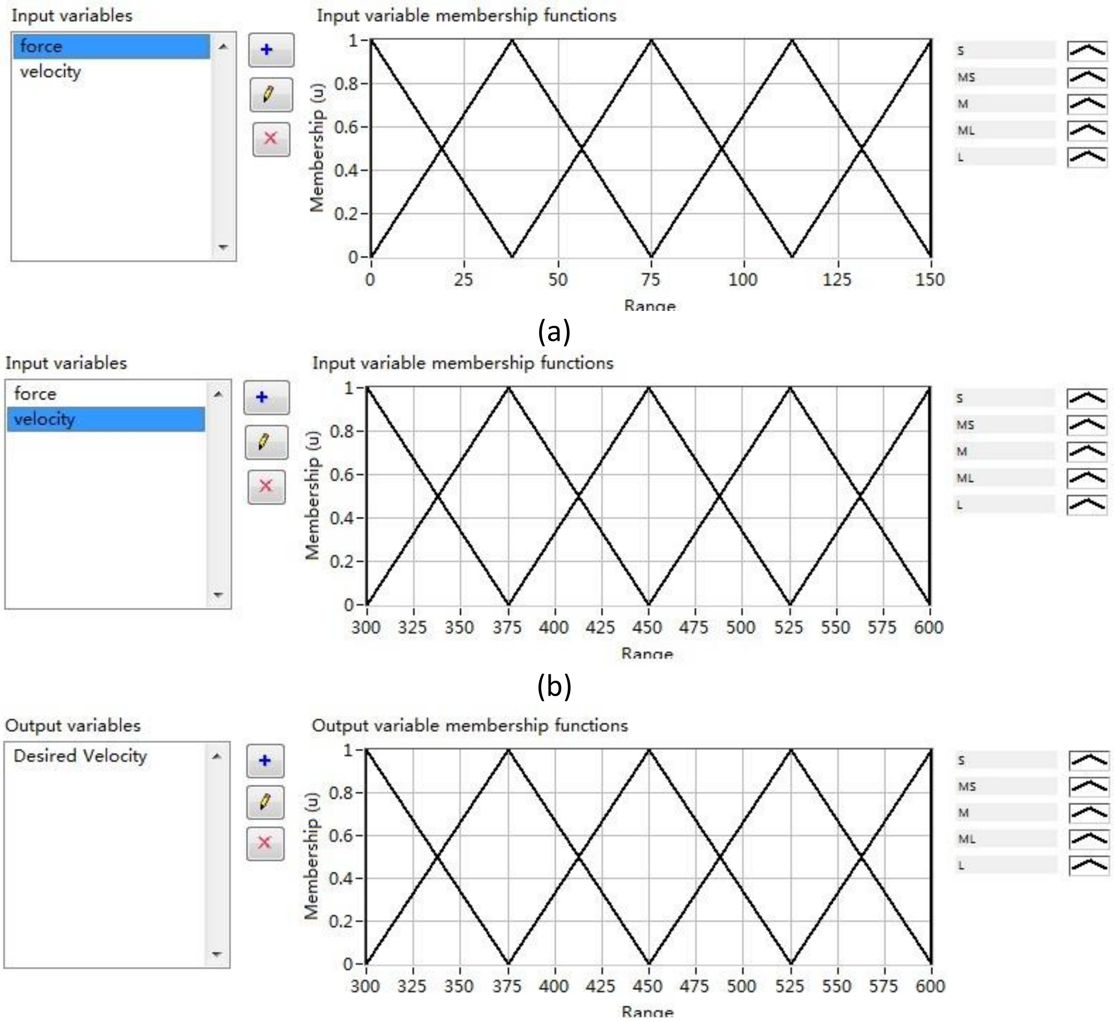

(a)

(b)

(c)

Figure 5.10 Fuzzy velocity controller implemented in LabView: a) force membership function; b) velocity membership function; c) desired velocity membership function

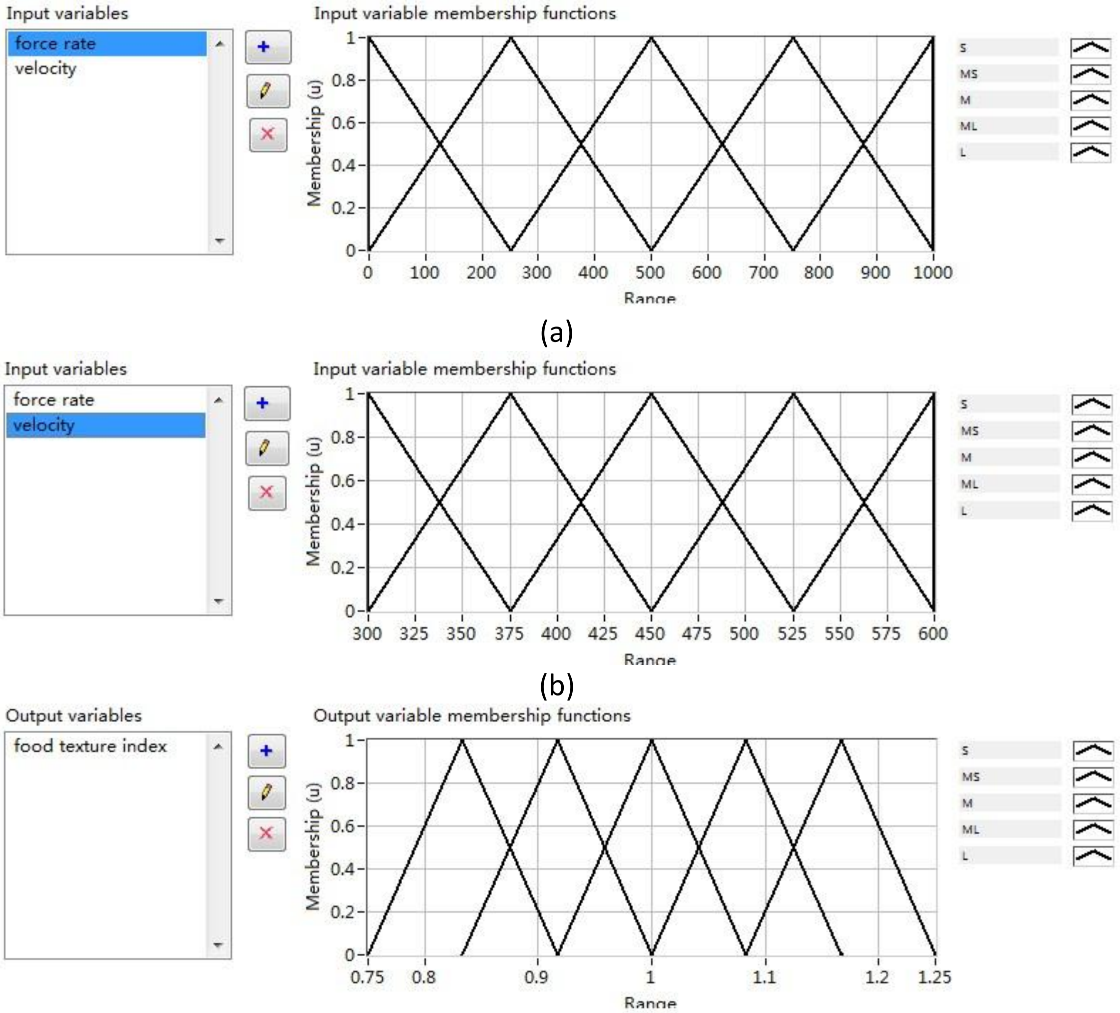

(a)

(b)

(c)

Figure 5.11 Fuzzy adaptation mechanism implemented in LabView: a) force rate membership function; b) velocity membership function; c) food texture index membership function

Figure 5.12 shows the implementation of fuzzy control in the control software of chewing robot in LabView. The fuzzy systems are loaded from the .fs files in the local disk of the computer. FL fuzzy controller VI (MISO) implements a fuzzy logic controller for a multiple-input single-output fuzzy system. Both fuzzy controller Vis are put into a while loop so that the output from the fuzzy controllers are calculated in real time. The adapted velocity is then sent to the motor velocity VI.

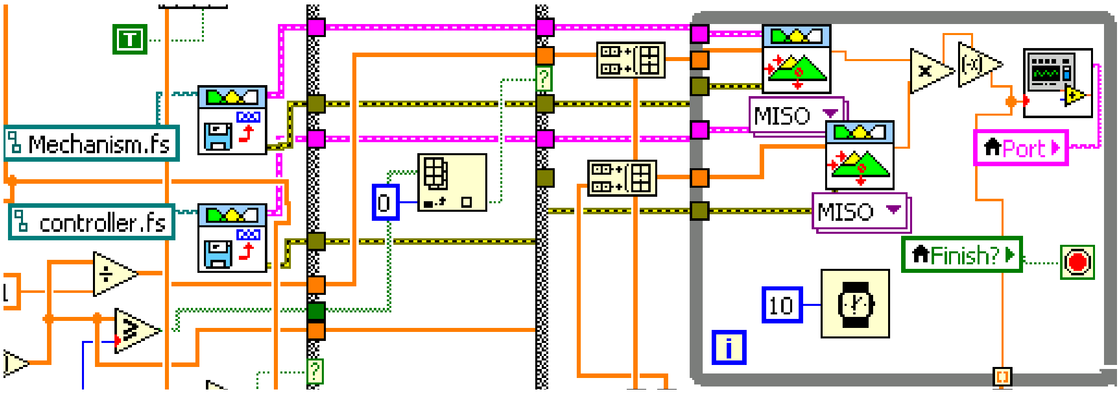

Figure 5.12 Fuzzy control implemented in LabView

## 5.4. Chapter Conclusion

Adaptive fuzzy control was proposed to implement in the chewing robot to achieve compliant force control. The adaptive fuzzy control system consists of one fuzzy velocity controller and one fuzzy adaptation mechanism controller. The adapted chewing velocity is determined by the product of the desired chewing velocity from the fuzzy velocity controller based on the chewing velocity and chewing forces and the food texture index from the fuzzy adaptation mechanism based on the vertical velocity and the chewing force rate. The fuzzy system was simulated in Matlab and integrated into the complete chewing robot system. The simulation results of the chewing robot with adaptive fuzzy control to “chew” the marshmallow model and the peanut model were presented. The simulation results showed that the adapted chewing velocity from the fuzzy control system varies based on the change of the food texture during the “chewing process”. The fuzzy control system was also implemented in the control software of the chewing robot in LabView. The experimental results of the chewing robot integrated with the fuzzy control system to chew the real food were presented and discussed in the next chapter.

# 6. EVALUATION OF CHEWING ROBOT

## 6.1. Introduction

This chapter presents the chewing results from the chewing robot experiment with real food. Firstly, image analysis to analyze the chewing results in terms of particle size distribution (PSD) is developed. This method shows an easy and effective way to process the chewing results. Moreover, the chewing experiments with peanuts are carried out. The chewing force profiles are presented. According to the chewing results of peanuts, the influences of parameters of chewing robot have been found out. Furthermore, the chewing results from chewing robot and human have been compared. The chewing results of chewing robot using compliance control on peanuts and marshmallow have also been presented.

## 6.2. Measurement Methods for Particle Size Distribution

The aim of this experiment research was to find a fast, easy and robust method to obtain the chewing results in particle size distribution and to examine the influence on the chewing results by varying the parameters of the chewing machine.

The tasks of the research were identified to be:

- To find out the chewing results with sieving method
- To find out the chewing results with image processing method
- To find out the effect of varying parameters of the machine on chewing results

### 6.2.1. *Chewing Results with Sieving Method*

Particle size distribution measurement using wet sieving and dry sieving is a common technique (Woda et al., 2006). The evaluation of the bolus can be processed through one sieve or multiple sieves. Single sieving evaluates chewing performance by determine the percentage weight of the bolus that passes through a sieve of a standard mesh size (Van Der Bilt & Fontijn-Tekamp, 2004).

Three different chewing sequences were tested against each other (9, 18, and 27 chews) with five replicates for each sequence. All the parameters of the chewing machine during all the chewing are consistent.

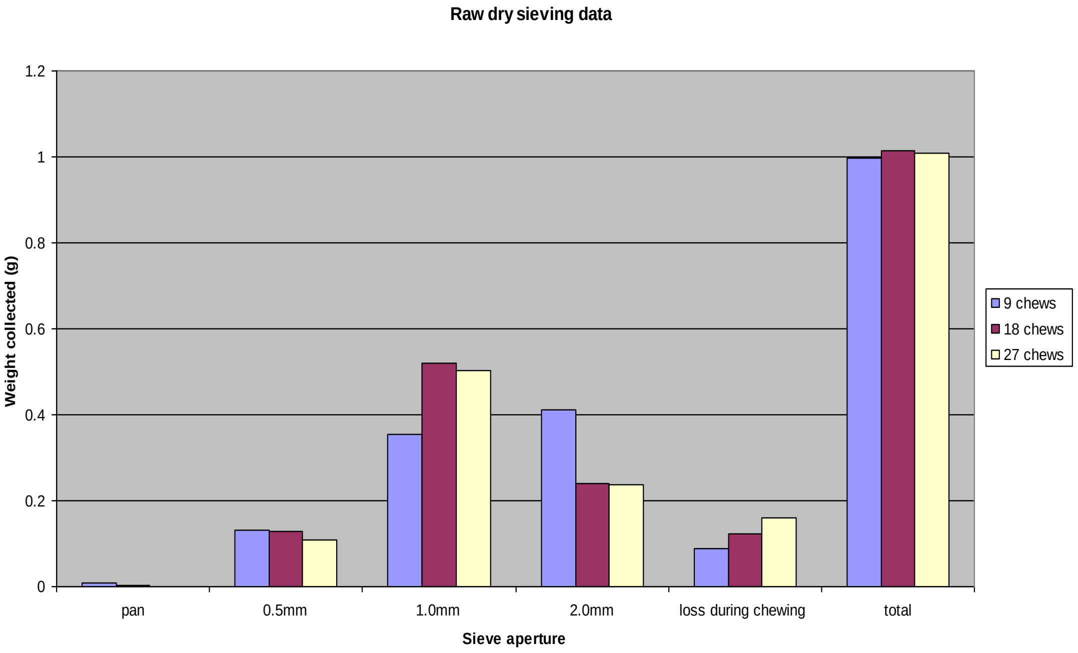

Figure 6.1: Raw dry sieving data

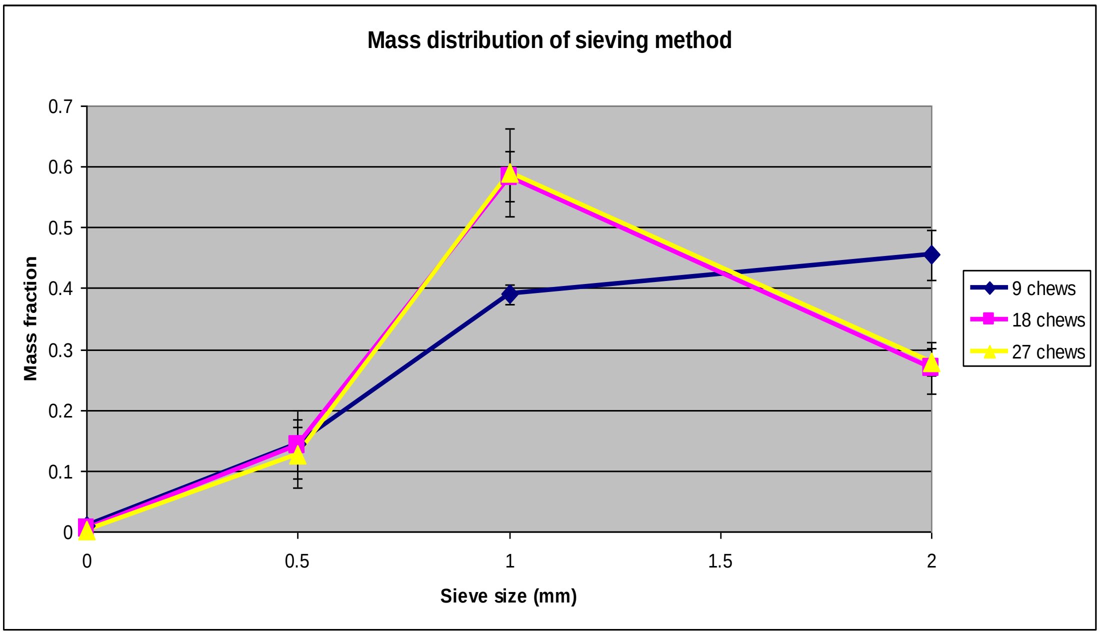

Figure 6.2 Mass distribution of sieving method

From Figure 6.1 and 6.2, some interesting facts can be found as follows:

- A big difference between 9 chews and other two on 2mm and 1mm size sieves.
- The loss of weight increases with the chewing cycles.
- The weight collected on the pan and 0.5mm size sieve decreases when the chewing cycles increases.
- Almost no difference of mass distribution between 18 chews and 27 chews.

From all the facts above, some assumptions have been made:

1. The more chewing cycles, the more fine particles created, the more agglomeration occurs.
2. The chewing machine works well on breaking particles down into 1mm, but not below 1mm.

To prove assumption 1, the photos of the samples for 3 different chewing cycles are taken:

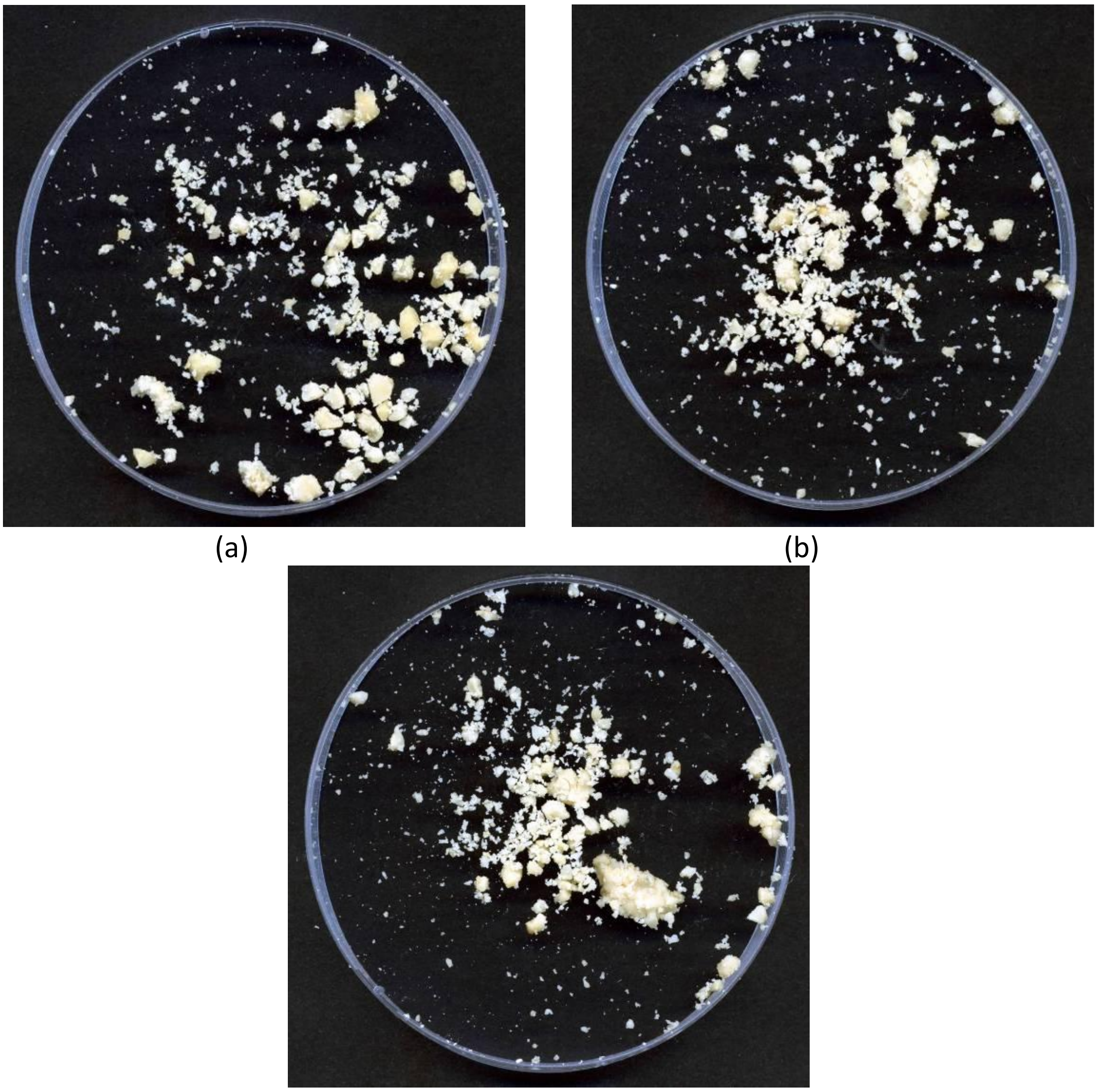

(a) (b)

(c)

Figure 6.3 Samples for 9 (a), 18 (b) and 27 (c) chewing cycles

From the above pictures, it can be seen that for nine chewing cycles, the chewing results have more large particles than the other two results. For the 27 chewing cycles, there are more fine particles, and these particles are likely to stick together. Therefore, the assumption one is correct. This makes it impossible to analyze the particle size with image analysis. To get rid of the agglomeration, wet sieving and image processing are both considered. However, in terms of the convenience and time consuming, image processing is the first option.

### 6.2.2. *Chewing Results with Image Analysis*

Image analysis is a technique where an image of the food bolus is analysed by computer software to evaluate the particle size distribution. Shi et al. (1990), Hoebler et al. (1998), and Hoebler et al. (2000) are examples studies that have used image analysis. A typical approach was taken by Hoebler et al. (1998) where bolus particles were spread out on a glass plate, photographed, digitised, and analysed using computer software. Results were displayed in histograms in terms of particle area. For the following experiment, the chewed food particles were scanned by an Epson scanner (Epson Perfection, 3490, Photo). The captured images were analysed by Image J® (1.37a, National Institute of Health, USA). A few trials were conducted in the following to obtain the optimized experimental material and software parameters to be used in the image analysis.

Two common solvent are considered to be used in the experiment. Ethanol works much better than water. Ethanol breaks down the oil molecule to eliminate the agglomeration. The sample with ethanol (Figure 6.4b) is very clear. In contrast, the sample with water (Figure 6.4a) is quite blurry with oil bubbles on the top. Thus, ethanol is selected in the following trials.

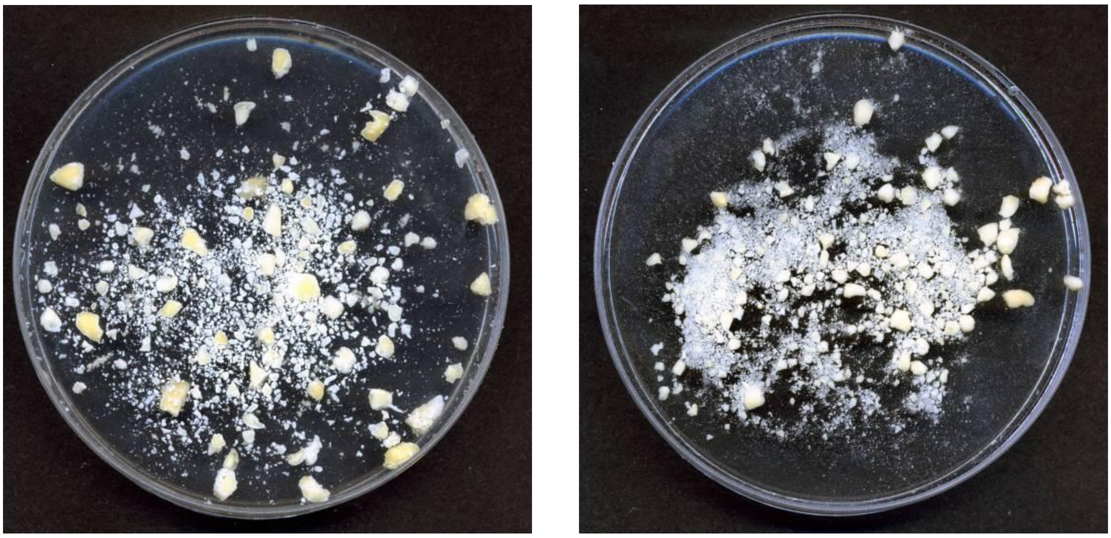
(a) (b)

Figure 6.4 Samples immersed in water (a) and ethanol (b)

Trial one:

Procedure steps:

1) Collect the chewed food sample from the teeth onto one Petri dish (140mm diameter) (Biolab, Auckland, New Zealan)
2) Pour 60 ml of ethanol (absolute) (Polychem Marketing Ltd, Auckland, New Zealand) in the Petri dish
3) Spread out evenly all the particles with the small brush

4) Put the Petri dish on the scanner and scan the sample at 800 dpi in grayscale.

The first trial is used for examining the repeatability of image processing software for one 9-chews sample, one 18-chews sample and one 27-chews sample. Steps 3 and 4 are repeated for five times. Therefore, there are five replicates for each sample.

The results are as follows:

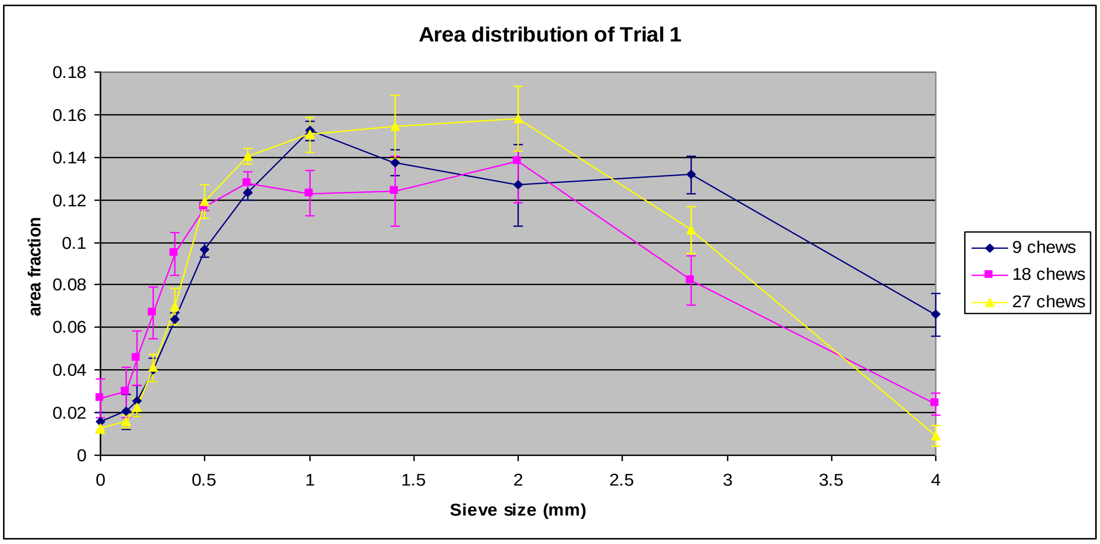

Figure 6.5: Area distribution of five 9-chews, five 18-chews and five 27-chews samples

From all the results above, the area distributions for each replicate sample are not consistent at all. The reason can be found from the following original pictures (Figure 6.6a,b,c).

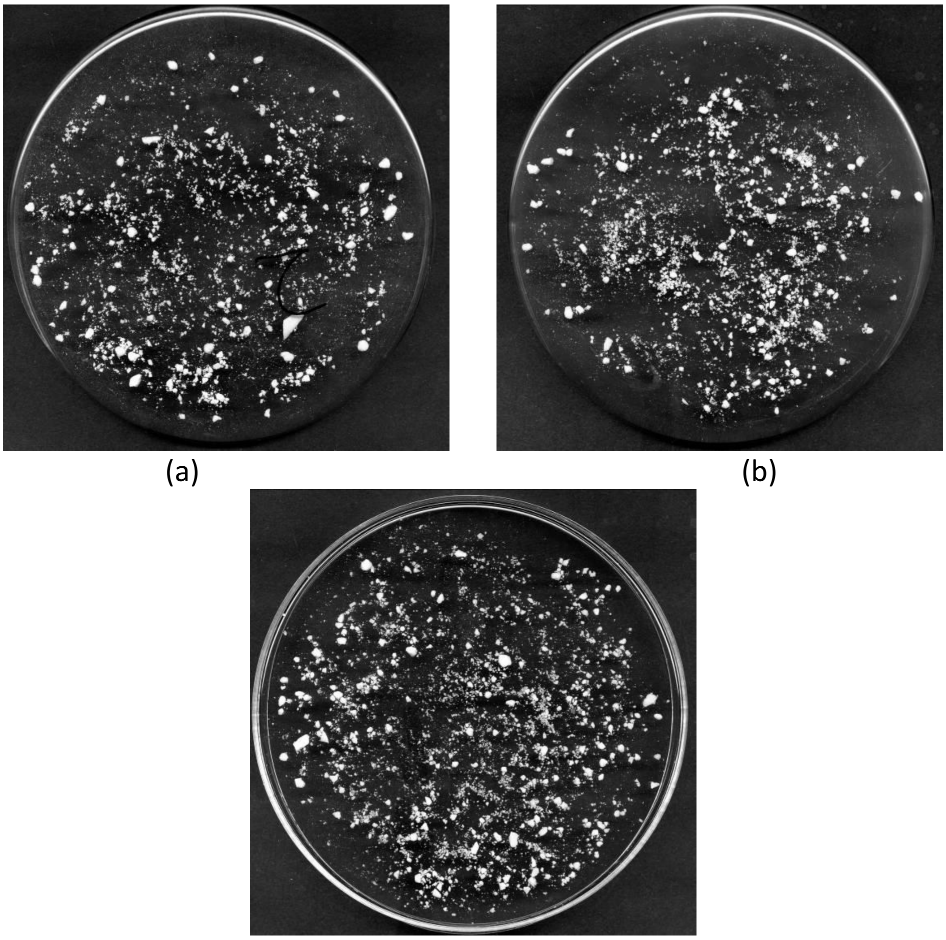

(a) (b)

(c)

Figure 6.6 9 chews (a), 18 chews (b) and 27 chews (c) samples with ethanol

From the above images, it can be seen that the image with the most chewing cycles (27) has most the fine particles than the image with 9 chewing and 18 chews. This resulted in generating more overlapping particles in the Petri dish. Because there are too much overlapping, the watershed algorithms cannot separate overlapping particles accurately. Thus, the area distributions of the replicate sample cannot be consistent.

Trial two:

To solve the overlapping problem, the samples are separated into several Petri dishes in this trial.

Procedure steps:

1) Put the food sample with ethanol in the test tube
2) Use the mixer vibrator to shake the tube for stirring till no agglomeration
3) Put the test tube stand-up for minutes to let the coarse particles settle down and fine particles floating
4) Suck out the ethanol with the fine particles by using the syringe put on with the silicon tube

5) Replace the silicon tube with the filter unit and inject the ethanol back to the test tube
6) Repeat from step 2 to 5 until few fine particles floating
7) Pour all the food particles and the ethanol in the test tube equally on three Petri dishes
8) Take all the larger particles onto the forth Petri dish with the tweezers and make sure no larger particles attached to each other and leave them dry
9) Pour ethanol in the first three Petri dishes and make sure the ethanol covers all the particles.
10) Spread out the particles on the first three Petri dishes with the small brush
11) Put the Petri dish on the scanner and scan the sample one by one.

To examine the repeatability with new procedure steps, steps 10 and 11 are repeated for three times. From the graph below, for the same chewing cycles, the area distribution from trial 2 is much more consistent than trial 1.

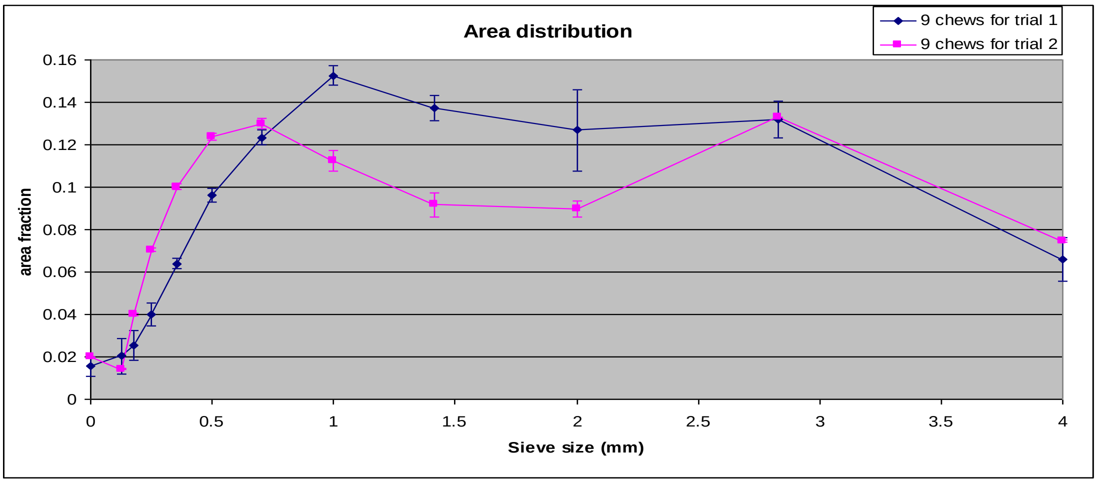

Figure 6.7: Area distribution of 9 chews sample for trial 1 and trial 2

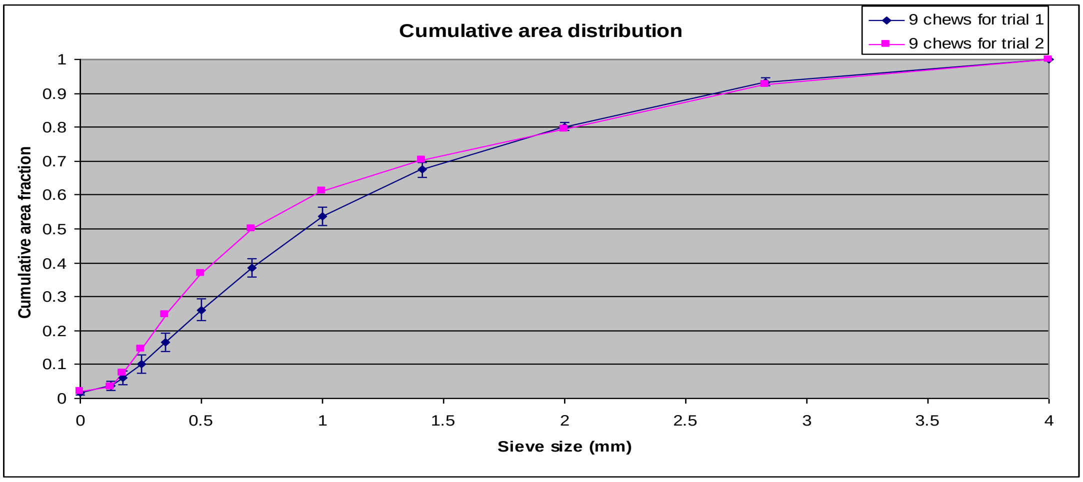

Figure 6.8 Cumulative area distribution of 9 chews sample for trial 1 and trial 2

From the above figures, the standard deviation of trial 2 is much bigger than trial one, especially on 2mm sieve. The results show the repeatability of trial 2 is much more stable than trial 1.

Trial 3:

Find out the optimal threshold algorithm.

The same chewing sample results are compared with three common automatic threshold algorithm provided by ImageJ software, which are Isodata (Jensen, 1996), Otsu and Maximum entropy. In Otsu's method, the histogram is divided in two classes and the inter-class variance is minimized (Otsu, 1975). Maximum entropy is very similar to Otsu's method. Rather than minimising the inter-class variance, it maximises the inter-class entropy (Sahoo et al., 1988). Entropy is a measure of the uncertainty of an event taking place. Isodata is considered to be an iterative thresholding scheme (Velasco, 1980).

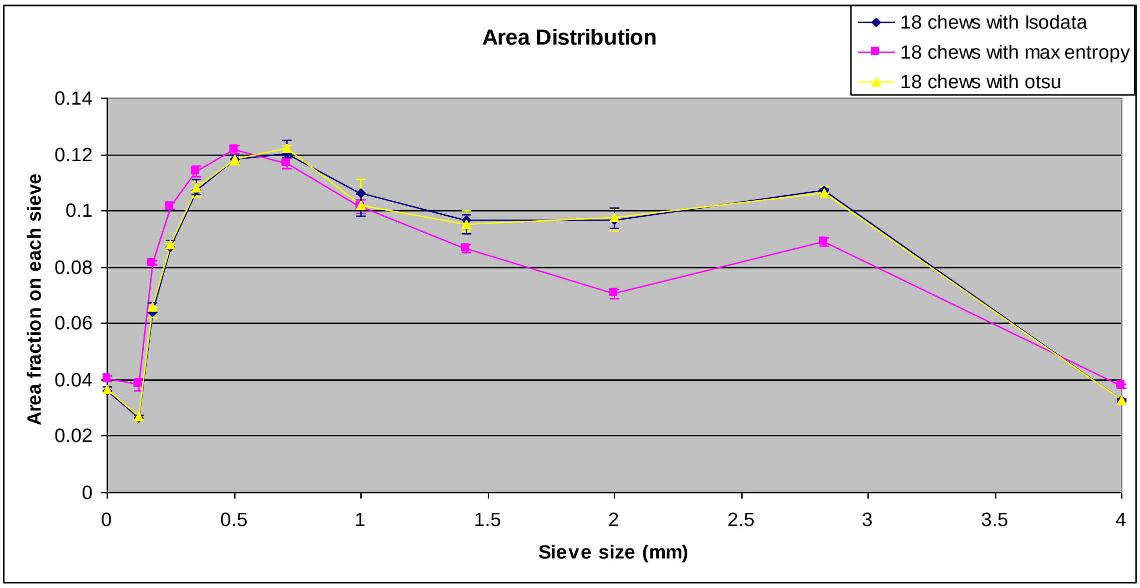

Figure 6.9: Area distribution by three different threshold algorithms

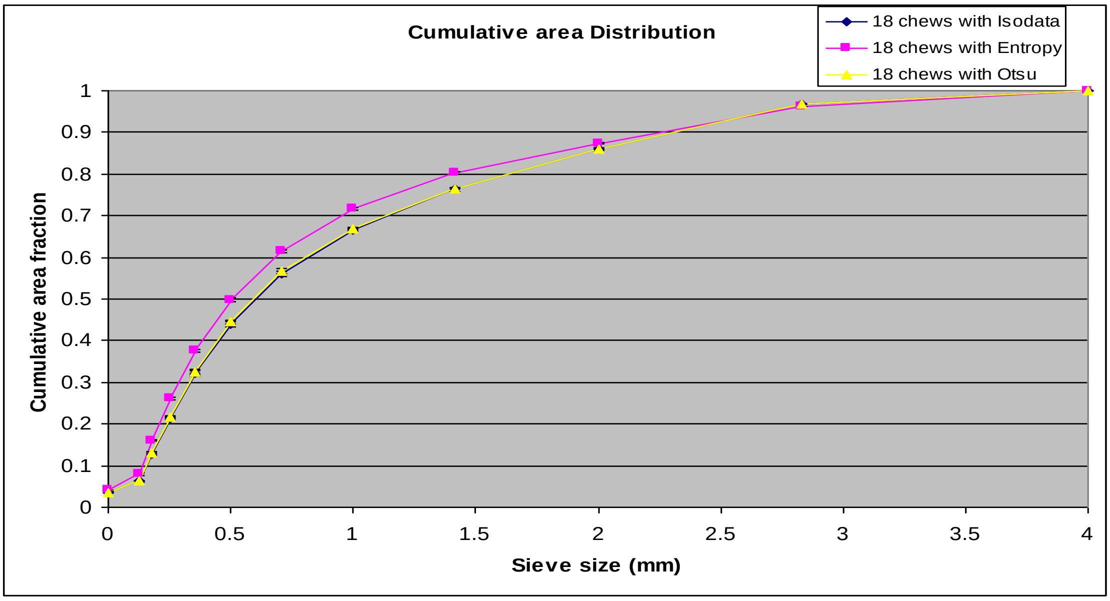

Figure 6.10 Cumulative area distribution by three different threshold algorithms

From the above two graphs 6.9 and 6.10, the results of using Isodata and Otsu algorithms are very similar to each other and very different to Max. entropy algorithm. However, it's very hard to find out which algorithm is better and correct from the graph. Thus, the following scanned pictures were captured after being processed by the algorithms. From the pictures below, Max. Entropy does not process the picture correctly as Isodata and Otsu do.

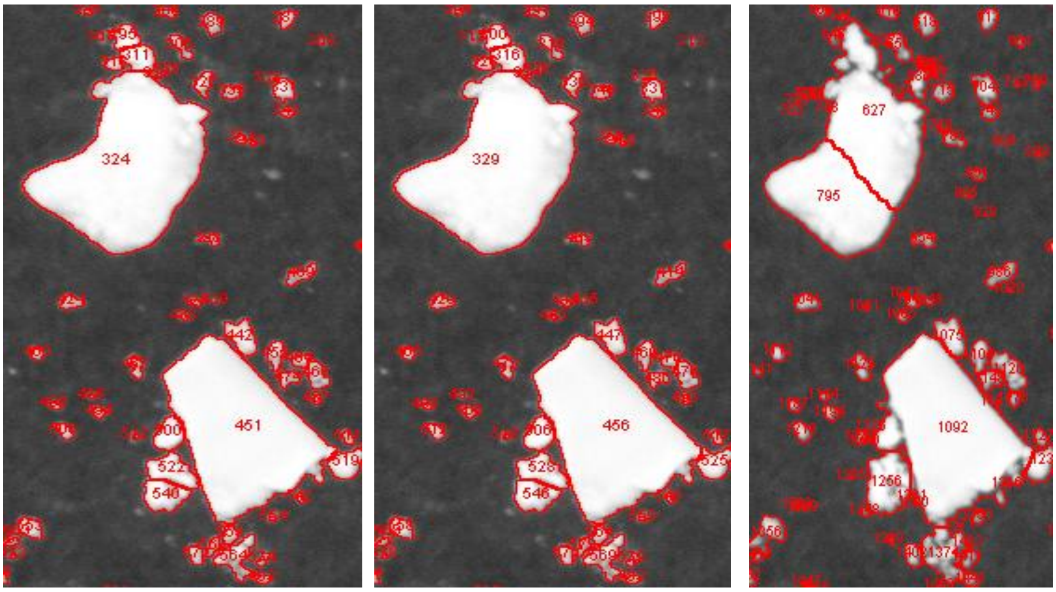

(a) (b) (c)

Figure 6.11: Scanned picture comparison between Isodata(a), Otsu(b) and Max. Entropy(c).

The following result shows that the standard deviation of Otsu is smaller than Isodata in general. Therefore, Otsu algorithm has been selected to use in the image processing for the following experiments.

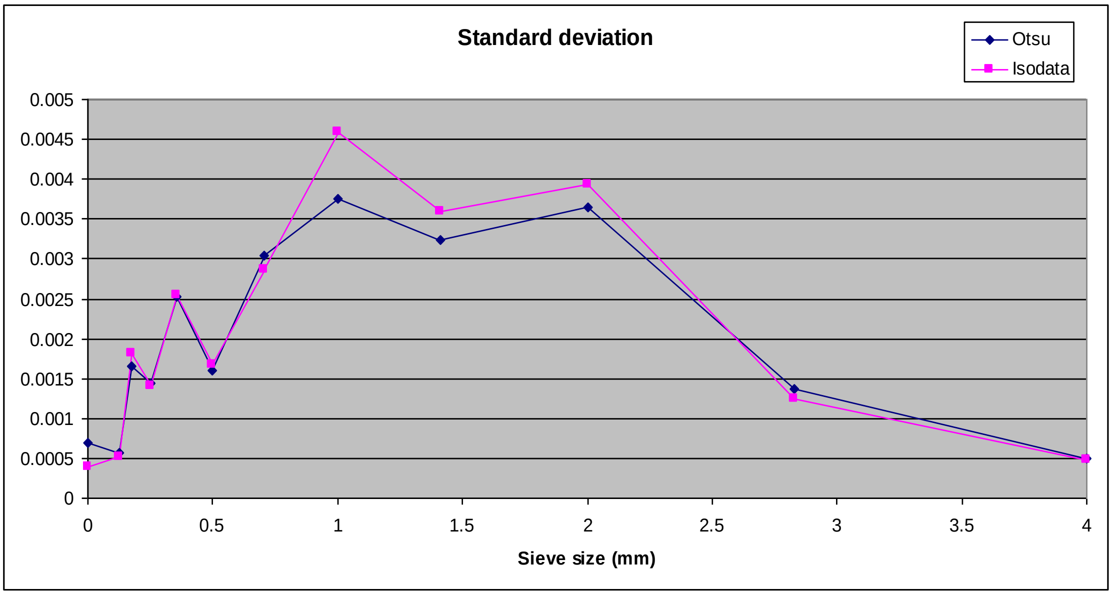

Figure 6.12: standard deviation comparison between Otsu and Isodata

From the comparison of the above results, the image processing method to analyse the particle size distribution of food bolus is a very good approach. Using this method the differences of results with different parameters of the machine are able to be distinguished.

## *6.3. Chewing Experiments for the Usefulness of the Chewing Robot*

A series of experiments were carried out under varying robot configurations, consisting of the trials on 3mm thick hard plastic model foods and on roasted unsalted peanuts (Virginia cultivar, Prolife Foods, Hamilton, New Zealand). The experiments were carried out to examine the reproducibility and sensitivity of the functional parameters of the chewing robot, including the number of chewing cycles, the spring pretightening force and the length of ground link to adjust shearing angle in the frontal plane. Flynn et al. (1987) found that the average number of chewing cycles for around two grams of peanuts was 18 cycles by human subjects. Therefore, two whole peanuts (2.0 ± 0.01g) were used in the chewing robot for 18 cycles in the chewing experiments with different functional parameters. According to the chewing force study by Kawata et al. (2007), the average compressive force during peanut chewing is 57.7±35.7N. Therefore, the spring pretightening force was adjusted to 35N and 70N. The length of ground link was varied from 38mm (vertical chewing) to 50mm (lateral chewing). Food repositioning frequency was also adjusted between each cycle and every three cycles by the food manipulation system. The chewing velocity of the robot was controlled to match human chewing velocity profile according to human measurements (Ogawa et al., 2001; Xu et al., 2008). The opening/closing time was set to 0.65 second and the occlusal time was set to 0.12 second. 3D force profiles were recorded dynamically for the entire chewing sequence. The chewing results for different manipulation frequency were also analysed.

Before each chewing experiment, a tight occlusion between the upper and lower teeth was assured by adjusting the lower teeth repositioning table. The chewing experiment started with the upper teeth at the most opening position and the peanuts were on the lower teeth. The experiment finished when the upper teeth returned to the starting position. After completion of a chewing sequence, the upper teeth and the food manipulation system together with the lower teeth were taken out from the robot. A tooth brush was used to make sure that all the particles were collected from the teeth and the food manipulation system and put into a Petri dish (diameter 14cm) (Biolab, Auckland, New Zealand). Each robot chewing experiment was replicated five times.

### 6.3.1. *Particle Size Measurements*

The particle size distributions of chewed peanuts were measured by image analysis. The chewed peanuts fragments were collected in a Petri dish and 60ml of ethanol added to assist in separating agglomerated fragments and to separate particles and to prevent fat globules from forming. The separation of individual particles was assisted with a plastic spatula and by shaking.

The contents of the petri dish were scanned at 1200 dpi (Epson Perfection, 3490 Photo,) in greyscale. The scan was then repeated after redispersal of the contents by shaking and respreading. Processing of the 4300 x 4300 pixel images was carried out in ImageJ 1.40g (National Institute of Health, USA). A black and white threshold was used to convert the greyscale images into binary images. Particle sizing was undertaken using a nucleus counter function, in conjunction with a watershed algorithm to separate any abutting particles.

Image dimensions of constituent particles were categorised into 9 particle size bins based on the standard sieve sizes, 0.25-0.354, 0.354-0.5, 0.5-0.707, 0.707-1, 1-1.414, 1.414-2, 2-2.828, 2.828-4, ≥4mm. The output from the Image J program (area for each counted particle) was exported to a software program (LabView 8.5, National instruments) in order to create particle size distributions based on surface area. For area distributions it was assumed the area of each particle was that of a circle and the diameter derived from this. The particle surface area size distribution was then calculated by sorting the diameters of particles into the 9 particle size bins.

Textural analysis of the peanuts was conducted with a Texture Analyser TA-XT2 (Stable Microsystems, Surrey, UK), using a uni-axial compression test with a flat cylindrical probe (diameter: 60mm). TPA of peanuts was conducted by compressing peanut halves to 50% strain with a test and post test speed of 1.67 mm/sec. Peanuts halves were placed face down. The texture analyser monitored force once it made contact with the surface of the peanut.

### 6.3.2. ***Chewing Force Profiles***

While the overall trajectory of the mandible may vary depending on food properties during the occlusion phase of a chewing cycle, the teeth trajectory is guided by the shape of the teeth as the surfaces of the upper and lower molars glide over each other (Bourne, 1975; Nakajima et al., 2001). To allow this complex motion during the occlusion phase, the chewing robot incorporates a spring system on the mandible. In this way the vertical component of the robot trajectory can alter to ensure teeth to teeth contact throughout occlusion.

The amount of force that must be exerted, before the vertical component of the trajectory changes is dependent on the spring constant and can be adjusted by its initial compression (pre-tightening force). If the teeth encounter an object (e.g. a food), the robot must provide enough force to deform the object and achieve the occlusal trajectory. Depending on the pre-tightening force, the full deformation of the food to allow true occlusion may or may not occur.

Figure 6.13 shows the differences in resultant chewing force from three dimensional forces on a 3mm thick hard plastic with different spring pretightening force. Because this material is not deformable, complete occlusion would not occur and instead the mandible molar teeth would slide along the surface of the plastic material rather than the surfaces of the maxilla molars. As shown by the solid line, the distance between upper and lower teeth during occlusion remained at 3mm. This indicated that there was no deformation of the plastic occurred during chewing. When the upper teeth started contacting the plastic, the spring installed behind the upper teeth began being compressed and generating compression forces onto the plastic. When the spring was pretightened before being compressed, the force applied from the spring increased by the pretightening force. For example in Figure 6.13, by adjusting the spring pretightening force from 0N to 45N, the maximum chewing force for each cycle was increased by 45N.

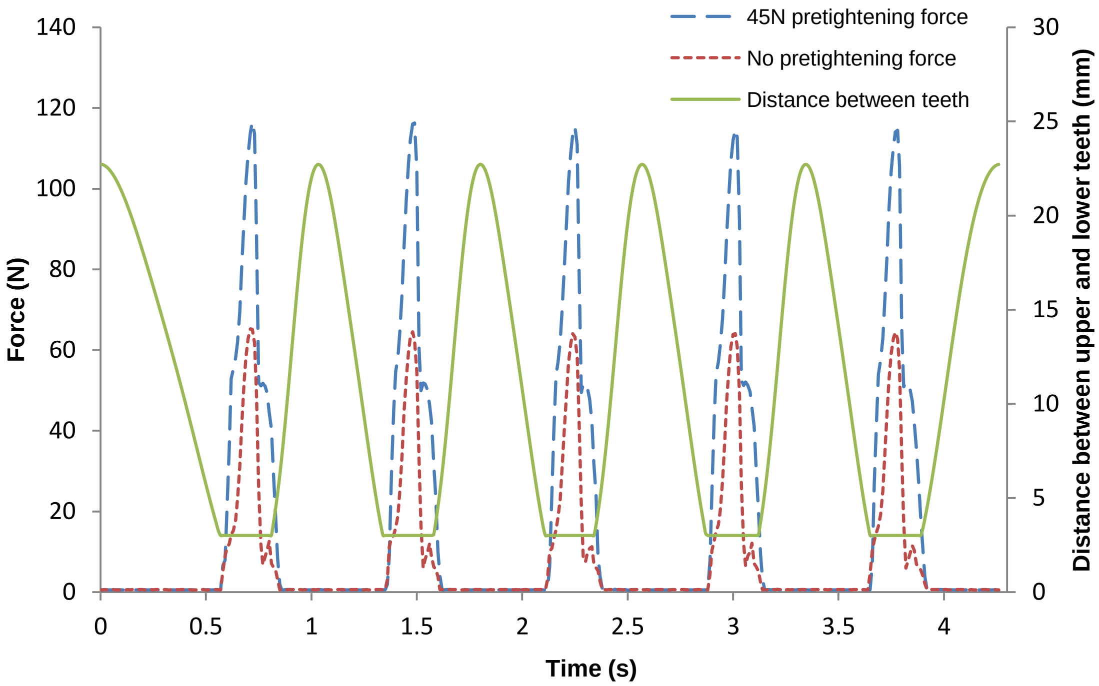

Figure 6.13 Changes to resultant chewing forces with different pretightening force throughout the chewing process of 3mm thick hard plastic

Figure 6.14 shows the chewing force profile for the experiment on peanuts with a pretightened spring force of 70N and maximum chewing angle in both sagittal plane and frontal plane. The chewing force in the z-axis (solid line) was applied vertically downwards on the food. The chewing force in the y-axis (long dashed line) was the shearing force in frontal plane. The chewing force in the x-axis (short dashed line) was the shearing force in sagittal plane. With continuation of the chewing process, the food thickness was reduced and the compression displacement of the spring was also reduced. As a result, the chewing force generated from the spring dropped. The irregular surfaces of the teeth along the forwards movement in the sagittal plane result in component forces along all axes.

The directions of the resultant force (in x-y-z coordinates) during the first cycle of the trial can be seen in Figure 6.15. As the upper teeth moved towards and compressed the food, the chewing force increased and reached the largest value (105N) at the centre of occlusion. The differences in directions between positional change and force propagation illustrate the importance of teeth shape on mastication mechanisms.

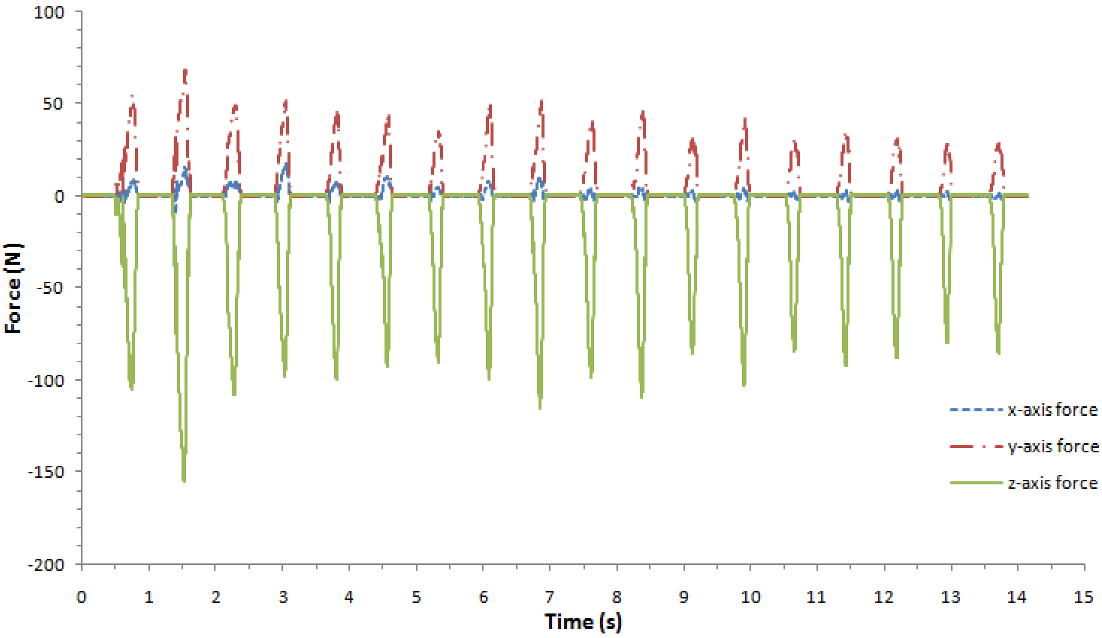

Figure 6.14 3D force profile for 18 cycles during chewing process of peanut

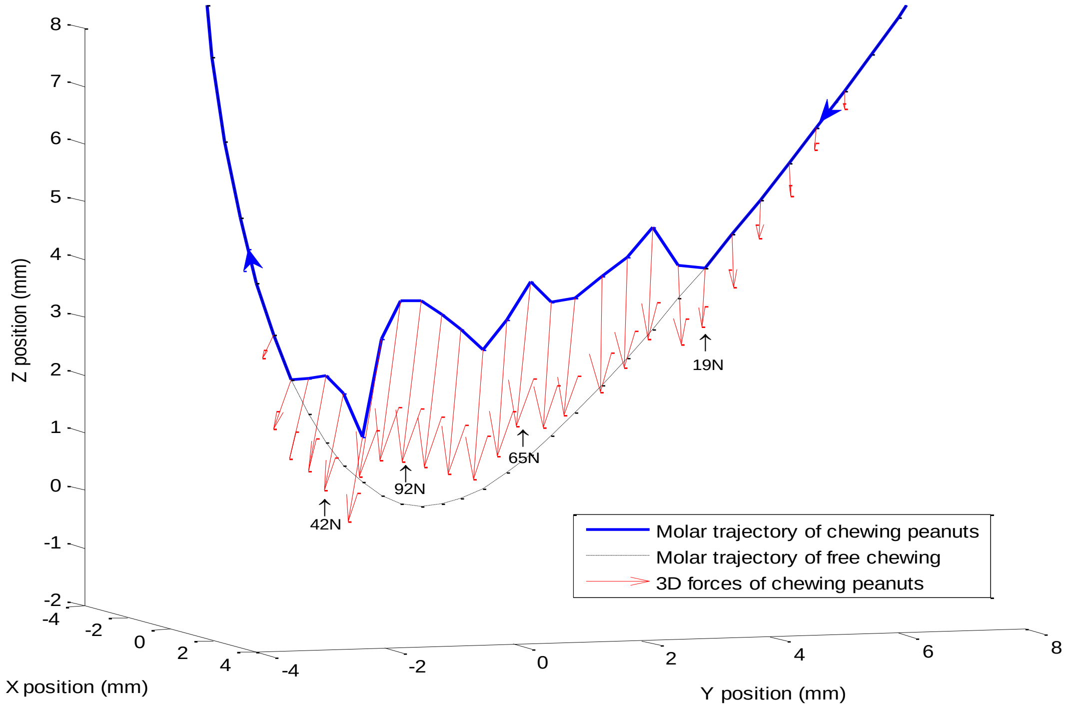

Figure 6.15 Resultant force vectors projected on the chewing trajectory of one cycle

Figure 6.15 demonstrates the changes in trajectory the mandible undergoes as a result of multiple fracture events occurring to the peanut particle. As the trajectory of the mandible progresses, Figure 6.15 shows that the vertical component of the movement deviates from the free trajectory by compressing the spring. Consequently there is a build up of force in the z direction which results in a fracture event. The compression or shape change of the food due to fracture allows the mandible molars to move closer to the free trajectory. This pattern is then repeated until the trajectory moves to the opening phase.

This multiple fracture failure mode is expected for hard brittle particles such as nuts and has been observed in classical texture analysis measurement methodology (Bourne, 2002). Figure 6.16 shows this fracture mode measured on peanuts using the traditional texture analysis methods. Similar breakage behaviour can be seen for example in hazelnuts by Saklar et al (1999).

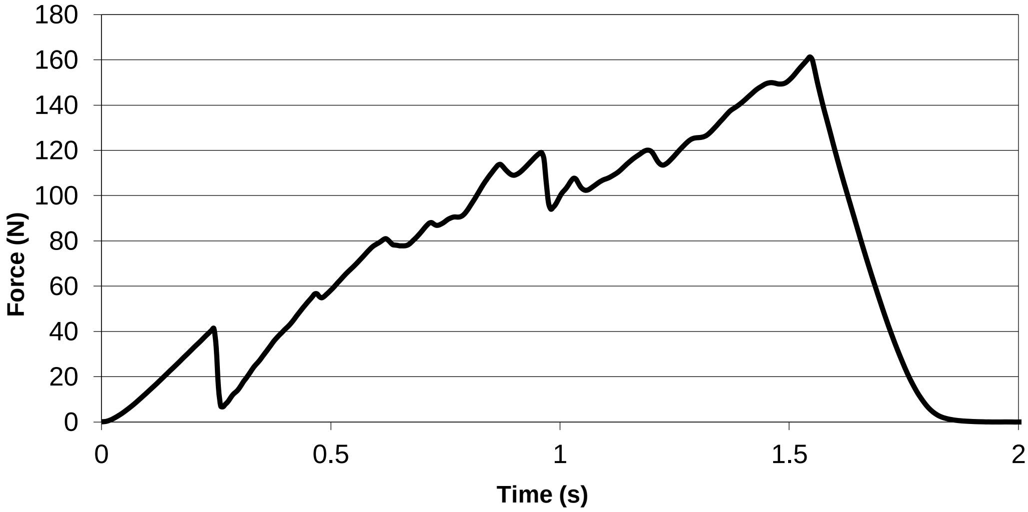

Figure 6.16 Example uni-axial force curve measured for roasted unsalted peanuts by compression by TATX2 showing fracture mode failure mechanism (Saklar et al., 1999)

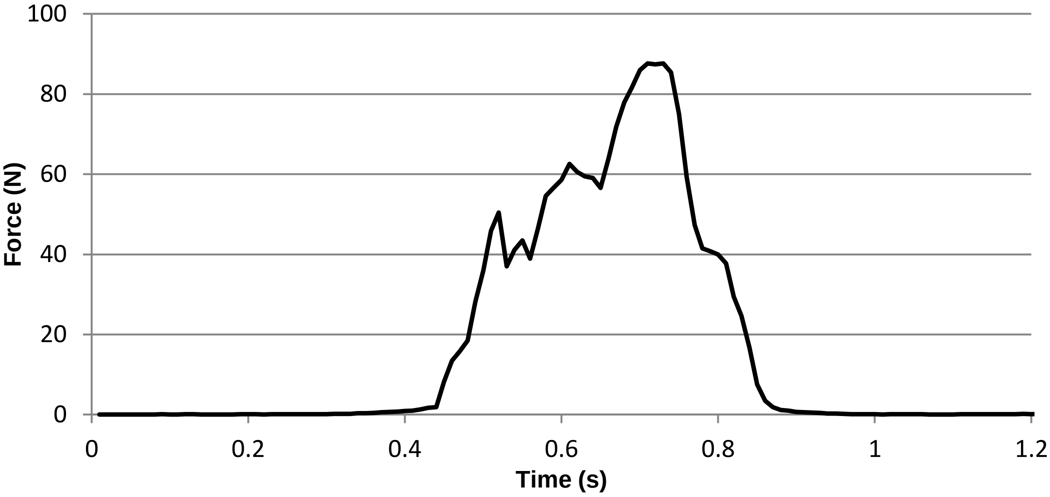

Figure 6.17 Resultant force profile throughout the chewing process of roasted unsalted peanuts

This pattern can also be seen in the resultant forces measured in the chewing robot as shown in Figure 6.17. While the pattern during fracture is similar between the chewing robot and traditional texture measurement, the magnitude of the forces applied are different. This is most likely to be due to the differences in particle deformation occurring between the two instruments and the directions the forces are applied.

### 6.3.3. *Motor Torque Profiles*

Texture profile analysis (TPA) of food was normally achieved by a compression test using a texture analyzer. Figure 6.18 shows a generalized texture profile analysis curve generated by the Instron Universal Testing Machine. The height of the force peak on the first compression cycle (first bite) was defined as hardness (Bourne, 2002). Fracturability was defined as the force of the significant break in the curve on the first bite.

Motor torque profile during mastication process of a 10x5x15 mm marshmallow for three chewing cycles was produced in Figure 6.19. In general, an increase in motor torque resulted in an increase in resultant chewing force. Peak force as well as motor torque during the first chewing cycle are the largest which is related to the hardness of marshmallow. As chewing continued, motor torque decreased as well as resultant force, which means that the hardness of the food was reduced because of texture change during mastication. Motor torque profile during chewing process of one gram peanut was presented in Figure 6.20. In the first cycle, fracturability of peanut can be observed as the force of the significant break where peak motor torque also happened. This could be explained that motor torque was also related to food texture. More experiments on various foods need to be carried out to justify that motor torque could provide useful information about food texture.

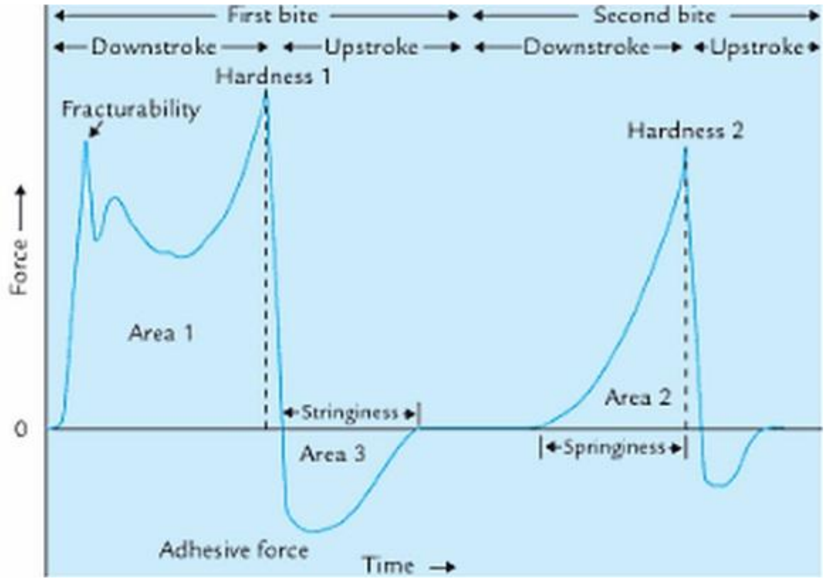

Figure 6.18 A typical force (F) vs displacement (d) curve obtained from a compression test using the texture profile analysis approach. (Bourne, 2002)

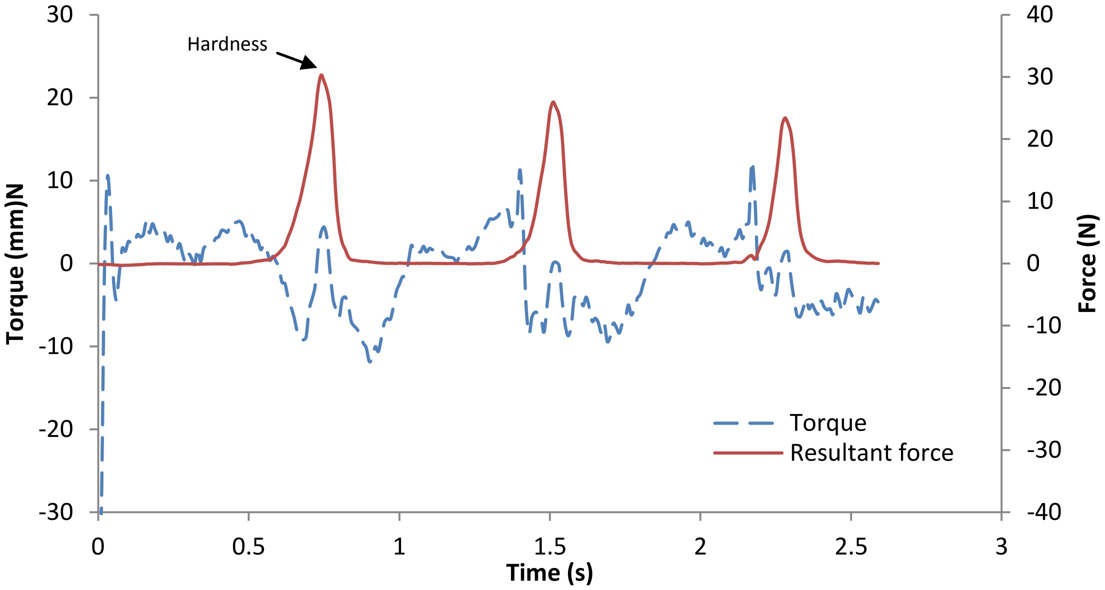

Figure 6.19 Motor torque and resultant force profile throughout the chewing process of marshmallow for three chewing cycles.

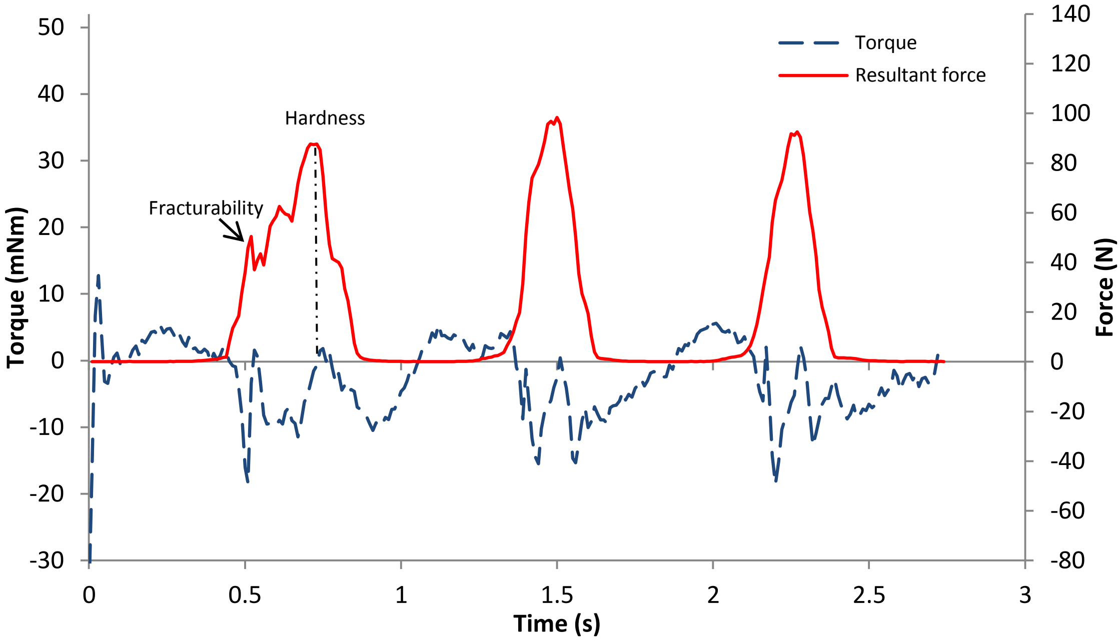

Figure 6.20 Motor torque and resultant force profile throughout the chewing process of peanut for three chewing cycles.

### 6.3.4. *Influence of the Robot's Functional Parameters*

The reproducibility and sensitivity to robot configuration were assessed through comparison of the particle size distributions measured in the resulting boluses collected after each trial. Experimental results with different chewing cycles (9 and 18) are presented in Figure 6.21. The results demonstrated the reproducibility of the device along with the changes in particle size distribution occurring over the duration of the mastication sequence. As expected, with the number of chewing cycles increasing, the small particles were produced more.

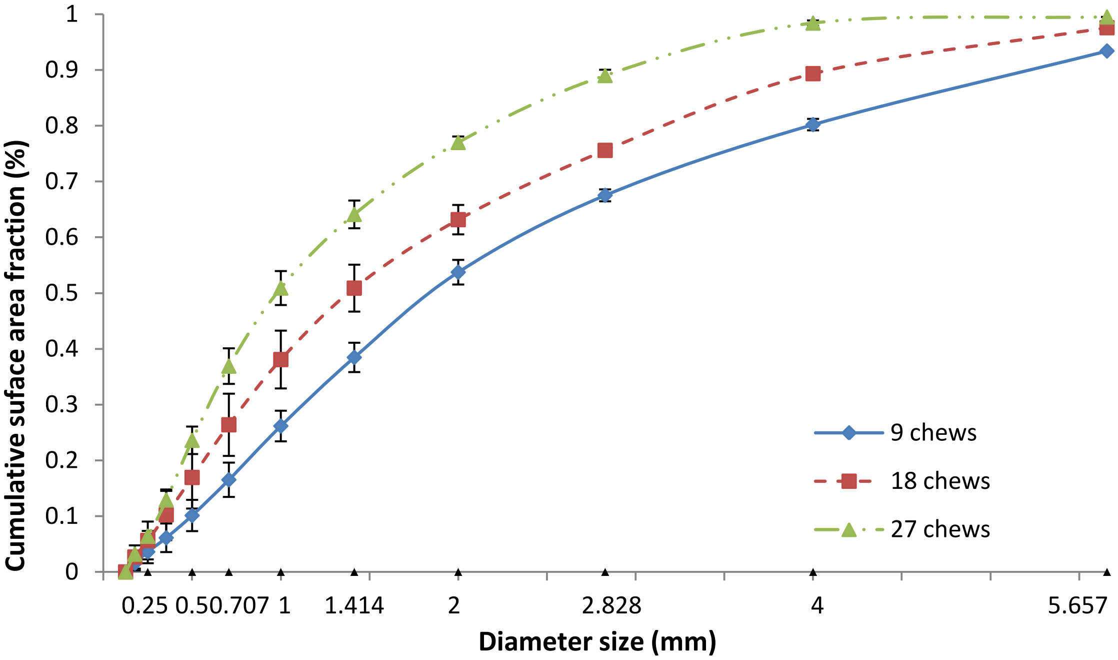

Figure 6.21 Cumulative particle size distributions (± standard error) of peanuts after 9 and 18 chewing cycles

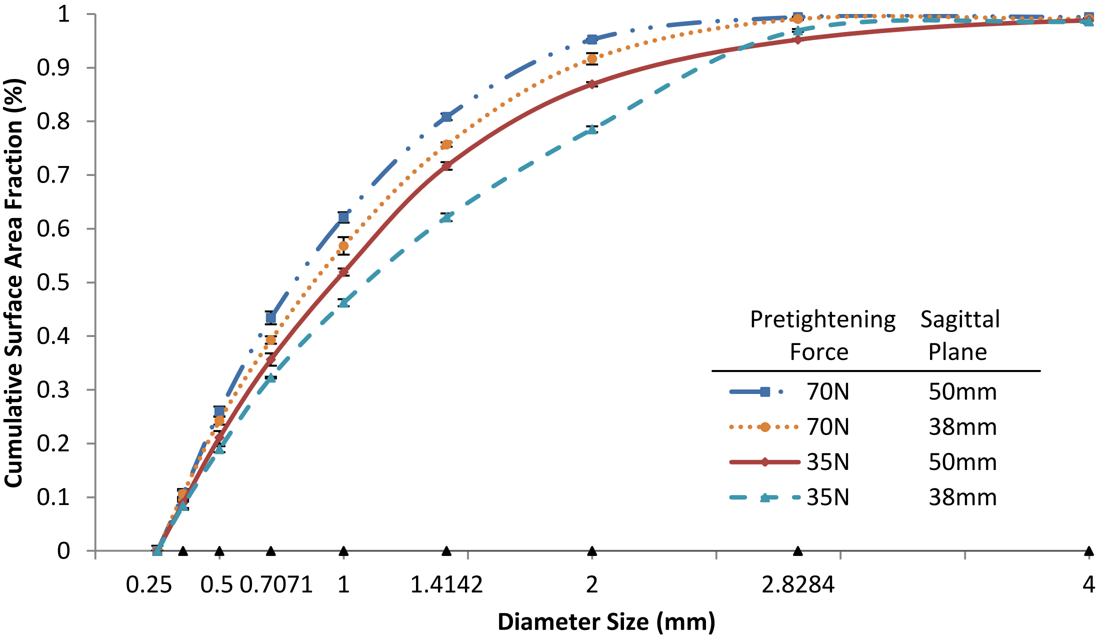

Figure 6.22 Cumulative particle size distributions (± standard error) of peanut fragments after 18 chewing cycles with four different parameters

The effects of chewing angle in the frontal plane (by changing the ground link length) and chewing force (by changing the pretightening force) are presented in Figure 6.22. In general, an increase in both chewing angle in the frontal plane and chewing force caused an increase in the extent of particle breakdown. For example, at 1.4142 mm size bin about 81% of total surface area was produced with 70N pretightening force and 50mm of the ground link length. When the pretightening force reduced to 35N and the ground link length was 50mm, the total surface area reduced to about 71% at 1.4142 mm size bin. When the length of ground link changes from 38mm to 50mm, chewing trajectory in frontal plane varies from vertical chewing (compression) to angular chewing (compressive shear) (see Table 1). Figure 6.22 shows that particle breakdown was more effective for peanuts with more angular chewing trajectories. This suggests that the application of shear during the compression failure of the peanuts results in a different particle breakage function where more rapid overall particle size reduction occurs. This result demonstrates the importance of teeth shape and trajectory on particle breakage and therefore the limitations in measuring textural information through commonly used one dimensional compression techniques.

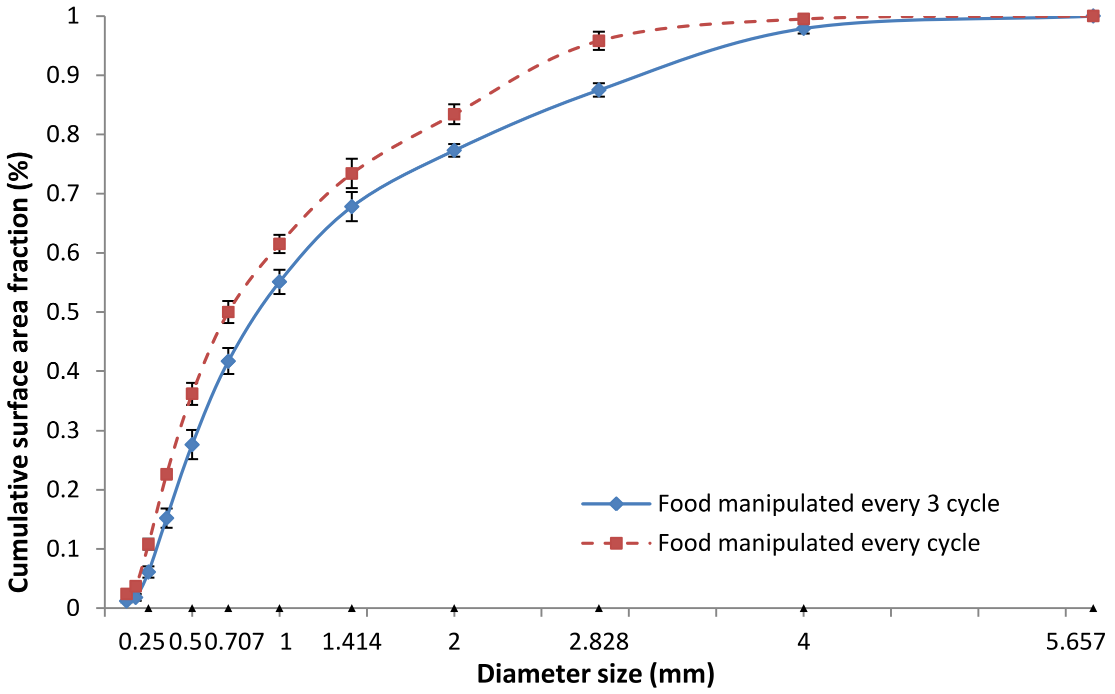

Figure 6.23 Cumulative particle size distributions (± standard error) of peanut fragments after 18 chewing cycles with different food manipulation frequencies

The tongue plays a crucial role throughout the complete food oral processing sequence and one of its key roles is as a mechanical device for food manipulations (Dellow & Lund, 1971). For the current chewing robot, the food manipulation system simulates the functionality of tongue and cheek to reposition food particles onto the teeth during chewing. In order to study the influence of food manipulation on particle size reduction, an experiment was carried out in which food was repositioned at various frequencies (Figure 6.23). It was found that when peanut particles were repositioned every cycle compared with every 3 cycles, smaller particles were much more produced. The robot with repositioning every three cycles was only able to chew the food particles left on the teeth when the food particles were not repositioned. However, the robot with repositioning every cycle was able to chew most of the particles through the whole chewing experiment, which results a better masticatory performance as shown in the above Figure. These results also proved that tongue movement during mastication is important for food particle reduction.

### 6.3.5. *Chewing Results Comparison*

In the mastication study by Flynn et al (1987), the cumulative volume fraction of the resulting boluses was determined using a wet sieving technique. Because of the different experimental methodology used in this work (image analysis), the reported cumulative volume fraction data reported by Flynn et al (1987) was converted into a surface area basis using the calculation method of Rhodes (2010). The converted data is presented in Figure 6.24 (solid line with marker +) and compared with the chewing results after 18 chewing cycles from the chewing robot. It was observed that the human chewing result of peanut below 1.4142 mm size bin was very close to the robot chewing result with 70N pretightening force and 38mm of ground link length and the human chewing result above 2mm size bin was very similar to the robot chewing result with 35N pretightening force and 50mm of ground link length. This shows that the human chewing result could be reproduced by the chewing robot with the pretightening force between 35N and 70N and the ground link length between 38mm and 50mm.

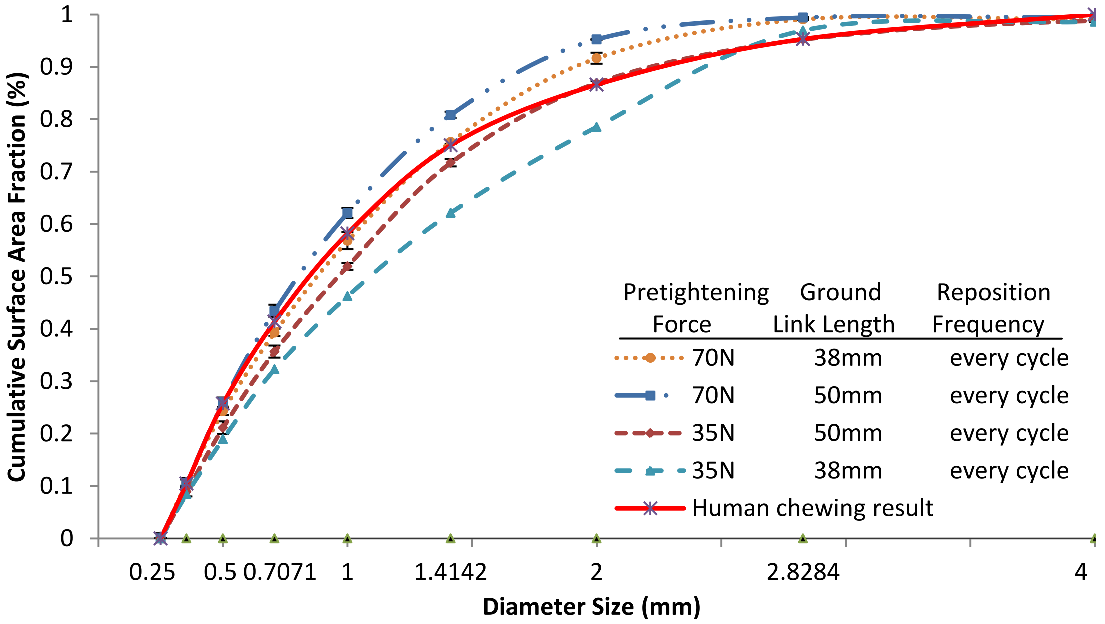

Figure 6.24 Cumulative particle size distributions (± standard error) of peanut fragments after 18 chewing cycles when applying different functional parameters compared with human chewing results

This result supports the findings of Agrawal et al (1975) who showed that hard and brittle foods (such as peanuts) were chewed with wider lateral movements than tougher properties. An analysis of fracture mechanics (Agrawal et al., 1997; Association, 1997; Lucas, 2004) showed that the rate of food comminution could be related to a single combined parameter, $(R/E)^{0.5}$ which they term the fragmentation index and includes the toughness (R) and elasticity (E) of the particle. Agrawal et al (1975) showed that the degree of lateral movement during chewing was also correlated with this parameter; Foods with low $(R/E)^{0.5}$ are chewed with more lateral movement. They speculated that this must be due to some interaction between the food particles and the teeth shape, perhaps differences in the way the features of opposing teeth line up during occlusion.

This analysis shows the potential application of the chewing robot for studying the fracture mechanics of particles as a function of the magnitude and direction of the force in simulated chewing scenarios. The ability to match human chewing outcomes demonstrates the robots use as a sample preparation device for in-vitro digestion assays.

## 6.4. *Chewing Experiments with Adaptive Fuzzy Control*

The chewing experiments on peanuts and marshmallow with adaptive fuzzy control implemented in the chewing robot are carried out. The chewing robot is set up with the pretightening force of 70N, ground link length of 50mm and food manipulation frequency at every cycle in the chewing robot. Five duplicates of experiments with 18 chewing cycles on peanuts were performed. Image analysis method was used on measurement of particle size distribution of peanuts. The initial chewing velocity was set to 300 degree per second. The adaptive fuzzy control is activated once the chewing force is more than 5N.

### 6.4.1. *Chewing Force and Velocity Profiles*

The chewing force and velocity profile of marshmallow for the first chewing cycle is shown in Figure 6.25. The chewing velocity starts to change to around 330deg/sec from 300deg/sec when the chewing force is around 5N. When the force increases to 15N, the chewing velocity increases from 330deg/sec to 377deg/sec. The chewing velocity reaches around 500deg/sec at 0.6 second just before the occlusion where the maximum chewing force is occurred. During the occlusion phase, the chewing force changes very slowly so that the force rate is very small. This results in a sudden drop on the chewing velocity to around 430deg/sec from 500deg/sec. After the occlusion, the upper teeth move away from the lower teeth. The force drops dramatically and the absolute force rate is very high. Therefore, the chewing velocity increases again from 430deg/sec to over 500deg/sec. When the force drops to 15N, the chewing velocity drops to 400deg/sec. The chewing velocity returns to 300deg/sec, after the chewing force drops below 5N. Overall, the chewing velocity increases with the chewing force for the marshmallow. The high chewing velocity plateau occurs just before the occlusion phase until the force drops to 15N. The reason is because of the high chewing force and high force rate during that period. This is in coincidence with the adaptive fuzzy control system implemented in the chewing robot.

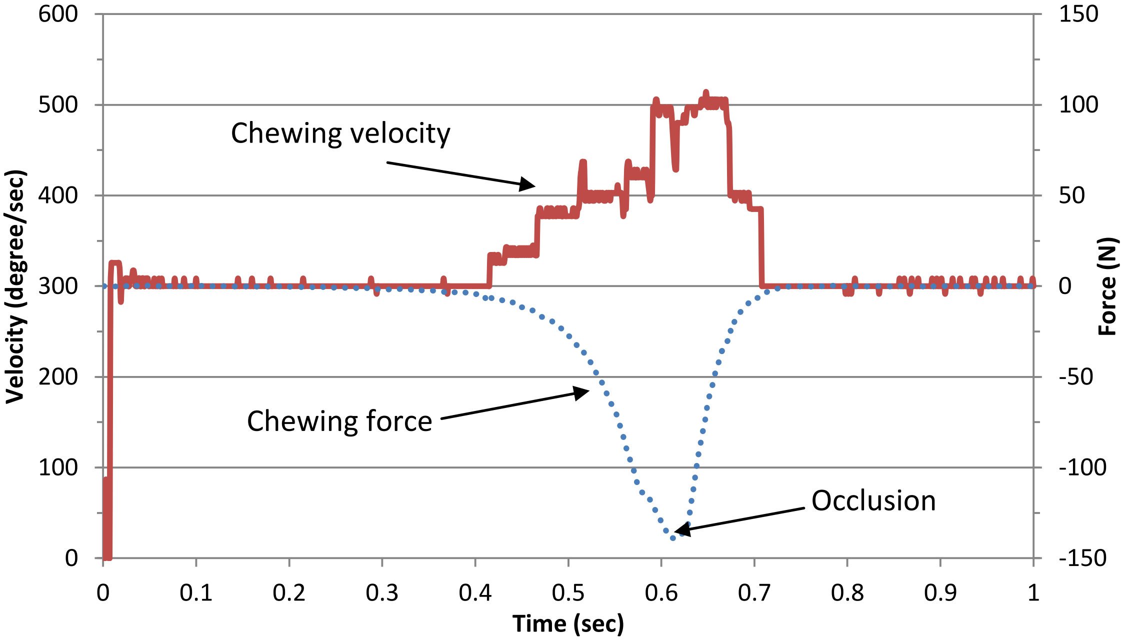

Figure 6.25 Chewing force and velocity profile of marshmallow during the first chewing cycle

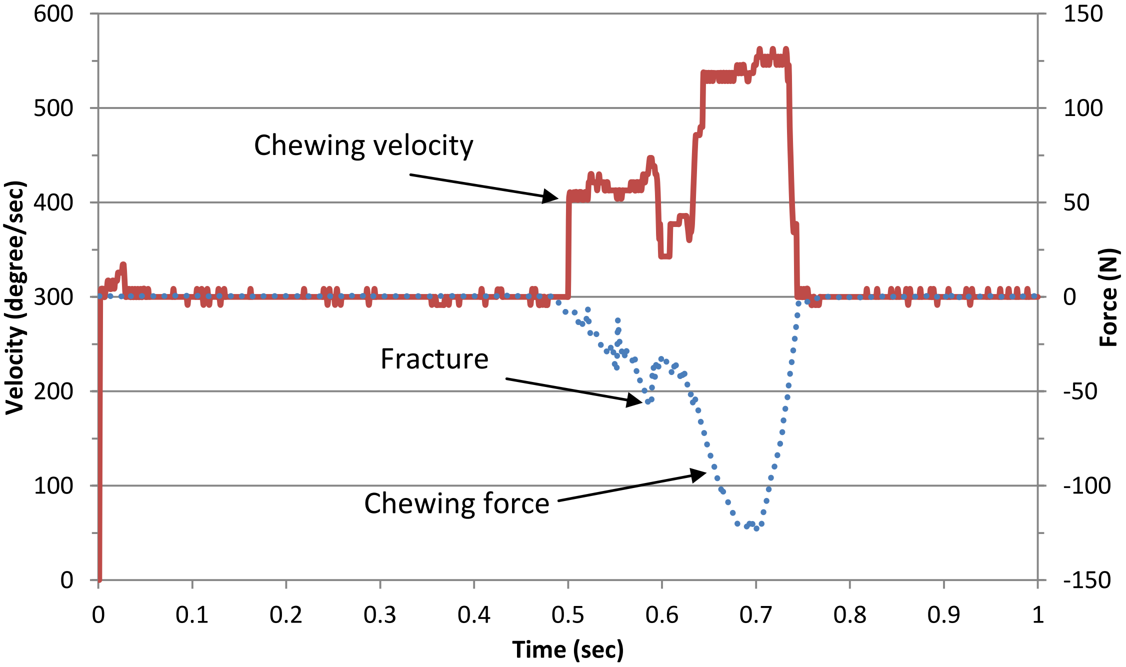

Figure 6.26 Chewing force and velocity profile of peanut #1 during the first chewing cycle

The chewing force and velocity profile of peanut #1 during the first chewing cycle is shown in Figure 6.26. In the beginning of the force contact with the peanut, the chewing velocity changes to over 400deg/sec. The chewing velocity changes between 400deg/sec and 450deg/sec until a big fracture occurs at around 54N. This causes the chewing velocity drops to 350deg/sec. After this, the chewing force rises so fast that the chewing velocity increases to 540deg/sec. The chewing velocity stays around 540deg/sec until the end of the force contact with the peanut. Overall, the chewing velocity from the adaptive fuzzy control is able to adapt to the texture change of peanut during fracture. More chewing velocity and force profiles are attached in Appendix A.

Compared between the chewing velocity and force results of peanut and marshmallow, the adaptive fuzzy control is able to control the chewing velocity to adapt to the food texture. For the soft food like marshmallow, the chewing velocity increases gradually along with the force. For the hard food like peanuts, the chewing velocity increases high in the beginning of the force contact due to the hardness, drops due to the fracture and then increases to a much higher value.

## *6.5. Chapter Conclusion*

A practical method to measure particle size distributions is developed by image analysis using a scanner. This method is proved to be more accurate and faster than conventional sieving method on the measurement of particle size distributions of peanuts. Chewing force profiles and motor torque profiles are generated during mastication of peanuts. These profiles have shown the relationship to the food texture. The influences on the particle size distributions by varying the functional parameters of the chewing robot have been investigated. It is found that the pretightening force of the spring, food manipulation frequency and chewing angles in frontal plane (ground link length) have more influences in particle area size distribution than the other parameters. The chewing experiments with compliance control for the chewing of marshmallow and peanut have been carried out. The results showed that the proposed compliance control adapts the chewing velocity very well in response to the change in the food texture during chewing process.

# 7. CONCLUSION

This thesis first achieved a few improvements to enhance the chewing robot so that the adaptive fuzzy control can be implemented and the evaluation of the chewing robot with real food chewing experiment can be carried out. These improvements include the installation of a 3D force sensor and correlated data collection hardware in the chewing robot to allow the real-time force data to be collected during chewing, the spring and hard stop system installed to replace the shock absorber to generate an adjustable force profile for the foods with different texture, and an automatic food manipulation system with a new set of 3D designed teeth. A food manipulation system, which is composed of three solenoids and a transparent plastic enclosure, was implemented around the bottom teeth. The food manipulation system with the new teeth improves the masticatory performance of the chewing robot to be close to the one of humans.

Analysis, modelling and control of the chewing robot have been investigated. DC motor and the velocity control in the existing Maxon motor control card are simulated in Matlab. Optimized PI parameters for the velocity control are obtained. The kinematics and dynamics of the linkage mechanism of the chewing robot have been analyzed. The simulation results of the analytical model compared with the results from the SolidWorks model show that the analytical model can accurately simulate the real chewing mechanism. The driving torques compared between the analytical model and real experimental data show that the analytical model is able to simulate the driving torque from the experimental data, especially when the food thickness is assumed constant (in the situation of raised bottom teeth as food resistance). Adaptive fuzzy control, consisting of one fuzzy velocity controller and one fuzzy adaptation mechanism controller, was proposed to control the chewing velocity. The adaptive fuzzy control enables the chewing robot to chew food according to the food texture like human. The simulation results of the chewing robot with adaptive fuzzy control to “chew” the marshmallow model and the peanut model showed that the adapted chewing velocity from the fuzzy control system varies based on the change of the food texture during the “chewing process”.

An image analysis method to analyse food particle size distributions is developed by experiments. Large amounts of chewing experiments with real food in the chewing robot are carried out to prove the usefulness of the chewing robot in food evaluation by analysing and comparing the chewing results of the chewing robot with the ones of humans. The chewing results showed the pretightening force of the spring, food manipulation frequency and chewing angles in frontal plane (ground link length) are three most important factors in the physical settings of the chewing robot to influence the chewing results in particle area size distribution. The chewing results also showed that the chewing robot with adaptive fuzzy control has better masticatory performance (generating more small particles) than the chewing robot without fuzzy under the same conditions. The chewing robot with adaptive fuzzy control generates a closer curve shape of particle size distributions to human results than the one without fuzzy.

Future works involving large numbers of chewing experiments with different foods are required on the parameters of the adaptive fuzzy control combined with the functional settings in the chewing robot to find out how to reproduce particle size distribution of human bolus. Chewing forces and motor torques profiles generated during chewing require further investigation for analysing the food texture.

# 8. REFERENCES

Abd-El-Malek, S. (1955). The part played by the tongue in mastication and deglutition. *Journal of Anatomy, 89*(Pt 2), 250.

Agrawal, K. R., Lucas, P. W., Prinz, J. F., & Bruce, I. C. (1997). Mechanical properties of foods responsible for resisting food breakdown in the human mouth. *Arch Oral Biol, 42*(1), 1-9.

Alemzadeh, K., & Raabe, D. (2007). Prototyping Artificial Jaws for the Bristol Dento-Munch Robo-Simulator; A parallel robot to test dental components and materials'. *Engineering in Medicine and Biology Society, 2007. EMBS 2007. 29th Annual International Conference of the IEEE*, 1453-1456.

Anderson, D. J. (1956). Measurement of Stress in Mastication. I. *Journal of Dental Research, 35*(5), 664-670.

Anderson, K., Throckmorton, G. S., Buschang, P. H., & Hayasaki, H. (2002). The effects of bolus hardness on masticatory kinematics. *Journal of Oral Rehabilitation, 29*(7), 689-696.

Anderson, R. J., & Spong, M. W. (1988). Hybrid impedance control of robotic manipulators. *Robotics and Automation, IEEE Journal of, 4*(5), 549-556.

Arimoto, S., Kawamura, S., & Miyazaki, F. (1984). Bettering operation of robots by learning. *Journal of Robotic systems, 1*(2), 123-140.

Arimoto, S., Liu, Y. H., & Naniwa, T. (1993). *Model-based adaptive hybrid control for geometrically constrained robots*.

Association, J. S. (1997). Hardness testing methods for rubber, vulcanized or thermoplastic. *JIS K, 6253*.

Astrom, K. J., & Wittenmark, B. (1994). *Adaptive control*: Addison-Wesley Longman Publishing Co., Inc. Boston, MA, USA.

Bourne, M. C. (1975). Is Rheology Enough for Food Texture Measurement? *Journal of texture studies, 6*(2), 259-262.

Bourne, M. C. (2002). *Food Texture and Viscosity: Concept and Measurement*: Academic Press San Diego.

Bruyninckx, H., Demey, S., S., D., & De Schutter, J. (1995). Kinematic models for model-based compliant motion in the presence of uncertainty. *The International Journal of Robotics Research, 14*(5), 465.

Carinena, J. F., & Ranada, M. F. (1993). Lagrangian systems with constraints: a geometric approach to the method of Lagrange multipliers. *Journal of Physics A: Mathematical and General, 26*, 1335.

Chauncey, H. H., Muench, M. E., Kapur, K. K., & Wayler, A. H. (1984). The effect of the loss of teeth on diet and nutrition. *Int Dent J, 34*(2), 98-104.

Chiaverini, S., & Sciavicco, L. (1993). The parallel approach to force/position control of robotic manipulators. *Robotics and Automation, IEEE Transactions on, 9*(4), 361-373.

Chiaverini, S., Siciliano, B., & Villani, L. (1997). *Parallel force/position control with stiffness adaptation*.

Chiaverini, S., Siciliano, B., & Villani, L. (1999). A survey of robot interaction control schemes with experimental comparison. *Mechatronics, IEEE/ASME Transactions on, 4*(3), 273-285.

Chong-Shan, S., Guan, O., & Tian-Wen, G. (1990). Masticatory efficiency determined with direct measurement of food particles masticated by subjects with natural dentitions. *The Journal of Prosthetic Dentistry, 64*(6), 723-726.

Colbaugh, R., Seraji, H., & Glass, K. (1991). *Direct adaptive impedance control of manipulators*.

Craig, J. J. (1989). *Introduction to robotics* (Vol. 7): Addison-Wesley Reading, MA.

De Schutter, J., Bruyninckx, H., Zhu, W. H., & Spong, M. (1998). Force control: a bird's eye view. *Control Problems in Robotics and Automation*, 1-17.

de Wit, C. A. C., Siciliano, B., & Bastin, G. (1996). *Theory of robot control*: Springer Verlag.

Dellow, P., & Lund, J. (1971). Evidence for central timing of rhythmical mastication. *The Journal of Physiology, 215*(1), 1.

Drake, B. (1971). A quasi-rheological model element for fracture *Journal of texture studies, 2*(3), 365-372.

Fields, H. W. (1986). Variables affecting measurements of vertical occlusal force. *Journal of Dental Research, 65*(2), 135-138.

Fontijn-Tekamp, F. A. (2000). Biting and chewing in overdentures, full dentures, and natural dentitions. *Journal of Dental Research, 79*(7), 1519-1524.

Guglielmo, K., & Sadegh, N. (1993). *Theory and implementation of a hybrid learning force control scheme*.

Hannam, A. C. (1997). Jaw muscle structure and function. *Science and Practice of Occlusion, Quintessence Publishing Co, Inc*, 41?49.

Hatch, J. P., Shinkai, R. S. A., Sakai, S., Rugh, J. D., & Paunovich, E. D. (2001). Determinants of masticatory performance in dentate adults. *Archives of Oral Biology, 46*(7), 641-648.

Hayashi, T., Kato, S., Yamada, S., Nakajima, S., Yamada, Y., & Kobayashi, H. (2000). A physiological control of chewing-like jaw movement for robotizedjaw simulator JSN/2A. *Engineering in Medicine and Biology Society, 2000. Proceedings of the 22nd Annual International Conference of the IEEE, 1*.

Heath, M. R. (2002). The oral management of food: the bases of oral success and for understanding the sensations that drive us to eat. *Food Quality and Preference, 13*(7-8), 453-461.

Heath, M. R., & Prinz, J. F. (1999). Oral processing of foods and the sensory evaluation of texture. *Food Texture: Measurement and Perception. AJ Rosenthal, ed. Aspen: Gaithersburg, MD*, 18-29.

Heinrichs, B., & Sepehri, N. (1999). *A limitation of position based impedance control in static force regulation: theory and experiments*.

Hiiemae, K. M., & Palmer, J. B. (1999). Food transport and bolus formation during complete feeding sequences on foods of different initial consistency. *Dysphagia, 14*(1), 31-42.

Hoebler, C., Karinthi, A., Devaux, M. F., Guillon, F., Gallant, D., Bouchet, B., . . . Barry, J. L. (1998). Physical and chemical transformations of cereal food during oral digestion in human subjects. *British Journal of Nutrition, 80*(05), 429-436.

Hoebler, M.-F. D., A. Karinthi, C. Belleville, J.-L. Barry, C. (2000). Particle size of solid food after human mastication and in vitro simulation of oral breakdown. *International Journal of Food Sciences and Nutrition, 51*(5), 353-366.

Hogan, N. (1984). Impedance control of industrial robots. *Robotics and Computer-Integrated Manufacturing, 1*(1), 97-113.

Hogan, N. (1985a). Impedance control-An approach to manipulation. I-Theory. II-Implementation. III-Applications. *ASME Transactions Journal of Dynamic Systems and Measurement Control B, 107*, 1-24.

Hogan, N. (1985b). *Impedance control: An approach to manipulation*.

Hogan, N. (1985c). Impedance control: an approach to manipulation 梲 art II: implementation. *Transactions of the ASME, Journal of Dynamic Systems, Measurement and Control, 107*(1), 8?6.

Hsu, F. Y., & Fu, L. C. (1996). *Adaptive fuzzy hybrid force/position control for robot manipulators following contours of an uncertain object*.

Huang, L., Xu, W. L., Torrance, J., & Bronlund, J. E. (2010). Design Of A Position And Force Control Scheme For 6RSS Parallel Robots And Its Application In Chewing Robots. *Int. J. Human. Robot., 7*(03), 477-489.

Hutchings, J. B., & Lillford, P. J. (1988). The perception of food texture- The philosophy of the breakdown path. *Journal of texture studies, 19*(2), 103-115.

Ishijima, T., Koshino, H., Hirai, T., & Takasaki, H. (2004). The relationship between salivary secretion rate and masticatory efficiency. *Journal of Oral Rehabilitation, 31*(1), 3-6.

Jantzen, J. (2002). *A tutorial on adaptive fuzzy control*.

Jensen, J. R. (1996). Introductory Digital Image Processing Prentice-Hall. *Englewood Cliffs, NJ*.

Jeon, D., & Tomizuka, M. (1993). Learning hybrid force and position control of robot manipulators. *Robotics and Automation, IEEE Transactions on, 9*(4), 423-431.

Julien, K. C., Buschang, P. H., Throckmorton, G. S., & Dechow, P. C. (1996). Normal masticatory performance in young adults and children. *Arch Oral Biol, 41*(1), 69-75.

Kapur, K. K., Garrett, N. R., & Fischer, E. (1990). Effects of anaesthesia of human oral structures on masticatory performance and food particle size distribution. *Arch Oral Biol, 35*(5), 397-403.

Kayser, A. F. (1981). Shortened dental arches and oral function. *J Oral Rehabil, 8*(5), 457-462.

Kim, S. W., & Park, M. (1991). *Fuzzy compliance robot control*.

Klir, G. J., & Yuan, B. (1995). *Fuzzy sets and fuzzy logic: theory and applications*: Prentice Hall PTR Upper Saddle River, NJ, USA.

Kohyama, K., Hatakeyama, E., Sasaki, T., Azuma, T., & Karita, K. (2004). Effect of sample thickness on bite force studied with a multiple-point sheet sensor. *J. Oral Rehabil, 31*, 327-334.

Kohyama, K., Hatakeyama, E., Sasaki, T., Dan, H., Azuma, T., & Karita, K. (2004). Effects of sample hardness on human chewing force: a model study using silicone rubber. *Archives of Oral Biology, 49*(10), 805-816.

Koshino, H., Hirai, T., Ishijima, T., & Ikeda, Y. (1997). Tongue motor skills and masticatory performance in adult dentates, elderly dentates, and complete denture wearers. *The Journal of Prosthetic Dentistry, 77*(2), 147-152.

Lavigne, G., Kim, J., Valiquette, C., & Lund, J. (1987). Evidence that periodontal pressoreceptors provide positive feedback to jaw closing muscles during mastication. *Journal of Neurophysiology, 58*(2), 342.

Lu, W. S., & Meng, Q. H. (1991). Impedance control with adaptation for robotic manipulations. *Robotics and Automation, IEEE Transactions on, 7*(3), 408-415.

Lucas, P. W. (2004). *Dental Functional Morphology: How Teeth Work*: Cambridge University Press.

Lucas, P. W., & Luke, D. A. (1986). Is food particle size a criterion for the initiation of swallowing? *J Oral Rehabil, 13*(2), 127-136.

Lucibello, P. (1993). *A learning algorithm for hybrid force control of robot arms*.

Luke, D. A., & Lucas, P. W. (1985). Chewing efficiency in relation to occlusal and other variations in the natural human dentition. *British Dental Journal, 159*(12), 401-403.

Mandel, I. D. (1987). The functions of saliva. *J Dent Res, 66*, 623-627.

Matko, D., Kamnik, R., & Bajd, T. (1997). *Adaptive impedance control of the industrial robot*.

Mioche, L., Hiiemae, K. M., & Palmer, J. B. (2002). A postero-anterior videofluorographic study of the intra-oral management of food in man. *Archives of Oral Biology, 47*(4), 267-280.

Mohsenin, N. N. (1986). Physical properties of plant and animal materials. *New York*.

Nakajima, J., Hideshima, M., Takahashi, M., Taniguchi, H., & Ohyama, T. (2001). Masticatory mandibular movements for different foods textures related to onomatopoetic words. *J. Med. Dent. Sci, 48*, 121?129.

Nussinovitch, A., Lee, S., Kaletunc, G., & Peleg, M. (1991). Model for calculating the compressive deformability of double-layered curdlan gels. *Biotechnology progress, 7*(3), 272-274.

Ogawa, T., Ogawa, M., & Koyano, K. (2001). Different responses of masticatory movements after alteration of occlusal guidance related to individual movement pattern. *Journal of Oral Rehabilitation, 28*(9), 830-841.

Olkku, J., & Rha, C. K. (1975). Textural Parameters of Candy Licorice. *J. Food Sci, 40*, 1050.

Otsu, N. (1975). A threshold selection method from gray-level histograms. *Automatica, 11*, 285-296.

Palmer, J. B., Hiiemae, K. M., & Liu, J. (1997). Tongue-jaw linkages in human feeding: a preliminary videofluorographic study. *Arch Oral Biol, 42*(6), 429-441.

Pandian, S. R., & Kawamura, S. (1996). Hybrid force/position control for robot manipulators based on a D-type learning law. *Robotica, 14*(1), 51-60.

Pedersen, A. M., Bardow, A., Jensen, S. B., & Nauntofte, B. (2002). SALIVARY GLANDS AND SALIVA Number 5 Saliva and gastrointestinal functions of taste, mastication, swallowing and digestion. *Oral Diseases, 8*(3), 117.

Peleg, M. (1976). Considerations of a general rheological model for the mechanical behavior of viscoelastic solid food materials. *J. Texture Studies, 7*, 243-255.

Peleg, M., & Campanella, O. (1989). The mechanical sensitivity of soft compressible testing machines. *Journal of Rheology, 33*, 455.

Pelletier, M., & Daneshmend, L. (1990). *An adaptive compliant motion controller for robot manipulators based on damping control*.

ROY, I., Campanella, O., Normand, M., & Peleg, M. (1989). A RESEARCH NOTE UNIAXIAL COMPRESSION OF DOUBLE LAYERS OF SOLID FOODS 1. *Journal of texture studies, 20*(4), 443-455.

Sahoo, P. K., Soltani, S., & Wong, A. (1988). A survey of thresholding techniques. *Computer vision, graphics, and image processing, 41*(2), 233-260.

Saklar, S., Ungan, S., & Katnas, S. (1999). Instrumental crispness and crunchiness of roasted hazelnuts and correlations with sensory assessment. *Journal of food science, 64*(6), 1015-1019.

Salles, C., Tarrega, A., Mielle, P., Maratray, J., Gorria, P., Liaboeuf, J., & Liodenot, J. J. (2007). Development of a chewing simulator for food breakdown and the analysis of in vitro flavor compound release in a mouth environment. *Journal of Food Engineering, 82*(2), 189-198.

Shama, F., & Sherman, P. (1968). An automated parallel plate viscoelastometer for studying the rheological properties of solid food materials. *Rheology and Texture of Foodstuffs*, 77?71.

Sherman, P. (1974). General Introduction to Rheological Properties of Foods. *Dechema-Monographien, 77*(9).

Slotine, J. J., & Li, W. (1987). *Adaptive strategies in constrained manipulation*.

Soitrov, Z., & Botev, R. G. (1993). *A model reference approach to adaptive impedance control of robot manipulators*.

Spong, M. W., & Vidyasagar, M. (2008). *Robot dynamics and control*: Wiley-India.

Swyngedau, S., Normand, M., & Peleg, M. (1991). Comparison of two types of models for concave force - deformation curves presentation 1. *Journal of texture studies, 22*(3), 265-275.

Swyngedau, S., Nussinovitch, A., & Peleg, M. (1991). Models for the compressibility of layered polymeric sponges. *Polymer Engineering & Science, 31*(2), 140-144.

Takanobu, H., Maruyama, T., Takanishi, A., Ohtsuki, K., & Ohnishi, M. (2000). Mouth opening and closing training with 6-DOF parallel robot. *Robotics and Automation, 2000. Proceedings. ICRA'00. IEEE International Conference on, 2*.

Takanobu, H., Takanishi, A., Ozawa, D., Ohtsuki, K., Ohnishi, M., & Okino, A. (2002). Integrated dental robot system for mouth opening and closing training. *Robotics and Automation, 2002. Proceedings. ICRA'02. IEEE International Conference on, 2*.

Thexton, A. J., & Crompton, A. W. (1998). The control of swallowing. *The Scientific Basis of Eating, 9*, 168-222.

Thompson, T. (1999). How to use and interret the coupler curve and centrode atlas. Retrieved from www.cedarville.edu/academics/engineering/kinematics/ccapdf/howto.htm

Torrance, J., Pap, J., Xu, W., Bronlund, J., & Foster, K. (2006). *Motion control of a chewing robot of 6 RSS parallel mechanism.* Paper presented at the in Proceedings of 3rd International Conference on Autonomous Robots and Agents (ACARA), Palmerston North, New Zealand.

Van der Bilt, A., Engelen, L., Pereira, L., Van der Glas, H., & Abbink, J. (2006). Oral physiology and mastication. *Physiology & Behavior, 89*(1), 22-27.

Van Der Bilt, A., & Fontijn-Tekamp, F. (2004). Comparison of single and multiple sieve methods for the determination of masticatory performance. *Archives of Oral Biology, 49*(3), 193-198.

Velasco, F. R. D. (1980). Thresholding using the ISODATA clustering algorithm. *IEEE Transactions on Systems Man and Cybernetics, 10*, 771-774.

Whitcomb, L. L., Arimoto, S., Naniwa, T., & Ozaki, F. (1997). Adaptive model-based hybrid control of geometrically constrained robot arms. *Robotics and Automation, IEEE Transactions on, 13*(1), 105-116.

Whitney, D. E. (1987). Historical perspective and state of the art in robot force control. *The International Journal of Robotics Research, 6*(1), 3.

Wikipedia, t. f. e. (Producer). (2012). Retrieved from http://en.wikipedia.org/wiki/Digastric_muscle

Woda, A., Foster, K., Mishellany, A., & Peyron, M. (2006). Adaptation of healthy mastication to factors pertaining to the individual or to the food. *Physiology & Behavior, 89*(1), 28-35.

Xu, W. L., Lewis, D., Bronlund, J. E., & Morgenstern, M. P. (2008). Mechanism, design and motion control of a linkage chewing device for food evaluation. *Mechanism and Machine Theory, 43*(3), 376-389.

Yu, B. (2000). Modeling, control design and mechatronic implementation of constrained robots for surface finishing applications.

Zeng, G., & Hemami, A. (1997). An overview of robot force control. *Robotica, 15*(05), 473-482.

# 9. APPENDIX

The following figure shows the chewing velocity and force profile of Crunchie Bar during one chewing cycle.

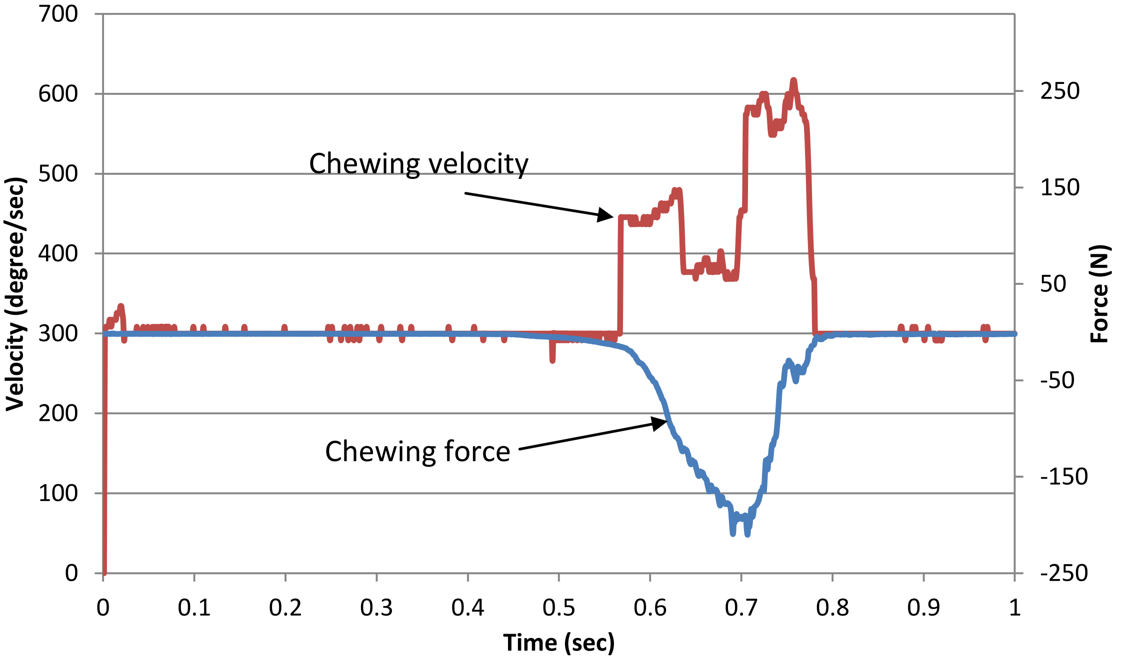

The following figure shows the chewing velocity and force profile of Apricot Bar during one chewing cycle

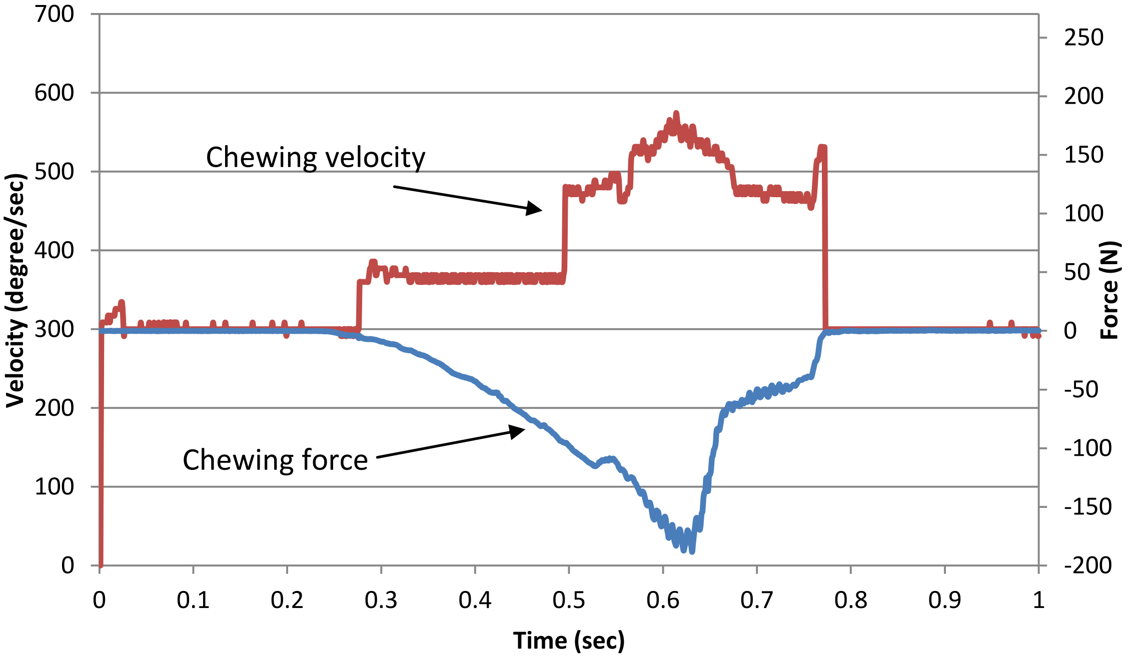

The following figure shows the chewing velocity and force profile of one of the peanuts during one chewing cycle.

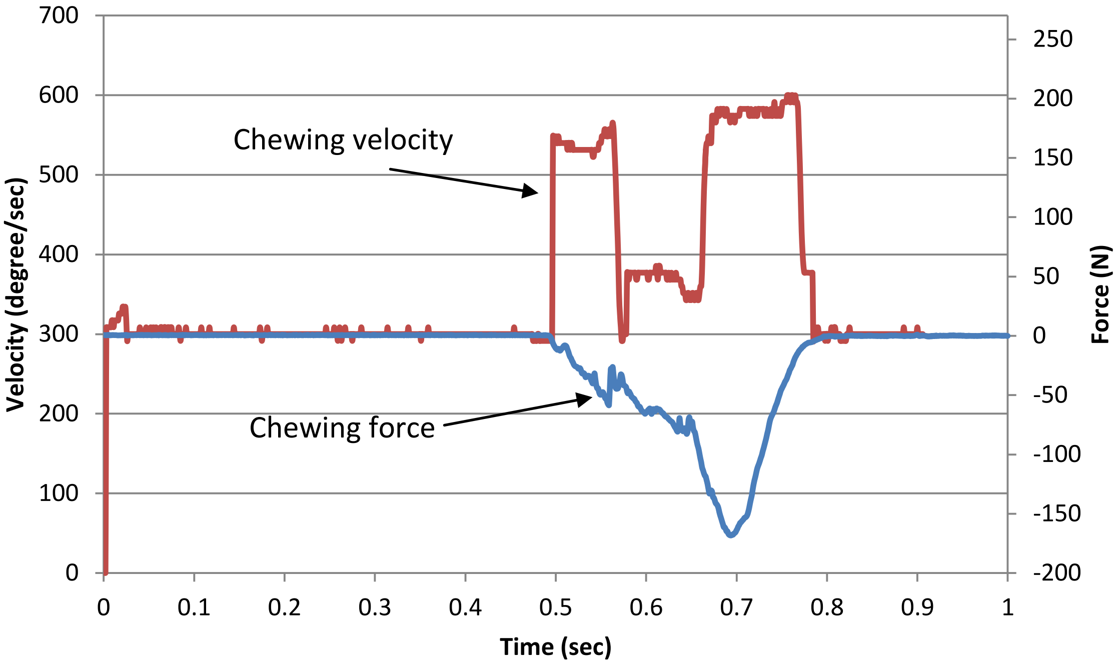

The following figure shows the chewing velocity and force profile of another one of the peanuts during one chewing cycle.